

**Reservoir characterization of Aptian carbonates;
Jebel Fadeloun and Jebel Garci, Tunisia**

by

Bjarte Lønøy

Master thesis

in sedimentology and petroleum geology



Department of geoscience

University of Bergen

June 2015

Abstract

This thesis presents the results of detailed petrographic and diagenetic analyses of the Aptian Serdj Fm. at the Jebel Fadeloun and Jebel Garci localities in northern Tunisia. The Serdj Fm. was deposited in a distally-steepened, open and temperate water carbonate ramp. The ramp was divided into eleven microfacies and eight sedimentary units, and vertical lithostratigraphic logging and petrographic studies were performed in order to establish the microfacies distribution. The ramp consists of four shallowing upward sequences deposited during an overall long-term regressive trend, and is dominated by packstones and grainstones. The sequences are separated by minor flooding events which are characterized by abrupt changes in grain size and sedimentary texture.

The Jebel Fadeloun locality is dominated by mid- to inner ramp facies, with early Aptian deposits represented by massive, locally karstified, orbitolinid- and miliolid-rich beds. Mid-Aptian deposits are characterized by intensively bioturbated bivalve-, echinoderm- and peloidal-rich beds with variable input of terrigenous quartz. Late Aptian is dominated by echinoderm-dominated deposits, and is capped by an unconformity representing the Aptian-Albian boundary. The Jebel Garci locality represents a more distal Aptian depositional setting with a condensed section of mid- to outer ramp deposits, capped by a highly bioturbated hardground.

Detailed thin-section studies and geochemical analyses indicate that the first stages of diagenetic alteration took place shortly after deposition, by microbial micritization and precipitation of fibrous to granular marine cements. Non-ferroan equant calcite cement precipitated at relatively shallow burial depths and/or during meteoric diagenesis. Pendant cement precipitated within the fresh-water vadose zone, during periods of subaerial exposure. Mouldic porosity formed by meteoric and/or burial diagenesis. Stylolites formed in response to increased pressure and associated pressure-dissolution during burial. Ferroan equant calcite cement is related to late diagenesis and postdates, at least to some extent, oil migration. Some of this cement was later dissolved.

Image analyses and plug measurements show that the porosity is mostly <6% in Jebel Fadeloun, and <1% in Jebel Garci. TinyPerm and plug measurements generally show permeabilities <0.1mD. A few beds show permeabilities of up to 1 Darcy, and are probably related to open fractures and/or measurement inaccuracies. Highest porosities and

permeabilities are observed within terrigenous-rich beds and inner ramp deposits, and reflect less cementation, increased fracturing, and increased dissolution of both grains and cements.

The observed reservoir quality may be significantly better in a reservoir situation due to the inhibiting effect of oil on late ferroan calcite cementation. STOOIP calculations based on minus-cement porosity (porosity plus ferroan calcite cement) show potential reserves that may be of economic significance.

Acknowledgements

I would like start of by thanking Gunnar Sælen for sharing his knowledge and experience, his outstanding enthusiasm and for giving me the opportunity to do research in Tunisia. Ståle Monstad is thanked and appreciated for his assistance, guidance and exciting scientific discussions during the development of this thesis.

Without the financial support and amazing backup from DNO international ASA, I wouldn't be able to participate at two comprehensive field seasons. By funding high quality petrographic thin sections, DNO gave me a good starting point.

During the two field seasons, Atef Bel Kahla and Thibault Cavailhes assisted both with their experience during field work, and also in terms of logistics. Their help have been greatly valued, and they have contributed in making the field work as efficient as possible.

In the field; several field assistants from Enterprise Tunisienne d'Activités Pétrolières (ETAP) helped out, and it would be difficult to mention everybody. They all gave a great effort in making the field days productive, but a few persons stood out from the crowd. Mohamed Riadh Chebbi, Nawel Jendoubi, Faycel Elferhi, Ahmed Klibi and Radouan Smaoui gave their best assistance during the whole field period and their help are much appreciated.

In desperate times, Irina (lab technician at University of Bergen) cleared her calendar and gave my Thin Sections (TS) a much needed polish. A more positive and helpful soul doesn't come around often. Thank you very much Irina.

I am most grateful for all the assistance, guidance and time my father, Arve, have set aside for me. By lending me his light microscope, he gave me the opportunity to take high quality pictures, and perform an extensive study of the thin sections.

I would also like to thank all my fellow students for all the good scientific discussions during the multiple coffee breaks.

Last but not least, I would like to thank my field partner, Fredrik Kjelkenes, for making the process of gathering data and research, a joyride. We have had several interesting scientific discussions, and I am pleased to have had such a great field partner.

Bergen, May 2015

Bjarte Lønøy

Bjarte Lønøy

Contents

1. Introduction.....	- 1 -
1.1 Aim.....	- 1 -
1.2 Study area.....	- 2 -
1.3 Previous studies.....	- 4 -
1.4 Outline.....	- 4 -
2. Geological framework.....	- 5 -
2.1 Tectonic history.....	- 7 -
2.1.1 Caledonian and Hercynian collision event – Ordovician to Carboniferous.....	- 7 -
2.1.2 Tethys rifting event – Late Carboniferous to Early Cretaceous.....	- 7 -
2.1.3 Austrian event – Cretaceous.....	- 8 -
2.1.4 Atlasic alpine event – Late Cretaceous to Pliocene.....	- 11 -
2.2 Stratigraphic framework.....	- 14 -
2.2.1 Precambrian.....	- 14 -
2.2.2 Paleozoic.....	- 14 -
2.2.3 Mesozoic.....	- 15 -
2.2.4 Cenozoic.....	- 22 -
3. Methodology.....	- 23 -
3.1 Fieldwork.....	- 23 -
3.2 Thin section studies.....	- 23 -
3.2.1 Ordinary light microscopy.....	- 24 -
3.2.2 Staining.....	- 24 -
3.2.3 Cathodoluminescence microscopy (CL).....	- 24 -
3.2.4 Fluid inclusions.....	- 25 -
3.2.5 Fluorescence microscopy.....	- 25 -
3.2.6 Photography.....	- 26 -
3.3 Porosity and permeability.....	- 26 -

3.3.1	TinyPerm II	- 26 -
3.3.2	Plug measurements.....	- 28 -
3.3.3	Image analysis	- 28 -
3.3.4	Lønøy's method for permeability estimation.....	- 29 -
3.4	Isotope analysis.....	- 29 -
3.4.1	Strontium.....	- 29 -
3.4.2	Carbon and Oxygen.....	- 29 -
4.	Results.....	- 31 -
4.1	Introduction	- 31 -
4.2	Microfacies	- 31 -
4.2.1	Microfacies 1 - MF1: Pelagic Mudstone/Wackestone	- 34 -
4.2.2	Microfacies 2 – MF2: Bivalve-Echinoderm-Peloidal Pack-/Grainstone	- 38 -
4.2.3	Microfacies 3 – MF3: Miliolid-Orbitolina-Peloidal Pack-/Grainstone.....	- 42 -
4.2.4	Microfacies 4 – MF4: Silty-Peloidal Pack-/Grainstone	- 44 -
4.2.5	Microfacies 5 – MF5: Intraclastic-Echinoderm-Peloidal Grainstone	- 46 -
4.2.6	Microfacies 6 – MF6: Benthic Foraminifera-Peloidal Pack-/Grainstone	- 49 -
4.2.7	Microfacies 7 – MF7: Red algal-Peloidal-Echinodermal Grainstone	- 51 -
4.2.8	Microfacies 8a – MF8a: Spiculitic-Peloidal Wacke-/Packstone.....	- 54 -
4.2.9	Microfacies 8b – MF8b: Spiculitic-Peloidal Packstone.....	- 57 -
4.2.10	Microfacies 9 – MF9: Peloidal Wacke-/Packstone	- 59 -
4.2.11	Microfacies 10 – MF10: Foraminifera-echinoderm-Peloidal Packstone	- 62 -
4.2.12	Grain size distribution	- 64 -
4.3	Sedimentary surfaces.....	- 65 -
4.3.1	Paleosol/caliche.....	- 65 -
4.3.2	Hardground.....	- 67 -
4.3.3	Paleokarst and ancient speleothems	- 69 -
4.4	Depositional units.....	- 73 -

4.4.1	Unit A	- 77 -
4.4.2	Unit B	- 78 -
4.4.3	Unit C	- 80 -
4.4.4	Unit D	- 81 -
4.4.5	Unit E	- 82 -
4.4.6	Unit F	- 83 -
4.4.7	Unit G	- 84 -
4.4.8	Unit H	- 86 -
4.5	Diagenesis	- 87 -
4.5.1	Micritization	- 87 -
4.5.2	Cementation and dissolution	- 90 -
4.5.3	Deep burial diagenesis	- 101 -
4.6	Geochemical analysis	- 103 -
4.6.1	Stable isotopes ($\delta^{18}\text{O}$ and $\delta^{13}\text{C}$)	- 103 -
4.6.2	Radiogenic isotopes	- 111 -
4.7	Fractures	- 114 -
4.8	Porosity and permeability	- 114 -
4.8.1	Introduction to porosity	- 114 -
4.8.2	Classification of pore types	- 116 -
4.8.3	Introduction to permeability	- 121 -
4.8.4	Pore types, porosity and permeability	- 125 -
5.	Discussion and summary	- 135 -
5.1	Depositional environment	- 135 -
5.1.1	Jebel Fadeloun	- 135 -
5.1.2	Jebel Garci	- 143 -
5.1.3	Paleotemperature, burial depth and age	- 144 -
5.2	Diagenetic evolution	- 146 -

5.3	Diagenetic evolution in a sequence stratigraphic framework.....	- 150 -
5.4	Reservoir quality/potential	- 153 -
5.5	Proposed further studies	- 159 -
6.	Conclusions.....	- 160 -
7.	References.....	- 163 -

1. Introduction

1.1 Aim

The aim for this master thesis in carbonate sedimentology and petroleum geology, is to study the reservoir quality of an Aptian temperate carbonate ramp outcropping in the anticline of Jebel Fadeloun (Jebel meaning mountain in Arabic), and as a condensed section in Jebel Garci (Figure 1.1). The study is based on field observation, petrographic studies, porosity estimations, permeability measurements and estimations, fluid inclusions and $\delta^{18}\text{O}$, $\delta^{13}\text{C}$, and $^{87}\text{Sr}/^{86}\text{Sr}$ analyses. This study is a part of DNO ASA and L'Entreprise Tunisienne d'Activités Pétrolières (ETAP) exploration of the Fkirine permit (Figure 1.1), and was carried out in parallel with Fredrik Kjelkenes's (fellow student) structural study of the same area. The results presented here, may provide useful data for DNO ASA and ETAP in deciding the location of drilling exploration wells, and to put potential cost against revenue. Data collected, interpreted and presented in this thesis, may also serve as a good analogue for petroleum reservoirs in similar depositional environments and to predict the subsurface facies distribution of the Fkirine permit.

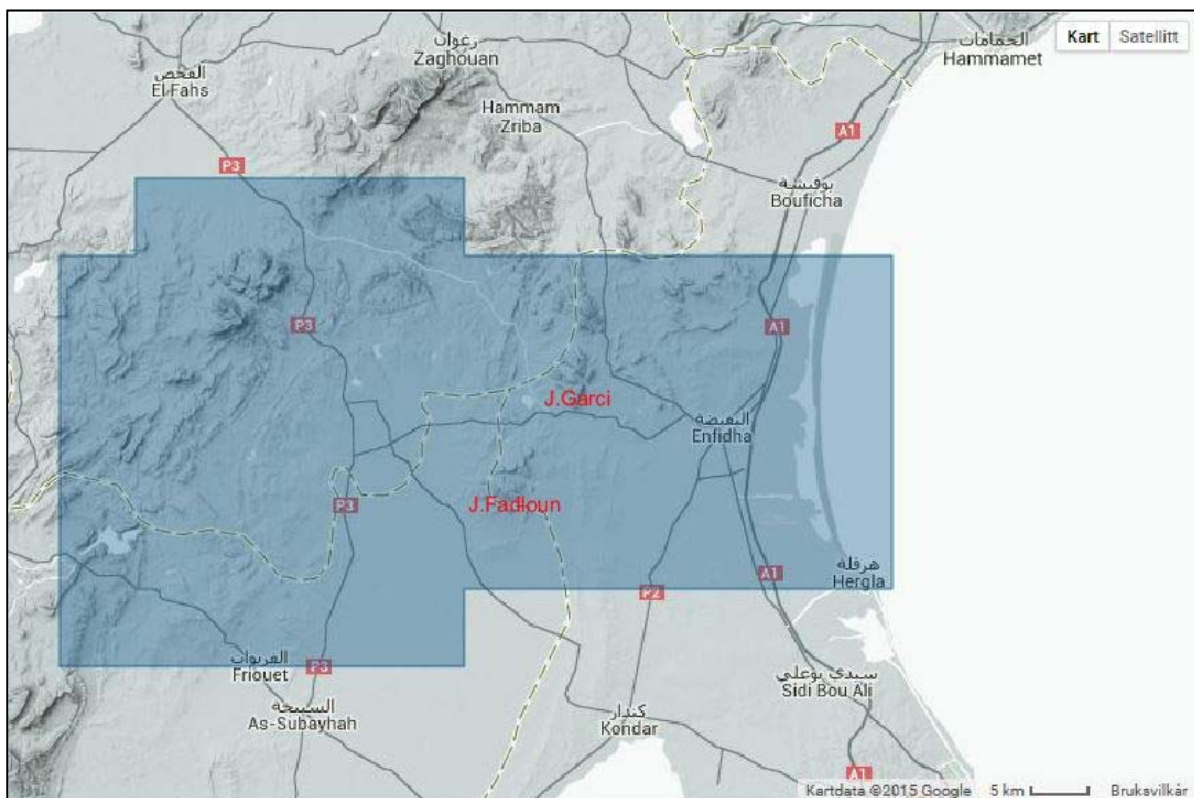


Figure 1.1: Map overview showing terrain and outlining the Fkirine permit (Modified from Google Earth).

1.2 Study area

The studied area is located in the eastern part of Tunisia in the Pelagian province (Figure 1.1 and Figure 2.2). Jebel Fadeloun (J.Fadeloun) is located on the border between the Sousse province and the Kairouan province. This location is approximately 30km west of the Gulf of Hammamet, and 20km west-southwest of the city Enfidha. J.Fadeloun comprises a major northeast – southwest trending anticline, dissected by complex faults, fractures, and joints. The anticline has sparse vegetation with large areas covered by debris. In combination with the high abundance of faults, this made a continuous logging a challenge. J.Fadeloun is approximately 3km long (north-south) and 4km wide (east-west). J.Fadeloun is on average 250m high (above sea level) (according to elevation profile made by Google Earth). The outcrops in J.Fadeloun consist predominantly of Aptian to Maastrichtian limestones, with minor coverage of Quaternary surficial deposits. The studied Aptian sequence belongs to the Serdj formation, and outcrops in several locations at J.Fadeloun (Figure 1.2).

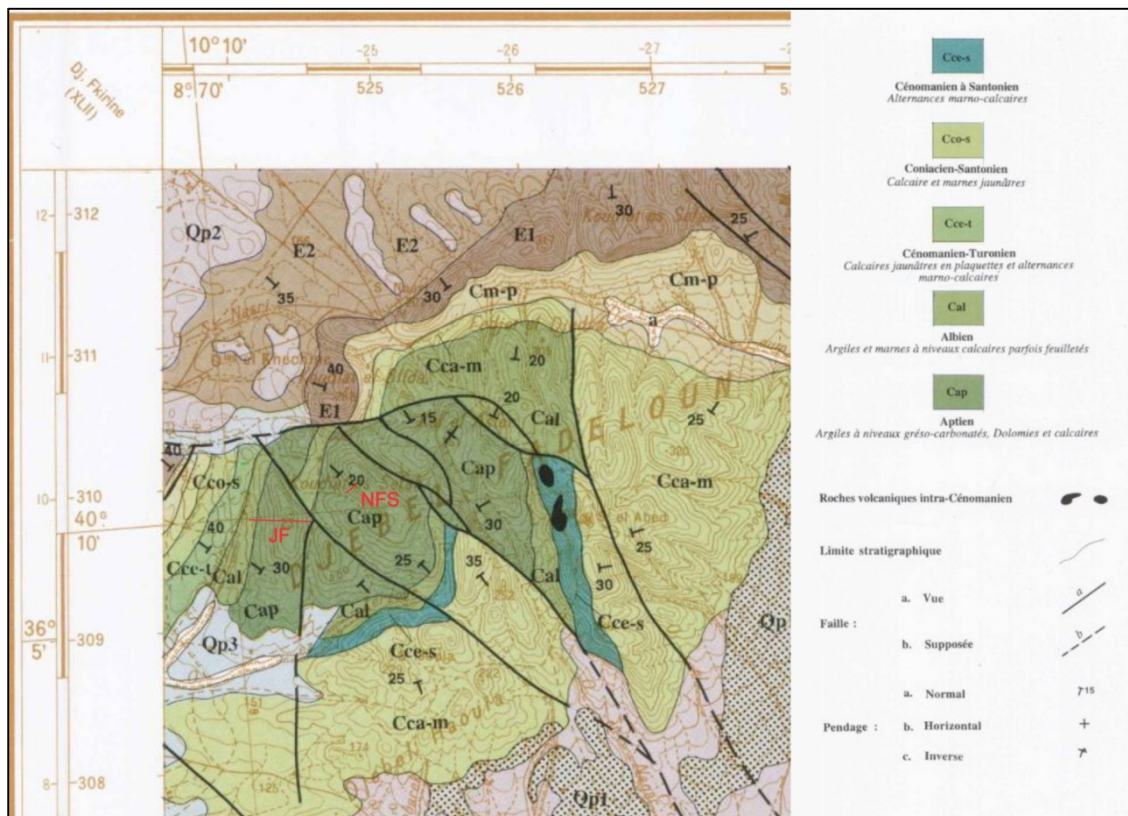


Figure 1.2: Geological map over J.Fadeloun. Red lines indicate logged section. JF = Southern J.Fadeloun section, NFS = Northern J.Fadeloun section (Modified from map published by Directin du Service Géologique, 2003).

In Jebel Garci (J.Garci), a 5m condensed section of Aptian sediments outcrops on the southern part of the mountain (Moez et al., 2012; Fadhel et al., 2014). The outcrop is proximal to a major fault zone (offset not visible and therefore not possible to measure), where Aptian (Serdj Fm.) sedimentary rocks are juxtaposed against Albian (equivalent to lower Fadhene Fm.) sedimentary rocks (Figure 1.3).

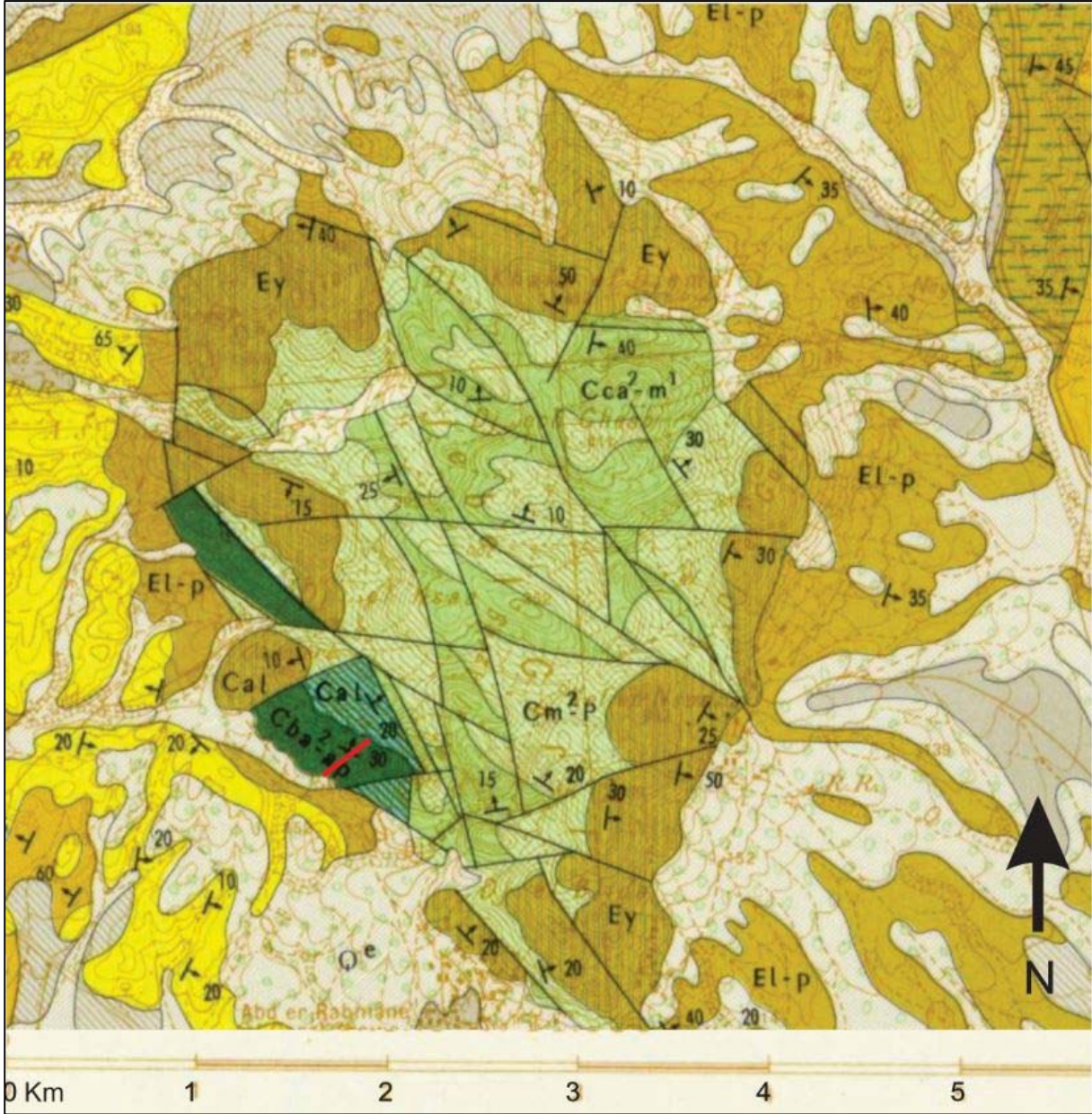


Figure 1.3: Geological map of J.Garci. The studied section is marked with a red line. Dark green = Barremian - Aptian, White/Green lines= Albian, Lighter green = Campanian - Maastrichtian, and Lightest green = Maastrichtian – Paleocene (Modified from map published by Directin du Service Géologique, 2003).

1.3 Previous studies

The Aptian-Albian outcrops at Jebel Fadeloun and Jebel Garci have only been little studied; there are no known publications of petrophysical studies in the Jebel Fadeloun area, and only a few internal reports made for DNO International ASA by Dr. Luigi Spalluto in 2012 were available. These reports focus on microfacies analysis of the Jurassic and Cretaceous carbonate units within the Fkirine permit, predominantly of Jebel Zaress, Jebel Fkirine, Jebel Fadhloun and Bent Saidane. Previous studies published on Jebel Garci include biostratigraphy on radiolarian and planktonic foraminifera. Fadhel et al. (2014); Moez et al. (2012) are a some of the known published studies done on Jebel Garci. However, little study from these localities has been carried out, and only a few publications have been made.

1.4 Outline

The geological framework is presented in Chapter 2, and primarily focuses on the stratigraphic and tectonic evolution of Tunisia. In Chapter 3 the methodology is described, while the results derived from these methods are presented in Chapter 4. Chapter 4 is subdivided into sections which include results from outcrop observation and subsequent petrographic and analytical work. The sections present data on microfacies, depositional units, sedimentary surfaces, diagenetic features and reservoir parameters. The results are discussed in Chapter 5 with emphasis on probable depositional environments, diagenetic history and evolution in a sequence stratigraphic framework, the reservoir potential, as well as suggestions for further studies of the area. A conclusion is presented in Chapter 6, whilst the Appendix contains complete records of the data obtained and stratigraphic logs.

2. Geological framework

Tunisia is located in the northern part of Africa, and borders Algeria to the west and Libya to the southeast. In the literature, Tunisia is often subdivided into several provinces constrained on the basis of topography, structure, history, lithology, location and so on. For the simplicity, in this thesis the nomenclature of Tawadros (2011) is applied. Tawadros (2011) sub-divides Tunisia into five tectono-stratigraphic provinces: Southern Tunisia (Sahara Platform), Eastern Tunisia (consists mostly of the Pelagian platform), Northern Tunisia (Atlas and Tell domain), Western Tunisia and Central Tunisia (see Figure 2.1)

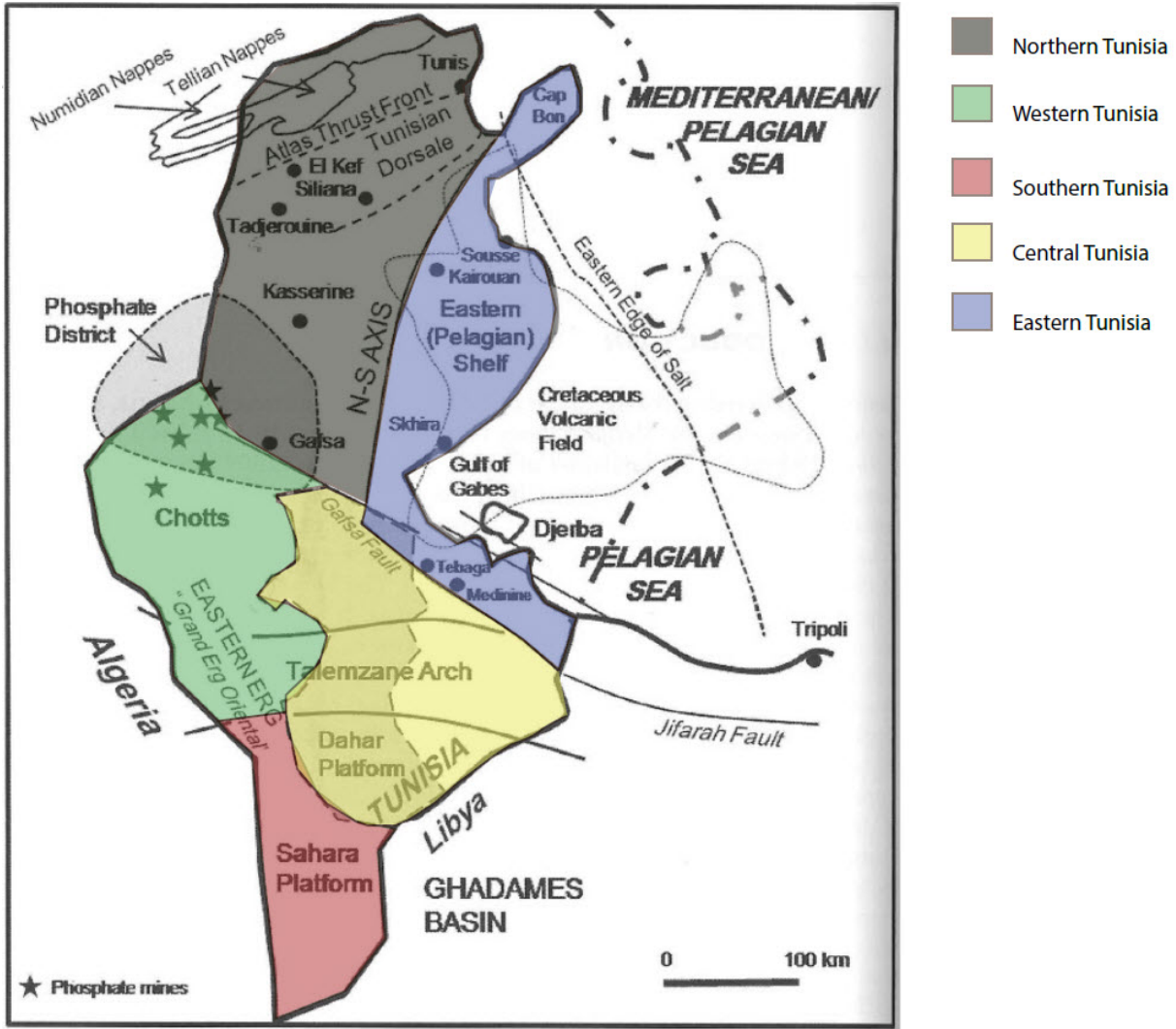


Figure 2.1: Map of Tunisia with main tectonic elements and subdivision of tectono-stratigraphic provinces. (modified after Tawadros (2011) and based on Buroillet (1991), Ahlbrandt (2001) and Mattoussi Kort et al. (2009))

The studied area belongs to the Pelagian Province, which is located mainly in the eastern Tunisia, and the northwestern Libya (Figure 2.2). In northern Tunisia, the N-S axis (NOSA) separates the Atlas and Tell domain from the Pelagian province. The province extends all the way to the Talemzane Arch and Jifarah Fault, in the southern part of Tunisia. A portion of the Pelagian province extends far into Malta and offshore Italy, as observed in the USGS-defined map of the province (Figure 2.2)

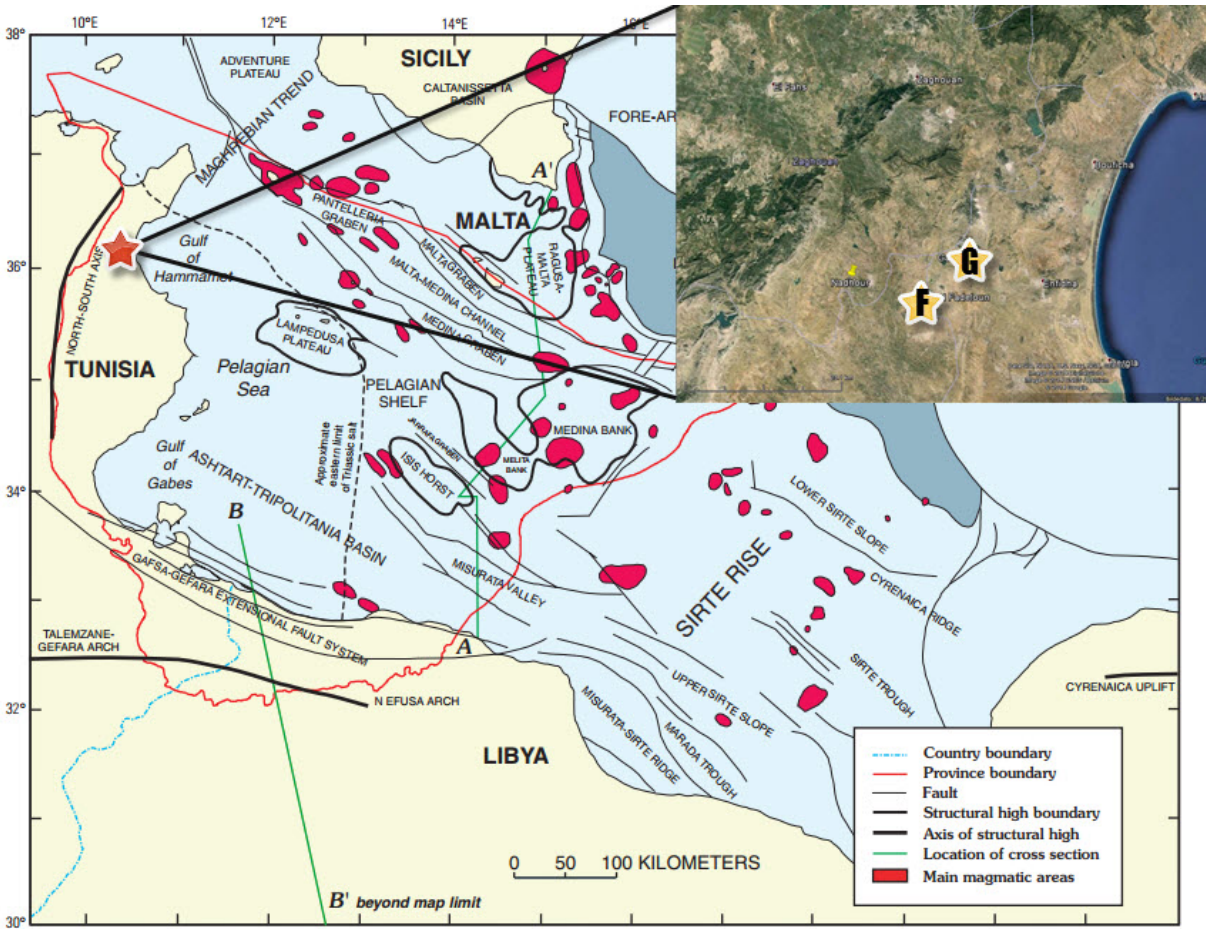


Figure 2.2: Map of northern Africa and the central Mediterranean Sea, showing the USGS-defined Pelagian province with major geologic structures. A map showing the localities for J.Fadeloun (yellow star with F) and J.Garci (yellow star with G) is inset in the upper right corner. The red star marks the location for the inset and the Enfidah area (modified from Finetti (1982), Jongsma et al. (1985) Bishop (1988), Buroillet (1991), Klett (2001) and Google Earth).

The Lower Cretaceous of the Enfidah area (marked with a red star in Figure 2.2) can be observed in the Fadeloun-Garci-Mdeker structure that is part of the studied area. Both the Jebel Fadeloun (J.Fadeloun) and the Jebel Garci (J.Garci) belong to the Fadeloun-Garci-Mdeker structure, which is composed of three anticlines (Moez et al., 2012). The anticlines

have a North-South trend and are considered as the prolongation of the N-S axis (Saadi, 1990; Moez et al., 2012). The J.Fadeloun and J.Garci anticlines are part of the Fkirine permit (Figure 1.1) and constitute the study area.

2.1 Tectonic history

The tectonic history of the Tunisian Precambrian is poorly known (Mejri et al., 2006), and is not described in this chapter. The tectonic evolution of Tunisia can best be divided into main sections described in the following chronological steps:

2.1.1 Caledonian and Hercynian collision event – Ordovician to Carboniferous

In Tunisia there is no exposed evidence of the Pangea forming collision between Gondwanaland and Laurasia. The occurrence of a major collision can be assumed, only based on geophysical and subsurface data gathered from wells in the southern Tunisia. Thickness and facies variations in Ordovician to Devonian series of the southern Tunisia, suggest discrete movements (Mejri et al., 2006). Older Paleozoic units have been folded, uplifted and eroded (Buroillet et al., 1978; Boote et al., 1998; Klett, 2001), resulting in a major unconformity where Carboniferous to Triassic horizons directly overlie older Paleozoic units of Cambrian to Carboniferous ages (Mejri et al., 2006).

2.1.2 Tethys rifting event – Late Carboniferous to Early Cretaceous

In the Late Carboniferous several rift basins and grabens started to form along the northern margin of the African plate, as a result of extension. The initial breakup of Gondwanaland and the opening of the Tethys Ocean, led to extensive crustal thinning and rifting predominantly oriented W-E and NW-SE (Klett, 2001). The rifting process peaked in the Late Cretaceous, and ceased in the early Tertiary (Guiraud, 1998).

In the Early Cretaceous, dextral shearing caused rifting along the African – European Rift Zone (often referred to as AERZ), resulting in subsidence of the Saharan Atlas (Klett, 2001).

Faults related to the rifting process controlled, and has continued to control the sedimentation in northern Tunisia, to the present day (Morgan et al., 1998).

Intense subsidence in the Mesozoic is reflected by thick accumulations of Triassic evaporites, superimposed by thick Jurassic-Cretaceous siliciclastic and carbonate units. In some areas of Tunisia, the overburden of Jurassic-Cretaceous sediments was sufficient to initiate flowage of Triassic evaporites, that continued into the late Cretaceous (Klett, 2001). The migration of evaporites caused surface penetrating diapirs and salt walls to form, and caused great lateral sediment thickness variations. Along the N-S axis (NOSA), the sediment thickness is very irregular due to local NS distension, and curvature of Triassic salts causing small scale tilting of small blocks (Mejri et al., 2006).

The NOSA separated the more stable eastern side from the more tectonic active western side, and worked as buffer for folding and faulting. The eastern area of the NOSA generally represented shallower water and the western area deeper water during the late Carboniferous to early Cretaceous. In general faults and depocenters along the NOSA, commonly trended roughly N-S and E-W during the Early Mesozoic, and played a major role in the depositional and structural pattern along NOSA (Klett, 2001; Mejri et al., 2006).

2.1.3 Austrian event - Cretaceous

North of the Talemzane Gefara arch (Figure 2.2) the depocenters of Late Paleozoic started to migrate northward simultaneously with the development of the Gafsa-Gefara extensional system (Figure 2.2). As a result, the area was extensively uplifted and eroded during the Aptian. Denudation were particularly high along the NOSA, and resulted in the Austrian unconformity (Figure 2.7) (Buroillet, 1991; Klett, 2001)

In the early Late Cretaceous there was a major change in drift of the African plate relative to the European plate. The African plate started to migrate northward towards the European plate as a result of sea-floor spreading both in the North and South Atlantic, a movement that has continued up to the present (Morgan et al., 1998). The migration resulted in dextral shearing and development of complex horst and graben structures as rifting occurred along the African and European plate boundaries (Morgan et al., 1998; Klett, 2001). The sedimentation during this period was strongly controlled by associated fault displacements

and the uplift of horst blocks (Morgan et al., 1998; Klett, 2001). The opening of the North Atlantic in the mid to late Cretaceous led to the initial drift of Iberia to the southeast. In the literature the exact timing of the initial drift is widely discussed, suggesting an initial migration as early as Albian (Coward and Dietrich, 1989) to as late as the Campanian-Turonian boundary (Dewey et al., 1989). However, this resulted in a reversal in the relative movement of the African plate and the European plate (shown in Figure 2.3). The reversal of migration led to dextral transpression in the African-European Rift Zone (AERZ)(Morgan et al., 1998).

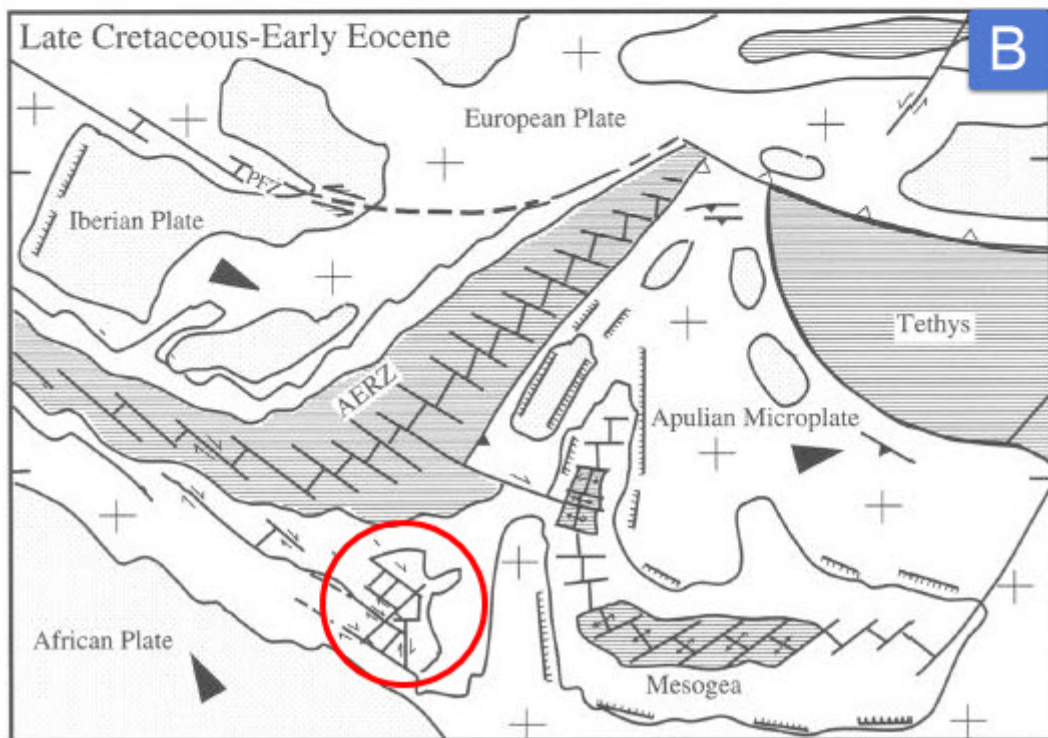
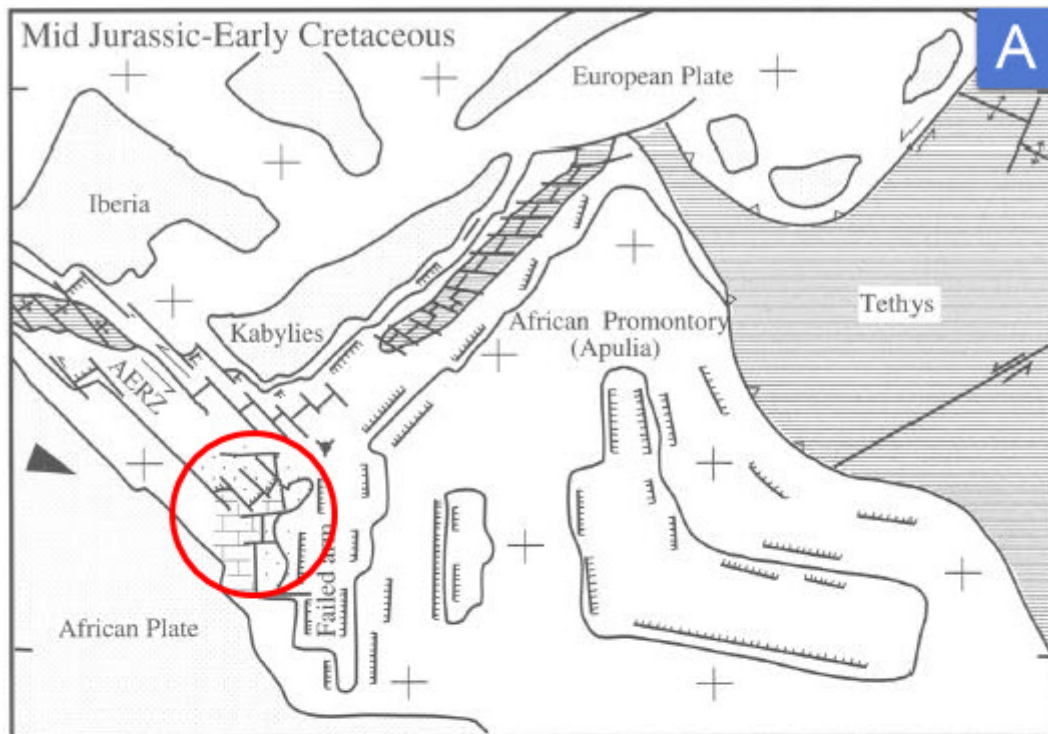


Figure 2.3: A) Mid Jurassic to Early Cretaceous plate tectonic model. B) Late Cretaceous to Early Eocene plate tectonic model of the Mediterranean area. Relative plate movements are shown with black arrows. The approximate location of the northeastern Tunisia is marked with a red circle. (Modified from Morgan et al, 1998).

2.1.4 **Atlassic alpine event – Late Cretaceous to Pliocene**

The initial convergence between the African and the European plates started in the Late Cretaceous (see above), and continued throughout the Cenozoic. During this period, a complex sedimentary and structural pattern emerged as a result of a poly-phase tectonic history.

In northern Tunisia, Late Cretaceous NW-SE oriented compression resulted in development of NE-SW trending folds. Proximal to the NOSA the axis acted as a barrier, forcing the folds and depocenters to a roughly N-S trend along the western margin. Several anticlinal and synclinal axes are scattered along the western side of the NOSA, and resulted in significant variation in thickness and facies. In the Pelagian province (east of NOSA), the ongoing extension that started during the Early Cretaceous times continued, and several NW-SE trending grabens started to form. Volcanism was active during part of this period (Mejri et al., 2006).

Reactivation of W-S and WNW-ESE transfer faults controlled the sedimentation during the Early Eocene (Klett, 2001). In the mid- to late Eocene, and simultaneous with the Pyrenean orogeny in Europe (often referred to as the Pyrenean event, as in Figure 2.7), the compressional phase acting on the NOSA was reversed. The stress state on the NOSA was rotated to approximately N-S, and the eastern region which was a high and stable region prior to the rotation now experienced strong subsidence. This led to the formation of the lowlands and flooded offshore regions that can be observed at present.

In the Oligocene the Kabylie microplate collided with the African margin and is marked by an angular unconformity at the base of the Oligocene section (Jongsma et al., 1985; Morgan et al., 1998; Klett, 2001). The collision resulted in development of a fractured mobile terrain along the northern margin of the Pelagian province, while leaving the southern area as a fixed passive platform (Klett, 2001). In the literature there are some controversies about the depositional history during the Oligocene-Miocene. Klett (2001) suggests that Late Oligocene to Miocene tectonic activity resulted in non-deposition or erosion of large areas in Tunisia. Klett (2000) also suggests that in some areas the entire Paleogene section is removed and whereas an angular unconformity is present in certain areas, a disconformity between Miocene and underlying older beds are present in eastern Tunisia. Bouaziz et al. (2002) on the other hand, suggest a deposition of thick clastic continental to shallow marine Miocene

sediments in the north-central Tunisia by erosion of reliefs relating to the compressional structures developed in the Late Eocene. In central Tunisia these conglomerates, sandstones and clays are widespread in the broad synclines, and commonly display normal fault populations and syn-faulting growth basins, commonly with a NW-SE trend (Bouaziz et al., 2002). The Miocene extensional phase led to subsiding basins all over Tunisia and during the Late Miocene to Early Pliocene several of the faults related to subsidence, were folded and reworked as right lateral strike-slip faults (Bouaziz et al., 2002).

The ongoing convergence between the African plate and the Sardinia block was intensified in the Late Miocene. Tortonian N-W movement of the African plate caused crustal shortening (Klett, 2001) and strike-slip movement along the main basement lineament occurred, resulting in folding throughout the Atlassic Tunisia (Klett, 2001; Mejri et al., 2006). In the end of Tortonian the structural and sedimentary processes was inverted. The tension related to the compressional phase decreased and led to a short period with relaxation and distension, associated with a marine transgression and deposition of evaporites (Mejri et al., 2006). Miocene ended with an intensified compression, which continued into the Pliocene, resulting in local erosions and angular unconformities in the base of Pliocene (Mejri et al., 2006).

In the Early Pleistocene a new important orogenic phase evolved, folding and in many places overturning nappes. Sinistral transpression occurring along the NOSA during the Late Miocene resulted in positive flower structures with overthrusting wedges that are subaerially exposed. This orogenic phase have a played a major role in shaping Tunisian to its recent topography and relief (Mejri et al., 2006). The major tectonic features developed through time can be observed in Figure 2.4.

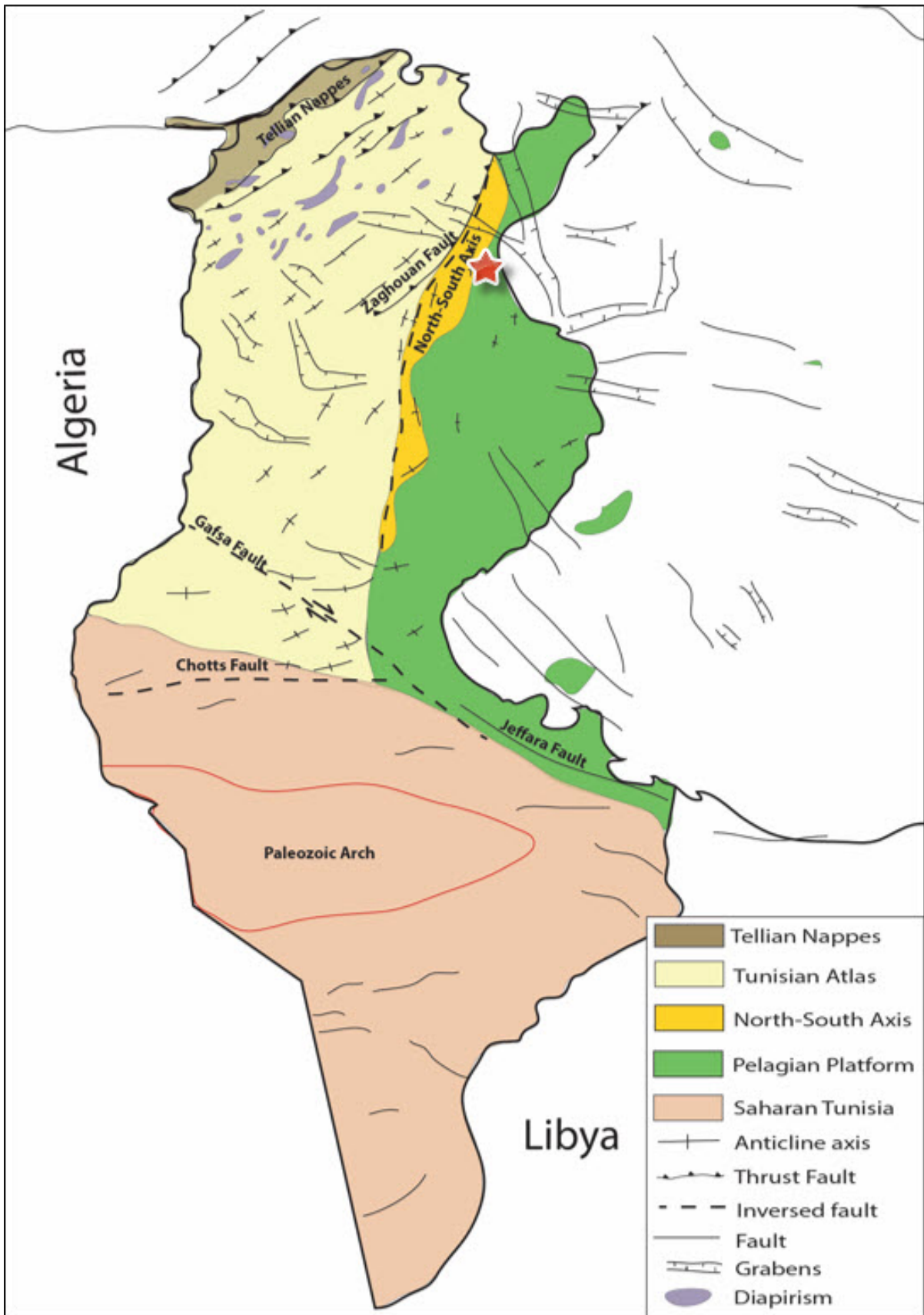


Figure 2.4: Tectonic sketch of Tunisia. Only major tectonic features are marked on the sketch. Red star indicates the approximate location of the study area (J.Fadeloun and J.Garci). Modified from Rykkje (2015) after (Esso, 1988; Burolet, 1991; Mejri et al., 2006; Bjorlykke, 2010).

2.2 Stratigraphic framework

The stratigraphic nomenclature applied in the following chapter, is derived from Mejri et al. (2006). A short overview of Precambrian – Cretaceous rocks is given below, with emphasis on the Mesozoic succession:

2.2.1 Precambrian

Precambrian rocks do not outcrop in Tunisia (Ben Ferjani et al., 1990; Burollet, 1991; Mejri et al., 2006; Tawadros, 2011), and only a few wells in the Saharan part of southern Tunisia have been drilled into the granitic or metamorphic Precambrian basement. In the northern and eastern Tunisia there is no information about the age, nature or depth of the basement. The base of the continental crust is indicated by a seismic geo-traverse to be 37-40 km deep below central Tunisia, with a shallowing towards the sea in the north and east (Mejri et al., 2006). Outcropping N-S, SW-NE and NW-SE oriented lineaments could be ascribed to basement features (Mejri et al., 2006).

2.2.2 Paleozoic

Paleozoic sedimentary rocks of Permian age only crop out as small exposures near Medenine in the Jebel Tebaga area of SE Tunisia (Figure 2.5) (Mejri et al., 2006). However, several wells have encountered the Paleozoic sedimentary rocks in the subsurface, and especially in the Saharan part of southern Tunisia since exploration for oil and gas has been primarily focused in this part of the country. The stratigraphic nomenclature of the Paleozoic is mostly derived from units located in this area (Bishop, 1975; Ben Ferjani et al., 1990). Several lithostratigraphic names also stem from neighboring countries, as Paleozoic outcrops are also present here (Mejri et al., 2006).

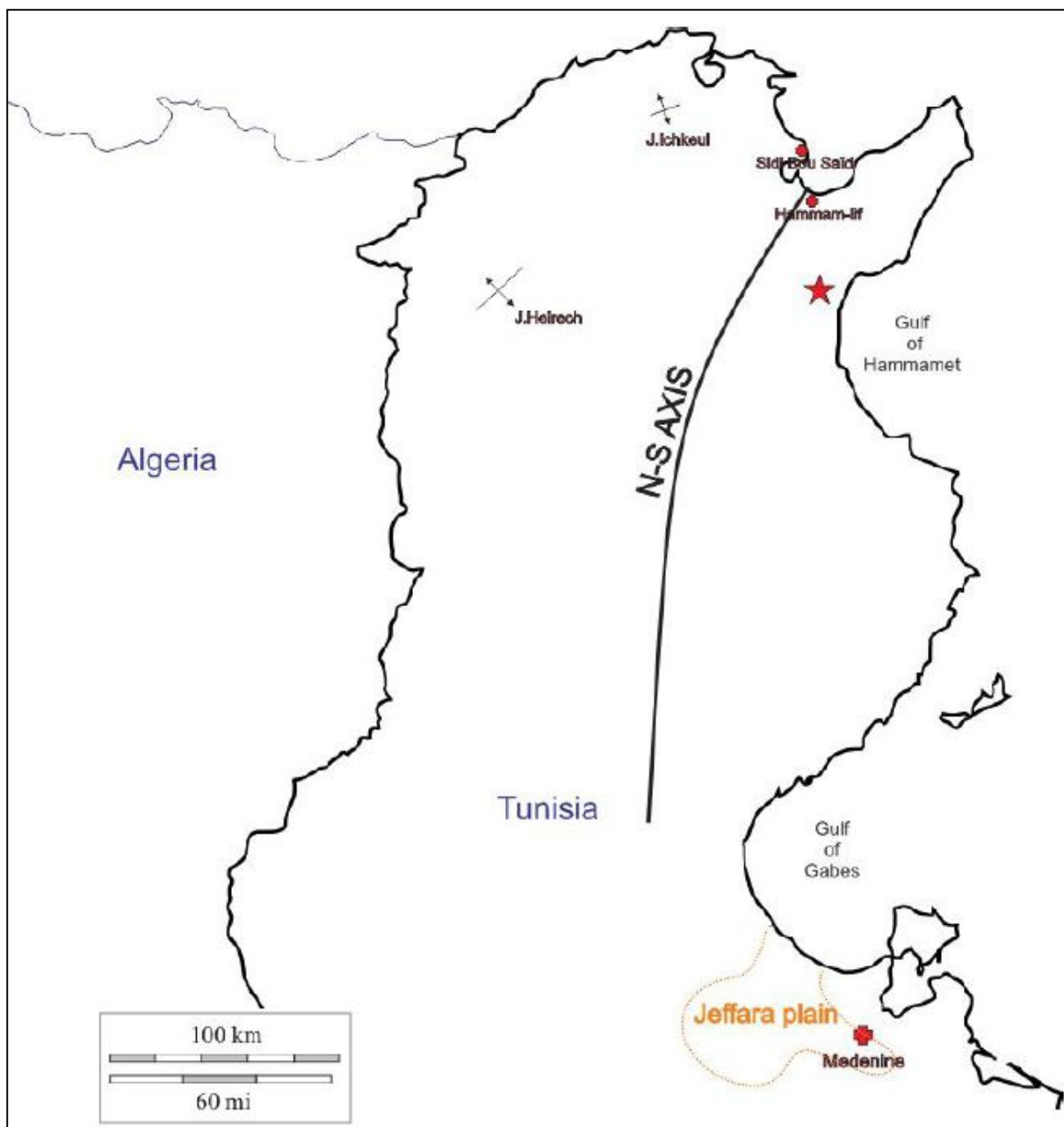


Figure 2.5: Sketch of Tunisia. Approximate location of localities described in Chapter 2. Red star indicate locality for studied area.

2.2.3 Mesozoic

Triassic

Triassic sedimentary rocks are found in several places in Tunisia, and are usually slightly metamorphic. The Triassic succession can be divided into a lower predominantly siliciclastic interval and an upper evaporitic interval (Bishop, 1975; Klett, 2001). The lower siliciclastic interval includes sandstones and mudstones ascribed to the Bir Mastoura, Ouled Chebbi and

the Kirchaou Fms. (and its equivalents) (Klett, 2001). The most prominent and well known outcrops of Triassic metamorphic sedimentary rocks are those of the two large anticlinal domes in northern Tunisia; J.Hairech and J.Ichkeul (Figure 2.5) There are only few outcrops of autochthonous Triassic sedimentary rocks known from southern Tunisia and they are all found in the Jeffara plain (Figure 2.5), between Medenine and the Libyan border. In all other locations, the Triassic series is outcropping as diapiric extrusions of mixed gypsum, silt, clay and dolomite. The mixture is quite chaotic and it is difficult to establish any stratigraphic succession (Mejri et al., 2006). The Triassic series thickens towards the north, in particular the evaporitic succession which has high abundance of halite. Hence, northwestern Tunisia has experienced a high frequency of strong salt driven tectonics. The migration of these Triassic salts has led to the present day evaporitic extrusions and underground domes in the Atlas and Tell domain (Northern Tunisia)(Mejri et al., 2006). In other areas of Tunisia the evaporitic layers are very thin and in some places completely absent, which is the case for the Pelagian province. The absence of evaporites in this province results in no décollements between the bedrock and the sedimentary cover. The Triassic sedimentary deposit of the Pelagian province were continental in the south to shallow marine in the north. However, northernmost subsurface extent of these siliciclastic rocks is not known (Bishop, 1975; Klett, 2001; Mejri et al., 2006).

Jurassic

Jurassic outcrops are observed in northern Tunisia, along the N-S axis from Hammamlif to Sidi Bou Zid (Figure 2.5) and are also found near Jeffara-Dahar. Jurassic sedimentary rocks have been encountered by numerous wells both onshore- and offshore Tunisia (Mejri et al., 2006). The Jurassic section is mostly comprised of carbonate rocks, that range from shallow marine in the south to increasingly deeper and more pelagic in the northwestward direction (Buroillet et al., 1978; Klett, 2001; Mejri et al., 2006). Terrigenous deltaic and lagoonal facies were present in the south and southwest in the Late Triassic, and prograded towards the northeast by the Early Cretaceous (Aptian) (Bishop, 1975; Buroillet et al., 1978; M'rabet, 1984; Klett, 2001; Mejri et al., 2006). Figure 2.6 shows the migration of facies through time during the Late Jurassic and Early Cretaceous.

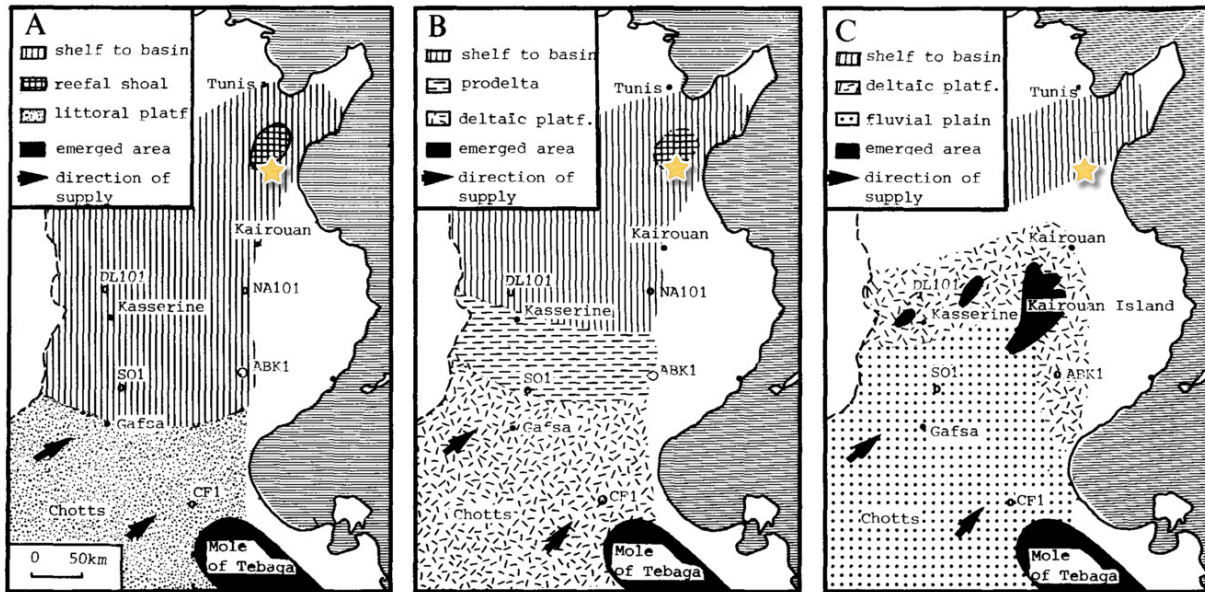


Figure 2.6: Paleogeographic reconstructions and depositional environments of the Northern- and Eastern Tunisia. A: During Tithonian (U.Jurassic), B: During the Berriasian (L. Cretaceous) and C: During the L.Hauterivian-Barremian (L.Cretaceous). The yellow star marks approximately the location for the studied area (modified from M'rabet (1984))

The Upper Jurassic Nara Fm. and the Upper Jurassic to Lower Cretaceous Sidi Khalif and M'Cherga Fms. are predominantly found offshore and composed of marine deposits including limestone, dolostone and marls (Salaj, 1978; Klett, 2001). Landwards, deposits include sandstones of the M'Rabatine and the Meloussi Fms., as shown in Figure 2.7.

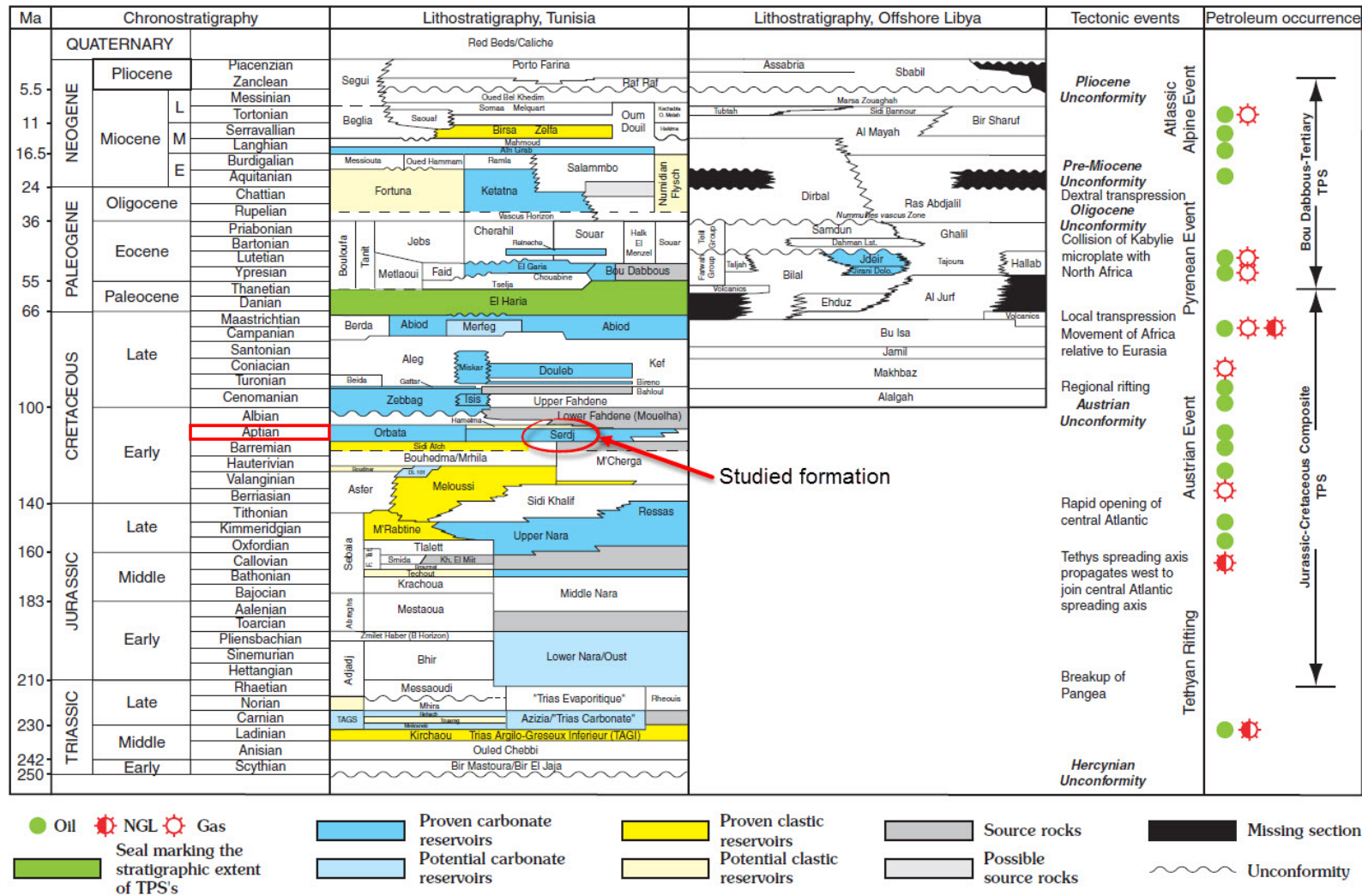


Figure 2.7: Overview of the stratigraphic nomenclature, major tectonic events and hydrocarbon occurrence of Tunisia and offshore Libya. Lithostratigraphy for Tunisia represent all tectono-stratigraphic provinces of Tunisia, including the Pelagian Province. Dashed lines show approximate position of formation boundaries. (Modified from Klett (2001), Hammuda et al. (1992) and Entreprise Tunisienne d'Activités Pétrolières (1997))

Cretaceous

Cretaceous outcrops are numerous, but are largely observed in northern Tunisia (Atlassic) and southern Tunisia (Saharan). A major unconformity close to the base of the Upper Albian beds, divides the Cretaceous system in Tunisia into two distinct parts. The Albian stage in Tunisia is therefore included in the Upper Cretaceous series (Mejri et al., 2006). The Cretaceous-Jurassic boundary is not easy to recognize in the field (Mejri et al., 2006).

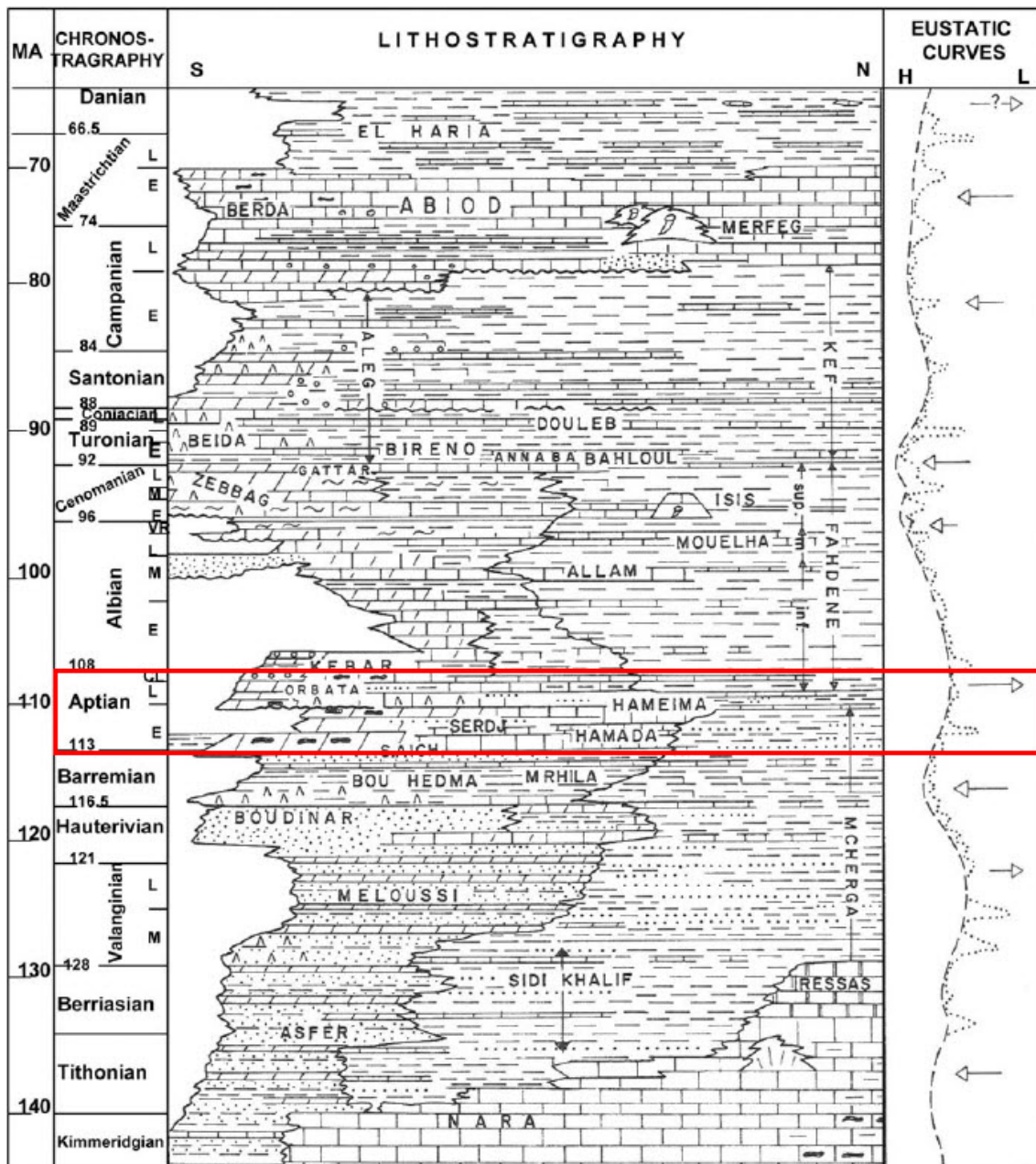


Figure 2.8: Lithostratigraphy of Cretaceous in Tunisia. Rocks of the studied interval pertain to the Aptian stage (red rectangle). Modified from Mejri et al. (2006).

In late Jurassic to early Cretaceous time, condensed sections (e.g. J.Garci), shoals and local reefs, developed along the N-S axis (Figure 2.1 and Figure 2.5) (Klett, 2001). The Cretaceous succession of the Saharan Platform (Figure 2.1), is characterized by a general gradation from neritic, lagoonal and continental facies in the south, to open marine and deeper marine facies (commonly referred to as the “Sillon Tunisien” in the literature) towards the north (Mejri et al., 2006). Irregular subsidence and migration of salt and block tilting throughout the Cretaceous have caused complex thickness and facies variations. Accumulation of pelagic sediments in a subsiding depositional trough can be observed in what is now known as the present day Gulf of Gabes (Buroillet et al., 1978; Salaj, 1978; Klett, 2001). According to Klett (2001), a maximum flooding event occurred during the Barremian (shown in Figure 2.9). Barremian rocks include the limestone, marl and interbedded sandstone and shales from the M’Cherga and Bouhemds formations, as well as the Sidi Aïch sandstone (Bishop, 1975; Salaj, 1978; Entreprise Tunisienne d’Activités Pétrolières, 1997; Klett, 2001). Aptian rocks consist of limestone, dolostone, sandstone, mudstone, marl and evaporites of the Orbata, Serdj and Lower Fahdene Fms (Figure 2.7 and Figure 2.8).

The Orbata Fm. consists of limestone and dolostone, and while its base is quite synchronous, the top is diachronous and controlled by sedimentation, subsequent erosion and onlap of the overlying members (Mejri et al., 2006). The Serdj Fm. (more thoroughly described in chapter 2.2.3.1) consists of reefal limestone and is the lateral equivalent to the Orbata Fm.

It is overlain by siliciclastic sediments, from either the Lower Fahdene Fm. or the deeper marine Hameima Fm., as can be observed in Figure 2.7 (Klett, 2001; Mejri et al., 2006).

The Late Aptian regression is observed as a clear low stand in sea level at the beginning of the Albian (shown in Figure 2.9), and caused a decrease (and in some areas a lack) in

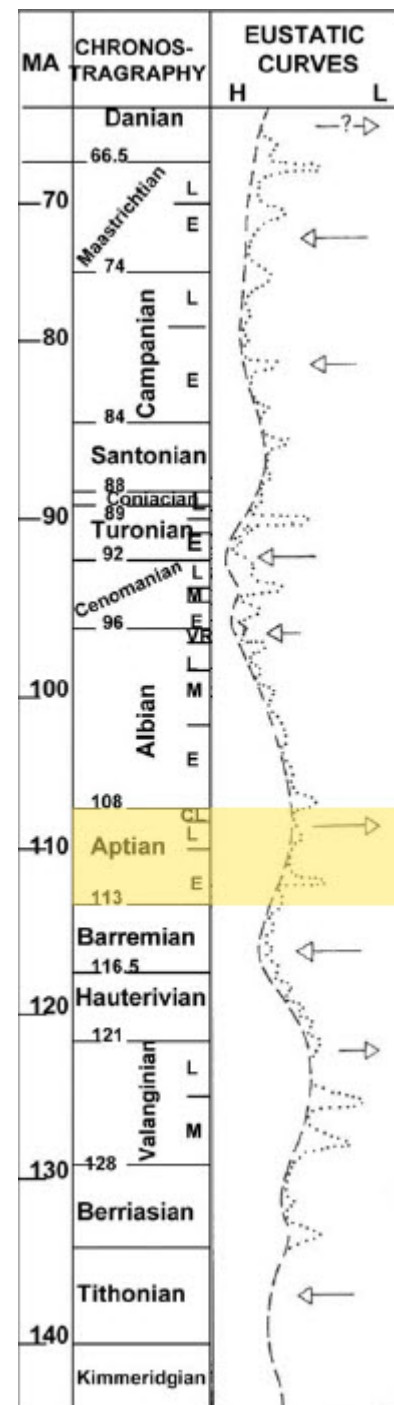


Figure 2.9: Eustatic sea-level curve during Cretaceous. Studied formations are of Aptian age and marked with pale yellow. Modified from Mejri et al. (2006).

sedimentation. Sedimentation rates were particularly slow in central and southern Tunisia (Mejri et al., 2006). Early Albian deposits are rare in Tunisia, and sedimentation after the Aptian only continued in the most subsiding zones in the northern and northeastern parts of Tunisia. In the Pelagian province Albian deposits are present as accumulations of dark-grey mudstone of the Lower Fahdene Fm. (Figure 2.7) (Klett, 2001).

The late Cretaceous is represented by the Sidi Mansour Group. Where sedimentation was continuous, the group is composed of three formations: Fahdene Fm. (Albian to Cenomanian), Kef Fm. (Turonian to Lower Campanian) and the Abiod Fm. (Campanian to the end of Maastrichtian) (Figure 2.7). The sedimentation was only continuous in the basinal areas of Tunisia, as in e.g. The Pelagian Province.

The Kef Fm. is mostly a dark gray shale with high abundance of planktonic microfauna and interbedded with argillaceous limestone, rich in shell remains of the bivalve *Inoceramus* (Mejri et al., 2006). The Abiod Fm. is well represented in Tunisia and is made up of: a) A lower carbonate member of a chalky mudstone rich in benthic foraminifera, b) A middle marl and clay member, and c) An upper carbonate member of chalky limestone with marl horizons (Klett, 2001; Mejri et al., 2006).

2.2.3.1 Serdj Fm.

The type locality of the Serdj Fm. is composed of thick series of bioclastic limestones consisting of oysters, algae, rudistids, corals and foraminifera, with interbedded argillaceous limestone, marls and silty beds. Serdj Fm. overlies Sidi Aich Fm. sandstones in the south and the Hammada Fm. limestones and marls in the north of Tunisia, forming a transition between the lower Orbata Fm. and the marine shales of the M'Cherga Fm. respectively. The Hammada Fm. is dated to be early Bedoulian and comprises dark marls interbedded with coquina of oysters or orbitolinids (Mejri et al., 2006). At Jebel Hamra, Epstein et al. (1953) defined four sequences within the Serdj Fm. bounded by erosional discontinuities or karstic dissolution surfaces (Mejri et al., 2006). Approaching the NOSA from the west to the east, the irregularity in facies and sediment thickness increases progressively (Epstein et al., 1953; Mejri et al., 2006).

2.2.4 Cenozoic

Mejri et al. (2006) sub-divide the Cenozoic era of Tunisia into three parts:

- I. Paleocene and Eocene; consisting of two shale units (El Haria and Souar) that are separated by the Metlaoui carbonate Fm. (Metlaoui).
- II. Oligocene and Early Miocene; consisting of various facies such as sandstone (Fortuna), flysch (Numidian), shale (Salammbô) and carbonates (Ketatna).
- III. Middle Miocene to Pleistocene; Synorogenic facies with molasses.

The paleogeography of the Paleocene and Eocene (part I) have more or less the same paleogeography as the Late Cretaceous, while the Oligocene and Early Miocene (part II) show facies distributions controlled the recent topography (Mejri et al., 2006). The present topography is related to uplift and emersion of western and southern Tunisia and an active subsidence east of the N-S axis, in the Pelagian Province.

3. Methodology

3.1 Fieldwork

Four weeks of fieldwork, spread over two field seasons, were carried out in collaboration with fellow student Fredrik Kjelkenes, supervisors Gunnar Sælen, Ståle Monstad (first fieldtrip) and Atle Rotevatn (second fieldtrip). The fieldwork took place 03rd – 15th of March 2014 and 6th - 21th September 2014 and focused on three localities within the Fkirine permit (Figure 1.1, 1.2 and 1.3). All three locations were extensively studied by detailed vertical sedimentological logging. The logs were used in combination with the study of thin-sections in subsequent classification of microfacies and facies associations. In addition permeability was measured vertically through the stratigraphy and laterally within selected beds by means of a portable TinyPerm instrument (see below).

3.2 Thin section studies

A total of 148 thin sections (87 unstained and 62 stained), were prepared from samples collected during the two field seasons. However, due to some issues with the services applied to preparation of the thin sections, the study had to be focused primarily on the stained thin sections. 49 of the stained thin sections (marked JF-##S, where ## indicates sample number and S indicates staining) are taken from the southern part of the Jebel Fadeloun limb. Duplicate numbers with annotation N or S in front of sample number (e.g. JF-N##S) indicate lateral sampling within the same bed, where N indicates north, and S indicates south of initial sample. Six of the thin sections (marked NFS-#, NFS = northern Jebel Fadeloun section) are sampled from the northern part of Jebel Fadeloun's eastern limb. The remaining six thin sections (marked GS-#) are sampled from Jebel Garci. Stained thin sections were prepared by Independent Petrographic Service Ltd (IPS) in Aberdeen and the non-stained thin sections were made by ETAP (Enterprise Tunisienne d'Activités Pétrolières – Direction des Services Pétroliers Laboratoire de Sédimentologie & Pétrophysique). Circular holes in the thin sections indicate sampling locations for stable isotope ($\delta^{18}\text{O}$ and $\delta^{13}\text{C}$) and Sr-isotope analyses (see below).

3.2.1 Ordinary light microscopy

Two different standard optical polarization microscopes were used for studying the petrographic properties. The light microscope Leica Z16 APO equipped with a Leica DFC-295 camera, has primarily been used to determine texture, detrital grains, allochems, structure, porosity, cement stratigraphy and for taking micrographs.

The second microscope, an Olympus BX51 with a connected Olympus DP72 camera, was used for fluid inclusion- and fluorescence studies.

Reflected light was used to differentiate between pyrite and organic material.

3.2.2 Staining

Staining of the thin section involved impregnation with blue dye for epoxy and staining with Alizarin red-S and K-ferricyanide. Blue dye epoxy was applied to enhance the visibility of porosity. The epoxy is applied in vacuum to ensure staining of both macro- and microporosity. Alizarin red-S and K-ferricyanide were applied to half the surface area of each thin section. Alizarin red-S stains calcite, aragonite, witherite and cerussite, whereas dolomite, siderite, magnesite and rhodochrosite remain unstained. Potassium ferricyanide (K-ferricyanide) distinguishes the distribution of ferrous iron by staining, making it possible to reconstruct the paragenesis of zoned ferroan cements (Dickson, 1966). Fe-rich calcite and dolomite are stained blue, whereas Fe-poor calcite is stained pink to pale pink, malachite are stained yellow and rhodochrosite are stained faint brown.

3.2.3 Cathodoluminescence microscopy (CL)

Cathodoluminescence microscopy was used to study the cement stratigraphy of the studied samples, by observing luminescence zonation, intensities and colour change. A Technosyn 8200 MKII cold cathode instrument (Department of Earth Science; University of Bergen) was used and operating conditions were approximately 16kV accelerating voltage and 150 μ A gun current.

3.2.4 Fluid inclusions

All non-stained halves of the thin sections were screened for fluid inclusions. A fluid inclusion preserves a record of the temperature, composition and pressure of the mineralizing environment. Interpretation of fluid inclusions data is based on the assumption that the inclusion will have the same chemical composition and volume, as at the time of formation in a closed system (Goldstein and Reynolds, 1994; Flügel, 2004; Sharp, 2007). Alterations may be caused due to changes in geometry and volume, or by temporarily or permanent opening of inclusions. Inclusions should not be subjected to overheating beyond the temperature of entrapment, and calcite crystals should display distinct growth zones (Flügel, 2004). Significant fluid inclusion results require a cluster of minimum 5-7 inclusions and inclusions of sufficient diameter (pers. comm. J.Rykkje, 2015). Inclusion diameter limitations commonly relates to accessible optics, and not the inclusion itself.

The inclusion commonly consists of two phases, liquid and gas. By heating or freezing the inclusion, it is possible to determine the likely temperature (heating) and salinity (freezing) of the original fluid. E.g. In a two-phase inclusion with a liquid phase along with a vapor bubble, simple heating to the point of resorption of the vapor bubble, gives a likely temperature for the original fluid during inclusion.

3.2.5 Fluorescence microscopy

An Olympus BX51 microscope connected to a fluorescence light emitter (model U-LH100HG), were used to study thin sections for hydrocarbons. By illuminating the thin sections with light of a specific wavelength that can be absorbed by fluorophores, it causes the organic material to emit light of a longer wavelength. The reflected light is observed as different colours than those of absorbed light, and the colour of the reflected light can be used to determine differences in petroleum fluid composition. However, the geochemical significance of these colour differences is difficult to ascertain, and in the literature several authors have related the colour differences to relative differences in density and API gravity (Burruss, 1991).

3.2.6 Photography

A Leica DFC 295 camera was used to take thin section micrographs in both plane polarized light and crossed polarized light of texture, detrital grains, allochems, structure, porosity and cements. The Leica DFC 295 was corrected for white balance between every use, and the following exposure settings were used:

Brightness: 65%

Saturation: 1.50

Gamma: 0.70

The Olympus DP72 camera has primarily been used to take high magnification micrographs of fluid inclusions and fluorescence. This camera was also corrected for white balance between each use.

3.3 Porosity and permeability

Porosity and permeability measurements were performed on four plugs and on 37 of the 49 hand samples (only permeability) collected at southern Jebel Fadeloun, while porosity and permeability estimates from Image-J analysis of thin-sections and poro-perm transforms were carried out for all samples both in Jebel Fadeloun, and in Jebel Garci. Permeability measurements were not performed on the sedimentary rocks in southern Fadeloun, where rocks were too tight or vegetation didn't allow for good measurements. In northern Fadeloun section and in the Garci section, measuring permeability was not possible because of instrument failure in the intense heat.

3.3.1 TinyPerm II

Permeability measurements were performed on 37 sample locations using a TinyPerm II instrument (Appendix WellCAD logs). At each location a total of six measurements were collected (Figure 3.1). A total of 222 measurements were collected.

TinyPerm II (TP) is a handheld air permeameter from New England Research Inc. that can be used either directly on flat clean outcrop surfaces, well cores, sample plugs or on hand specimens. The front of the TP probe consists of a rubber tip that makes a tight seal between the probe and the sample, and prevents leakage. Probe nozzle is pressed firmly against preferred surface and air is forced into sample. The microcontroller attached to the instrument monitors the volume of air that leaves the instrument, and computes a characteristic value according to the measured parameters (Filomena et al., 2014). A measured value (T) is presented on the microcontroller, and relates to the air permeability (K) expressed through Equation 3-1 (according to the TinyPerm II operational brochure):

Equation 3-1: Calibration equation converting measured TinyPerm (TP) values into millidarcies. T represents measured value, and K represents permeability in mD.

$$K = 10^{\frac{12.8737 - T}{0.8206}}$$

The TinyPerm II is constructed for field measurements, and is referred to in several articles (e.g. Filomena et al., 2014; Huysmans et al., 2008). All measurements were taken parallel to bedding plane and the reported horizontal air permeabilities (in Darcy), are Klinkenberg corrected.

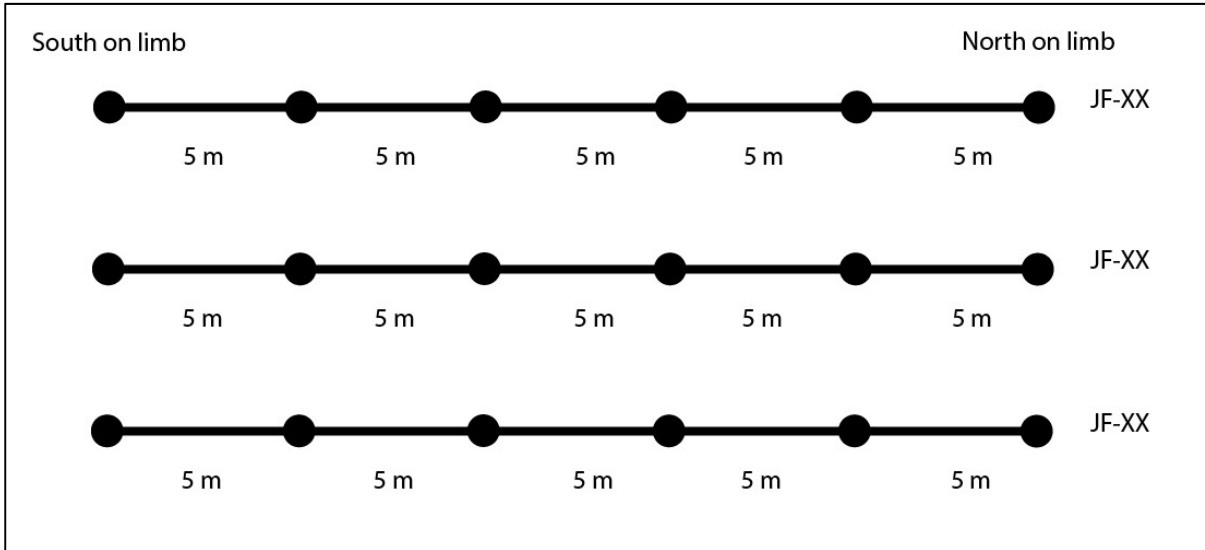


Figure 3.1: Illustration of permeability measurement procedures. The annotation XX indicates sample number. Lateral distance between measurements is 5 meters. Vertical distance between beds varies and is not shown in this illustration.

3.3.2 Plug measurements

Helium porosity, Nitrogen permeability and grain density for 4 plugs (2 vertical and 2 horizontal) from hand samples collected by Atef Ben Kahla, were analyzed by ETAP (Enterprise Tunisienne d'Activités Pétrolières – Direction des Services Pétroliers Laboratoire de Sédimentologie & Péetrophysique). The reported permeabilities are Klinkenberg corrected.

3.3.3 Image analysis

ImageJ is an image processing software, that can be used to calculate 2D porosity from epoxy impregnated thin sections. There is some uncertainty associated calculating porosity by means of the software, due to difficulties in assigning the boundary between pore space and grain perimeter. As each thin section has some variation in light penetration, the software settings must be corrected for difference in light intensity and heterogeneity of epoxy colour. ImageJ is not suitable for estimating micro porosity with a light microscope, due to difficulties in differentiating microporosity in the fine-grained matrix. Backscatter-electron microscopy (BSE) of thin sections solve this problem since microporosity is recognizable by this method (McCutchan et al., 2003), and microporosity can subsequently be added to the estimated meso- and macroporosity from light microscopy. Typically, the microporosity of a number of randomly selected areas on the thin-section investigated by means of BSE microscopy would be calculated and presented as a mean value and corresponding standard deviation.

In the present study porosity estimation was only based on ImageJ calculations from colour micrographs taken of thin-sections under the ordinary light microscope, and hence only meso- and macro porosity were accounted for. Microporosity is observed as a green matrix (from the penetration of green-dyed araldite), although individual pores cannot be differentiated. The images used, were taken with similar magnification to get the most consistent porosity estimation. Large fractures have been omitted during the image analyses.

3.3.4 Lønøy's method for permeability estimation

Lønøy's porosity-permeability transforms for dominant pore types were used in estimating permeability from ImageJ-derived porosity (Lønøy, 2006). This pore-type classification system is primarily based on pore geometries, pore sizes and porosity distribution, and is composed of 20 pore types (Table 4-5). The dominant pore type is determined from examining the thin sections.

3.4 Isotope analysis

Isotope analysis was performed for $^{87}\text{Sr}/^{86}\text{Sr}$, $\delta^{18}\text{O}$ and $\delta^{13}\text{C}$ and the methods are briefly reviewed in this chapter.

3.4.1 Strontium

$^{87}\text{Sr}/^{86}\text{Sr}$ analysis was performed on a total of 14 bulk rock samples containing grains, matrix and carbonate cement by means of a Finnigan MAT 262 mass spectrometer at the mass spectrometer laboratory, University of Bergen (Table 4-3). All results are normalized to NIST-SRM 987 with a certified isotopic ratio of 0.710240, and repeated long-term measurements ($n = 57$ in 2012) of this standard gave an average measurement = 0.710233 and an analytical precision of $\pm 20 \times 10^{-6}$ (2 s.d.). Eight samples were sampled from the southern Fadeloun section (JF), three samples from the northern Fadeloun section (NFS) and three samples from the Garci section (GS).

3.4.2 Carbon and Oxygen

Stable isotope analysis of $\delta^{18}\text{O}$ and $\delta^{13}\text{C}$ was performed on a total of 22 bulk rock samples containing grains, matrix and carbonate cement, using conventional methods. Samples were reacted individually with a Kiel IV carbonate device and analysed for their $\delta^{18}\text{O}$ and $\delta^{13}\text{C}$ compositions on a Finnigan MAT253 mass spectrometer at the Bjerknes Centre for Climate Research and Department of Earth Science (University of Bergen). Results (Table 4-1) are

reported as per mil (‰) deviation from the Vienna Pee-Dee Belemnite (vPDB) calibrated using NBS-19. NBS-18 was also used as cross check. Long-term external precision of replicate standards is 0.06‰ and 0.04‰ for $\delta^{18}\text{O}$ and $\delta^{13}\text{C}$, respectively.

Sixteen samples were sampled from the southern J.Fadeloun section (JF), three samples from the northern J.Fadeloun section (NFS) and three samples from the J.Garci section (GS).

4. Results

4.1 Introduction

The results of this study are mainly based on fieldwork, light-, fluorescence- and cathodoluminescence (CL) microscopy, Sr-isotope and stable isotope analyses, fluid inclusion investigation, porosity and permeability measurements. First, the microfacies are classified based on detailed light microscopy of the sampled sections. The sedimentary surfaces and depositional units are then described and distribution of the various microfacies within each depositional unit is then investigated. Furthermore the diagenetic features based on thin-section analysis and outcrop-scale information are described, and finally the porosities and permeabilities of the studied successions will be presented. The locality of the samples is marked in the stratigraphic log in Appendix WellCAD logs, and in various overview pictures Figure 4.36 to Figure 4.38.

4.2 Microfacies

Early definitions of microfacies only considered the study of petrographic and paleontological features observed in thin section, whereas today the total of all sedimentological and paleontological data that can be derived from thin sections, rock slabs, peels and rock samples, are used to classify microfacies (Flügel, 2004). Sedimentary microfacies are defined to assist in organizing observation, to interpret depositional environments and to predict geometric patterns, trends and relationships. In many instances, reservoir properties are closely related to or influenced by depositional facies. In other cases the diagenetic evolution is the predominant factor controlling the reservoir properties (Tucker and Wright, 2009).

The study of sedimentary microfacies has both descriptive-objective elements (texture, grain size, allochem composition, sedimentary structures, and more) and interpretative-subjective elements (depositional environments, paleo-depth, water chemistry, paleotemperature, sequence stratigraphy, diagenetic environments and so on).

Detailed microfacies classification becomes un-practical because it requires a multiplicity of types and sub-types. In a practically applied stratigraphic procedure the goal is to define the

“minimum” of microfacies that are adequate for the study. Obviously this is a relativistic approach, and different geologists will most likely come up with different microfacies classification schemes for the same region. The important thing is to understand the procedure and to establish microfacies classification and to consider any classification as “end member” of an infinite number of variations.

The simplest and probably the most recognized and widely used method for classifying carbonate rocks, is the Dunham classification scheme (1962), which was later modified by Embry and Klovan (1971) (Figure 4.1), and is the one applied in the present study. Based on depositional texture, Dunham (1962) noticed that there are several textural features that are practical for classifying carbonate rocks, and he subdivided carbonates into nine classes on basis of:

- The presence or absence of matrix
- The abundance of carbonate grains
- Supporting mechanism (grain supported vs matrix supported)
- Evidence of organic binding of sediments during deposition.

Carbonate rocks containing matrix were separated into three classes on basis of the amount of grains present and the supporting mechanism. Mudstone contains less than 10% grains and is matrix supported. Wackestone contain more than 10% grains and is matrix-supported, whereas packstone is grain-supported. It is important to notice that the origin of the matrix is not specified as clastic, and thus may include both mechanically deposited and chemically precipitated micrite.

Grainstones lack mud and is grain-supported (Dunham, 1962). Most grainstones have traces of micrite, and many sedimentologists defines grainstones as having less than 5% mud (pers. comm. A.Lønøy, 2015; Esso, 1988).

Embry and Klovan (1971) introduced the terms *floatstone* and *rudstone* for wackestones and packstones/grainstones with grain-diameter >2mm, respectively.

Carbonate rocks with a total lack of recognizable depositional texture are classified as *crystalline*, whereas carbonate rocks showing signs of being bound during deposition are classified as *boundstones* (Dunham, 1962). Crystalline rocks are related to extensive dolomitization or recrystallization of limestones, whereby the primary texture is obliterated (Flügel, 2004). Wright (1992) reviewed previous classifications in order to integrate the major

textural types (depositional, biological and diagenetic) into one single system. Limestones (not dolostones) with no initial depositional fabric preserved as result of oblitative recrystallization or replacement, are divided into *sparstones* and *microsparstones* based on crystal size. Sparstones are limestones dominated by sparry calcite crystals (inequant, blocky mosaics), with a crystal size $>10\mu\text{m}$ in diameter, whereas microsparstones are dominated by crystal sizes in the range 4-10 μm in diameter (Wright, 1992).

Dunham's classification scheme was later expanded by Embry and Klovan (1971) by subdividing boundstone into:

- *Framestone*: Organisms building rigid frameworks.
- *Bindstone*: Sessile organisms encrusting and binding loose sediment together.
- *Bafflestone*: The organisms trap the sediment without building rigid frameworks themselves.

In the literature, it is common to combine the classification name with the dominating grain type to give a more detailed description of the carbonate rock. In the present study I have used the Dunham (1962) textural classification and additionally specified up to three of the most important allochems. The most common grain type is placed closest to the texture description; e.g. Echinoderm-Peloidal Packstone indicates that echinoderms and peloids are the most common grains, with peloids being the most dominant. It is important to note that abundance in this study is a subjective scale which takes both grain area and frequency into consideration. By only considering grain frequency, fauna or flora consisting of large grains would be underestimated, and if only grain area is taken into consideration, smaller e.g. pelagic grains would be underestimated. The lithological successions studied at J.Fadeloun and J.Garci, are subdivided into eleven microfacies, and in the following description of microfacies, the sample location is marked in Appendix WellCAD logs.

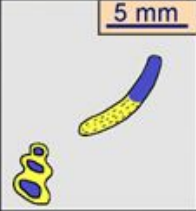
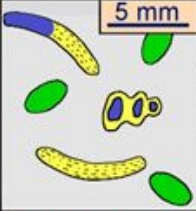
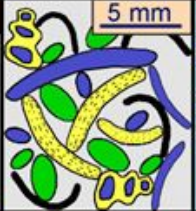
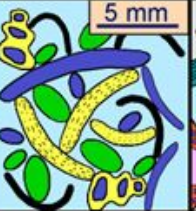

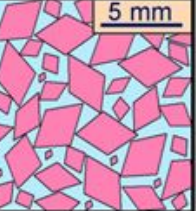






Depositional texture recognizable					Depositional texture not recognizable
Components not bound together during deposition			Components were bound together during deposition		
Contains carbonate mud (clay / fine silt)		Grain supported	Lacks mud and is grain supported		
Mud supported					
Less than 10% grains	More than 10% grains				
Mudstone	Wackestone	Packstone	Grainstone	Boundstone	Crystalline
					
	Floatstone (large grains)	Rudstone (large grains)		Framestone	
				Bindstone	
				Bafflestone	

Figure 4.1: Dunham's classification scheme (1962) for carbonate rocks, as modified by Embry and Klovan (1971). Floatstone and Rudstone have at least 10% grains with diameter >2mm. Sketch from <http://www.beg.utexas.edu/lmod/IOL-CM01/cm01-step03.htm#>.

4.2.1 Microfacies 1 - MF1: Pelagic Mudstone/Wackestone (Samples: JF-87S & JF-80S)

Observations:

Microfacies 1 is situated within the southern J.Fadeloun section, and overlies a relatively coarse grained (average grain diameter of 450µm) echinoderm- and peloidal-rich grainstone (MF7 and MF5). The microfacies is well sorted, fine grained (average diameter of 25µm), and matrix supported. The dominating grain types are pelagic in origin, and comprise evenly distributed planktonic globigerinid foraminifera and small spar-filled calcispheres (Figure 4.2). Organic material, as defined from reflected light microscopy, is a major constituent and

can be observed as dispersed dark brown to black circular spots with high relief. It is important to notice that according to the geological map published by Direction du Service Géologique in 2003, sample JF-87S is of Albian age. In outcrop there is an apparent fault just above sample JF-80S (fault not marked on the geological map) and, since the texture and biotic components of sample JF-80S is similar to sample JF-87S and Albian deposits recorded in the area by previous authors (Klett, 2001; Mejri et al., 2006), it is inferred to be of Albian age too. Hence, the succession above the fault is probably of Aptian – Albian age (Figure 4.3 and Figure 4.4).

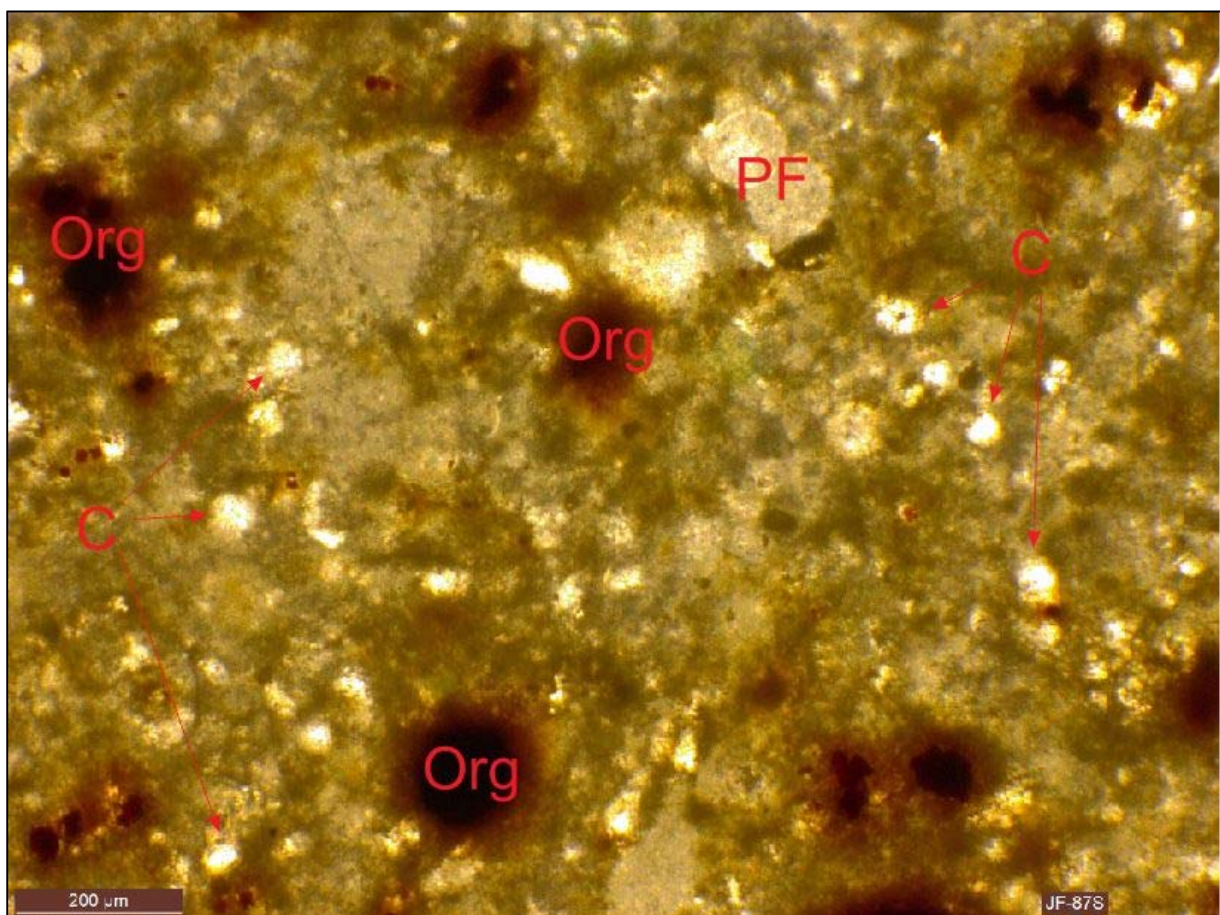


Figure 4.2: Pelagic mudstone from microfacies 1. Matrix supported limestone with planktonic foraminifera (PF), calcispheres (C) and organic material (Org) evenly dispersed in lime mud. Thin section in plain polarized light (PPL).

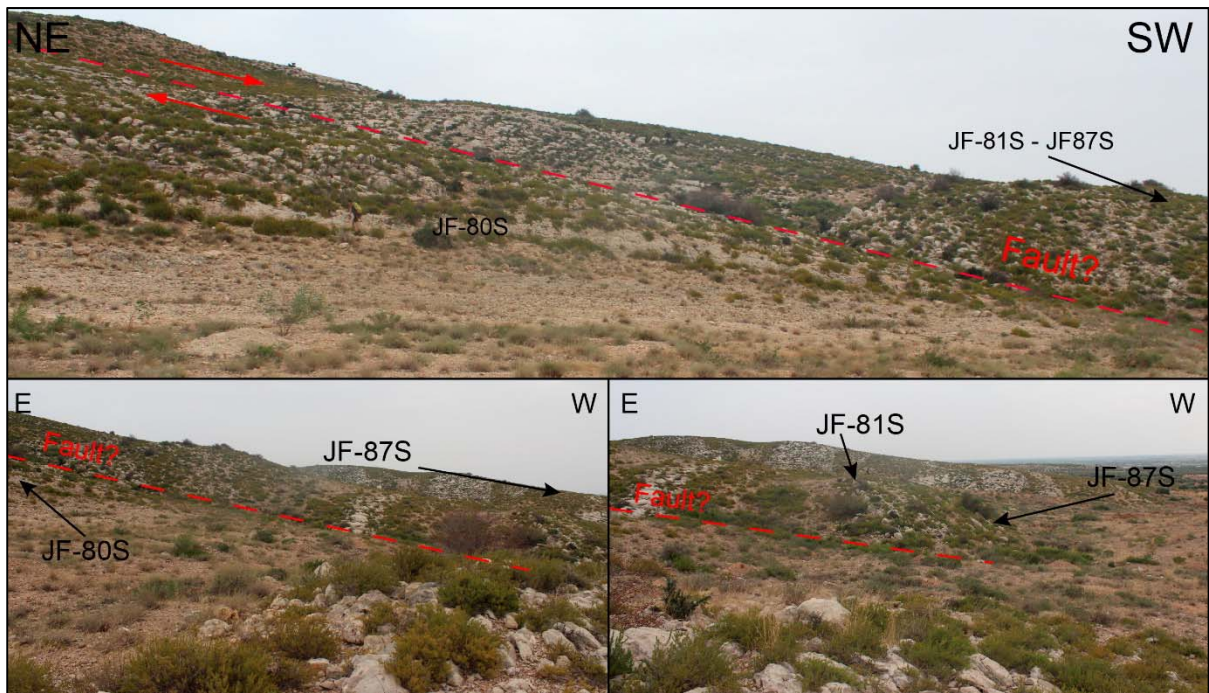


Figure 4.3: Overview of the repetitive sequence and associated sample distribution. Note that beds are not possible to trace laterally. The apparent offset alone is not a clear evidence for a repetition, but combined with the associated microfacies and isotope analysis (see below), they indicate a repetition of the top Aptian/base Albian (Figure 4.4).

Unit F	MF1	☼ _P ☉ M/W	Albian	JF-87S
Unit E	MF7	☼ _R ☉ ★ G	Aptian	Fault?
	MF2	☼ ☉ ★ P/G	Aptian	
	MF1	☼ _P ☉ M/W	Albian	JF-80S
Unit D	MF5	☼ ☉ ★ G	Aptian	
	MF6	☼ _B ☉ P/G	Aptian	
	MF2	☼ ☉ ★ P/G	Aptian	

Figure 4.4: Stratigraphy across the presumed fault between samples JF-80S and JF-87S. Only the uppermost part of Unit D is shown. The Albian age of sample JF-80S is indicated by its texture and biotic components as well as by the stable-isotope signature (Figure 4.51).

Interpretation:

The matrix-supported texture and relatively low grain content, show that this is a mudstone/wackestone according to Dunham (1962). Mud-supported textures are typical for low-energy environment below wave base, and the strong dominance of planktonic fauna and the high organic content suggest deposition in a relatively deep marine, basinal environment. During the late Early Cretaceous, the association of planktonic foraminifera and calcispheres as observed in this microfacies, typically represent basinal deposition in open oceans (Flügel, 2004). Most planktonic foraminifera are restricted to marine salinities of 30-40‰ and commonly live in the photic zone of the water column, and are virtually absent below 200 meters depth (Flügel, 2004). The thin-walled spherical globigerinids commonly prefer the uppermost part of the water column, and are characterized by their planispiral or trochospiral test with typical globular chambers. Planktonic foraminifera commonly avoid terrigenous input, and thus accumulations of planktonic foraminiferal shells are often found in the bathyal zone of open-marine basins (Flügel, 2004).

Small-sized, hollow, spherical to egg-shaped microfossils with calcitic walls, are commonly classified as calcispheres. Calcispheres are thought to be remnants of algae and algal spores, and are predominantly found in pelagic limestones. Mesozoic and Cenozoic calcispheres are often ascribed to calcified dinoflagellate algae. Calcispheres from these eras are distributed across a wide climatic range in temperate regions, and are predominantly found in sediments of the deeper shelf to slope and basinal settings (Flügel, 2004). The associated mud-rich texture and fossil assemblage thus indicate a deep marine depositional setting possible in the bathyal zone.

The assumption that sample JF-80S is Albian in age, is supported by the texture and biotic components (Klett, 2001; Mejri et al., 2006) stable-isotope signature (Chapter 4.6.1 and Figure 4.51).

4.2.2 Microfacies 2 – MF2: Bivalve-Echinoderm-Peloidal Pack-/Grainstone

(Samples: JF-85S, JF-83S, JF-71S, JF-70S, JF-69S, JF-51S, JF-50S, JF-49S, JF-48S, JF-45S, JF-43S, JF-40S, JF-37S, JF-33S, NFS-5S, NFS-9S and NFS-4S)

Observations:

Microfacies 2 is present throughout the southern and northern J.Fadeloun sections. The microfacies is moderately to well-sorted in some sections, and moderately to poorly sorted in others. Average grain diameter ranges from 75-250 μ m, and grains are predominantly composed of peloids, echinoderm plates and spines and bivalve fragments (Figure 4.5). Other observed biogenic grains are red algae, benthic foraminifera (miliolids and other undifferentiated planispiral, biserial and uniserial foraminifera), ostracods and sponge spicules. Most shell fragments are very small, disintegrated, and difficult to classify. Bivalve fragments occur with primary internal structures preserved, or as cement-infilled moulds. Some intraclasts may be present, but their existence is difficult to determine due to the small grain size and close packing. Several grains have isopachous dark (almost black) micritic rims along their grain margins.

Patchily-distributed clay and local sparry calcite cementation is observed in some of the samples. Evenly distributed organic material is observed as small brown circular spots within the matrix and grains. Virtually all of the primary and secondary pore spaces are cemented, with only some open interparticle micro porosity (the stained epoxy that fill the micro porosity gives the matrix a green appearance) and minor fracture porosity preserved. Fractures and some moulds tend to be filled with ferroan-rich equant calcite cement (stained blue by Alizarin Red-S and K-ferricyanide). Overall, the microfacies is grain supported and classified as packstones to grainstones, according to Dunham (1962).

Sample JF-37S shows a distinct pedant cement below the grains (Figure 4.7), while NFS-5 has long irregular voids that are filled with equant calcite cement (Figure 4.6).

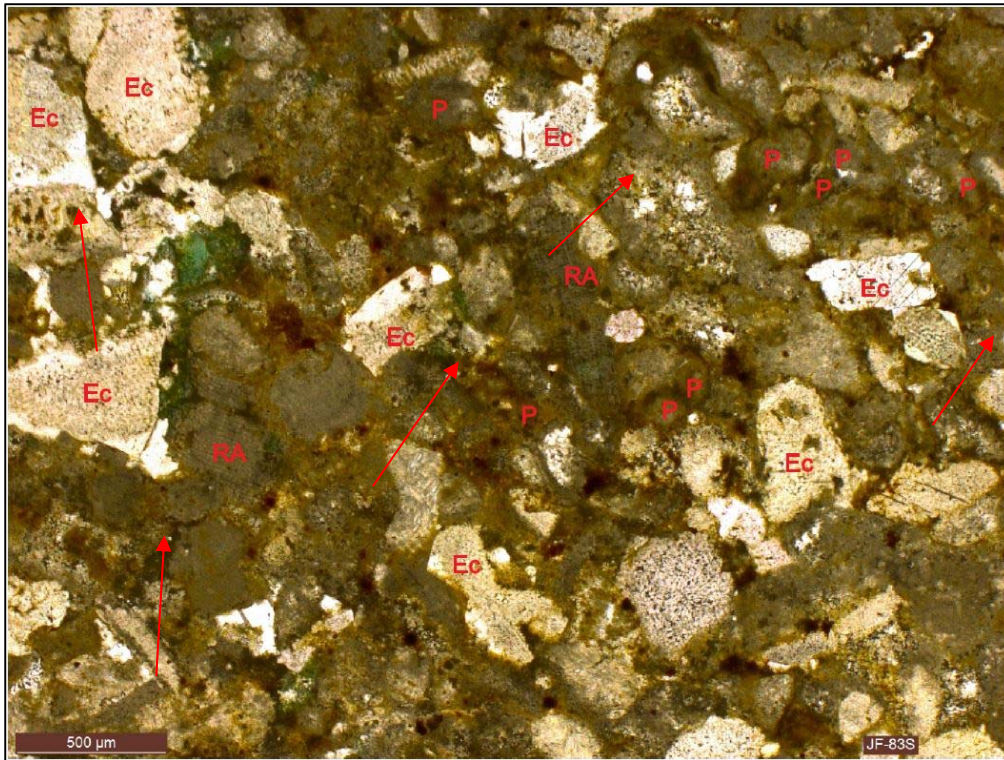


Figure 4.5: Representative micrograph of a bivalve-peloidal-echinoderm packstone from Unit E. High abundance of echinoderm plates and spines (Ec) in optical continuity with syntaxial cement overgrowths (red arrow). Peloids (P) and few fragments of red algae (RA) are evenly distributed. Minor open porosity (artificially stained green), but virtually all porosity is cemented by syntaxial calcite overgrowths around echinoderm fragments. Thin section in PPL.

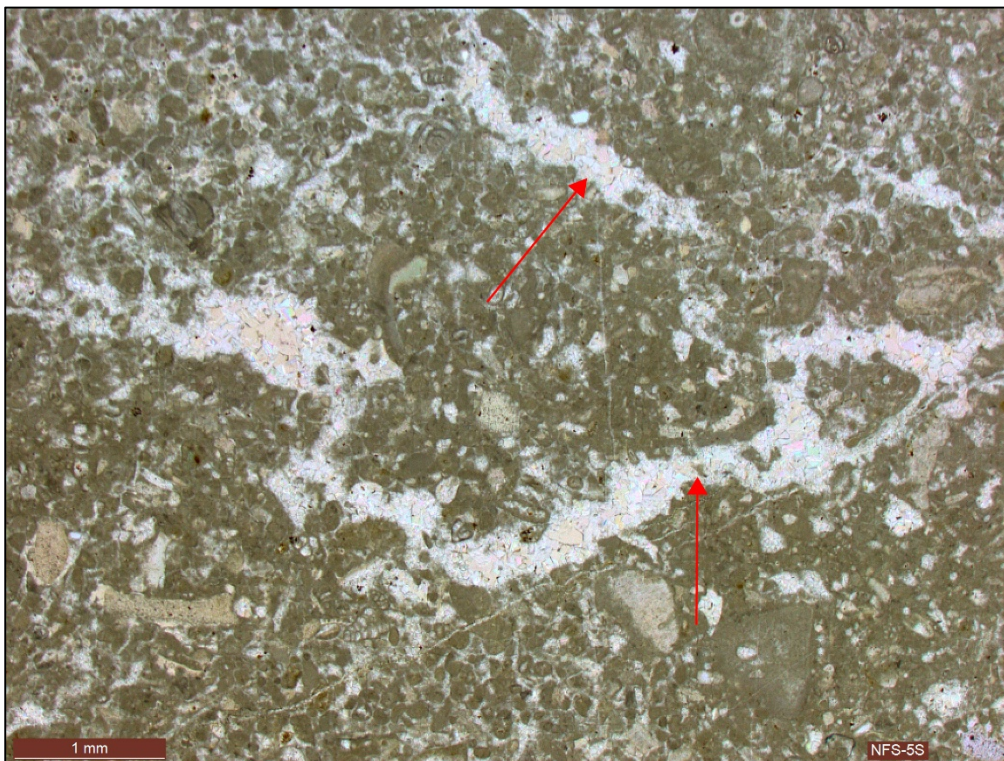


Figure 4.6: Fenestral structures (red arrows) represented by long irregular voids cemented with equant calcite cement. Thin section in PPL.

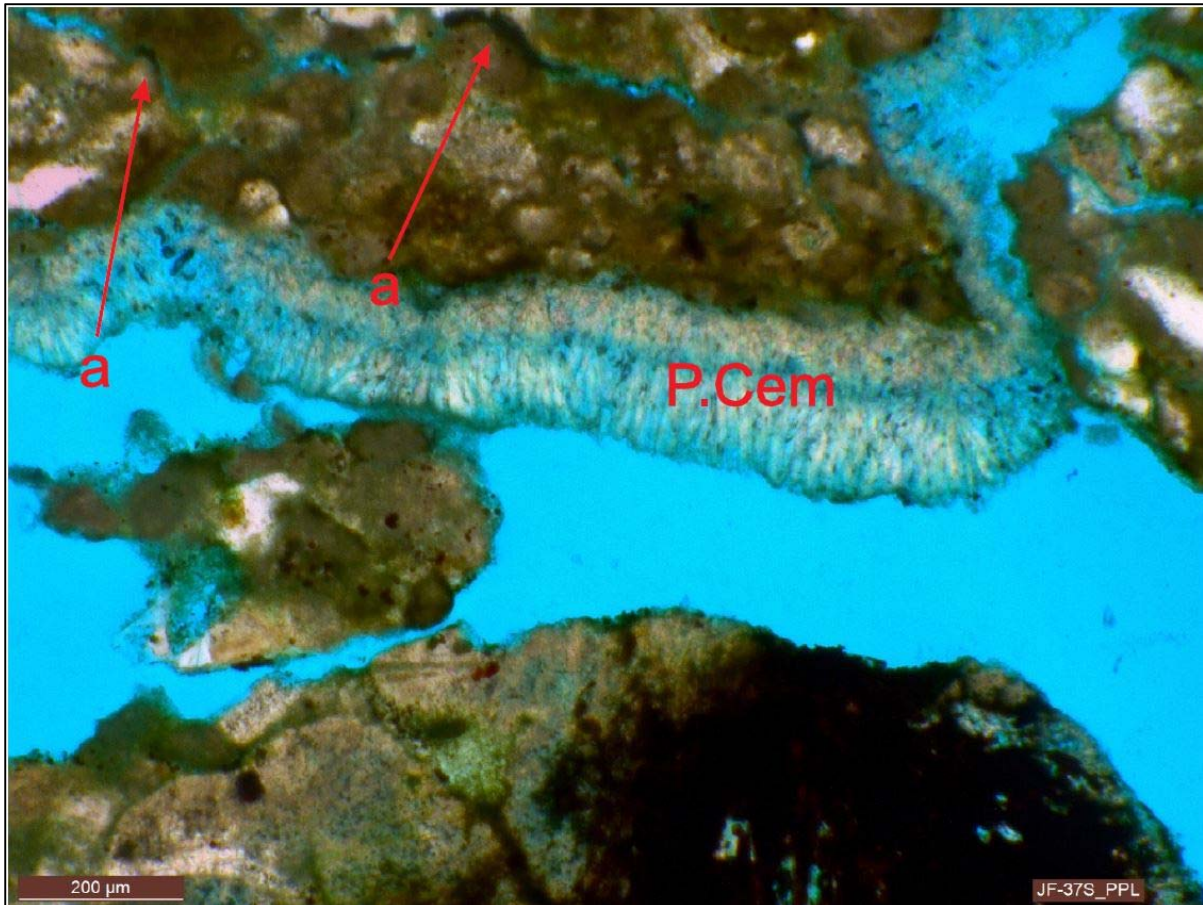


Figure 4.7: Bivalve-peloidal-echinoderm packstone with pendant (microstatactitic) cement (P.Cem). The cement only occurs on one side (presumed underside) of the grains, and apparently consists of at least two cement generations. 1st cement generation is composed of apparently denser calcite crystals, whereas the 2nd cement generation consists of a more porous crystal arrangement with crystals having a high length/width ratio. Pendant cement typically forms in the fresh-water vadose zone, but may also form in the marine vadose zone (sea water splash zone). Note the organic material (as defined from relected light microscopy) partly infilling fractures (a). The picture is presented “right way up” as indicated by the pendant cement. Thin section in PPL.

Interpretation:

Small sub-rounded or rounded and spherical micritic grains, commonly without internal structure, are called peloids, and whereas peloids comprise micritized grains in general, the term pellets is restricted to peloids of fecal origin (Tucker and Wright, 1990). Peloids are formed by complete micritization of grains related to micro-boring activity of organisms, and usually start off as a micritic envelope along exposed grain surfaces (Chapter 4.5.1). Peloids are common in shallow-marine tidal and subtidal shelf carbonates, but can also occur in deep-marine settings. In tropical and sub-tropical shallow-marine environments (platforms, ramps, reefs etc.), peloids are commonly abundant, but are rare or absent in non-tropical cool-water carbonates (Flügel, 2004). If micritization was caused by endolithic algae, micritization must have taken place in the photic zone in a water depth shallow enough for zooxanthellate corals

to thrive. However, micritization caused by fungi can occur at significantly deeper waters (Zeff & Perkins, 1979). The absence of zooxanthellate corals thus indicates that the temperature and/or nutrient conditions were not favourable for their existence.

A distinct thickening of cement crusts, forming a gravitational beard-like pattern beneath grains and within fractures, is the result of cement precipitation from water in the vadose environment. This cement, which is typically composed of calcite, is called pendant cement. The cement precipitates below the zone of capillarity and above the water table within the meteoric-vadose zone, or sporadically in the marine-vadose diagenetic environment (Flügel, 2004). The marine-vadose zone includes beaches and tidal flats where pore space is filled with air and marine waters, whereas the pore space in meteoric-vadose zone is filled with air and meteoric waters (Flügel, 2004).

The long irregular voids cemented with equant calcite cement are interpreted to be fenestral structures. Tebbutt et al. (1965) suggested the name *fenestra* for primary or penecontemporaneous gaps in the rock framework larger than grain-supported interstices (Flügel, 2004). Fenestral pores are commonly millimeters to centimeters in size, have an irregular geometry and are elongated and planar in the direction parallel to bedding. The pores can be open, partially or completely filled by cements, surface derived-material or diagenetic internal sediment (Tebbutt et al., 1965; Flügel, 2004; Ahr, 2008). Fenestral pores form by desiccation or by expulsion of gas during decay of organic matter, and do not have any apparent support in the framework of primary grains composing the sediment (Lucia, 1999; Flügel, 2004; Ahr, 2008). The pores differ from growth-framework pores or solution voids, which have some support in the framework of the primary grains. Fenestral pores are common in peritidal carbonates in tidal-flat and lagoon environments, where sediments are alternately wet and dry (Tebbutt et al., 1965; Flügel, 2004; Ahr, 2008; Tucker and Wright, 2009).

The combination of grain-supported texture, biogenic composition and fenestral structures suggest an intertidal inner-ramp setting, whereas the presence of pendant cement in sample JF-37S indicates intermittent exposure to the marine- or meteoric vadose zone.

4.2.3 **Microfacies 3 – MF3: Miliolid-Orbitolina-Peloidal Pack-/Grainstone** (Samples: JF-66S, JF-64S, JF-26S, JF-24, JF-23S, JF-22S, JF-21S, JF-17S, JF-16S and JF14S)

Observations:

Microfacies 3 is only present in southern J.Fadeloun. The microfacies is moderately to poorly sorted and is composed of closely packed relatively large grains, with an average grain diameter ranging from 250-900µm. Grains are very large compared to those of the other microfacies and are predominantly composed of relatively large benthic foraminifera (Orbitolinids, miliolids and other undifferentiated ones), peloids and echinoderm- (plate and spines) and bivalve fragments. Orbitolinids and miliolids are clearly the most prominent grains and are observed in large numbers. The undifferentiated benthic foraminifera comprise planispiral, uniserial and biserial species, but are not as prominent as the aforementioned foraminifera. Quite a few of the observed bivalve fragments have their primary internal structure intact, and some have thin isopachous rims of dark brown to black micritic rims along their grain margins. Other allochems observed in microfacies 3 are a few fragments of red algae, bryozoans, gastropods, intraclasts and coral fragments. Some quartz grains are observed in MF3 samples close to the base of Unit A.

In the upper part of MF3 in Unit A, there is an increase in cemented irregular voids, with at least two generations of calcite cement. The voids are predominantly filled with iron-poor equant calcite cement (stained red by Alizarin Red-S and K-ferricyanide), with some iron-rich equant calcite (stained blue by Alizarin Red-S and K-ferricyanide) towards the center. Fractures with small aperture are seemingly cemented with larger fractions of the iron-rich equant calcite. Sub-planar non-serrate dissolution seams are observed as dark brown irregular laminae between grain boundaries (Figure 4.8).

Pore space is dominated by interparticle, mouldic and intraparticle pores cemented with blocky/equant and drusy sparry calcite. Most of the open primary and secondary pores are filled with cement that seems to have its origin as syntaxial overgrowths on echinoderm fragments, but some pore space is still preserved as interparticle and mouldic micro porosity.

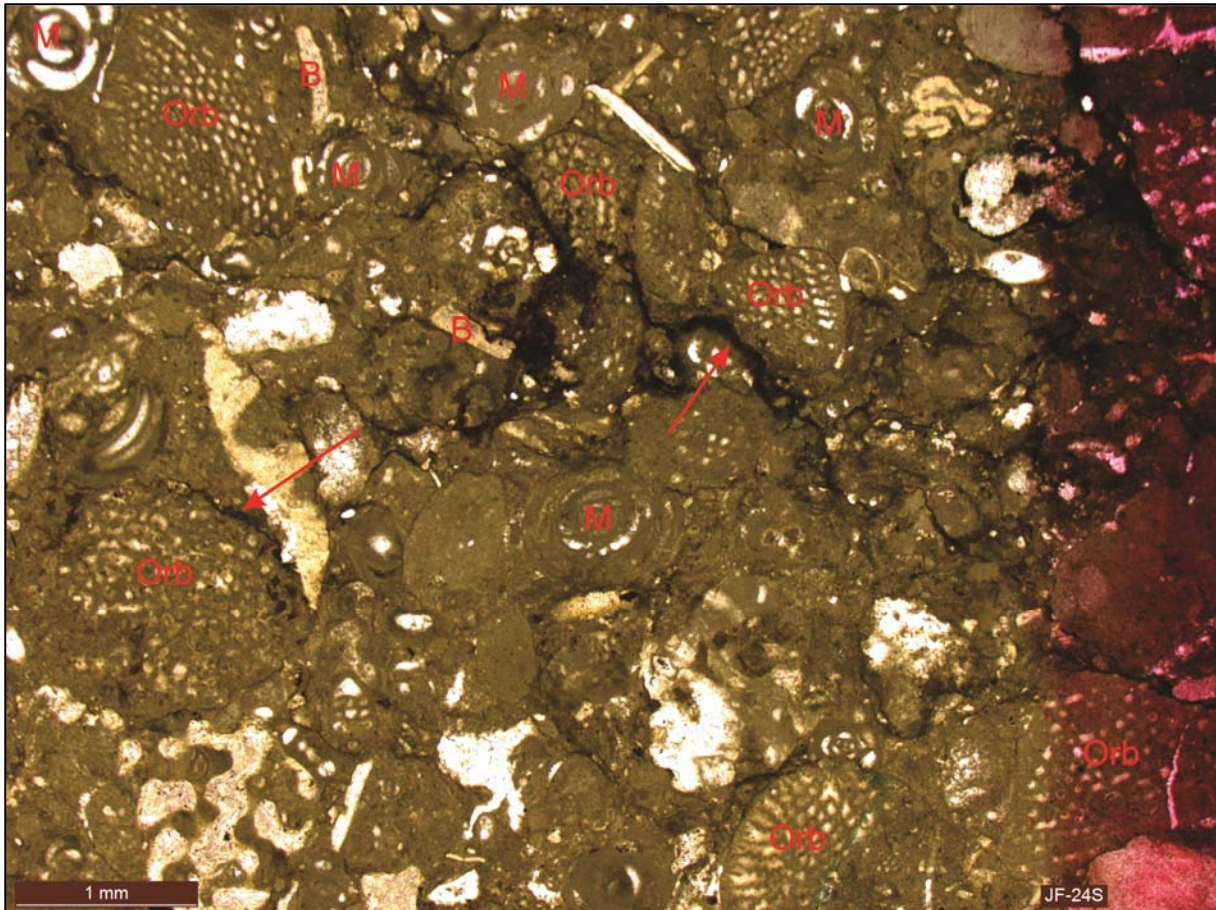


Figure 4.8: Miliolid-Orbitolina-Peloid rich packstone. Miliolid (M) and *Orbitolina* sp. (Orb) are evenly dispersed and closely packed. Some bivalve (B) fragments are present. Note the relative large grain diameters and the red arrows pointing to early stage dissolution seams (incipient stylolites). All visible porosity is cemented with equant calcite cement. Right-hand side of section is stained with Alizarin Red-S and K-ferricyanide (method described in Chapter 3.2.2).

Interpretation:

Microfacies 3 is grain supported with various amounts of micritic matrix and/or sparry calcite, and thus is classified as a pack- to grainstone. The relatively low abundance of mud and the grain-supported texture, indicate a high-energy depositional environment. Unlike sandstones, grain size in carbonates does not necessarily reflect depositional energy and transport processes, as carbonate grain size is at least partially faunal and flora dependent. Several factors such as sorting, grain shape, bulk density, angularity and so on, must be taken into consideration when carbonate grain size is taken as a guide to depositional energy levels.

The relatively large grains and the low abundance of mud suggest that MF3 is deposited in a shallow marine setting. Orbitolinids and miliolids are commonly indicative of shallow

relatively warm seawater with normal salinity in an inner platform setting (Kalantari, 1986; Flügel, 2004).

4.2.4 Microfacies 4 – MF4: Silty-Peloidal Pack-/Grainstone

(Samples: JF-57S, JF-56S, JF-54S, JF-52S, JF-47S, JF-42S, JF-41S and JF-10S)

Observations:

Microfacies 4 are only present in southern J.Fadeloun. This microfacies is moderately to well sorted, and comprise relatively small and tightly packed grains. The average grain diameter is ranging from 100-125µm. MF4 is not only composed of grains of a recognizable biogenic origin, but also has a high abundance of peloids and quartz (Figure 4.9). Minor constituents are grains of echinoderm fragments (plates and spines), red algae, benthic and planktonic foraminifera, ostracods, calcispheres and bivalve fragments. The benthic foraminifera observed, comprise undifferentiated planispiral, uniserial and biserial species. Biogenic grains are often small and disintergrated fragments with dark brown to black micritic rims. Sample JF-42S shows apparent circum-granular cracking, whereas JF-54S may exhibit incipient circum-granular cracking. Organic material is observed partly infilling fractures, as intraparticle infill and/or dispersed in the mud, as dark brown coloured spots (often with higher relief). Open fractures are crosscutting cemented fractures.

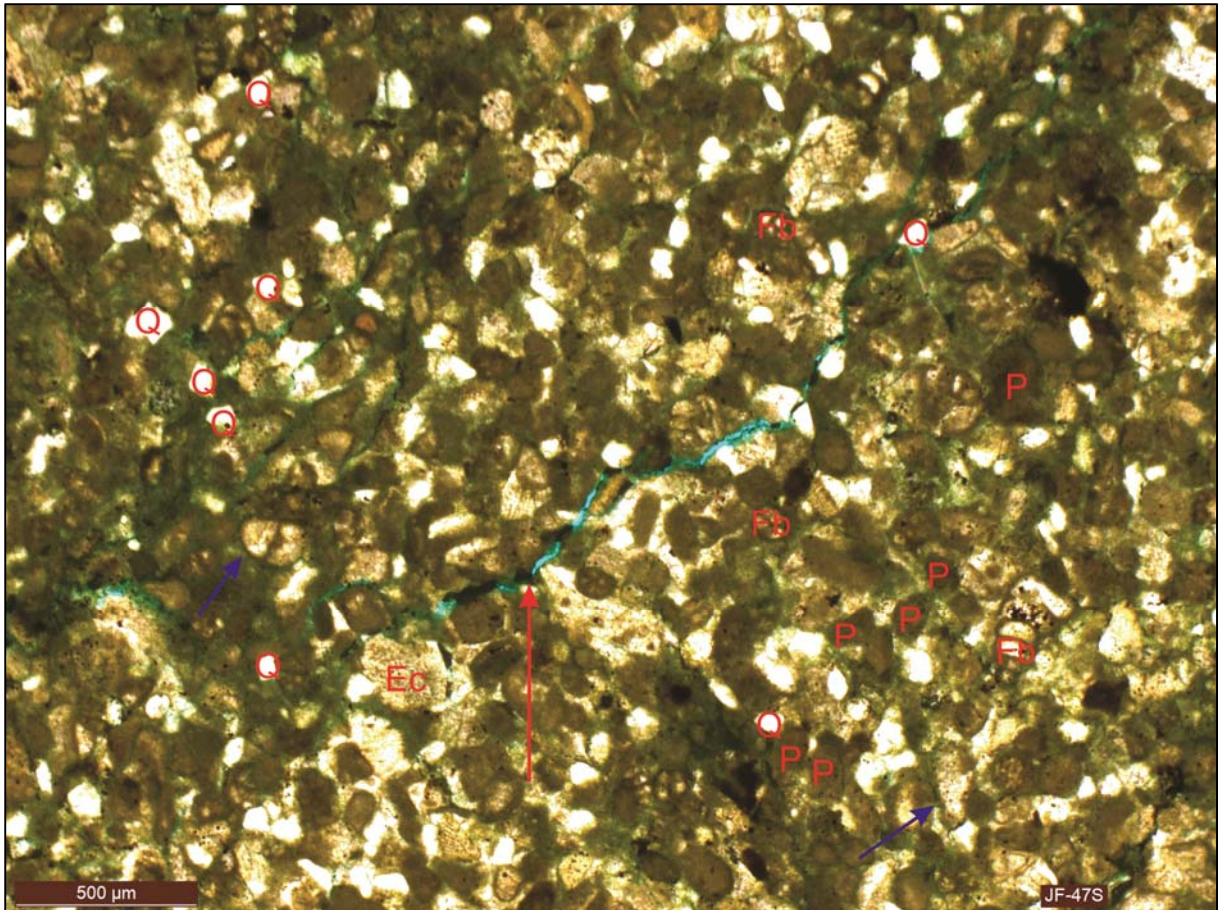


Figure 4.9: Silty-Peloidal Packstone. Quartz (Q) grains of silt size, peloids (P), echinoderm fragments (Ec) and undifferentiated benthic foraminifera (Fb) evenly distributed and tightly packed. Purple arrow = micritic envelope along grain margins. Red arrow = fracture partly filled with organic material. Thin section in PPL.

Interpretation:

Microfacies 4 is grain supported with various amounts of micritic matrix or sparry calcite, and thus is classified as a pack- to grainstone. The faunal assemblage of MF4 is light-“independent”, commonly termed heterozoan (James, 1997; Flügel, 2004). Heterozoan faunal assemblages are often characteristic for the cool-water and temperate realm (generally colder than 20°C) of high-energy settings such as ramps and open shelves, where reefal buildups and protective barriers are generally uncommon (Brandano et al., 2009). Invertebrates with photosymbionts such as corals thrive in subtropical to tropical waters, whereas heterozoan associations prevail in temperate-cool water and/or in high nutrient-level environments (Lees and Buller, 1972; James, 1997; Lucia, 2007).

Textural maturity and the relative low abundance of mud indicate agitated waters in a high-energy depositional environment (Flügel, 2004). The presence of peloids and grains

exhibiting micritic envelopes (described in chapter 4.5.1) within MF4, are commonly indicative of shallow marine environments (Flügel, 2004), but could also occur in deeper waters by micritization caused by fungi (Zeff and Perkins, 1979). The occurrence of terrigenous quartz could indicate a riverine and an eolian origin of the quartz (see below) (Flügel, 2004). Circum-granular cracking and the presence of organic material suggest episodic events of subaerial exposure (see below). Most factors thus indicate deposition in a shallow marine mid- to inner ramp setting, with episodic subaerial exposure.

4.2.5 Microfacies 5 – MF5: Intraclastic-Echinoderm-Peloidal Grainstone (Sample: JF-78S)

Observations:

Microfacies 5 is only present in southern J.Fadeloun, within Unit D. This microfacies is poorly sorted, and is composed of relatively large and sparsely packed grains. The average grain diameter is 400µm. Dominating grain types in MF5 are intraclasts, echinoderm fragments and peloids. Minor constituents are fragments of red algae, bivalves, belemnites and bryozoans. Many grains, especially bivalve fragments, have relatively thick micritic envelopes, and micritization also occurs in grains within intraclasts. Several bioclasts and intraclasts have microcrystalline isopachously-distributed calcite cement. This cement even occurs on grains within the intraclasts (Figure 4.10).

Equant calcite cement fills most interparticle and mouldic pore space and postdates micritic envelopes. The cement is mainly stained red with Alizarin Red-S and K-ferricyanide, but scattered blue-stained crystals also occur (Figure 4.11). Syntaxial calcite cement overgrowths occur on echinoderm fragments and grow in optical continuity with the single-crystal bioclasts.

Fractures are more or less completely cemented by red- and blue-stained (in thin section) equant calcite cement.



Figure 4.10: Intraclastic-echinoderm-peloidal Grainstone. Peloids (P) and echinoderm fragments (Ec), with early marine cementation (red arrow) along grain boundaries (Chapter 5.2). Grains are evenly distributed in sparry calcite. Thin section in PPL.

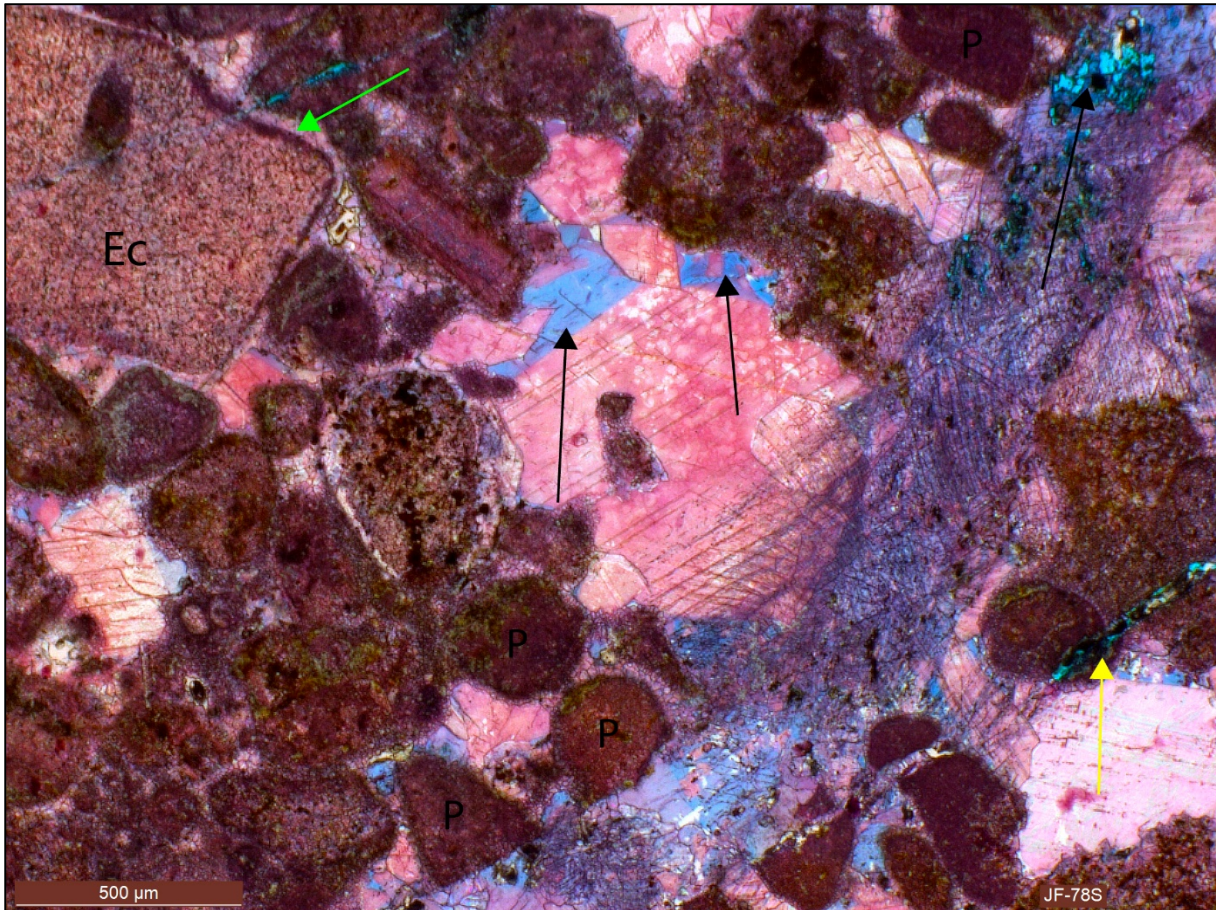


Figure 4.11: Grainstone from MF5 with red and blue stained calcite cement. Open interparticle porosity (stained bluish-green, black arrow in upper right corner) is probably related to secondary dissolution of cement. Note the micritic envelope (green arrow) along the echinoderm grain boundary, and the open fracture (yellow arrow). Note the colour difference between porosity and ferroan calcite cement, and the presence of cleavage within the ferroan calcite. Abbreviation: Ec = Echinoderm and P = Peloids. Thin section is stained by Alizarin Red-S and K-ferricyanide, and is shown in PPL.

Interpretation:

Microfacies 5 is grain-supported and lacks mud, and is therefore classified as a grainstone. This texture indicates a relatively high energy depositional environment. In combination with coralline algae (red algae) and peloids (as described in MF2), this texture and faunal composition is commonly indicative of an mid- to inner-ramp setting (Burchette and Wright, 1992; Flügel, 2004).

The red-stained (Fe-poor) isopachously-distributed calcite cement (Figure 4.10) is a typical early marine cement (Munnecke et al., 1997). The presence of this cement both within and on intraclasts indicates at least two episodes of early marine cementation; before and after lithification of the clasts. The ferroan calcite cement (stained blue) fills the central part of the pores, and thus postdates the Fe-poor calcite cement (stained red) which occur near the grain

margins. Ferroan equant calcite cement also postdates early marine cement. Different generations of calcite cement suggest a change in chemical composition of pore-waters through time.

The combination of low mud content, high abundance of intraclasts and interparticle sparry calcite, and presence of early marine cement, suggest deposition in a high-energy inner-ramp setting (Flügel, 2004).

4.2.6 Microfacies 6 – MF6: Benthic Foraminifera-Peloidal Pack-/Grainstone (Samples: JF-76S, JF-35S and JF-27S)

Observations:

Microfacies 6 samples are only present in southern J.Fadeloun, within Unit D, B and A. This microfacies is moderately to well sorted, and is composed of relatively small grains. The average grain diameter is 100µm. The dominating grain type in MF6 is peloids, undifferentiated benthic foraminifera (planispiral, uniserial and biserial) and echinoderm fragments (Figure 4.12). Minor constituents are fragments of red algae, bivalves, ostracods, calcispheres and sponge spicules. Sample JF-76S is mud-supported and show several generations of laminated fibrous to bladed calcite cement (possibly infilling part of a large void), whereas JF-35S is predominantly supported by evenly distributed equant to blocky sparry calcite, with only small patches being supported by micritic matrix. JF-27S is mud-supported and have prominent circum-granular cracks. All the MF6 thin sections have grains with isopachous micritic rims. Virtually all primary and secondary porosity is either cemented with equant calcite cement or filled with micrite, and is dominated by intraparticle and mouldic pores. JF-35S stands out by its high abundance of interparticle pores cemented by equant to blocky calcite cement (stained both blue and red by means of Alizarin Red-S and K-ferricyanide). The only open porosity observed, relates to open fractures and circum-granular cracks.

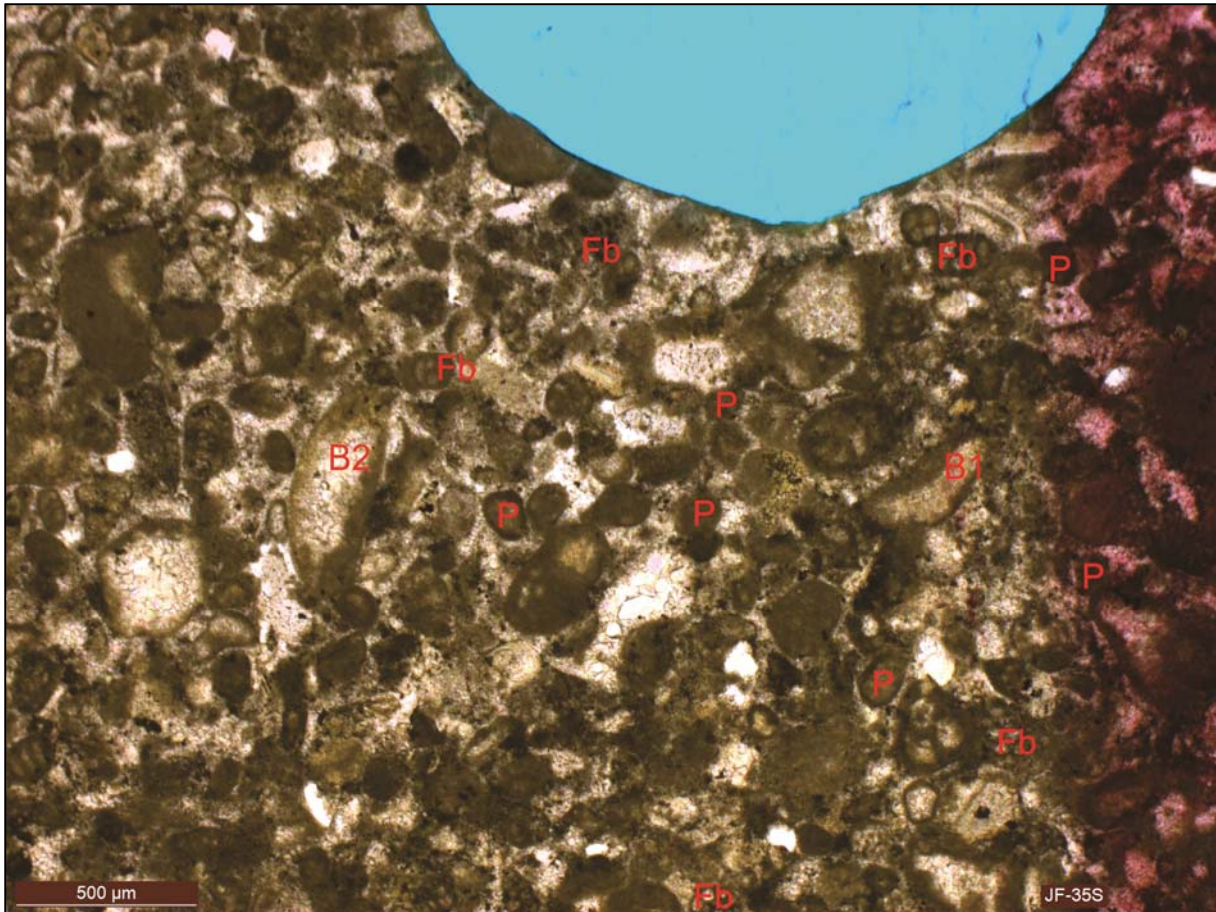


Figure 4.12: Benthic Foraminifera-Peloidal Packstone/Grainstone of MF6. Evenly distributed undifferentiated planispiral, uniserial and biserial benthic foraminifera (Fb) and peloids (P). Bivalve fragments were originally composed of low-Mg calcite (B1), aragonite (B2) or a mixture. The coarser crystalline nature (B2) indicates former aragonite, whereas the laminar part (B1) may indicate preservation of the original shell (composed of LMC). Bivalve shells have typically shells composed of both aragonite and LMC layers. Micritic envelopes can be observed as isopachous dark brown to black coloured rims along grain boundaries. Thin section in PPL.

Interpretation:

Microfacies 6 constitutes samples with both mud- and cement-supported texture, and is thus classified as a packstone/grainstone. MF6 have a heterozoan faunal assemblage (described in Chapter 4.2.4), with little to no quartz grains. As discussed in MF4, low textural maturity, presence of micritized grains (i.e. peloids), circum-granular cracks and the faunal association, suggest a shallow marine inner-ramp depositional setting.

4.2.7 Microfacies 7 – MF7: Red algal-Peloidal-Echinodermal Grainstone (Sample: JF-86S)

Observations:

Microfacies 7 is only present in southern J.Fadeloun, at the top of Unit D. This microfacies is moderately to poorly sorted, and is composed of relatively large and sparsely packed grains. The average grain diameter is 450µm. Dominating grain types in MF7 are red algae, peloids and echinoderm fragments (plates and spine). Minor constituents are fragments of bivalves, belemnites, and intraclasts. Several grains have relatively thick and dark brown coloured isopachous micritic rims (Figure 4.13). Grains tend to have remnants of microcrystalline granular and bladed cement surrounding grain margins. The calcite cement supporting the grains is blocky to equant, whereas there is syntaxial cement around echinoderm fragments. The pore space is predominantly filled with red and blue stained equant calcite cement, with only minor open interparticle (primary and secondary) and mouldic (secondary) porosity (Figure 4.14 and Figure 4.15). Secondary interparticle pores are related to partial dissolution of interparticle ferroan and non-ferroan calcite cements.

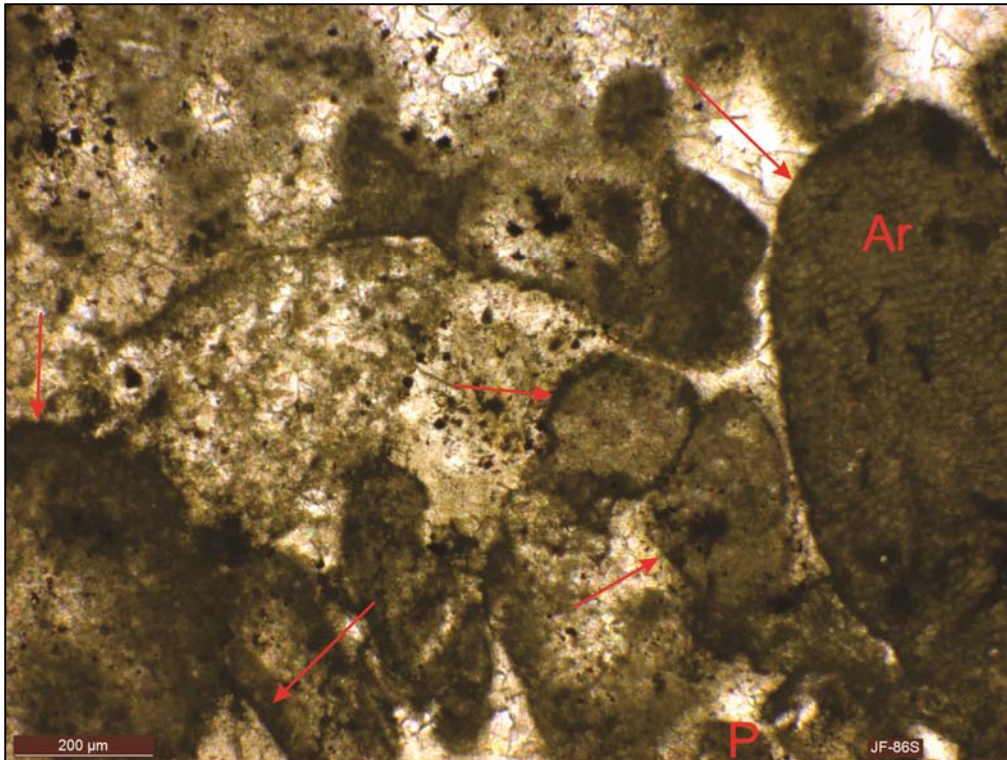


Figure 4.13: Red algae-Peloidal-Echinoderm Grainstone. Red algae (Ar) and Peloid (P) observed in sparry calcite. Most grains have incipient micritic rims (red arrows) related to micro-boring organisms (Flügel, 2004). Thin section in PPL.



Figure 4.14: Grainstone with some mouldic porosity (yellow arrow), shown as bright light blue spots, as opposed to ferroan calcite which has a dull blue/purple colour. The red arrow indicates close up area shown in Figure 4.15. Right-hand side of section is stained with Alizarin Red-S and K-ferricyanide. Thin section in PPL.

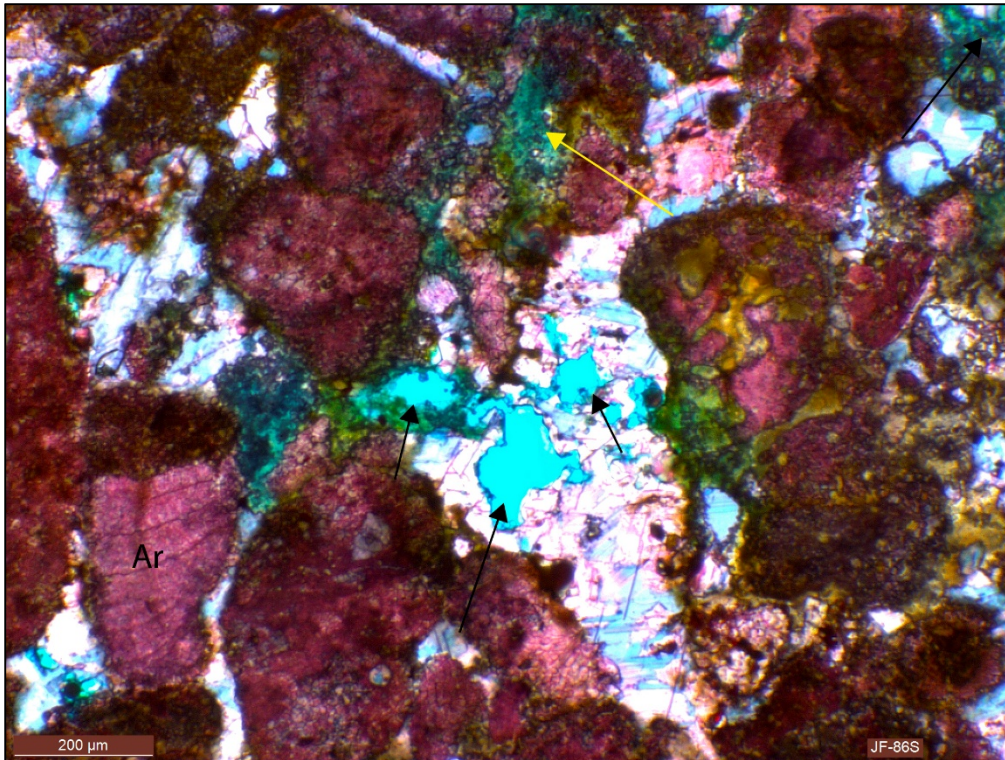


Figure 4.15: Grainstone (close up of Figure 4.14, red arrow) with partial dissolution of interparticle calcite cement (black arrows). It is sometimes difficult to differentiate between secondary interparticle (formed by dissolution of interparticle cement) and mouldic porosity, and some, but not all, of the calcite dissolution could actually relate to complete grain dissolution. Blue stained epoxy fills microporosity and gives the matrix a green-bluish hue (yellow arrow). Ar = Red algae. Thin section is stained with Alizarin Red-S and K-ferricyanide, and is shown in PPL.

Interpretation:

Microfacies 7 has a striking resemblance to MF5, both in texture, grain composition and average grain diameter. The major difference between MF7 and MF5 is the considerably higher abundance of red algae, and the lower abundance of intraclasts, in MF7. Thus MF7 is also indicative of an inner-ramp setting (Flügel, 2004). Rims of microcrystalline granular to bladed calcite cement are not as prominent as in MF5, but indicate early marine cementation (as described in 4.2.5). The high abundance of equant bluish calcite cement suggests late diagenetic cementation of primary or secondary (related to fabric selective dissolution of matrix, cements and grains) porosity during burial (Choquette and James, 1987). Red algae prefer very shallow (<25m) sub tidal environments with high light penetration, but may be found down to 250m water depth. They can withstand fairly agitated waters, but are less tolerant to salinity variations (Flügel, 2004). The texture (low mud content and high abundance of sparry calcite) and faunal composition thus suggest shallow-water sub-tidal deposition of an inner-ramp setting.

4.2.8 Microfacies 8a – MF8a: Spiculitic-Peloidal Wacke-/Packstone

(Sample: JF-11S)

Observations:

Microfacies 8a is present within southern J.Fadeloun. The microfacies is very fine grained, with an average grain diameter of 50µm, and well sorted. Grains are evenly dispersed in the matrix and dominantly matrix supported, with only some local areas that are grain supported. MF8a is mostly composed of calcitic sponge spicules, calcispheres and peloids, with minor abundance of planktonic globigerinid foraminifera- and bivalve fragments (Figure 4.16 and Figure 4.17). Interparticle pores are mostly filled by micrite giving a wackestone/packstone texture. Microfacies 8b has some organic material, observed as dark brown to black spots and brown laminations in thin section.

The sponge spicules and bivalve fragments have been partly dissolved, resulting in formation of secondary moldic pores that are subsequently filled with equant calcite cement. Additional pores include common primary intraparticle and minor primary interparticle. Mouldic pores are mostly cemented with red-stained equant calcite cement, except for some bivalve fragments that contain blue-stained calcite crystals. A relatively high fracture density with variable fracture apertures is observed. Fractures are completely cemented and have cross-cutting relationships. Fractures contain red- and blue-stained equant calcite cement, and although the paragenetic sequence is poorly defined, ferroan calcite seems to postdate non-ferroan calcite cement (Figure 4.18).

Microfacies 8a shows both mud- and grain-supported sedimentary textures, and always contains >10% grains.

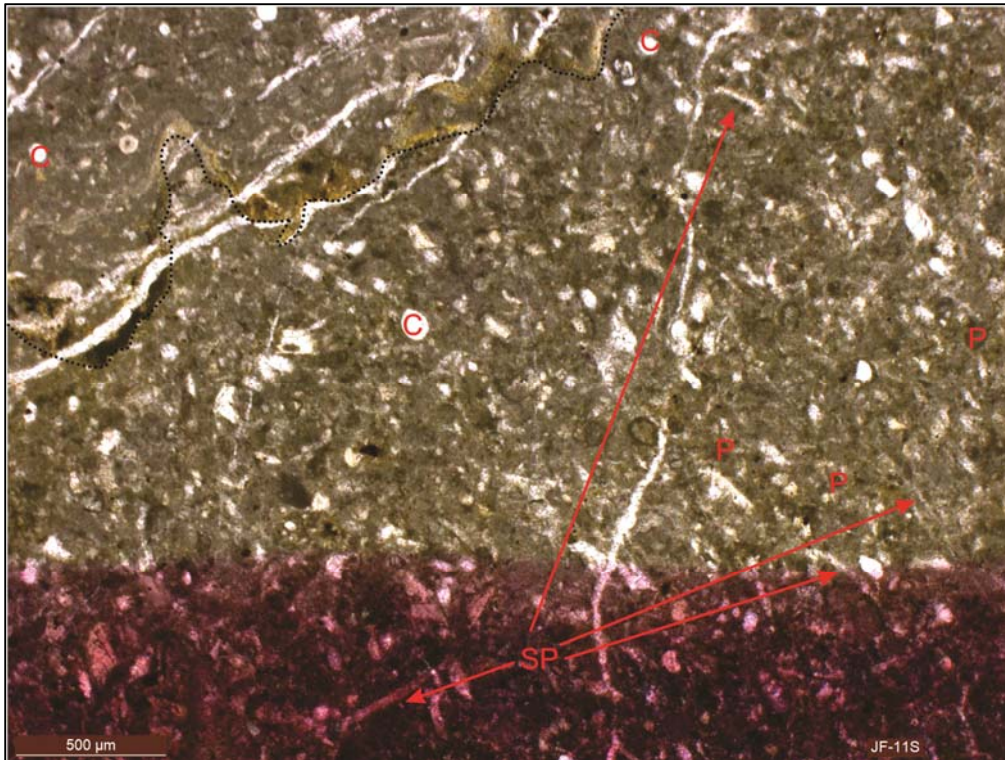


Figure 4.16: Spiculitic-Peloidal Packstone containing evenly distributed sponge spicules (SP), calcispheres (C) and very small peloids (P). Dashed black line outlines a dissolution seam. The lower part of the thin section is stained with Alizarin Red-S and K-ferricyanide. Thin section in PPL.

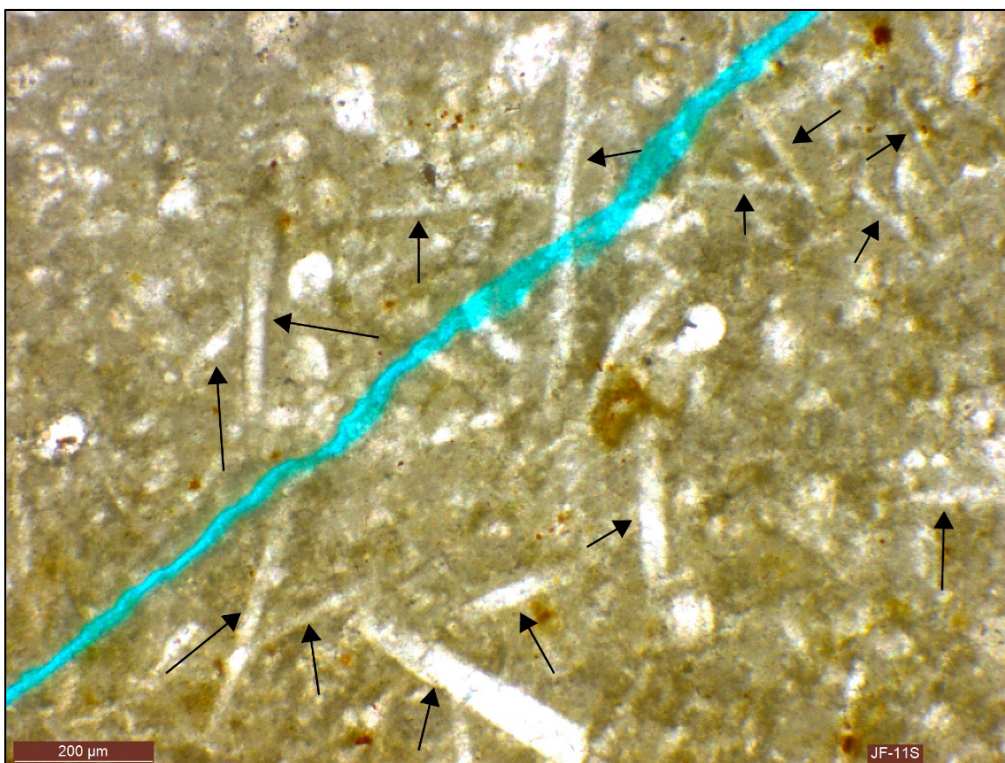


Figure 4.17: Close up of thin section JF-11S highlighting the high abundance of sponge spicules (black arrow). Thin section in PPL.

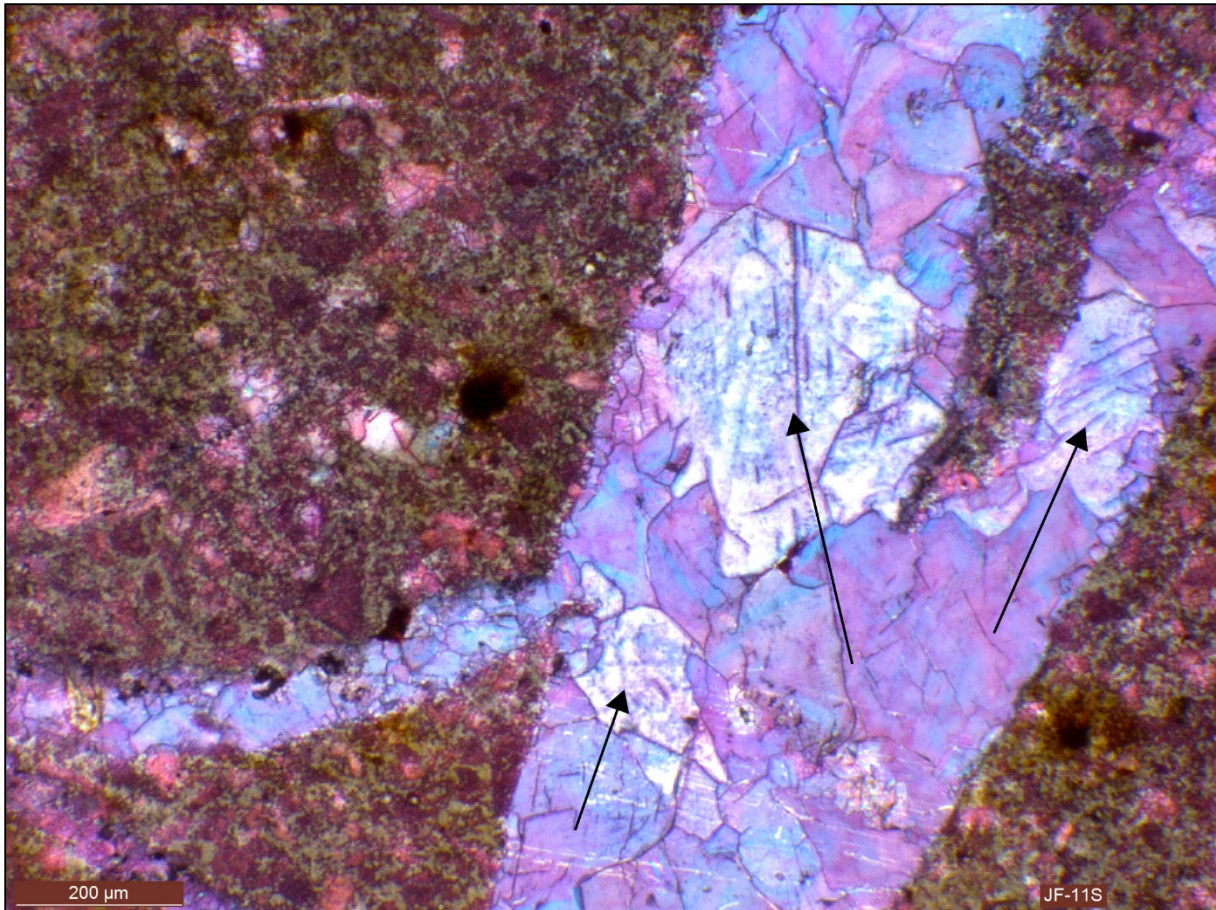


Figure 4.18: Fracture filled with ferroan (blue stained, arrows) and “non”-ferroan equant calcite cement. The paragenetic sequence is poorly defined, but ferroan calcite seems to postdate non-ferroan. Thin section is stained with Alizarin Red-S and K-ferricyanide, and is presented in PPL.

Interpretation:

The muddy sedimentary textures combined with a relatively high grain content classify microfacies 8a as a wacke-/packstone (Dunham, 1962). The association of sponge spicules, calcispheres and mollusc fragments, suggests temperate waters (Lees and Buller, 1972). Sponges are sessile metazoan and occur in all depositional settings from intertidal to deep marine, in predominantly quiet water conditions (Flügel, 2004).

Micritic grains have irregular geometries and variable sizes suggesting that these are peloids rather than true fecal pellets. The abundance of peloids, which require the presence of micro-boring organisms for their formation, could indicate that the sediment was deposited within the photic zone (Flügel, 2004). The mixed planktonic-benthonic faunal assemblage may suggest deposition in a slope environment, but could also represent a mid-ramp environment (Flügel, 2004).

4.2.9 Microfacies 8b – MF8b: Spiculitic-Peloidal Packstone

(Samples: NFS-3S, NFS-2S, NFS-1S, JF-36S and JF-30S)

Observations:

Microfacies 8b occurs throughout the southern J.Fadeloun, and at the base of the succession at northern J.Fadeloun. The microfacies is fine grained, with an average grain diameter of 50µm, and is well to very well sorted. The grains form a grain-supported texture and are mostly composed of sponge spicules and micritic grains, with minor abundance of calcispheres, planktonic globigerinid foraminifera- and bivalve fragments (Figure 4.19). The micritic grains have irregular sizes and geometries, and occasionally have preserved internal structures. Interparticle pores are mostly filled with micrite (i.e. packstone texture). Microfacies 8b has trace to minor abundance of organic material, as defined from reflected light microscopy. The sediment is rich in mud and has a grain-supported sedimentary texture.

All samples have experienced some dissolution of bivalve fragments and spicules, resulting in the formation of secondary mouldic pores. Additional pores include primary intraparticle and minor primary interparticle. Virtually all pores, both primary and secondary pores, are filled with calcite cement. Mouldic pores are mostly cemented with red-stained equant calcite, and locally with minor blue-stained equant calcite.

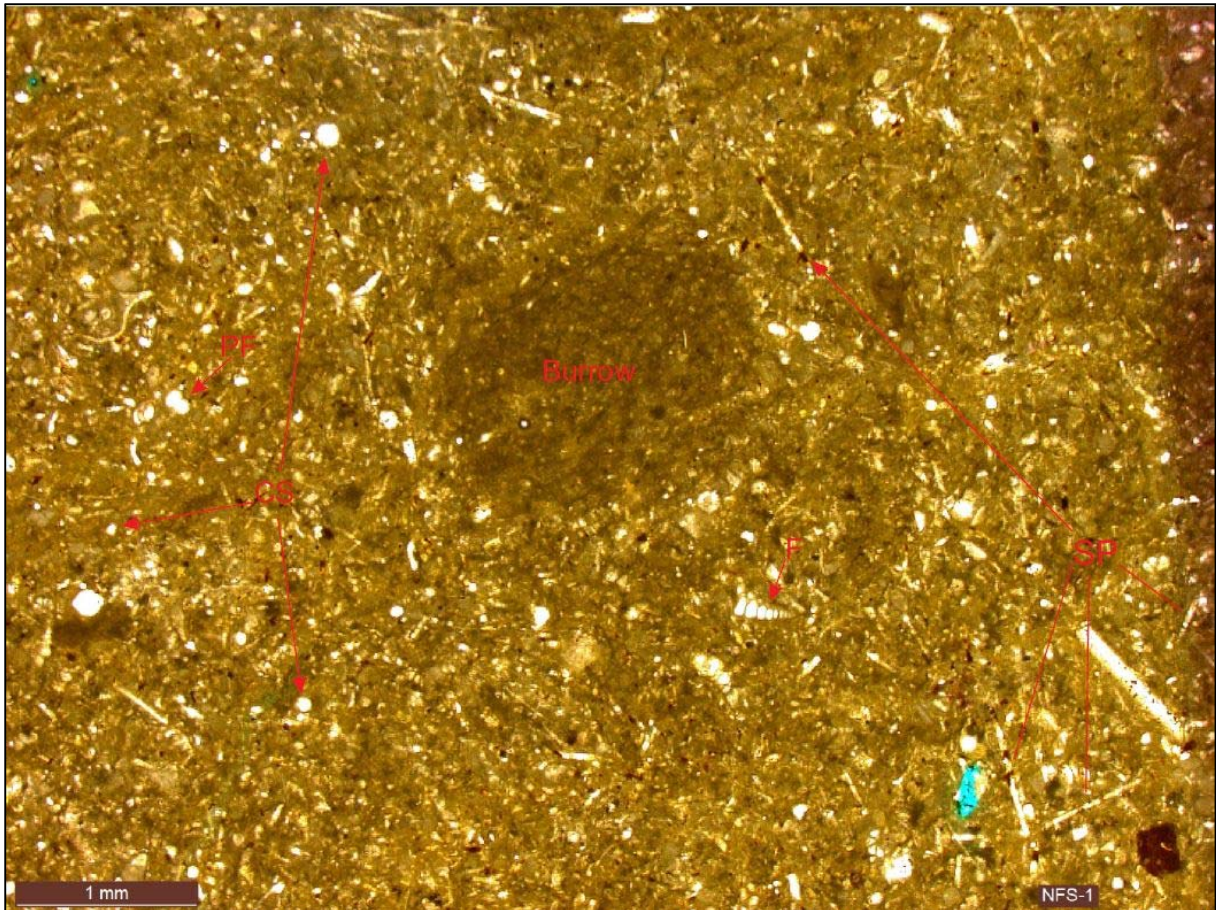


Figure 4.19: Spiculitic-peloidal packstone from Unit 2, containing evenly distributed calcareous sponge spicules (SP), calcspheres (CS), planktonic globigerinid foraminifera (PF), burrow, a biserial undifferentiated foraminifera, and abundant peloids. The small size of the peloids makes it difficult to differentiate them from the matrix. Organic material, observed as small dark brown to black spots, was defined from reflected light microscopy. Thin section in PPL.

Interpretation:

The mud-rich and grain-supported sedimentary texture classify microfacies 8B as a packstone (Dunham, 1962). The association of sponge spicules, foraminifera (both planktonic and benthic) and mollusc fragments, suggest temperate waters (Lees and Buller, 1972). Temperate water conditions are also supported by $\delta^{18}\text{O}$ analyses of bulk sediment which indicate ambient water temperatures of 16-18 °C (Appendix E and Figure 4.55).

Sponges are sessile metazoans and occur in all depositional settings from intertidal to deep marine, in predominantly quiet water conditions (Flügel, 2004). Rounded, micritic grains of uncertain origin are defined as peloids (Esso, 1988; Lønøy, 2005) and usually indicate deposition within the photic zone. The close association between microfacies 8b and overlying microfacies representing mid-inner ramp deposition, the mud-rich sedimentary texture, and the occurrence of planktonic fauna, suggest deposition in a mid-ramp setting.

4.2.10 Microfacies 9 – MF9: Peloidal Wacke-/Packstone

(Samples: GS-6S, GS-5S, GS-3S and GS-1S)

Observations:

Microfacies 9 is only present within the J.Garci section. This microfacies is well sorted, and is composed of relatively small and tightly packed grains. The average grain diameter is approximately 60µm, and grains are predominantly peloids with minor abundance of bivalve- and echinoderm fragments (plates), benthic and planktonic foraminifera, ostracods, calcispheres and sponge spicules (Figure 4.20). The peloids are very small making it difficult to separate them from the surrounding lime mud.

Organic material, as defined from fluorescence microscopy, occurs within fracture-filling ferroan calcite cement and within chambered grains. It also occurs within micritic mud, as observed in reflected and plane polarized light microscopy. The fractures have two different orientations perpendicular to one another, and are infilled with calcite cement that is stained bluish by means of Alizarin Red-S and K-ferricyanide. Fracture aperture varies, and range from approximately 4-300µm. Horizontal and oblique burrows are observed in outcrop, but are not clearly visible in thin section.

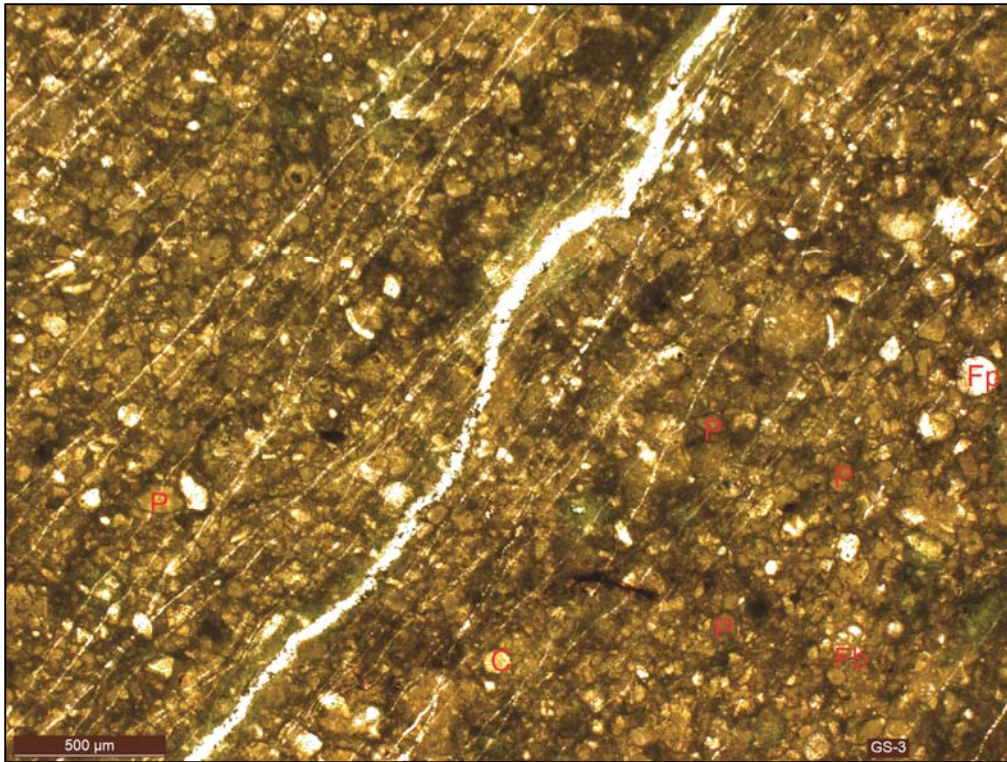


Figure 4.20: Peloidal packstone (MF9). High abundance of peloids (P) with few scattered fragments of benthic foraminifera (Fb), planktonic globigerinid foraminifera (Fp) and calcispheres (C). Patches of dark brown organic material are observed throughout the thin section, and within cemented fractures of MF9. Fractures are completely infilled with cement, comprising predominantly Fe-rich equant calcite cement. Non-stained thin section in PPL.

Interpretation:

The high abundance of mud and horizontal burrows suggest calm waters, possibly in the distal parts of a ramp (mid-outer ramp). Burrowing organisms tend to burrow in soft sediments, and the depth and angle of burrow is dependent on the nature of the seafloor sediment, oxygen content and nutrient flux (Flügel, 2004). In agitated sea water, the burrowing organism will commonly develop vertical burrows to get shelter from the ambient waves and currents, whereas in calm waters the organisms tend to develop horizontal burrows in the search for food (Seilacher et al., 2005; Seilacher, 2007). Horizontal burrows, high abundance of mud in association with grains and planktonic microfossils indicate that MF9 was deposited in an outer ramp setting.

The ferroan calcite cement (stained blue) in fractures indicates precipitation during a later-stage diagenesis (as discussed in chapter 4.5.2). According to Kjelkenes (2015) a cross-cutting fracture relationship indicates at least two tectonic events. However, the lack of offset

between the fractures may also be indicative of one single fracture generation. The organic material within fracture-filling ferroan calcite cement in MF9 is revealed by its light-bluish fluorescence when exposed to ultraviolet light (Figure 4.21 and Figure 4.22). The intracement distribution of the organic material suggests that the organic material is oil, and that oil migration is synchronous with or predates ferroan calcite cementation. The importance of this in reservoir evaluation is discussed in Chapter 5.4.

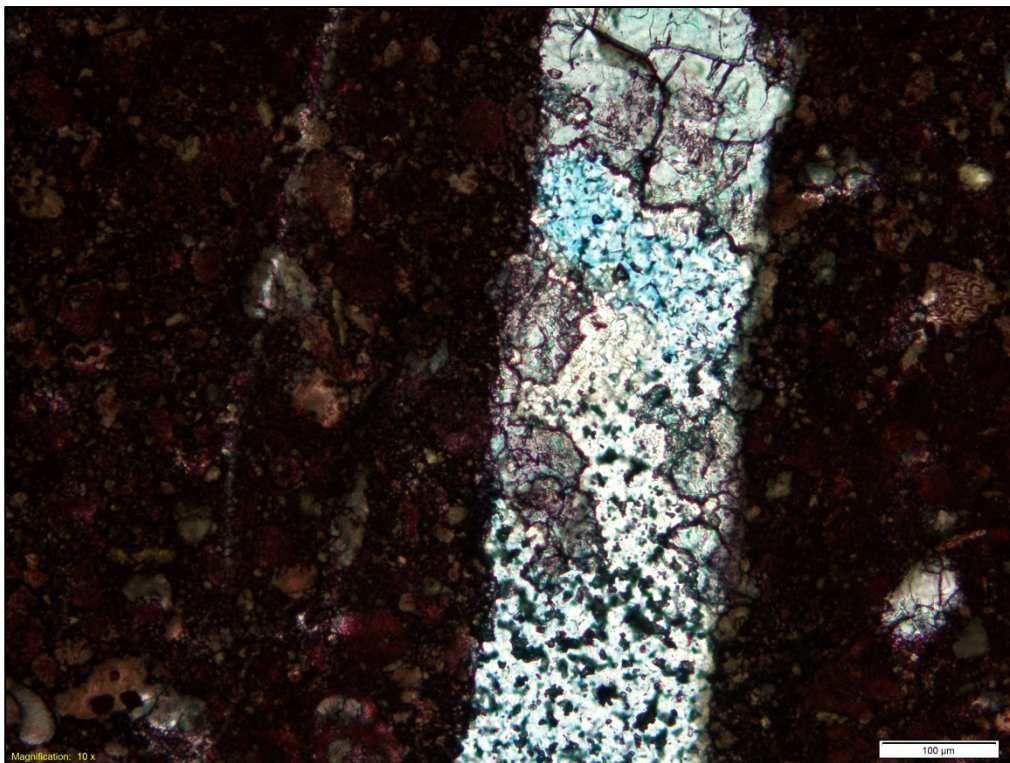


Figure 4.21: GS-6S, fracture apparently completely filled with ferroan calcite cement. Stained thin section in PPL.

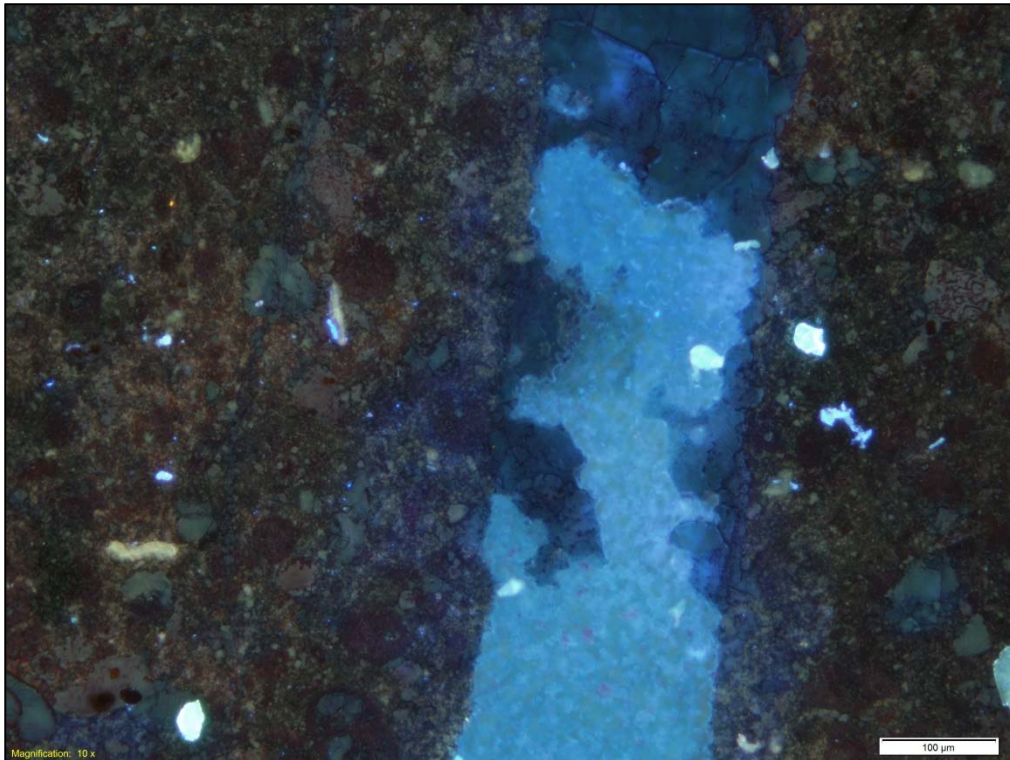


Figure 4.22: GS-6S, fracture depicted in Figure 4.21 under ultra violet light. The fluorescence indicates that hydrocarbons were trapped during precipitation of the ferroan calcite cement (George et al., 2001).

4.2.11 Microfacies 10 – MF10: Foraminifera-echinoderm-Peloidal Packstone (Samples: GS-4S and GS-2S)

Observations:

Microfacies 10 is only present within the J.Garci section. This microfacies is moderately to poorly-sorted and has an approximately average grain diameter of 100μm. MF10 is predominantly composed of peloids, echinoderm fragments (plates), and benthic foraminifera (Figure 4.23). Other minor constituents are bivalve fragments, planktonic foraminifera, ostracods and sponge spicules. Most shell fragments are very small and disintegrated, and thus difficult to classify. Throughout the microfacies, clay and organic material is patchily distributed. Organic material is observed as small brown circular spots within the matrix, grains and along walls of open fractures. Virtual all primary and secondary pore spaces are cemented, with only some open interparticle micro porosity (commonly along fracture zones) and minor fracture porosity. Most fractures are infilled with bluish-stained calcite cement and

open fractures show a cross-cutting relationship. The microfacies components mostly consist of reddish-stained calcite, and bluish-stained calcite cements occur in fractures and some moulds.

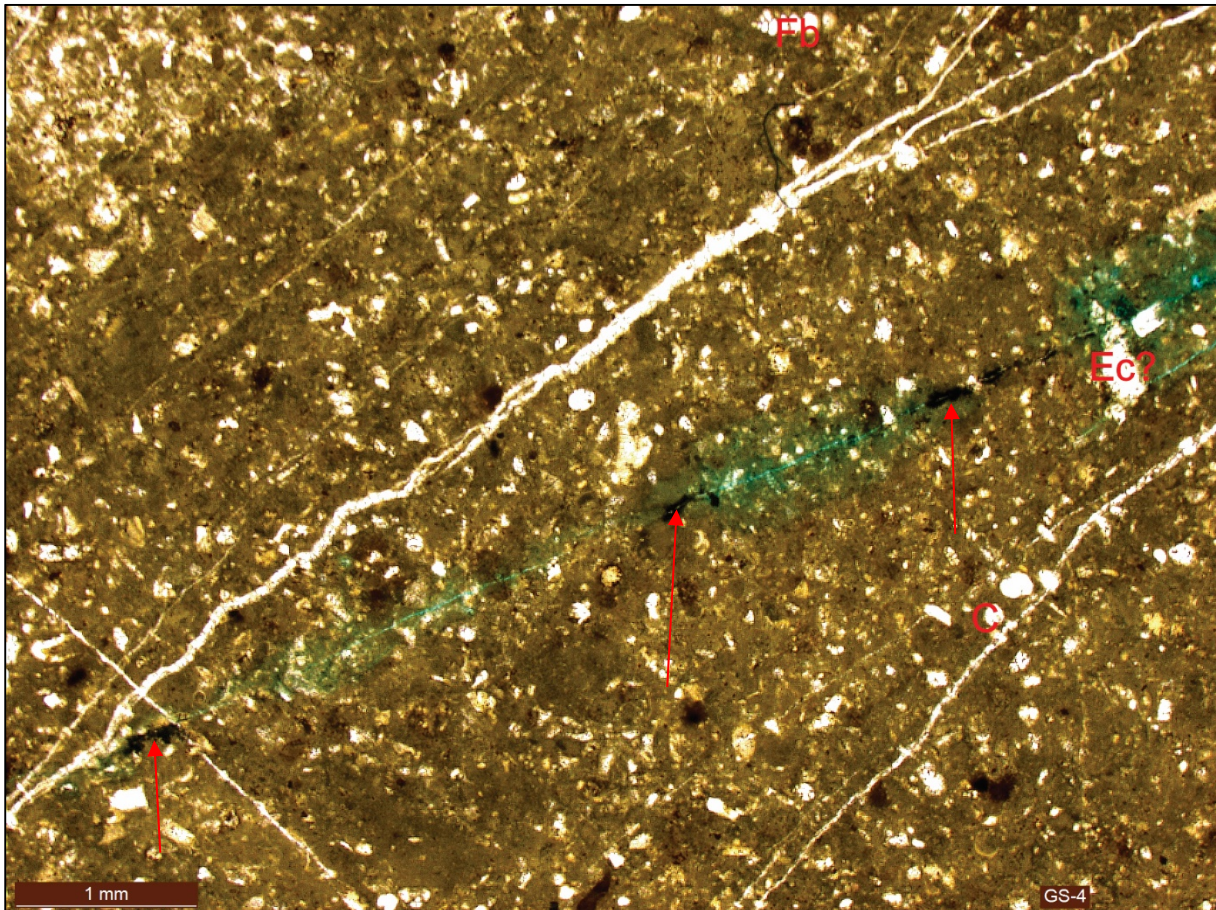


Figure 4.23: Packstone of Unit H within the J.Garci section, comprising high abundance of peloids. Note the organic material (as defined from reflected light microscopy), following and lining the walls of the open fracture (red arrows). Abbreviation: C = Calcsphere, Fb = Benthic foraminifera and Ec? = Possible echinoderm fragment. Thin section in PPL.

Interpretation:

Microfacies 10 has more or less the same faunal assemblage as MF9, but with a higher frequency of benthic foraminifera and coarser average grain size. The skeletal grains are commonly disintegrated, and isopachous micritized rims are not as common in MF10 as in other microfacies, indicating a slightly deeper depositional environment (see below). The combination of matrix-supported texture and minor micritization of grains suggest deposition in a mid- to outer-ramp setting (Flügel, 2004). Crosscutting fractures indicate at least two

fracture orientations. The lack of offset between cross-cutting fractures indicates that different fracture orientations possibly represent the same fracture generation.

4.2.12 Grain size distribution

The grain size distribution varies widely in studied sections. Between the microfacies the average grain diameter ranges from 22µm to 450µm, as shown in Figure 4.24. The larger grain sizes are most abundant in the microfacies representing high energetic inner ramp deposits, whereas the smaller grain sizes typically represent calm waters in a mid- to outer ramp setting. Large grain sizes are also most common in the upper part of the shallowing upward cycles.

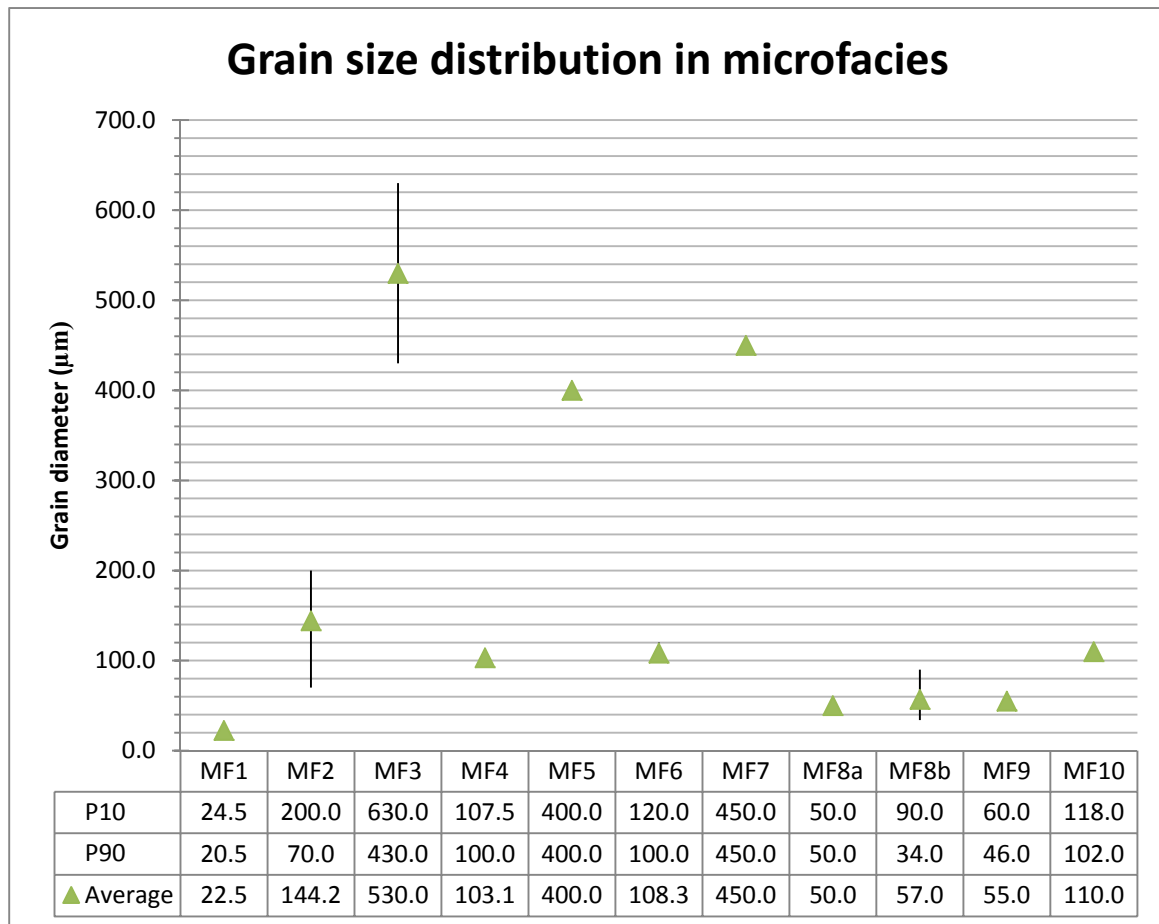


Figure 4.24: Grain size (average, P10 and P90) for each microfacies. Vertical lines represent the P10 (top) to P90 (bottom) range, with average grain size given as green triangles. P10 (P90) is a probability measure and means that 10% (90%) of the grain sizes exceed the P10 (P90) estimate.

4.3 Sedimentary surfaces

Three different sedimentary surfaces have been observed in outcrop and thin section studies. Sedimentary surfaces observed in the outcrops comprise discontinuity surfaces relating to subaerial exposure of the sediment surface. These surfaces are mainly recognized on the basis of geometry, depositional features and bedding contacts. Exposure related horizons thus contain vital information for interpreting the depositional, diagenetic and sequence-stratigraphic history (Flügel, 2004).

4.3.1 Paleosol/caliche

Observations:

Thin sections JF-27S, JF-36S, JF-37S and JF-42S in Unit B and C, are characterized by open circum-granular cracking of very fine grained (average grain diameter 100µm) packstones with finely crystalline matrix (Figure 4.25). Thin section JF-36S only shows incipient circum-granular cracking. The packstones mostly comprise fine-grained skeletal fragments, often with micritic envelopes, organic material and peloids, with selective dissolution of the matrix.

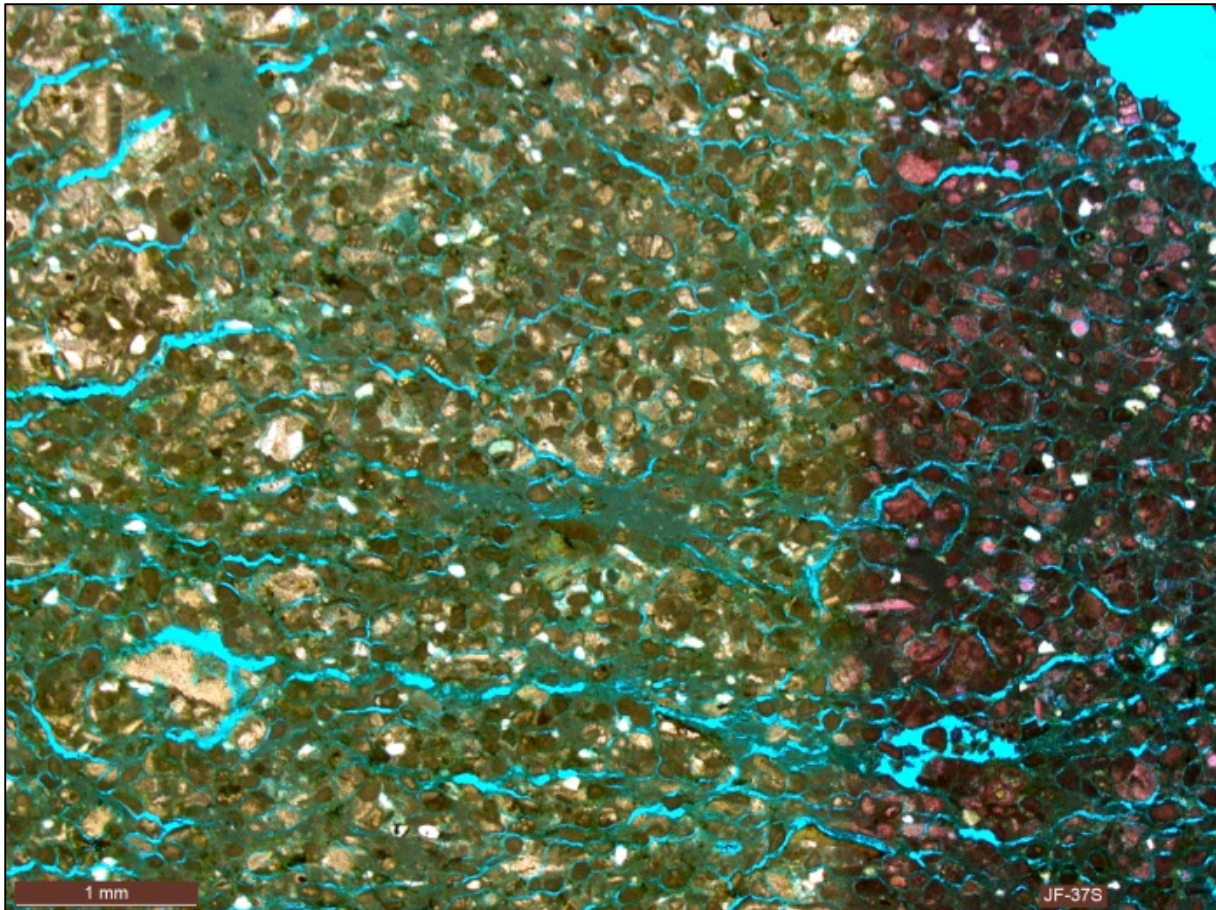


Figure 4.25: Circum-granular cracking in sample JF-37S. Cracks following grain boundaries observed throughout the thin section. Thin section in plane polarized light, and right side artificially stained red

Interpretation:

Paleosols are often described as “a buried soil horizon of geological past”, but in a broader sense it describes a subaerial exposed horizon (Flügel, 2004). Sand and silt sized polygenetic peloidal grains are commonly ubiquitous in caliche (Wright, 1994). They can develop as a result of fragmentation of the host micrite by wetting and desiccation, forming circum-granular cracks (Wright, 1994; Suchý, 2002). This process is termed “granification” and can produce large quantities of peloids with grains being rounded due to abrasion (Wright, 1994). Some of the most characteristic fabrics of subaerial horizons are laminations, micritic peloids, multiple fracture generations, root voids, and variations of carbonate cement morphologies (Harrison and Steinen, 1978; Wright, 1989). Peloidal-rich limestones with circum-granular cracking are commonly diagnostic microscopic criteria of caliche facies developed through repeated wetting and drying processes, commonly landward of the intertidal area (Esteban and Klappa, 1983; Calner, 2002; Suchý, 2002). The abundance of organic material and the

presence of circum-granular cracks indicate that these beds have been subjected to subaerial exposure, either due to progradational depositional processes, sea-level oscillations or a combination of these. It is reasonable to interpret these beds (JF-27S, JF-36S, JF-37S and JF-42S) as paleosols, and the horizons could be useful as bounding surfaces in development of the sequence stratigraphic history.

4.3.2 Hardground

Observations:

A massive bed of light gray to brown and orange-coloured bioclastic wacke- to packstone (see Figure 4.26 and Figure 4.27), is observed at the top of the Aptian sequence in the J.Garci section, The bed is extensively bored by endolithic organisms, and have high abundance of ferruginous echinoderms, belemnites and some bivalve fragments. At J.Garci this horizon is approximately 10-20cm thick and represents an unconformity between the Aptian and the overlying Albian.

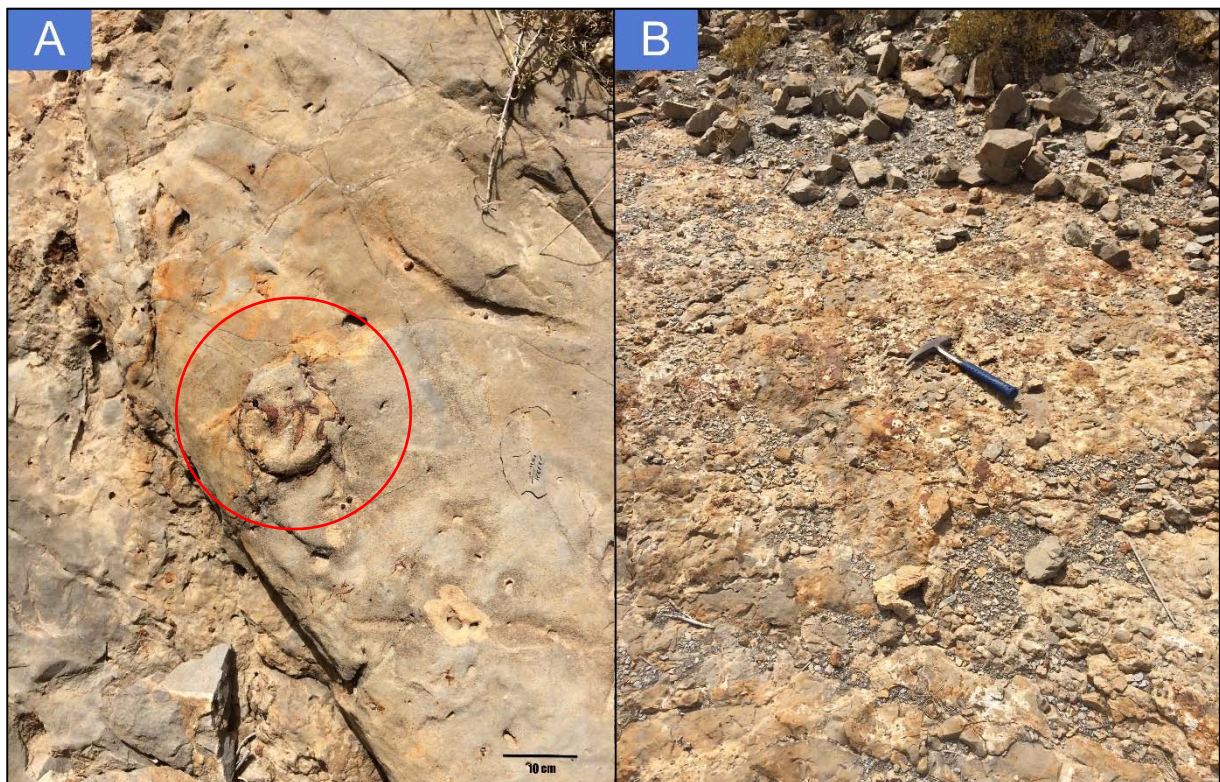


Figure 4.26: Top Aptian hardground at J.Garci. A) Hardground with accumulations of echinoid fragments. Red circle is shown as a close-up in Figure 4.27. B) Rubbly and nodular ferroan rich, red/brown-stained hardground. Geological hammer for scale. Photo by: Atef Bel Kahla.



Figure 4.27: Close-up of a cluster of echinoid plates and spines observed on the hardground. Photo by: Atef Bel Kahla

Interpretation:

A smooth and discontinuous centimeter-thick surface with limestone clasts and heavily bioturbated carbonates (Figure 4.28), are commonly related to synsedimentary submarine lithification, and is termed a hardground (Figure 4.26) (Shinn, 1969; Flügel, 2004). They are commonly related to non-deposition (Flügel, 2004) or low sedimentation rates, low sediment stability and initial high internal permeability, in waters with normal salinity and temperature, and are commonly formed at depths down to 30 meters (Shinn, 1969; Flügel, 2004). The ferruginous-rich crusts observed at the top of the Aptian at the Garci section were probably formed by microbial mediated processes under low-energy hydrodynamic conditions (Flügel, 2004)

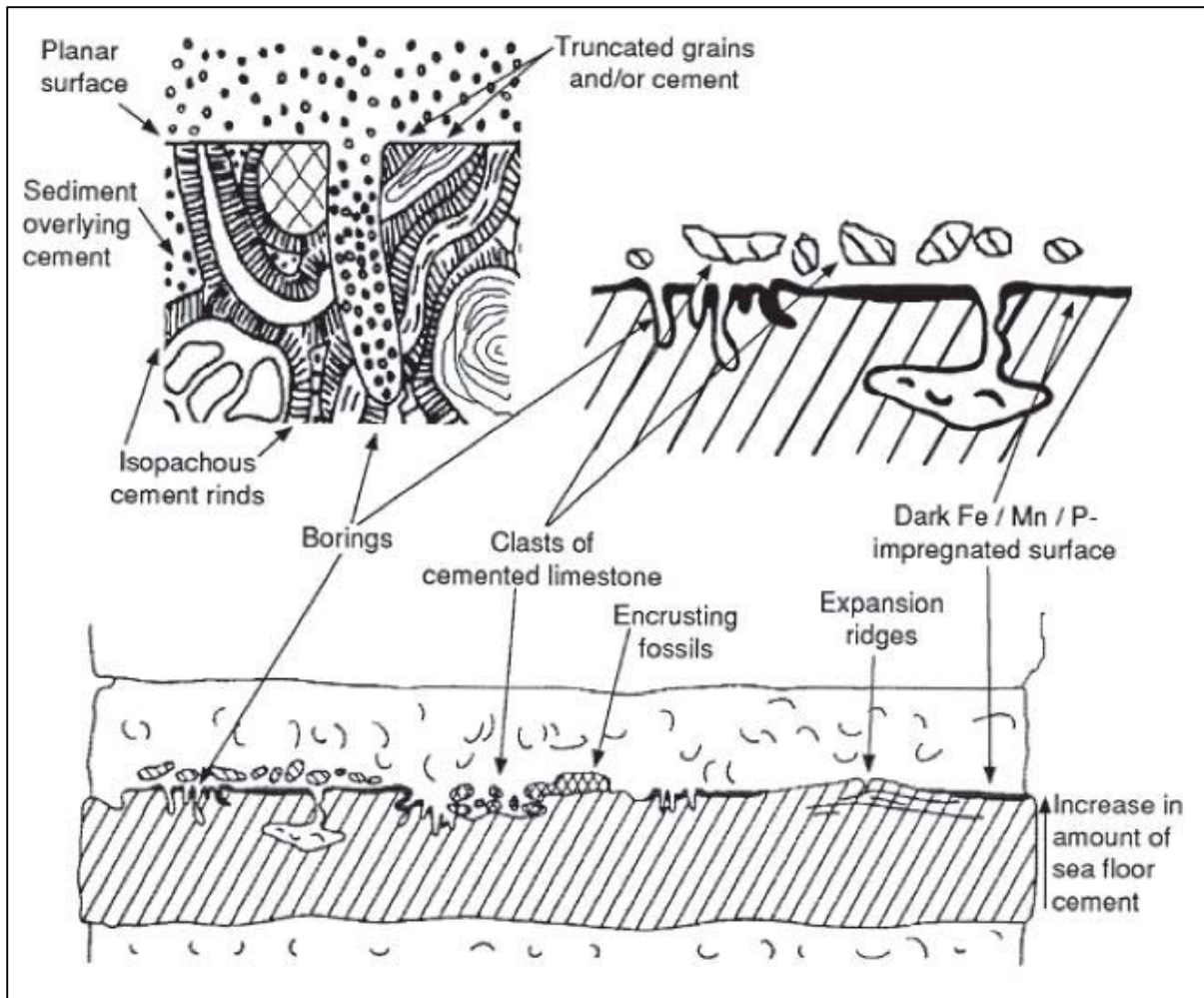


Figure 4.28: Principle sketch of features related to the formation of hardgrounds. After Flügel (2004) and James and Choquette (1983)

4.3.3 Paleokarst and ancient speleothems

The following features are observed:

Paleokarst surface

An irregular discontinuous surface with both cemented and open voids is observed in Unit A (Chapter 4.4) at southern J.Fadeloun (Figure 4.29).

Paleokarst surfaces (Figure 4.29) are difficult to recognize in the stratigraphy and are often represented only by an irregular bedding contact (James and Choquette, 1984). The smooth irregular bedding contact observed in Unit A at the southern J.Fadeloun section may thus represent a paleokarst surface developed by subaerial exposure.



Figure 4.29: Paleokarst surface at southern J.Fadeloun within a bioclastic grainstone of Unit A. The exposure surface is represented by an irregular bedding contact, outlined in the photo by a red dashed line. Geological hammer for scale.

Paleokarst caves

Large voids and caves with large lateral extent, proximal to the locality of thin section sample NFS-9S, occur in Unit G (Chapter 4.4). The voids and caves follow the bedding of the bioclastic grainstone laterally (Figure 4.30), varying in size from small vugs on a centimeter scale, up to large open caves with diameters up to several meters. The vugs and caves increase in size towards the west.

Voids and large open caves in shallow-marine limestones represent dissolution of the limestone, typically by fresh water charged with CO₂ penetrating and percolating downward through fissures, fractures and voids (Figure 4.30). Karst is the general term for features related to the meteoric dissolution of limestone, and karstification is often associated with

solution collapse and with formation of sinkholes, dolinas, caves and underground rivers (James and Choquette, 1984; Flügel, 2004). Paleokarst is ancient karst commonly buried by younger sediments, and is typically formed during relative sea-level low stands in humid climates (Flügel, 2004).



Figure 4.30: Large epigenic karst caves and vugs in a bioclastic grainstone at the northern J.Fadeloun section. Note that the karst caves get progressively larger towards the west and that the beds dip gently towards the west. Persons for scale. Photo by: Atef Bel Kahla

Speleothems

Thin sections JF-21S and JF-76S from the southern J.Fadeloun section show several generations of laminated fibrous to bladed calcite cements (Figure 4.31) The cements occur within the margins of the thin sections, and all sides of the cemented pore space are thus not observable. The cement distribution within the pore space is therefore uncertain.

Laminations or bands of fibrous calcite cements, is often indicative of precipitation of speleothems developed during precipitation from freshwater supersaturated with respect to calcium carbonate in karst caves (Flügel, 2004). The freshwater percolating down through the

surface and into the carbonate rock (Figure 4.32) contains CO₂ at a higher partial pressure than at the surface. The weight of the overlying water column and the lower ambient temperature causes the partial to increase. Increased partial pressure of CO₂ will promote increased dissolution until the water flows out of the rock or reaches a cave and regains equilibrium with the atmospheric pressure, resulting in degassing of CO₂. The degassing of CO₂ could result in supersaturation of calcium carbonate followed by subsequent precipitation of speleothems (James and Choquette, 1988; Bjorlykke, 2010), as observed in Figure 4.31.

The location of the laminated fibrous cement along the margin of the thin sections, with corresponding uncertain cement distribution, may represent either phreatic (more uniform cement distribution within the pore) or vadose (pendant cement distribution within pore) cementation.

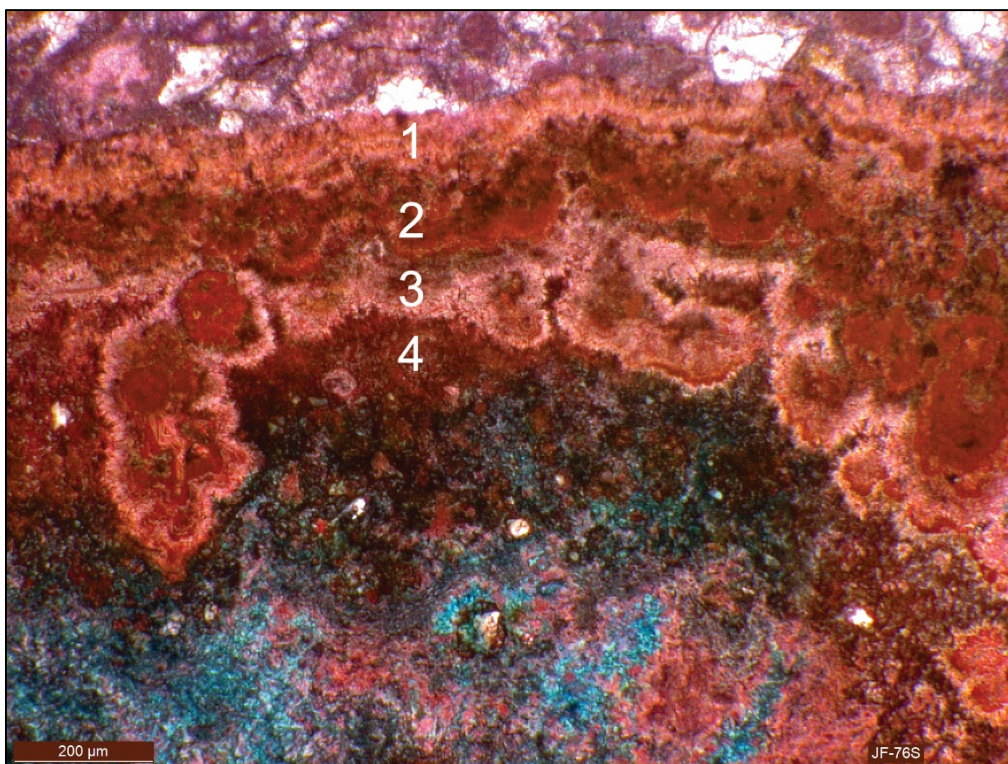


Figure 4.31: Several generations of laminated fibrous calcite cement. Image showing at least four generations of calcite cements, labelled 1 through 4. Thin section stained with Alizarin Red-S and K-ferricyanide.

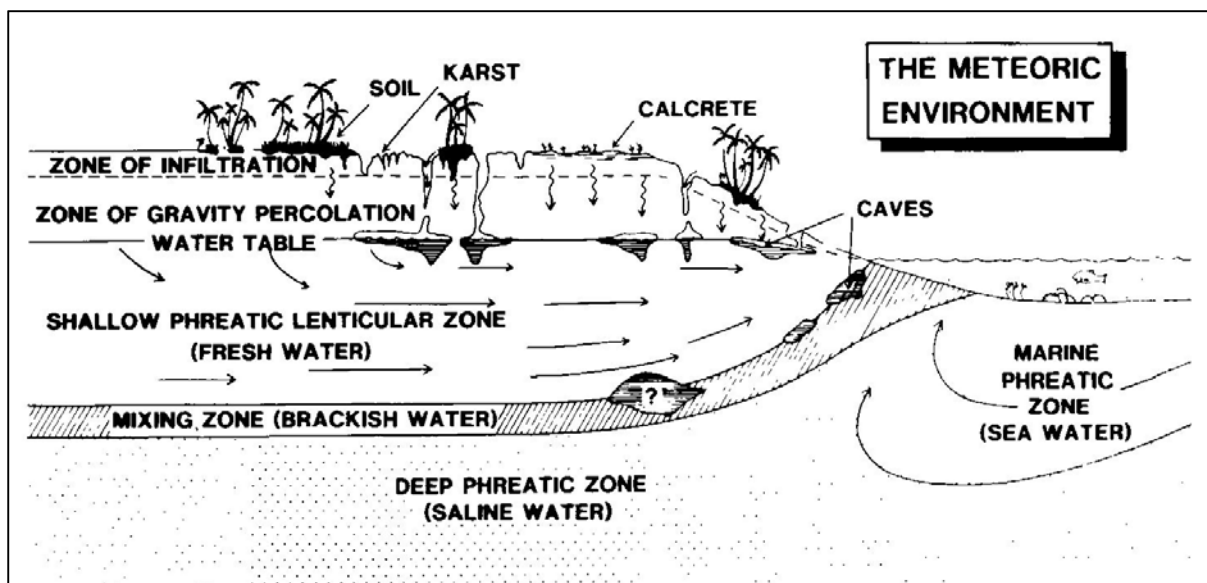


Figure 4.32: Principal sketch of the main zones of meteoric and mixing-zone diagenetic environments. After James and Choquette (1984).

4.4 Depositional units

Eight depositional units are defined based on cyclic trends. Each unit shows a coarsening upwards trend and an associated change in sedimentary texture (wacke- to grainstone). In carbonate rocks it is important to realize that grain size is not only indicative of hydraulic energy but also reflects the original faunal and floral composition and bioturbating organisms, which again is related to grain morphology (Flügel, 2004). However, even though several factors may influence grain size, the grain-size distribution will in many cases reflect wave and current energy. The vertical microfacies distribution within each unit is gradually going from mud-supported texture with low grain content, to more grain-supported texture as the mud content decreases. High abundance of mud is commonly indicative for calm waters, whereas low mud content and high grain content, often indicates agitated waters and high energy environments (Flügel, 2004). The gradual increase in grain size combined with decrease in mud content make up four cycles in the studied sections, thus indicating cyclic trends. Each unit is thoroughly discussed in Chapter 5. The units are marked in Appendix WellCAD logs and Appendix I 1-3.

A microfacies classification scheme was developed by Wilson (1975) by defining 24 Standard Microfacies types (SMF). Flügel (2004) realized that the SMF-classification of Wilson (1975) was idealized for rimmed carbonate shelf and was not applicable to carbonate ramps. By surveying various articles, Flügel (2004) noticed that several microfacies types appear to dominate different parts of a carbonate ramp, and thus distinguished 30 Ramp Microfacies Types (RMF). Classification is based on grain types, grain frequency, matrix type, depositional fabrics, depositional texture and fossils (Figure 4.33).

The different ramp zones (Figure 4.34) contain diagnostic RMF types as shown in Figure 4.33, and can therefore be used as a quick guide for interpreting depositional environments. In the following description of the Units A-F, a correlation between the already classified microfacies (see above) and RMF is applied where possible.

Outer ramp

Thin- to medium-bedded, fine-grained, often burrowed limestones and marls. Laminated marls alternate with lime mudstones. Skeletal grains commonly well preserved, not worn. Mudstones, wackestones, packstones. Some tempestite beds (grainstones). Mud mounds (see Sect. 16.1.2).

RMF 1: Calcisiltite and mudstone with peloids, very fine skeletal debris, sponge spicules, sometimes fine-laminated (SMF 1).

RMF 2: Argillaceous burrowed mudstone and wackestone; rare agglutinated foraminifera, ostracods, echinoderms.

RMF 3: Burrowed bioclastic wackestone and packstone with diverse, common to abundant fossils (bivalves, brachiopods, echinoderms) and peloids. Skeletal grains not worn; whole fossil preservation common (SMF 8).

RMF 4: Peloidal wackestone and packstone (~ SMF 2).

RMF 5: Pelagic mudstone with planktonic microfossils and open-marine nektonic fossils (e.g. ammonites) (SMF 3).

RMF 6: Graded, laminated and finely cross-bedded bioclastic and peloidal grainstone (tempestite).

Mid-ramp

Medium-bedded, fine-grained bioclastic limestones and marls, often burrowed. Skeletal grains often worn. Echinoderms common. Mudstone, wackestone, packstone, some grainstones. Distally steepened ramps exhibit slumps and various signs of reworking and transport of fine-grained ramp material. Distal steepening occurs in outer ramp settings or near the mid-ramp-outer ramp boundary. Calcareous sand shoals and sand banks (see right side). Various kinds of reefs occur in mid-ramp and inner ramp settings (e.g. coral patch reefs, coral-red algal reefs).

RMF 2, **RMF 3**, **RMF 5** and

RMF 7: Bioclastic packstone with abundant echinoderms and common bivalves and foraminifera. Skeletal grains worn (SMF 10).

RMF 8: Burrowed packstone and grainstone with various skeletal grains, intraclasts, oncoids and peloids.

RMF 9: Wackestone, packstone, floatstone with micritic intraclasts and ramp-derived bioclasts; sometimes microbreccias (distally steepened ramps) (~SMF 5).

RMF 10: Limestone conglomerates (distally steepened).

RMF 11: Marls with intraclasts and limestone pebbles (distally steepened).

RMF 12: Boundstones comprising coral and coral-crust framestone, red algal framestone (SMF 7).

Inner ramp

Inner ramp sediments are bedded, microfacially differentiated limestones and dolomites forming relatively thin sequences. Marls are of minor importance. The inner ramp comprises open-marine environments with good water circulation, protected environments with restricted water circulation, sand shoal and bank environments characterized by oolitic and bioclastic grainstones and packstones (see below), lagoonal environments behind shoals or islands and peritidal environments. The latter are separated from other inner ramp parts as back-ramp environments (Fig. 14.3). Common texture types of open and protected inner ramps are bioclastic packstones and wackestones. Coral and coral-

ed algal boundstones (RMF 12) and other reef limestones (bivalve reefs) are common in open inner ramps. Other reefs, e.g. serpulid biostromes, occur in protected inner-ramp settings.

Open inner ramp environments

RMF 13: Bioclastic wackestone and packstone with abundant larger foraminifera (e.g. orbitolinids) (SMF 18-FOR).

RMF 14: Bioclastic packstone and wackestone with skeletal grains, various amounts of intraclasts and some ooids (near-shoal).

RMF 15: Bioclastic floatstone with various reef-derived material (near-reef coral-, algal- or bivalve-debris) (~SMF 6).

Protected and low-energy inner ramp environments

A common microfacies type in these environments is RMF 7 characterized by common to abundant echinoderm fragments. Associate skeletal grains occurring in different quantity are bivalve shells, gastropods, bryozoans, and benthic foraminifera. Other microfacies types are packstones and grainstones with larger foraminifera (RMF 13).

RMF 16: Mudstone, wackestone or packstone with abundant miliolid foraminifera (SMF 18-FOR).

RMF 17: Bioclastic wackestone with dasyclad green algae (SMF 18-DASY).

RMF 18: Bioclastic wackestone with ostracods.

Lagoonal environments

RMF 17 (low-diverse flora) and

RMF 19: Non-burrowed lime mudstone.

RMF 20: Bioclastic wackestone and packstone with calcareous algae and benthic foraminifera.

RMF 21: Oncoid packstone and floatstone (SMF 22).

Peritidal zones

RMF 19 and **RMF 21** and

RMF 22: Fine-laminated dolomitic/lime mudstone (SMF 19).

RMF 23: Fenestral bindstone (SMF 21).

RMF 24: Intraclast mudstone and packstone.

RMF 25: Laminated evaporite-carbonate bindstone (SMF 25).

Carbonate sand shoals and banks

Storm-dominated ramps are characterized by accumulations of ooids, skeletal grains and peloids. These grains occurring separately or associated, form grainstone and packstone textures. Bedding and cross bedding are common. These sediments originate in mid-ramp and inner-ramp settings. Bioclastic banks may be formed by storm-induced but also by coast-parallel bottom currents.

RMF 26: Medium- and coarse-grained bioclastic grainstone and packstone with various benthic skeletal grains.

RMF 27: Bioclastic grainstone and packstone composed of few dominant skeletal grains (e.g. predominantly echinoderms, or predominantly foraminifera).

RMF 28: Bioclastic floatstone and rudstone exhibiting a strongly disorganized fabric.

RMF 29: Ooid grainstone with densely packed concentric ooids (common in shoals and banks) (SMF 15-C).

RMF 30: Shelly ooid grainstone and packstone (common in banks).

Figure 4.33: Microfacies of Paleozoic and Mesozoic carbonate ramps. The list starts with microfacies in deep marine outer ramp zones, and progressively gets into more shallow mid- to inner ramp zones. Numbers in brackets correspond to the Standard Microfacies types (SMF) developed by Wilson (1975). Classification scheme after Flügel (2004).

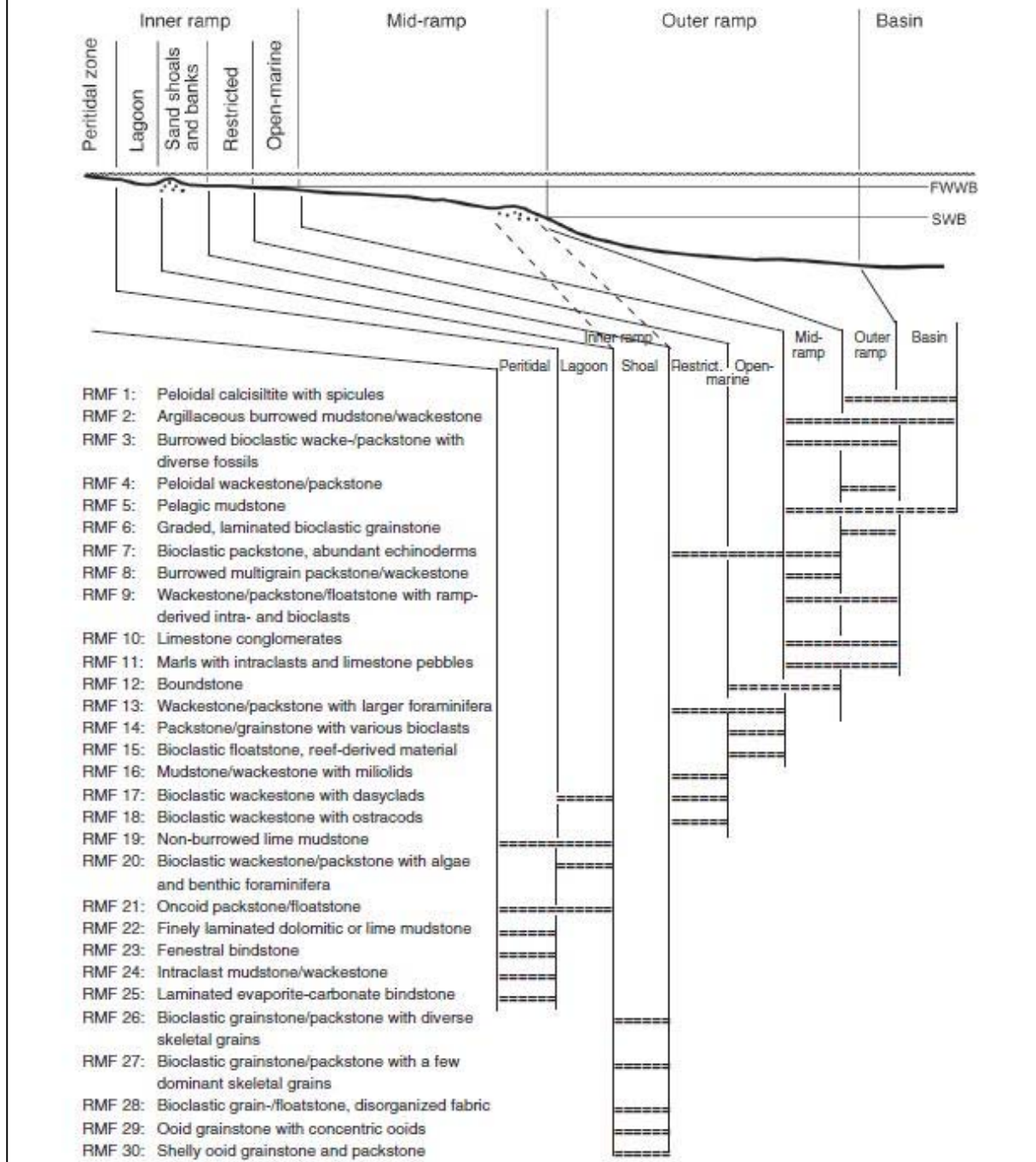


Figure 4.34: Distribution of ramp microfacies (RMF) over a homoclinal carbonate ramp. RMF 10 and RMF 11 commonly occur in distally steepened ramps. After (Flügel, 2004)

4.4.1 Unit A

Observations:

The lower part of Unit A consists of an 18.45m thick wackestone/packstone sequence assigned to MF8a, with an average grain diameter of 50 μ m. It is characterized by a high abundance of sponge spicules and peloids. Overlying MF8a is a silt- and peloid-rich packstone (MF4) with an average grain diameter of 100 μ m. The upper part of Unit A shows alternating textures of packstone and grainstone (MF3) with a concomitant increase in the grain size. In MF3 the average grain size ranges between 250 and 900 μ m and the composition is characterized by moderately sorted large benthic foraminifera (dominantly orbitolinids and miliolids), peloids, echinoderm fragments (plates and spines), coral fragments and traces of red algae. Within this relatively thick and massive part of Unit A, an irregular and discontinuous bedding surface is observed (Figure 4.29). A well-sorted packstone (MF6) with high abundance of benthic foraminifera, peloids, circum-granular cracks and organic material is capping Unit A.

Interpretation:

The lower part of Unit A is characterized by mud-rich textures and faunal composition indicative of deposition below the storm wave base (SWB) in a mid-ramp setting (Figure 4.35). The irregular discontinuous bedding contact observed, could suggest episodes of subaerial exposure and development of a paleo (epigenetic) karst surface (Figure 4.29). This observation suggests a shallowing upwards trend consistent with a ramp progradation and subsequent eustatic sea-level fall. By comparison with the Ramp Microfacies (RMF) developed by Flügel (2004), it is obvious that MF3 is similar to RMF13 and RMF16 (Figure 4.33), indicating that Unit A ends with an inner ramp environment with fluctuating energy (open- to protected inner ramp).

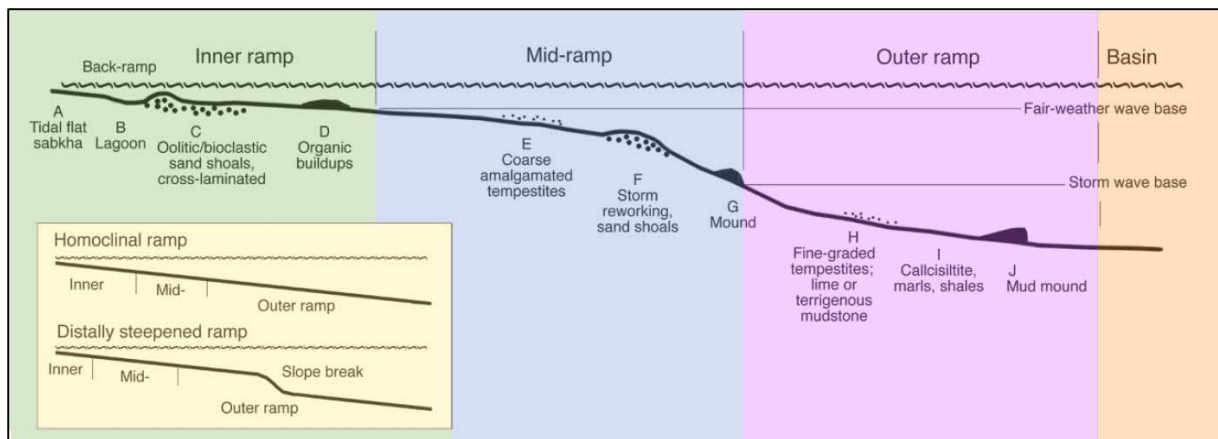


Figure 4.35: Carbonate ramp model distinguishing inner, mid-, outer ramp and basin. The subdivision applies for both homoclinal and distally steepened ramps. The slope dip is strongly exaggerated. According to Wright and Burchette (1998) the slope dip is commonly less than 1°. The length of carbonate ramps vary from tens to hundreds of kilometers. Modified after Flügel (2004) and Burchette and Wright (1992).

4.4.2 Unit B

Observations:

Unit B is a 5.6m thick sequence (Figure 4.36) consisting of a moderately to well sorted packstone (MF8b) with an average grain diameter of 75µm in the lower part, and 150 µm in the upper part. The packstone is characterized by high abundance of sponge spicules and peloids, with minor abundance of quartz grains, undifferentiated benthic foraminifera and possible traces of belemnite rostra. Overlying MF8b is a coarser grained moderately to well sorted packstone (average grain diameter of 200µm), with high abundance of echinoderm fragments, peloids and some bivalve fragments. Virtually all grains exhibit micritic envelopes and show traces of both micro-borings. Thin dark brown to black irregular dissolution seams of clay are observed within the sequence. Unit B is capped by a grainstone with an average grain diameter of 100µm, and is characterized by high abundance of echinoderm fragments, undifferentiated uniserial and biserial benthic foraminifera and peloids.

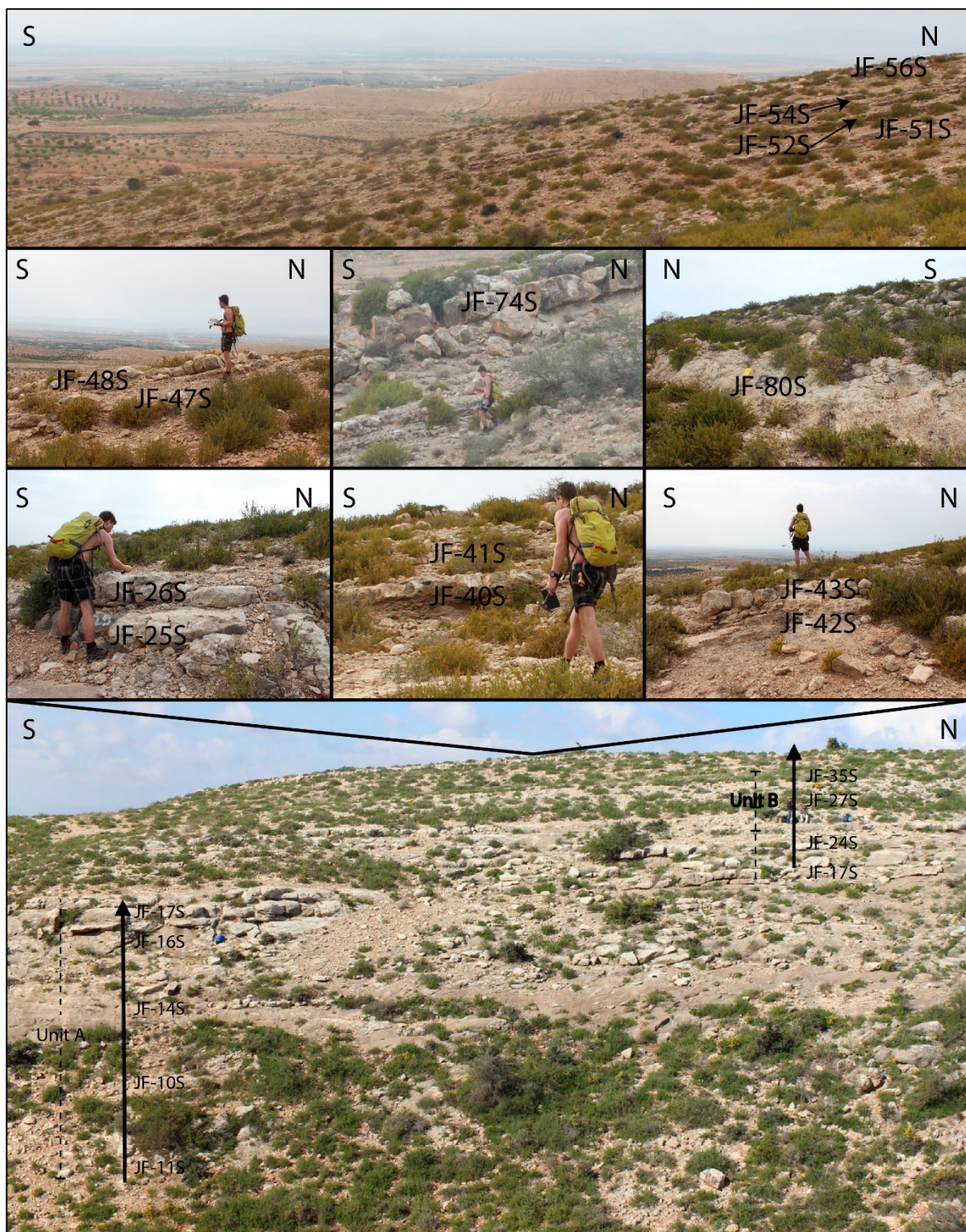


Figure 4.36: Overview of southern Jebel Fadeloun section (JF) with associated sample locations (black text). The seven picture collage in the upper part of the image represents outcrops exposed over the edge of the hill (black triangle). The vertical black arrows indicate logged sections. Due to the large area and difficult topography, all sample locations were not pictured or shown. Note persons for scale and that the picture angle give a wrong impression of bed thicknesses. Photo by: Bjarte Lønøy and Fredrik Kjelkenes

Interpretation:

The lower part of Unit B has a mud-rich texture and biogenic composition indicative of deposition below SWB in a mid-ramp setting. The abundance of micro-crystalline matrix decreases towards the top the unit, suggesting a drop in relative sea level and shallower depositional environments. The grainstone texture and biogenic assemblage of the upper part of Unit B is similar to RMF27 (Figure 4.33), and suggest deposition of carbonate sand shoals in agitated waters in an inner-ramp setting.

4.4.3 Unit C

Observations:

Unit C is a 53.4 meter thick sequence (Figure 4.36). The lower part consists of a 0.7m thick moderately to well sorted packstone (MF8b) with an average grain diameter of 100 μ m. Overlying MF8b, is a 45.8m thick packstone-grainstone (MF2 and MF4) with a slight coarsening upwards trend (from 100 to 200 μ m grain diameter). Sedimentary texture alternates between packstone and grainstone (MF2 and MF4). Grains are dominated by bivalve- and echinoderm fragments, peloids, ammonites and locally abundant silt-sized quartz grains. The upper part of Unit C is composed of a 6.9m thick sequence of relatively coarse grained (600 μ m) and poorly sorted packstones (MF3), characterized by high abundance of bivalve- and echinoderm fragments, peloids, benthic foraminifera (orbitolinids and miliolids) and some bryozoan fragments. The unit is capped by elongated and irregular cavities. Micritic envelopes are observed with various degree of grain alteration, throughout the unit.

Horizontal burrows increase in abundance towards the top of the unit and are quite extensive close to MF3.

Interpretation:

The base of Unit C is characterized by the same microfacies as in Unit B (MF8b), and it is thus reasonable to suggest deposition in a mid-ramp setting, below SWB. According to Flügel (2004), intraclasts may occur in all ramp settings, but are mostly characteristic for mid- to outer ramp settings in distally steepened ramps (RMF9).

The middle part of the unit consists of a relatively thick succession of alternating MF2 and MF4 (close proximity to RMF27 and RMF7). These microfacies indicate shallow marine deposition in a mid- to inner ramp setting (Figure 4.33 and Figure 4.34). The moderately to well-sorted terrigenous, silt-sized quartz grains may represent eolian input (Flügel, 2004), into the overall shallow marine environment. Development of pendant cement is often indicative of deposition within the vadose zone, whereas circum-granular cracking (described in Chapter 4.3.1) is mostly indicative of paleo-caliche formed during subaerial exposure (Flügel, 2004). Thus relative sea-level must have been fluctuating, possibly periodically exposing the carbonate ramp. However, the paleo-caliche may be a recent development and thus may not relate to an intra-Cretaceous subaerial exposure.

The upper part of Unit C is characterized by large benthic foraminifera- and peloid-rich packstones which are comparable to RMF13 (Figure 4.33 and Figure 4.34), suggesting deposition in an inner ramp setting (Kalantari, 1986). The irregular/equidimensional cavities in the upper part of the unit are fenestral structures, and are typically formed in peritidal environments (Flügel, 2004).

Unit G shallows upwards from mid-inner ramp to periodically subaerially exposed inner ramp deposits.

4.4.4 Unit D

Observations:

Unit D is a 13m thick sequence (Appendix I1) which in its lower part consists of a moderately to well sorted packstone/grainstone (MF2) with an average grain diameter of 100µm. The packstone/grainstone is characterized by high abundance of echinoderm- (plates and spines) and bivalve fragments, and peloids, with minor abundance of undifferentiated biserial benthic foraminifera and ostracods.

Overlying MF2 is a moderately sorted packstone/grainstone (MF6) with an average grain diameter of 125µm and with high abundance of bioclastic material consisting of echinoderm- and bivalve fragments, peloids, undifferentiated benthic foraminifera, miliolids, ostracods, calcispheres and sponge spicules.

The upper part of the unit consists of a poorly sorted grainstone (MF5) with an average grain diameter of 400µm, containing high abundances of echinoderms, peloids and intraclasts. Thin isopachous cement coatings of fibrous to bladed calcite are observed within this section.

Note that the uppermost part of Unit D and the lowermost part of the overlying sequence are covered by debris, and a continuous log was not possible.

Interpretation:

Unit D starts with a relatively thick sequence of MF2, with grain-supported textures and biogenic composition suggesting a microfacies closely resembling RMF27 in the Flügel (2004) ramp microfacies type classification (Figure 4.33 and Figure 4.34). This RMF type is commonly indicative for sediments originating in high-energetic shoals of mid- to inner ramp settings (Flügel, 2004). Upwards in the unit, the frequency of benthic foraminifera, calcispheres and sponge spicules increase as the abundance of matrix decreases. The depositional environment is probably still a mid- to inner ramp setting, but the high diversity of grains could suggest that the microfacies is similar to RMF26 (Figure 4.33). The upper part of Unit D is composed of a relatively coarse-grained (average grain diameter of 400µm) and poorly sorted grainstone (MF5), with high abundance of intraclasts, peloids and echinoderm fragments (spines and plates). Isopachous rims of bladed to fibrous cement represent early marine cementation. Cementation probably took place close to the sediment/sea-water interface, and indicates periods of slow sedimentation and low erosion rates in a shallow-marine ramp setting (Flügel, 2004). Concentration of intraclasts combined with grain-supported depositional textures could indicate reworking in an inner ramp setting.

4.4.5 Unit E

Observations:

Unit E is a 44.2m thick sequence with large areas covered by debris and vegetation. The lower part the unit consists of very fine-grained (grain diameter of 20µm), organic-rich wackestone (MF1), with high abundance of planktonic foraminifera and calcispheres. Overlying MF1 is a poorly to moderately sorted packstone/grainstone (MF2), with an average grain diameter of 200µm. The packstone/grainstone is characterized by a high abundance of

echinoderm- (plates and spines) and bivalve fragments, and peloids, with minor red algae, undifferentiated benthic foraminifera ostracods and intraclasts. The top of Unit E is characterized by a moderately to poorly sorted packstone/grainstone (MF7) with a high abundance of red algae, echinoderm fragments and peloids, and with an average grain diameter of 450 μ m.

Interpretation:

In chapter 4.2.1 MF1 is interpreted to be an Albian deep marine basinal deposit, probably deposited within the bathyal zone. Unit E becomes progressively coarser grained and more grain supported towards the top, with low diversity of biogenic grains, indicating mid- to inner ramp settings (Flügel, 2004). The unit may represent a downfaulted section of the Upper Aptian-Lower Albian (Figure 4.4). This will be discussed further in Chapter 5.

4.4.6 Unit F

Observations:

Unit F consist of only one microfacies (MF1), a well-sorted mudstone with very small grains with average grain diameter of 25 μ m. The base of Unit F show a sharp boundary to the underlying unit, and grains are dominated by planktonic foraminifera, calcispheres and some sponge spicules. MF1 is more thoroughly described in chapter 4.2.1.

Interpretation:

Unit F consists of only one microfacies, with no general trend within the unit. Unit F is of Albian age according to the geological map (Figure 1.2), and is interpreted to represent deep marine basinal deposits, deposited within the bathyal zone (see Chapter 4.2.1). The sharp boundary between the Unit F and the underlying Aptian shallow marine deposits thus represents an unconformity.

4.4.7 Unit G

Observations:

Unit G is a 55.8m thick unit which form all of the northern J.Fadeloun section (Figure 4.37). MF8b constitutes most of the unit, and consists of well to very well sorted fine-grained (average grain diameter 40µm) packstones. The microfacies is dominated by sponge spicules, peloids, planktonic foraminifera and calcispheres, with minor abundance of bivalve- and echinoderm fragments. The upper part (MF2) consists of relatively thin beds of poor to well sorted packstones to grainstones, and is dominated by peloids, echinoderms, bivalves and benthic foraminifera. Planktonic foraminifera are a minor constituent. There is a slight coarsening upward trend and thinning of bed thickness towards the top of the unit. Large open karst caves and vugs are observed towards the top of the outcrop (close to NFS-9S). Sample NFS-9S is sampled proximal to the observed open karst caves and vuggy pores, and have a quite high abundance of equant to blocky Fe-rich calcite cement. Undulating cavities infilled with blocky/equant calcite cement is observed in the uppermost sample (NFS-5S) in the unit.



Figure 4.37: Overview of northern Jebel Fadeloun section (NFS) with associated sample locations. The boundary between MF8b and MF2 is marked with red dashed line. The black dashed line indicates a possible collapse breccia. Note persons for scale and that the picture angle gives a wrong impression of bed thickness. Photo by: Atef Bel Kahla

Interpretation:

The lower part of Unit G (Figure 4.37) is rich in sponge spicules and pelagic grains (MF8b), has a depositional texture and grain composition analogous to RMF7 and RMF8. This indicates deposition in an mid-ramp setting, according to the Flügel (2004) classification of microfacies on carbonate ramps. Towards the top of the unit the mud content decreases, which is indicative of more agitated waters. MF2, an important constituent of Unit G which closely resemble RMF7 and RMF27 is interpreted to represent relatively shallow marine deposition, probably in a mid- to inner ramp setting. The irregularly shaped and cemented cavities are believed to be fenestrae (Figure 4.6), and are common features in intertidal areas of ramps (Flügel, 2004). Thus, Unit G represents a shallowing upward section from a mid- to an inner ramp setting.

4.4.8 Unit H

Observations:

Unit H is 5m thick, and represents all of the Garci section (Figure 4.38). The unit is composed of alternating moderate to well sorted wackestone/packstones (MF9) and moderate to poorly sorted packstones (MF10). MF9 is relatively fine grained (average grain diameter of 60 μm), has low mud content, and is composed of a faunal assemblage similar to RMF4 (Figure 4.33 and Figure 4.34). The faunal assemblage and larger average grain size (average grain diameter of 100 μm) of MF10 is similar to RMF7 (Figure 4.33 and Figure 4.34).

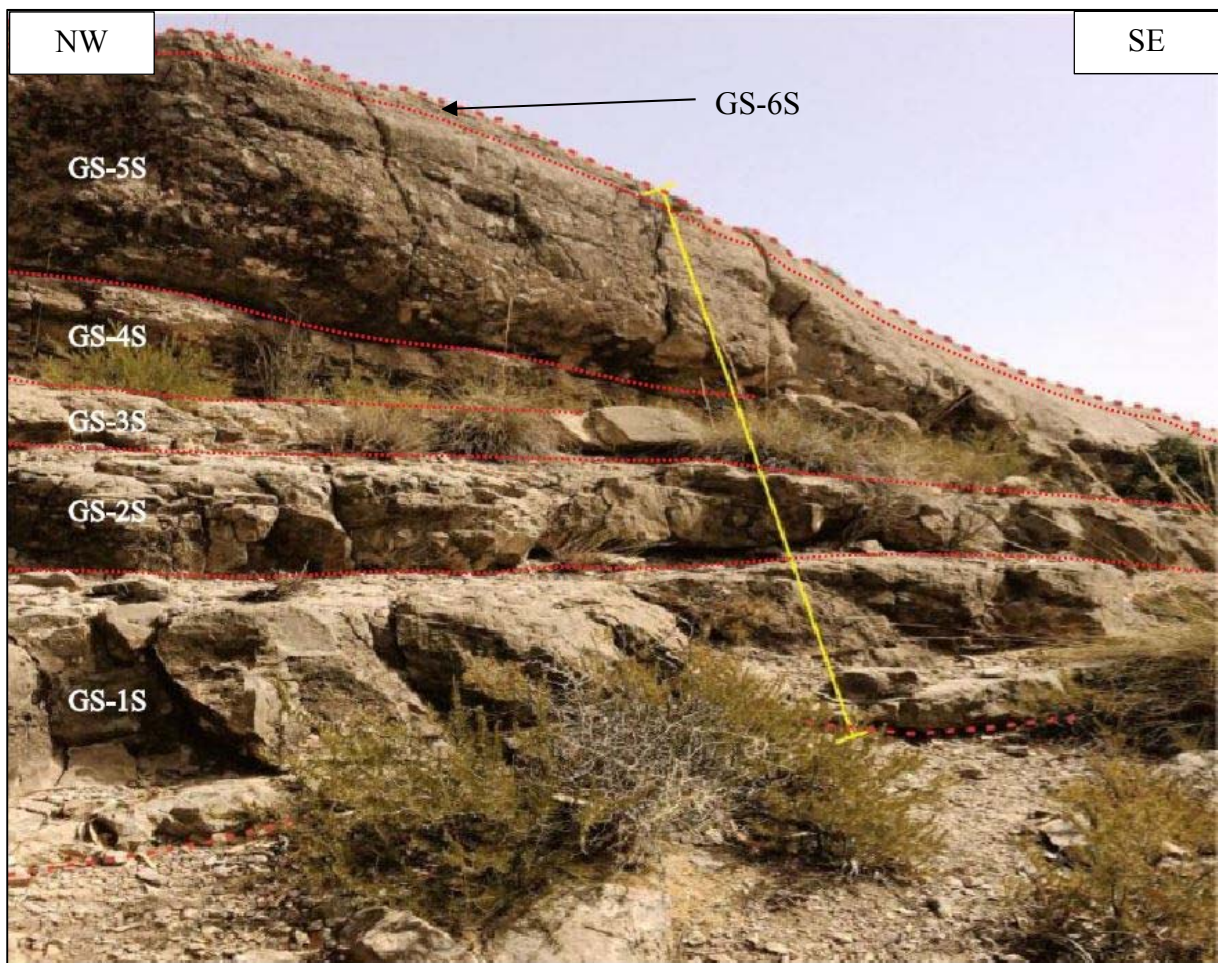


Figure 4.38: Overview of Jebel Garci section (GS) with associated sample locations. The photo is arranged NW – SE. Abbreviations: Red dashed line = bedding boundaries; Yellow line = Logged section; GS-xS = Sample location, x indicating sample number. Photo modified from: Ahmed Klibi.

Interpretation:

The J.Garci section is described as a condensed Aptian section on geological maps and in the literature, and Unit H apparently forms a complete Aptian section (Directin du Service Géologique, 2003). Unit H consists of microfacies similar to RMF4 and RMF7, which represents deeper marine depositional environments, below FWWB in a mid to outer-ramp setting. The alternation between fine-grained (MF9) and coarse-grained (MF10) microfacies within the unit probably reflects relative sea level fluctuations. The low micritization of grains suggests that deposition took place below the photic zone. The microfacies assemblage of Unit H is similar to RMF4 and RMF7 (Figure 4.33 and Figure 4.34) of the Flügel (2004) ramp classification, and may thus represent a more distal depositional environment compared to the J.Fadeloun section.

4.5 Diagenesis

This chapter describes the post-depositional alterations to the studied carbonate rocks. Diagenetic alteration of a carbonate rocks is mainly controlled by the mineralogical- and chemical composition of grains, dissolution and precipitation rates, grain size, migration of pore fluids, chemical composition of pore fluids and by biological factors (Flügel, 2004). Diagenetic alterations observed are predominantly related to microbial micritization and to dissolution and cementation.

The diagenetic alteration experienced by the Serdj Fm. at both J.Fadeloun and J.Garci have been studied by ordinary light-, fluorescence- and cathodoluminescence microscopy, fluid inclusions and isotope analysis. The results of these studies are presented in this chapter, whereas their implication for reservoir potential is discussed in Chapter 5.

4.5.1 Micritization

Observations:

In the studied microfacies, early diagenetic alteration appears to relate to the formation of individual micro-borings, and the formation of circum-granular micritic envelopes on skeletal grains (Figure 4.39). This observation applies to all Aptian microfacies of the J.Fadeloun

sections with the exception of MF1 (sample JF-80S and JF-87S) where borings and micritic envelopes are absent or not clearly visible. In the J.Garci section micritization of grains is not as extensive as for the the J.Fadeloun sections, although it is recognized in all of the studied samples. In the microfacies with a high mud content micritization of grains can be very difficult to pinpoint.

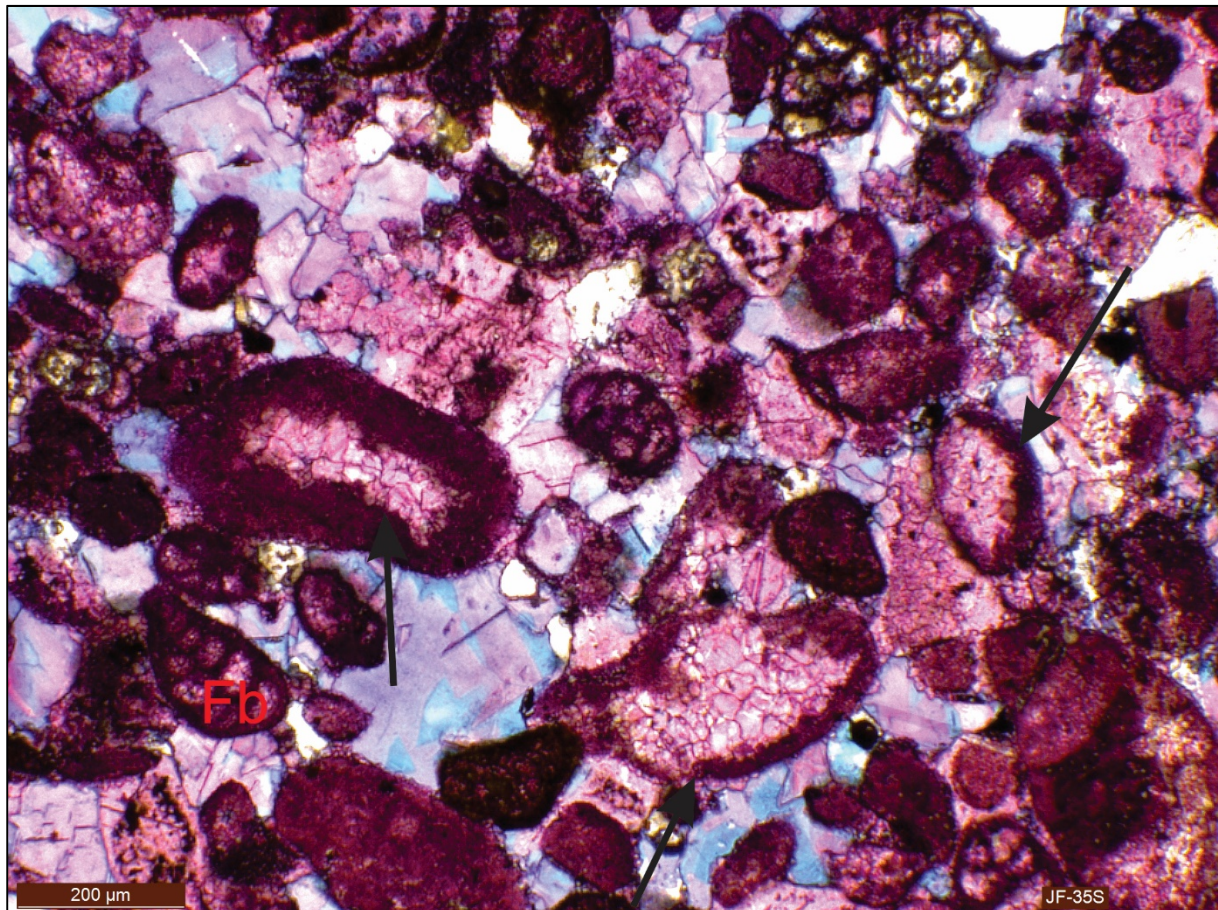


Figure 4.39: Microbial micritization of possible former aragonitic bivalve fragments and foram tests. Micritic envelope develops along grain perimeters (black arrow). Fb = Biserial undifferentiated benthic foraminifera. The thin section is stained for both non-ferroan calcite cement (red) and ferroan calcite cement (blue). Thin section in PPL.

Interpretation:

Boring of skeletal grains and hard substrates by endolithic organisms is a common particle alternation process that occurs preferentially in very shallow marine and freshwater (rare) environments (James and Choquette, 1983; Flügel, 2004). Endolithic organisms that produce micro-borings include green algae, blue-green algae, red algae, fungi, sponges and bacteria, and range in size from less than 1μm to over 100μm (Budd and Perkins, 1980). Micro-borings relates to biochemical dissolution of hard substrates by the aforementioned organisms, and

provide shelter, nutrition and wave- and scavenger protection for the endolithic organism (Budd and Perkins, 1980; Smith and Nelson, 2003). Their boring activity is restricted vertically by light penetration and latitudinally by water temperature (Budd and Perkins, 1980; James and Choquette, 1983). Thus, in the upper part of the photic zone at depths down to 70m, phototrophs like blue-green and green algae appear to be most effective, whereas heterotrophs like fungi are more effective of depths below 500m (Smith and Nelson, 2003).

The micritic envelopes are rims of micrite-filled voids that are a result of vacated microborings produced by the endolithic organisms (Figure 4.40). This process is commonly cyclic and happens in three main stages: (i) The organism bore into the substrate wall, (ii) The organism die and decay, (iii) micritic aragonite or high-Mg calcite fills the vacated tubes (Bathurst, 1966; James and Choquette, 1983). Micritic envelopes will commonly withstand dissolution, whereas more soluble grains will often dissolve in contact with under-saturated pore waters. The dissolution of the initial grain commonly develops moulds. These moulds could either be open pore spaces, partially or completely filled with cement or matrix, or collapse as a result of compaction (Bathurst, 1966). Preservation of micritic envelopes is often controlled by the internal solubility contrasts as a result of mineralogical differences between envelope and grain (Winland, 1968), or by differences in mineralogical stabilization rates (James and Choquette, 1984).

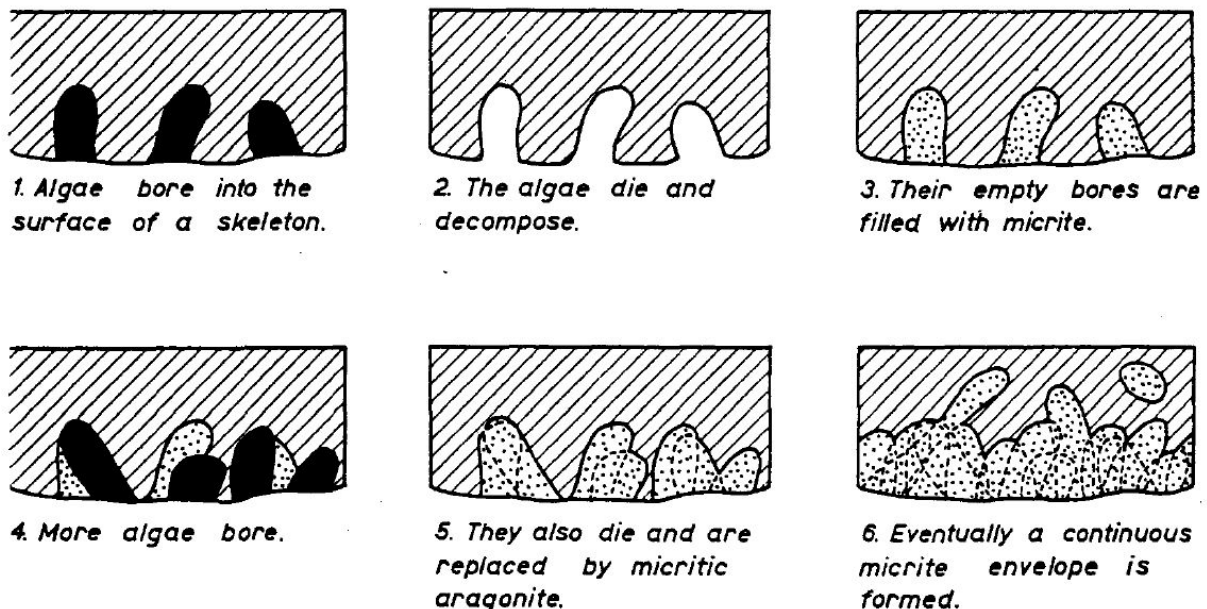


Figure 4.40: Illustration describing the sequence of events leading to the formation of a micrite envelope. This sequence of events may occur several times, leading to more extensive boring. The depth of the boring may also vary and thus this is only a principle sketch. After Bathurst (1966).

If infestation is intense and prolonged, the entire substrate or grain may be completely bored, and transformed into a lump of microcrystalline Mg-calcite or aragonite, without any traces of the original internal structure (James and Choquette, 1983). These “diagenetic peloids” will be very difficult to separate from fecal pellets and it may be impossible to determine the origin of the grain (James and Choquette, 1983).

4.5.2 Cementation and dissolution

This chapter describes the marine and meteoric diagenesis of southern J.Fadeloun- (JF), northern J.Fadeloun- (NFS) and J.Garci sections, with respect to cementation and dissolution. Cement is a chemical precipitate from solution growing in open pore space, and precipitation requires supersaturation of the ambient pore fluid with respect to the cement mineral (Flügel, 2004).

4.5.2.1 Cementation

The following cement types have been observed:

- 1) Isopachous fibrous to granular cements

Isopachous rims of inclusion-poor microcrystalline granular to fibrous cement occur on bivalve- and bryozoan fragments, peloids, intraclasts and benthic foraminifera (Figure 4.41). This type of cement is predominantly observed within sample JF-78 of Unit D.

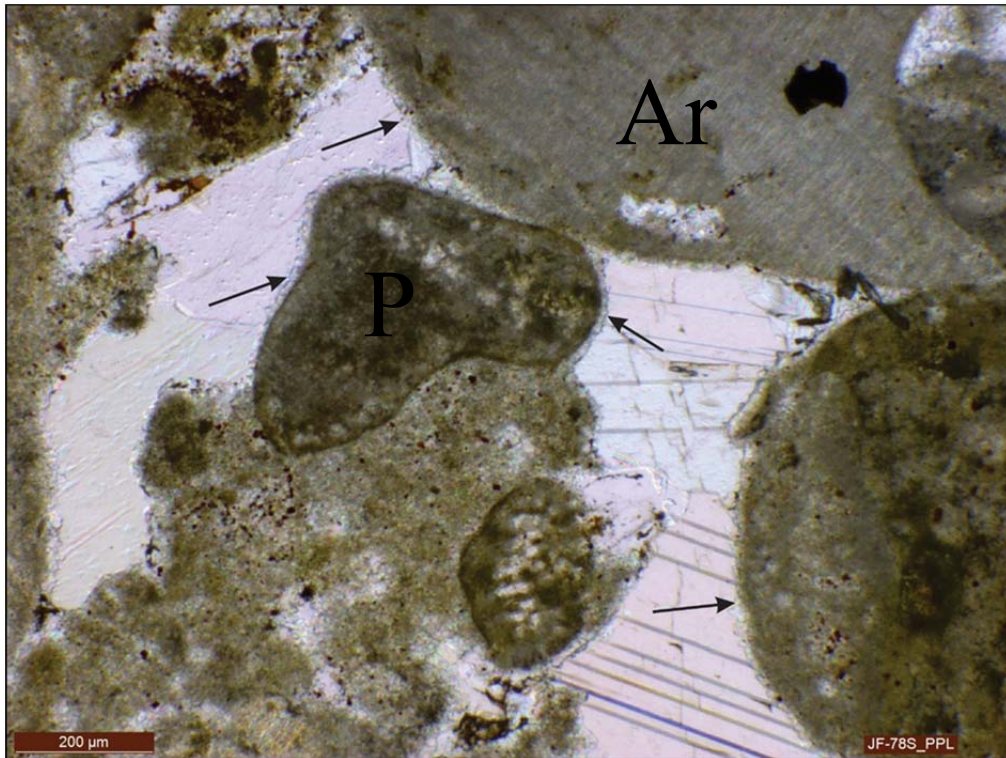


Figure 4.41: Grainstone with microcrystalline calcite cement rims (black arrows) around peloid grains (P), and possible red algal fragment (Ar). Equant interparticle calcite cement with twinning postdates the microcrystalline calcite cement. Thin section in PPL.

Isopachously-distributed fibrous to granular microcrystalline calcite cement is commonly indicative of early marine cementation, binding grains shortly after deposition (Munnecke et al., 1997). Modern early marine cementation with aragonite or high-Mg calcite occurs in shallow waters near the sediment-sea water interface and commonly represents very slow sedimentation and/or erosion, and continuous flushing with sea water. This cement type is commonly strongly controlled by factors such as permeability, water temperature and salinity (Flügel, 2004). However, during the Cretaceous the marine cements were probably composed of low-Mg calcite (Given and Wilkinson, 1985).

The isopachous calcite cement is interpreted to be early diagenetic in origin and was probably precipitated shortly after deposition (more or less syndepositional), in a marine environment. The cement is considered to represent the earliest cementation phase of the Serdj Fm.

2) Syntaxial cement overgrowths

Inclusion-poor syntaxial cement overgrowths on echinoderm fragments (plates and spines), is present within all microfacies of sections J.Fadeloun and J.Garci. The abundance of syntaxial cement overgrowths is strongly controlled by the frequency of echinoderm fragments present, and the abundance of interparticle lime mud. Samples with high abundance of lime mud tend to exhibit less syntaxial cement overgrowth, simply because there was limited or no space available for cementation. The outer boundary of the syntaxial cement overgrowth can easily be distinguished because crystal and grain are in optical continuity, and experience simultaneously extinction in crossed-polarized light (Figure 4.42 and Figure 4.43).

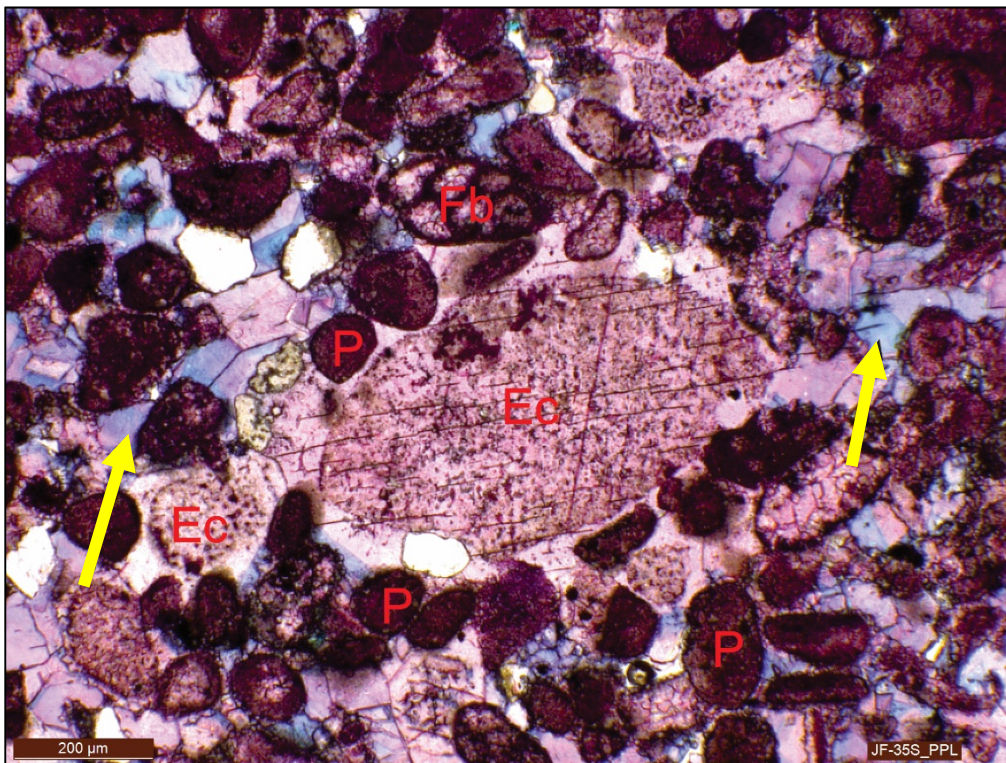


Figure 4.42: Syntaxial calcite cement overgrowth encasing echinoderm fragments (plates). Equant ferroan- and non-ferroan calcite cements are infilling pore space between grains. Abbreviations: Ec = Echinoderm, P = Peloids, Fb = Benthic foraminifera and yellow arrows = Equant ferroan calcite cement. Stained thin-section in PPL.

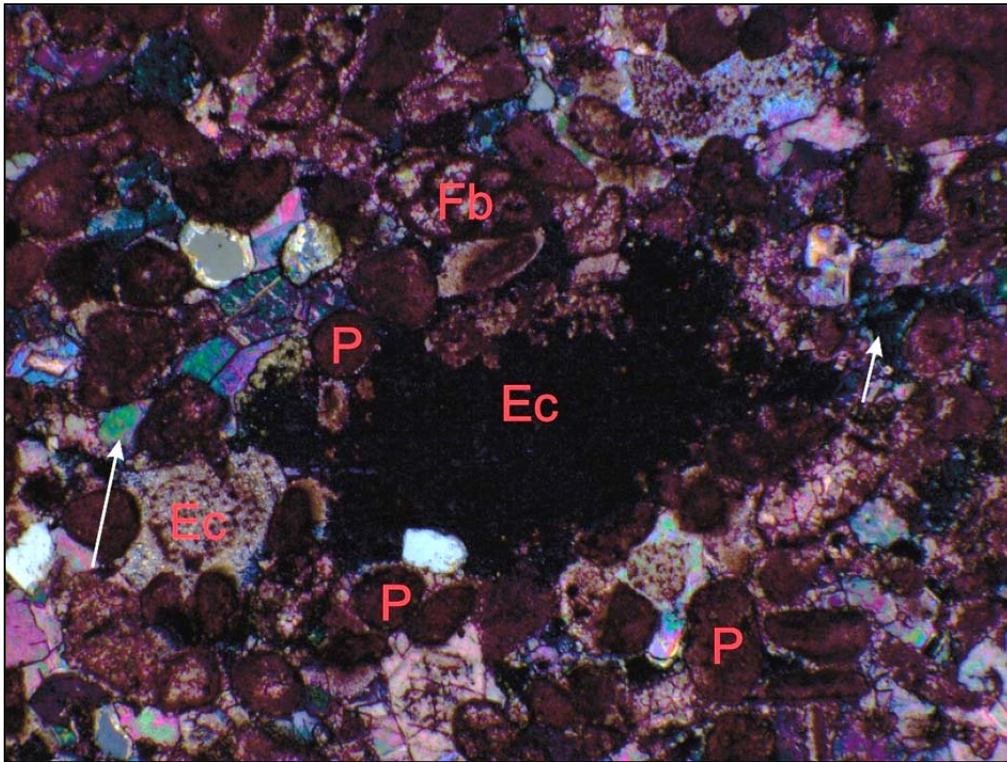


Figure 4.43: Syntaxial calcite cement overgrowths enclosing echinoderm fragments (plates). Grains and associated syntaxial cement show simultaneous extinction. Abbreviations: Ec = Echinoderm, P = Peloids, Fb = Benthic foraminifera and white arrows = Equant ferroan calcite cement. Stained thin-section in crossed-polarized light (XPL).

Overgrowths of calcite cement on single-crystal grains, is common in near-surface marine, vadose-marine, meteoric-phreatic and in deep burial environments (Bathurst, 1971). Inclusion rich cements with a cloudy appearance are commonly indicative for near-surface, vadose-marine and meteoric-phreatic environments, whereas a clear overgrowth often relates to deep burial environments (Flügel, 2004). The cement is usually low-Mg calcite and is commonly observed as overgrowth on echinoderm fragments.

Precipitation of syntaxial cement overgrowths probably started shortly after deposition of the sediment, possibly synchronously with the precipitation of the early marine isopachous calcite cement, and may have continued during burial of the sediment.

3) Equant calcite cement

Two types of equant calcite cement, Fe-rich and Fe-poor, fill pore spaces between grains, moulds, fractures and primary intraparticle pore spaces. Fe-poor calcite cement

commonly line grain surfaces, whereas ferroan calcite cement often occurs as chaotically-distributed crystals in the center of the pores. The ferroan calcite distribution for different microfacies is presented in Figure 4.44.

Cements are present throughout all sections, but are most common in microfacies MF7, MF5, MF6, MF3 and occasionally in MF2. The equant cements are usually evenly distributed within grainstones, whereas they have a patchy distribution in packstones. The cements tend to be more abundant towards the top of the units, due to the higher primary porosity in grainstones capping the units.

Some samples have scattered secondary porosity related to later dissolution of the cements (Figure 4.45), and/or partial dissolution of echinoderm fragments (Figure 4.46).

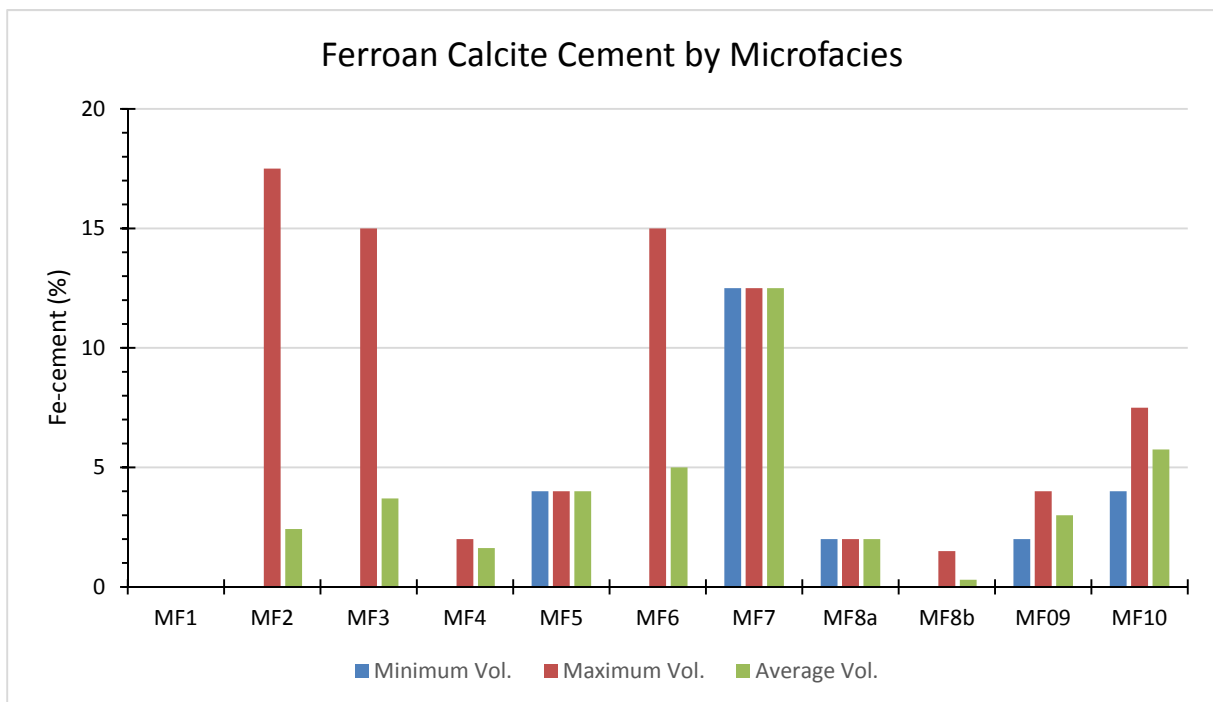


Figure 4.44: Visually estimated ferroan calcite cement distribution with associated microfacies.

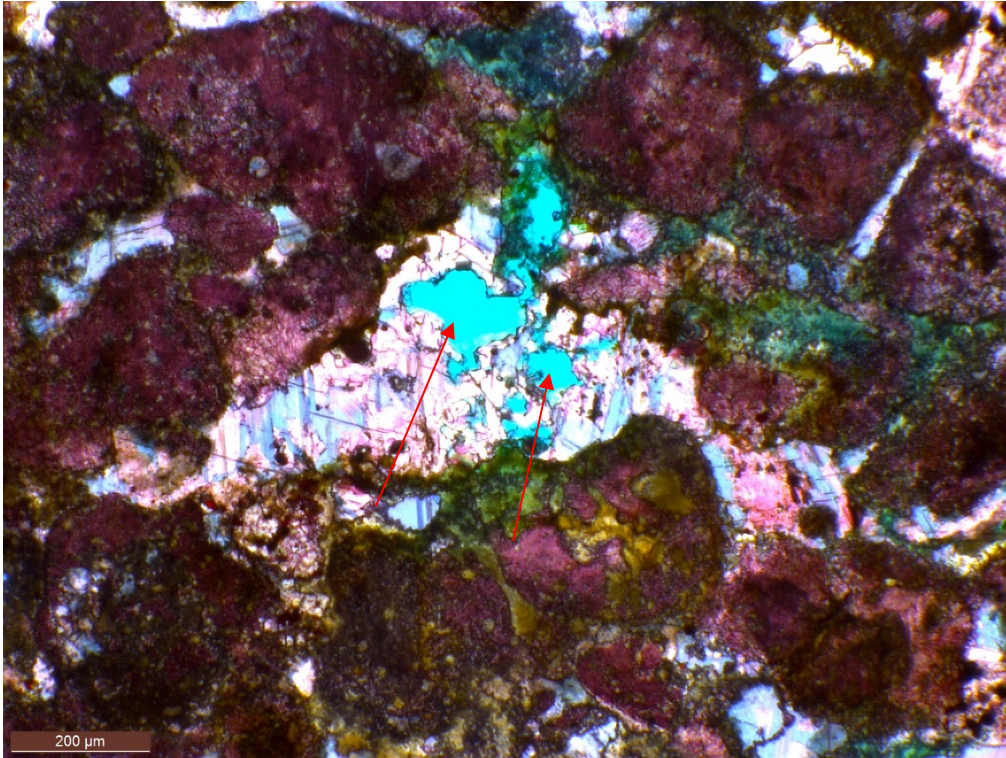


Figure 4.45: Sample JF-86S with open porosity (red arrow) related to dissolution of cement crystals. Thin section in PPL.

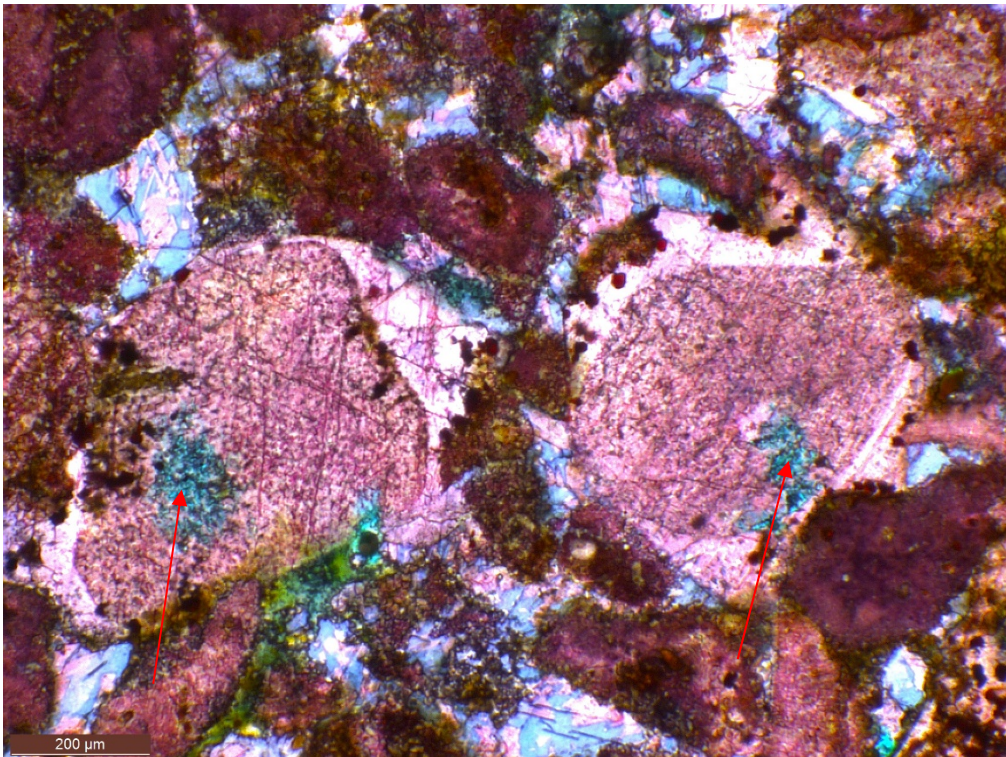


Figure 4.46: Sample JF-86S with open microporosity (red arrow) related to partial dissolution of echinoderm fragments. Note syntaxial cement overgrowths on echinoderm fragments. Thin section in PPL.

Several moulds are infilled with ferroan and non-ferroan equant cement crystals. The cement distribution apparently is controlled by grain type, with sponge spicules, calcispheres and bivalve molds commonly being infilled by iron-rich calcite, and all other moulds commonly being infilled by non-ferroan calcite. Ferroan calcite cements are often related to burial cementation taking place at temperatures of 40-250°C, representing burial depths of a few hundred meters to several kilometers (Choquette and James, 1987). The formation waters from which ferroan calcite has precipitated have stagnant to moderately rapid flow rates, and are often brackish to highly saline (Choquette and James, 1987).

Cemented fractures tend to be completely filled by ferroan and/or non-ferroan equant calcite cement. In some samples calcite cemented fractures are observed in cross-cutting relationships. When both cements are present in the fractures, the Fe-poor cement tends to line fracture walls, whereas the iron-rich cement fills the central part of the fractures.

Primary intraparticle pore space cemented with equant calcite cements is commonly restricted to chambered fossils with stable primary mineralogical composition (low-Mg calcite). The calcite cements filling these chambers are predominantly non-ferroan, with a few exceptions (especially larger benthic foraminifera) filled with ferroan cements.

Precipitation of ferroan cement is controlled by the redox potential and trace-element composition of the pore water and available pore space.

In Unit D virtually all microfacies consist of Fe-poor equant calcite cement. Fe-rich cement is restricted to some fractures and coarser-grained facies with high abundance of primary interparticle pores (top of the unit).

Equant calcite cement is commonly precipitated after dissolution of aragonite grains and cements, or late diagenetic by infilling of remaining pore space. The cement is typical in meteoric (phreatic and vadose) and burial environments (Flügel, 2004). Shallow burial equant cement typically contain no to little iron if precipitation takes place from positive Eh pore waters (Tucker and Wright, 1990)

Fe-rich cements are more common during late diagenetic burial cementation (Lindholm and Finkelman, 1972; Richter and Füchtbauer, 1978; Chilingarian et al., 1992) . The uppermost meter or so from the water-sediment interface commonly gets depleted in Fe^{2+} as a result of pyrite formation by the activity of sulphate reducing bacteria within the sediment (Berner, 1974; Chilingarian et al., 1992). Thus the uptake of Fe^{2+} by calcite in marine connate waters commonly occurs below the sulphate reducing zone, or may not happen at all if there is no iron available after the formation of pyrite.

4) Pendant cement (gravitational/micro-stalactitic cement)

In JF-37S (Unit C), distinct thickening of microcrystalline and fibrous calcite cement occur beneath grains and fracture walls (Figure 4.47). The cement hangs like “droplets or curtains” beneath the outer walls.

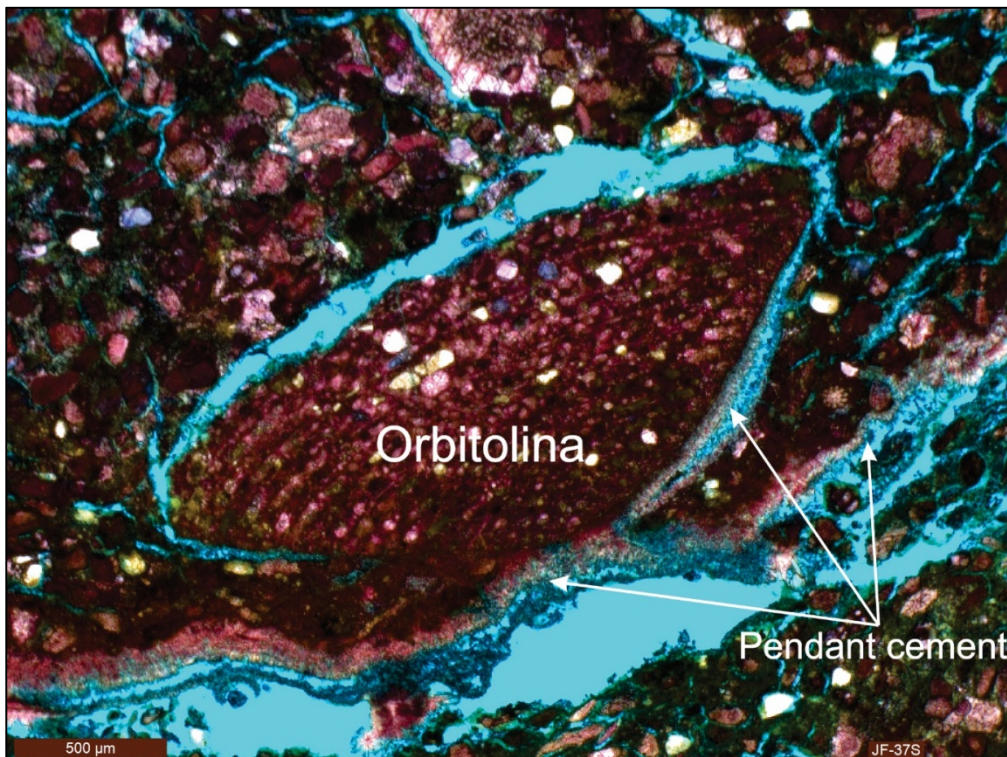


Figure 4.47: Packstone within Unit C with pendant calcite cement. Cement crystal morphology shows similarities to laminated, fibrous speleothem cements shown in Figure 4.31 and described in text paragraph below. Note the “downwards” growth of the cement. Thin section in plane polarized light.

In the literature, pendant cement is also often referred to as gravitational cement, micro-stalactitic druse cement or stalactitic cement (Figure 4.49). The cement forms during gravitational migration of saturated mobile pore fluids. Once the fluid vacate the pore space, a thick supersaturated water film will remain as coat on the underside of grains and after multiple phases of drainage and precipitation, pendant calcite cement will form (e.g. Flügel, 2004; Bjorlykke, 2010). Pendant cement is formed below the zone of capillarity and above the water table within the meteoric-vadose zone (Figure 4.48), and is often associated with meniscus cement. In rare occasions this cement can also occur in the marine-vadose diagenetic environment (sea water splash zone) (Flügel, 2004).

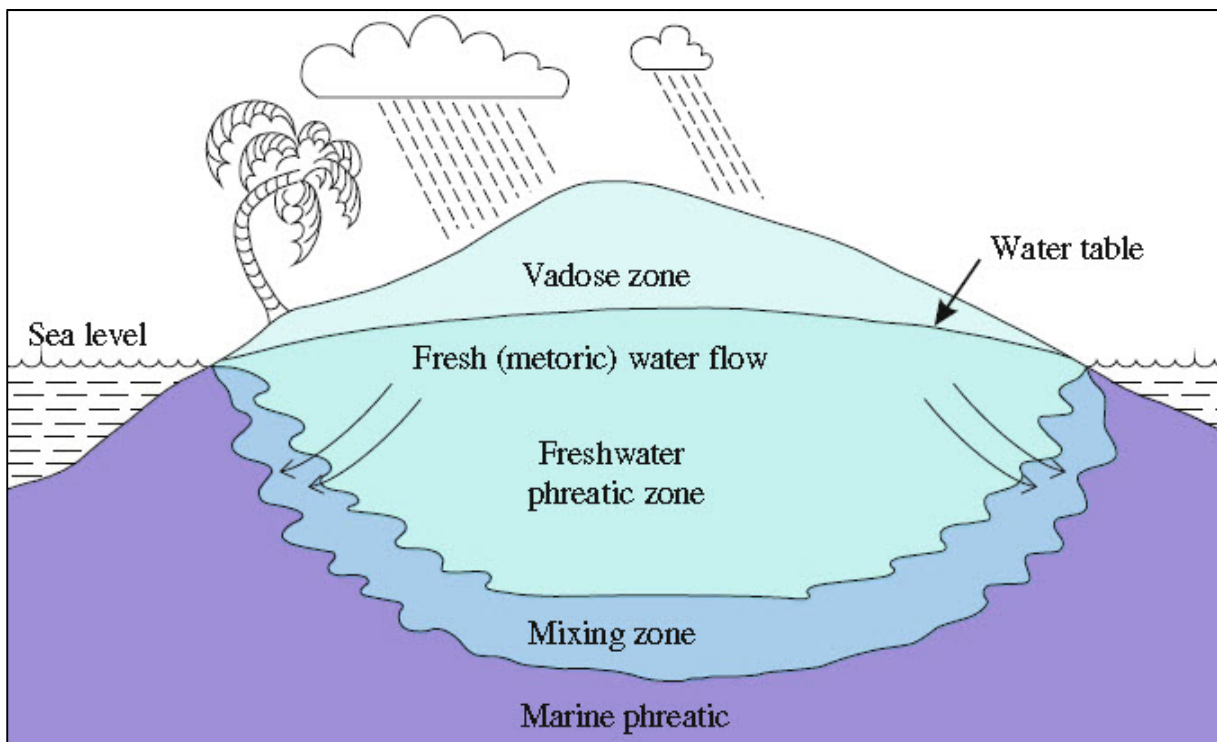


Figure 4.48: Sketch of an idealized permeable carbonate island with associated distribution of major diagenetic environments. The vadose zone is subaerially exposed and pores space is occupied by water and air. Pore space below the water table is permanently saturated by fresh water, whereas in the mixing zone less dense water floats on top of the denser saline waters. Sketch from Bjorlykke (2010)

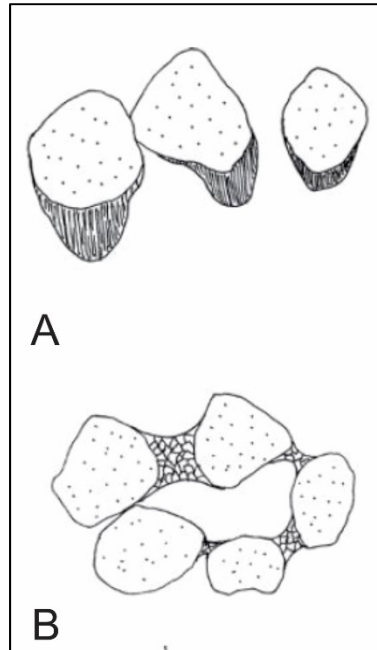


Figure 4.49: Illustration of pendant cement. A) Dripstone cement: distinct thickening of cement crust beneath grains and solution voids. This is observed in thin section as a gravitational beard-like pattern. B) Meniscus cement: Cement precipitated in a meniscus style proximal or at grain contacts. Meniscus cement is commonly associated with dripstone cement. Modified after Flügel (2004).

5) Laminated fibrous cement

Thin section JF-21S and JF-76S show several irregular laminations of fibrous to bladed calcite cement (Figure 4.31). The cement is growing outwards into the pore space that developed during late diagenetic dissolution of primary grains and matrix. Laminations show variations in colour and thickness, and consist of non-ferroan calcite cement.

Laminations or bands of fibrous calcite cements, are often indicative for precipitation of carbonate cements formed as speleothems in karst caves (Flügel, 2004). Karst caves are formed by chemical dissolution from under-saturated meteoric waters percolating downwards into the rock (“surface karst”), or from migration of aggressive hydrothermal fluids in the subsurface (“subsurface karst”). The dissolution results in development of open voids and cavities (e.g. vugs and caves) (Flügel, 2004).

Speleothems are indicative of precipitation from freshwater super-saturated with respect to calcium carbonate in “surface karst”, rather than “subsurface karst”. The

freshwater contains CO₂ at a higher partial pressure than at the surface due to the weight of the overlying water column and the lower ambient temperature. Increased partial pressure of CO₂ will promote increased dissolution until the water flows out of the rock or reaches a cave and regains equilibrium with the atmospheric pressure, resulting in degassing of CO₂. This could result in supersaturation of calcium carbonate and formation of speleothem (Bjorlykke, 2010; Boop, 2014). Changes in mineralogical composition and cement types are reflected in the colour change and geometry of the cement generations observed, and may reflect short- or long-termed cyclic oscillations of climatic factors (Flügel, 2004).

Brief summary of cements:

The marine cement (1) represents an early, almost syn-sedimentary diagenetic phase (eogenetic). (2) Syntaxial cement overgrowths on echinoderm fragments probably started precipitating shortly after deposition (eogenetic), although precipitation may have continued during burial diagenesis (mesogenetic). (3) Equant non-ferroan calcite and ferroan cements probably precipitated at shallow burial or in the meteoric freshwater zone, and at deeper burial, respectively. (4) Pendant cement and (5) speleothems precipitated during subaerial exposure of the ramp.

4.5.2.2 Dissolution

Dissolution of carbonate grains commonly occur early in the history of burial (eogenetic stage) and is often associated with meteoric diagenesis (Longman, 1980). The meteoric waters are often acidified from atmospheric- and soil CO₂, resulting in dissolution within the vadose zone and the upper phreatic environments. When the pore waters become supersaturated with respect to calcite, as a result of evaporation or degassing of CO₂, pendant- or meniscus calcite cement may precipitate (Longman, 1980). Dissolution in phreatic environments commonly relates to differences in mineral solubility, whereas in a mesogenetic stage (late burial), hydrocarbon maturation or shale dewatering may provide aggressive pore fluids that are highly corrosive with respect to carbonate minerals (Longman, 1980; Moore, 2001).

The dissolution of carbonate grains is controlled by pore-fluid saturation and its chemical composition, grain mineralogy and grain surface area. Large surface areas are more prone to extensive dissolution than small surface areas, as the solvent can corrode on a larger area simultaneously. The grain surface area is reflected by the size of the grain and its surface microstructures (Walter and Morse, 1984), whereas the grain mineralogy controls the solubility and determine whether the grain dissolves or undergo neomorphism (Moore, 2001). Low-Mg calcite is chemically relative stable, whereas high-Mg calcite typically will undergo neomorphism, with no gain in porosity. Aragonite is chemically unstable and will dissolve and form secondary porosity which, if preserved, can account for significant pore volumes. Heterozoan faunal associations are dominated by calcitic grains (high- and low-Mg calcite), and secondary porosity is usually poorly developed. Photozoan faunal associations, however, often have a high content of aragonitic grains and therefore has a much better potential for secondary porosity development (Lucia, 2007).

High-Mg calcite commonly dissolves incongruently, and gets depleted in magnesium without any significant transport of calcium carbonate. Dissolution of high-Mg therefore generally will not develop moulds. Dissolution of metastable aragonite on the other hand, results in significant transport of calcium carbonate away from the dissolution site, resulting in development of mouldic pore space (Moore, 2001). High-Mg calcite is generally very unstable in freshwater and thus easily transforms to low-Mg calcite during incongruent leaching, with little to no internal change in microstructures and micro-fabrics (Flügel, 2004). The pre-diagenetic mineralogical composition of carbonate grains can therefore be predicted by light microscope studies, as grains of low-Mg or high-Mg calcite in origin will commonly preserve their internal structures, whereas aragonitic grains typically appear as open, partly cemented or completely cemented moulds.

In the studied sections, dissolution of aragonitic grains has resulted in the development of moulds that have subsequently been completely or partially cemented with non-ferroan and ferroan calcite. The cemented moulds observed within the Serdj Fm. predominantly occur in bivalve fragments and sponge spicules (Appendix I 1-3).

4.5.3 Deep burial diagenesis

Burial diagenesis is in general defined as any change, or the collection of changes, that occur

below the zone of near-surface diagenesis, but above the realm of low-grade metamorphism (Choquette and James, 1987). The extent of burial diagenesis can vary widely from one sedimentary basin to another, or even within the same basin, and is mainly a consequence of changes in hydrology, pore fluid chemistry, temperature and pressure (Choquette and James, 1987). Deep burial diagenesis includes several processes that result in different products, but can be separated into two main processes; physical and chemical compaction.

Physical compaction

Physical compaction starts at shallow burial by grain rearrangement and denser packing of grains. At increased uniform or differential stress from the overburden rock, pressure dissolution and brittle and/or ductile grain deformation takes place (Choquette and James, 1987). Pressure dissolution starts with dissolution seams that eventually develop into stylolites. The presence of stylolites suggest a burial depth of at least a few hundred meters (Flügel, 2004).

Physical compaction causes a reduction in sediment thickness, porosity and permeability (Choquette and James, 1987).

Chemical compaction

Chemical compaction or pressure solution is the result of higher pressures at greater burial depths (Choquette and James, 1987), and is by Lloyd (1977) defined as the loss of porosity and decrease of thickness caused by “autochthonous” carbonate cements brought into limestones by pressure solution. Increased pressure due to overburden or tectonic stress is transmitted and concentrated at grain or crystal contacts, increasing the solubility and associated dissolution of the stressed grain/crystal contacts. The most obvious product of chemical compaction is stylolites, which form by dissolution of soluble load-bearing material, leaving insoluble minerals (Choquette and James, 1987).

Physical compaction is often related to an earlier diagenetic phase, whereas chemical compaction is often related to a later phase of deep burial diagenesis. Within the different microfacies, both mechanical- and chemical compaction is observed, as described for each microfacies in Chapter 4.2.

4.6 Geochemical analysis

Geochemical analyses were performed on 36 bulk rock samples (14 radiogenic isotope analyses and 22 stable isotope analyses). The bulk rock samples contain grains, matrix, and ferroan and non-ferroan calcite cements.

4.6.1 Stable isotopes ($\delta^{18}\text{O}$ and $\delta^{13}\text{C}$)

Stable isotope analysis may provide information on the temperature and salinity of the ambient water and terrigenous input, and can also provide useful information on the changes in carbon cycling of ancient systems and global climate fluctuations (Flügel, 2004). The oxygen isotopic signal of carbonates precipitated from seawater is strongly controlled by temperature-dependent fractionation and ambient seawater $\delta^{18}\text{O}$ -composition (Epstein et al., 1953), whereas the carbon isotopic signal is mainly a function of the ambient seawater $\delta^{13}\text{C}$ - composition and the availability of isotopically light organic carbon (Tucker and Wright, 1990). Carbon isotope ratios of organisms commonly also reflect the isotope ratios of their diets (vital effect), and thus the ratio of stable isotopes can change between diet and consumer due to differential digestion, or fractionation during absorption and metabolic processes (McCutchan et al., 2003). Species-specific metabolic effects are common in controlling the carbon isotopic fractionation in echinoderm skeletal parts (Weber, 1968).

The isotopic signature of marine and other calcium carbonate cements are commonly preserved and thus the different cement signatures can be distinguishable (James and Choquette, 1983). Marine cements (isopachous, radiaxial fibrous, micritic and botryoidal) typically develop in equilibrium with ambient marine waters which have $\delta^{18}\text{O}$ and $\delta^{13}\text{C}$ -values close to zero (Sharp, 2007). The succession of cements developed in limestones undergoing burial diagenesis, tend to be enriched in lighter oxygen isotopes, and generally but not necessarily, accompanied by enrichment of lighter carbon isotopes (James and Choquette, 1983). Enrichment of lighter oxygen and carbon isotopes in cement is a result of re-equilibration with ambient pore waters at increasing temperatures and/or precipitation from meteoric water (James and Choquette, 1983).

The stable-isotope results of bulk samples from the Serdj Fm. are presented in Table 4-1 and Figure 4.50 to Figure 4.53Figure 4.51, with ranges and averages for different cement compositions given in Table 4-2.

Table 4-1: Samples and associated stable $\delta^{18}\text{O}$ - and $\delta^{13}\text{C}$ - values. Ferroan calcite cement abundance is based on visual estimations from thin-sections.

Stable oxygen and carbon isotope values			
Sample*	$\delta^{13}\text{C}$ Mean (‰ vPDB)	$\delta^{18}\text{O}$ Mean (‰ vPDB)	Ferroan calcite cement abundance**
GS-1S	3.1	-3.32	
GS-4S	2.91	-2.76	
GS-6S	3.67	-3.15	
JF-14S	3.15	-2.76	
JF-16S	3.37	-2.35	
JF-17S	2.93	-3.19	
JF-22S	3.2	-2.66	
JF-30S	3.09	-2.56	
JF-35S	2.26	-2.05	
JF-40S	3.14	-2.19	
JF-45S	2.93	-2.45	
JF-49S	3.29	-2.4	
JF-57S	3.35	-2.06	
JF-60S	2.64	-2.44	
JF-66S	3.08	-3.16	
JF-69S	3.08	-2.46	
JF-74S	2.33	-3.16	
JF-80S	2.09	-1.78	
JF-87S	0.82	-1.75	
NFS-1S	3.69	-2.46	
NFS-3S	3.96	-2.69	
NFS-5S	3.54	-1.83	

* GS = J.Garci section, JF = J.Fadeloun section and NFS = Northern J.Fadeloun section

**Red: No ferroan calcite; pale blue: 1-3% ferroan calcite; medium blue: 3-6% ferroan calcite; dark blue: >6% ferroan calcite (ferroan calcite content and stable isotope results will not be compared due to patchy cement distribution; see main text for further comments).

Table 4-2: $\delta^{18}\text{O}$ and $\delta^{13}\text{C}$ ranges and averages for different cements compositions.

Samples	$\delta^{18}\text{O}$ (‰)		$\delta^{13}\text{C}$ (‰)	
	Range	Average	Range	Average
All	-1.75 to -3.32	-2.53	0.82 to 3.96	2.98
Non-ferroan calcite only	-1.75 to -2.66	-2.30	0.82 to 3.69	2.97
1-3% ferroan calcite	-1.78 to -2.76	-2.35	2.09 to 3.96	3.07
3-6% ferroan calcite	-3.15 to -3.32	-3.20	2.33 to 3.67	3.02
>6% ferroan calcite	-2.05 to -2.76	-2.41	2.26 to 3.91	2.59

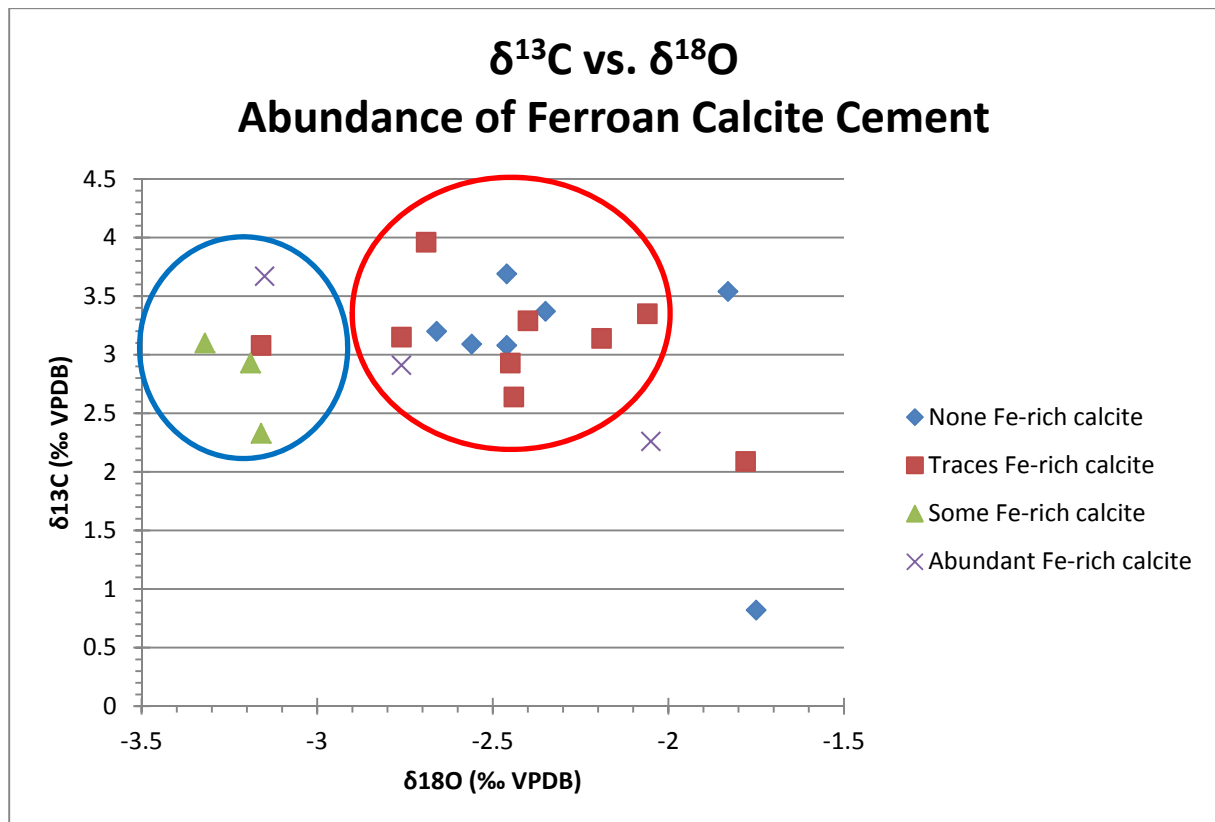


Figure 4.50: Abundance of Fe-rich calcite cement and associated stable oxygen and carbon isotope values. Note the relationship between the abundance of Fe-rich calcite cement and $\delta^{18}\text{O}$ values (red and blue circles). Heavier oxygen isotopes (less negative $\delta^{18}\text{O}$ values) tend to be associated with low ferroan calcite content (red circle), whereas lighter oxygen isotopes (more negative $\delta^{18}\text{O}$ values) are associated with higher ferroan calcite cement content (blue circle).

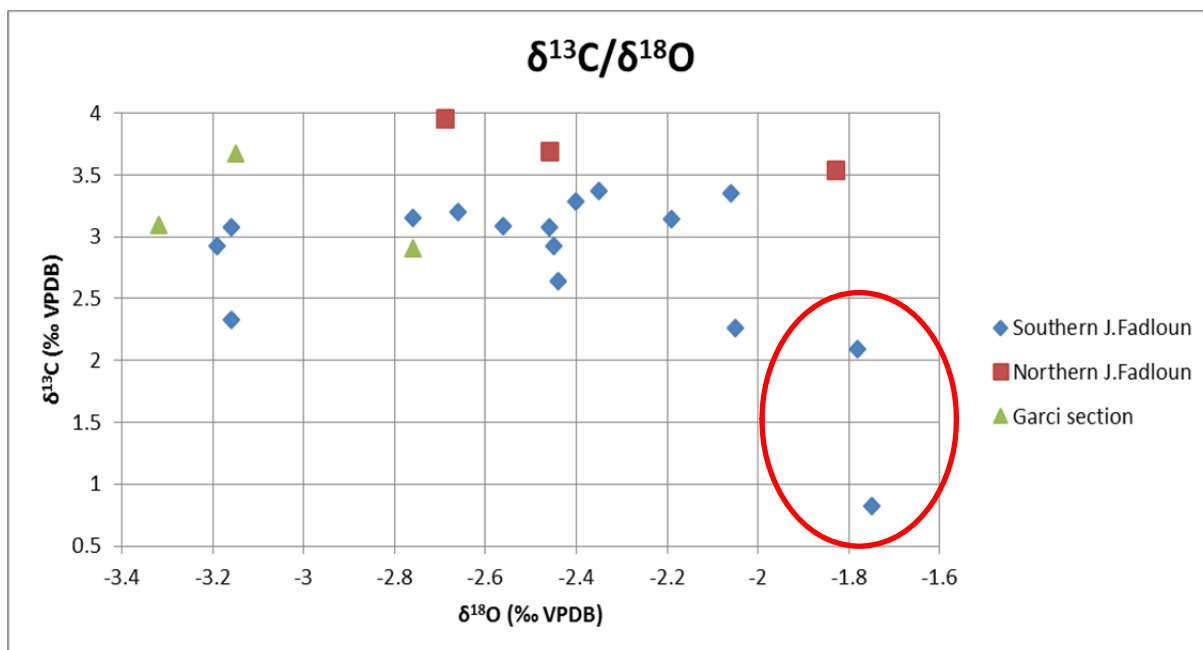


Figure 4.51: Stable isotope values (‰ VPDB) of $\delta^{13}\text{C}$ and $\delta^{18}\text{O}$ for different localities. Samples marked with a red circle are of Albian age, and their $\delta^{18}\text{O}$ and $\delta^{13}\text{C}$ compositions deviate from the stable-isotope composition of the Aptian samples.

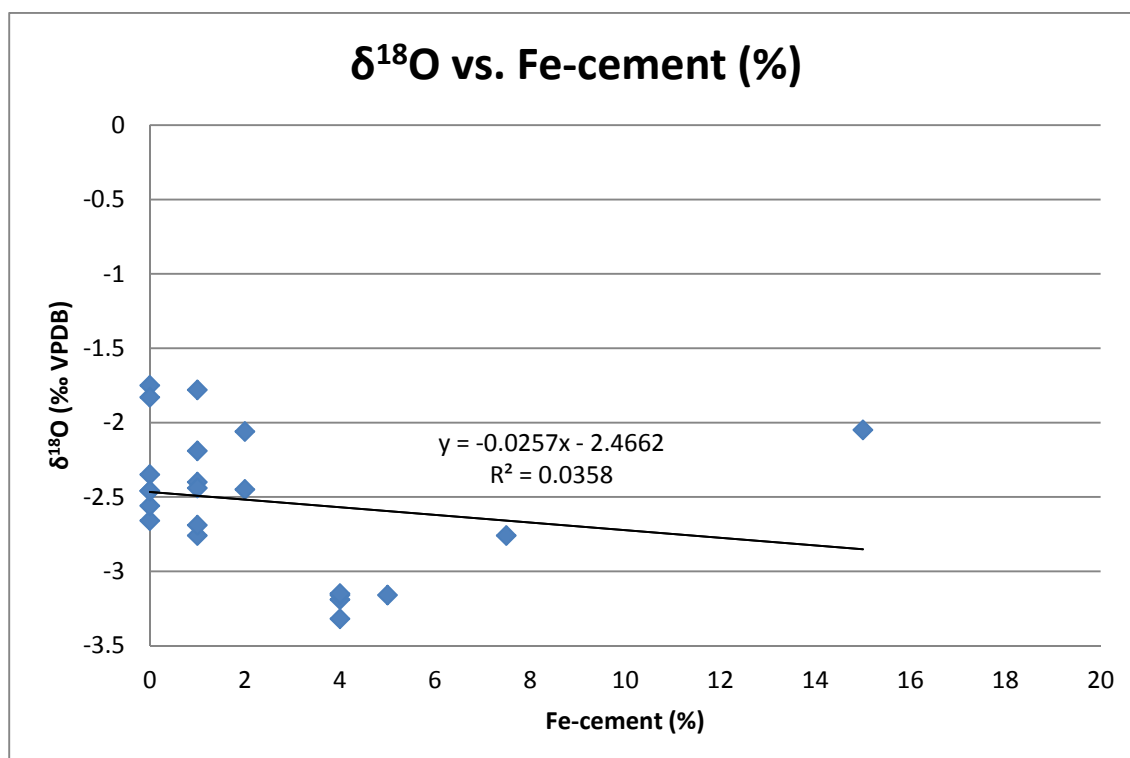


Figure 4.52: $\delta^{18}\text{O}$ and Fe-calcite cement (%) relationships. All measured values are presented. Note the low R^2 -value. Raw data is presented in Appendix H. Number of samples: 20.

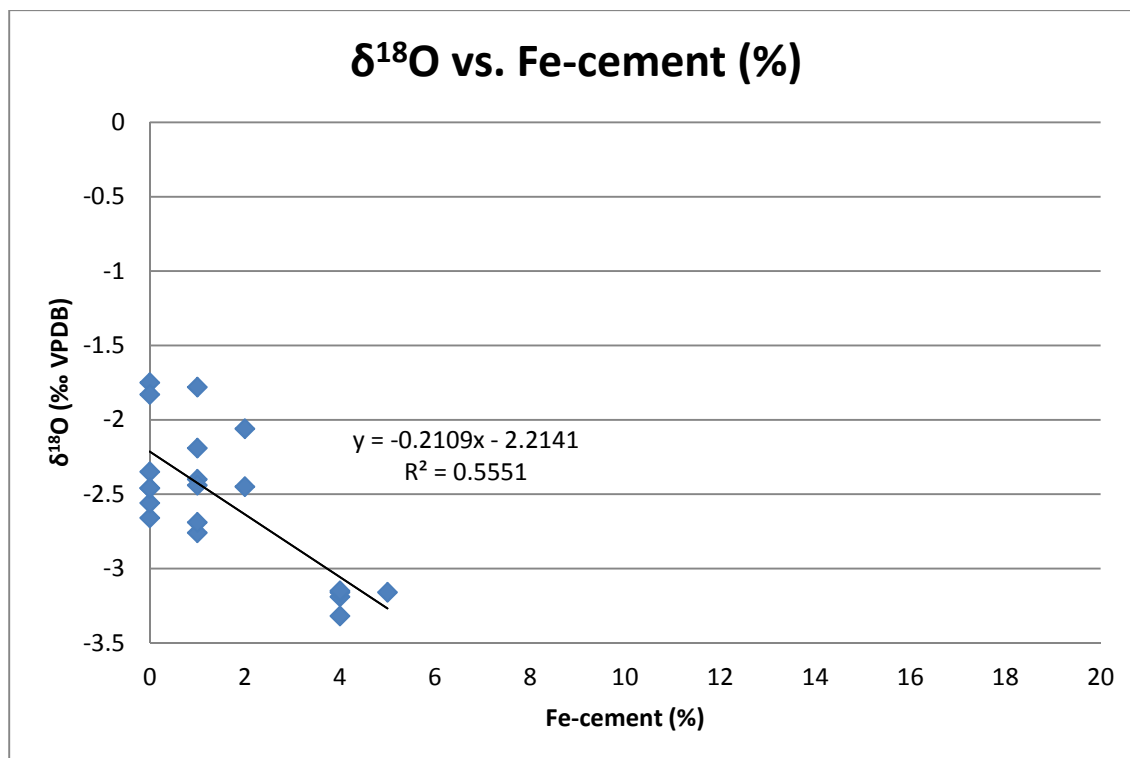


Figure 4.53: $\delta^{18}\text{O}$ and Fe-calcite cement (%) relationships. Thin section studies reveal that sample JF-35S has a patchy Fe-cement distribution and that the sampled area is not representative for the whole sample. Sample GS-4S have a Fe-cementation restricted to clusters of certain grain types (probably originally aragonitic bivalve fragments) and to fracture infill, thus the area sampled is not representative for the measured isotope values. Samples JF-35S and GS-4S are therefore removed from the plot, resulting in an increase in the R^2 -value, indicating a more accurate trend. Raw data is presented in Appendix H. Number of samples: 18.

The data show that increased abundance of Fe-rich calcite cement is associated with enrichment of the lighter ^{16}O isotope, whereas there is no obvious change in $\delta^{13}\text{C}$ values (Figure 4.50). By comparing the measured $\delta^{18}\text{O}$ values with the percentage of ferroan calcite cement it is possible to get a rough estimate of the $\delta^{18}\text{O}$ value of the cement (Figure 4.52 and Figure 4.53). The present pore space cemented by ferroan calcite cement was estimated subjectively by visual comparison with Terry and Chilingar (1955) comparison chart for visual percentage estimation. Thin-section studies show that the ferroan calcite cement in two samples is patchily distributed, and that the percentage ferroan cement within the isotope sampled area is not representative for the total thin section. These samples were therefore excluded from the data set in order to get a more representative comparison of percentage ferroan calcite and $\delta^{18}\text{O}$. This gave a significant increase in the coefficient of determination (R^2) value, indicating a better fit of data in the statistical model. Even though there is not enough isotope samples collected to give a statistically significant result, a weak inverse trend between Fe-rich calcite cement and $\delta^{18}\text{O}$ is observed (Figure 4.53). The predicted average

$\delta^{18}\text{O}$ for 100% ferroan calcite cement was calculated to -23.3 (‰ vPDB), based on the equation given in Figure 4.53.

Paleotemperatures

Paleotemperatures from $\delta^{18}\text{O}$ (‰ vPDB) were calculated using an equation from Hays and Grossman (1991) (Equation 4-1). The results are given in Figure 4.54 and Figure 4.55.

Equation 4-1: Paleotemperature equation for stable oxygen isotopes (Hays and Grossman, 1991).

$$T(^{\circ}\text{C}) = 15.7 - 4.36 (\delta_c - \delta_{SW}) + 0.12 (\delta_c - \delta_{SW})^2$$

where:

$\delta_c = \delta^{18}\text{O}$ of calcite (sample measurement)

$\delta_{SW} = \delta^{18}\text{O}$ of sea water. -2.5 to -2.0 ‰ vPDB in late Aptian, based on Grossman (2012)

T = Temperature ($^{\circ}\text{C}$)

Calculated paleotemperatures for samples lacking ferroan calcite cement (Figure 4.55) range between 13 and 17 $^{\circ}\text{C}$. The calculated temperatures are probably close to the temperatures of the ambient waters from which the calcite formed, and as cool/temperate ramp carbonates generally accumulate in seawaters colder than 20 $^{\circ}\text{C}$, the paleotemperatures derived from $\delta^{18}\text{O}$ -analysis suggest precipitation from temperate waters (James, 1997).

The precipitation temperature for the ferroan calcite cement, using Equation 4-1, is calculated to ca. 160 $^{\circ}\text{C}$.

There is a significant uncertainty in the prediction of the $\delta^{18}\text{O}$ and temperature of the ferroan calcite cement, due to:

- Few data points.
- Available data points are clustered into two main groups.
- No data points with more than 5% ferroan calcite are available.
- Relatively low coefficient of determination ($R^2=0.55$).

- Ferroan calcite content was estimated from visual estimation.
- Bulk volumes applied for stable isotope analyses (3D volume) and ferroan calcite quantification (2D area) are not the same.

In spite of the low statistical significance it can be concluded that ferroan calcite cement probably is late diagenetic in origin and that it precipitated at elevated temperatures.

Fluid inclusions in the ferroan calcite cement would probably give more accurate paleo-temperatures. However, no inclusions were observed.

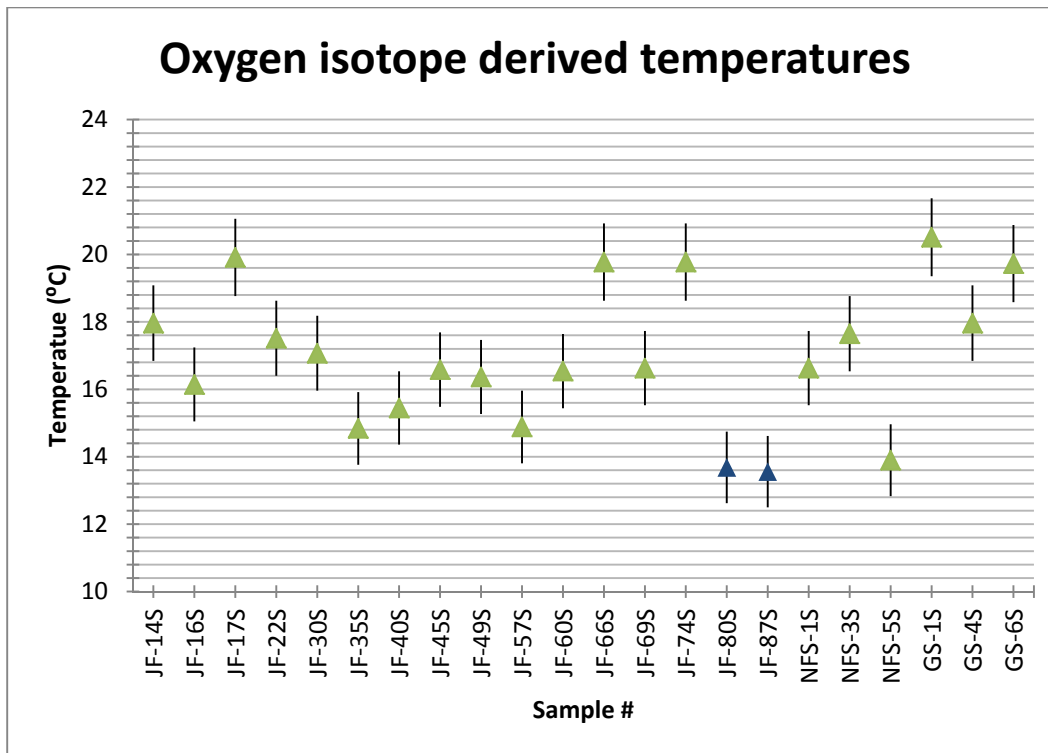


Figure 4.54: Marine water temperatures of all samples (ferroan and non-ferroan calcite cemented) derived from stable isotope analysis of oxygen (method described in Chapter 3.5). Line = temperature range based on max and min $\delta^{18}\text{O}$ values for each sample; Triangle = calculated mean value, green = Aptian, blue = Albian.

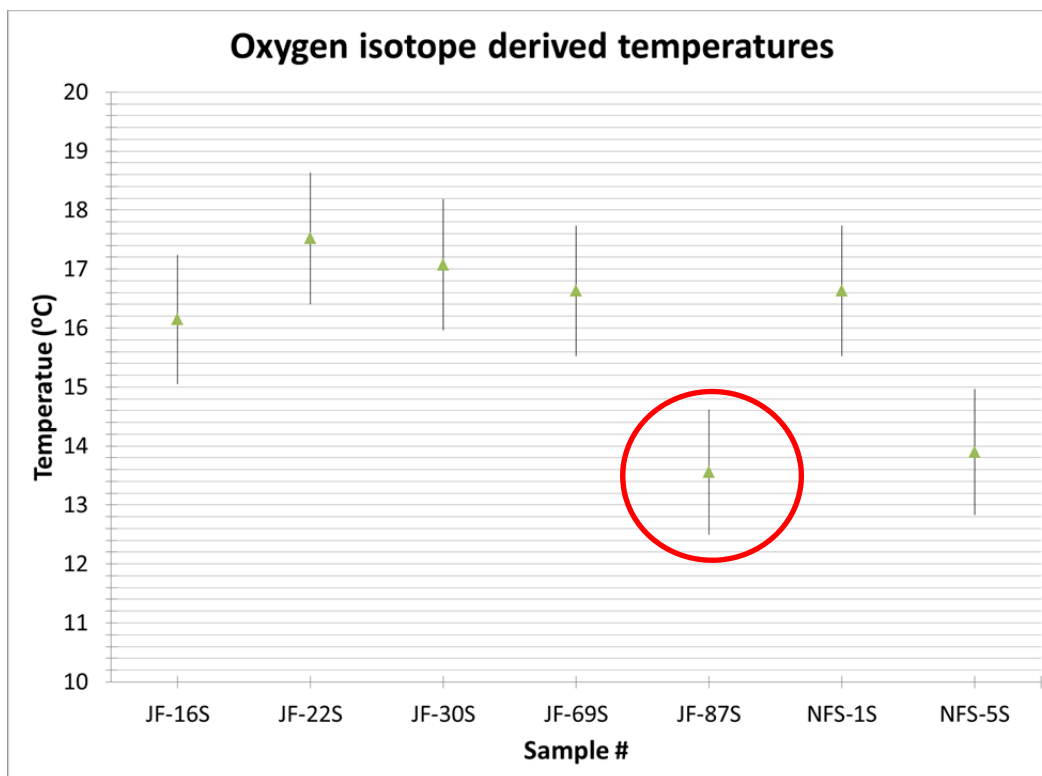


Figure 4.55: Marine water temperatures of samples with non-ferroan calcite cement, derived from stable isotope analysis of oxygen (method described in Chapter 3.5). These samples have a variable abundance of non-ferroan calcite cement, which may have an impact on the calculated paleo-water temperatures. Meteoric cements would lower $\delta^{18}\text{O}$ and give a higher calculated paleo-water temperature. Line = Temperature range based on max and min $\delta^{18}\text{O}$ values for each sample; Green triangle = Calculated mean value; Red circle = Albian.

4.6.2 Radiogenic isotopes

Radiogenic isotopes are either unstable or decay to another nuclei, as opposed to stable isotopes whose abundance is unchanged during radioactive processes. Sr-isotope analysis offers a mean to date and correlate carbonate deposits, provided that the analyzed material has persevered the original seawater Sr-isotope signal. Low-Mg calcite (LMC) shells of marine taxa are preferred candidates for strontium-isotope stratigraphy since they are diagenetically more stable than those of aragonitic origin (McArthur, 1994; Martin et al., 1999). By measuring the $^{87}\text{Sr}/^{86}\text{Sr}$ of carbonate rock, it is possible to determine the time of mineral precipitation (McArthur, 1994). The measured values and associated ages of the studied sections are presented in Table 4-3 and Figure 4.56 to Figure 4.58. Age is determined by correlating reported $^{87}\text{Sr}/^{86}\text{Sr}$ -values with ages presented by McArthur et al. (2001).

Table 4-3: Measured $^{87}\text{Sr}/^{86}\text{Sr}$ values and estimated ages for the sampled sections at J.Fadeloun and J.Garci.

Sample #	Depth (m)	$^{87/86}\text{Sr}$ corrected	Age (Ma)		
			Min	Best fit	Max
JF-87S	-1,50	0.707608	>75.59	75.76	<75.93
JF-80S	45	0.707622	>74.94	75.13	<75.30
JF-69S	59.9	0.707551	>78.54	78.78	<79.03
JF-66S	68.3	0.707568	>77.60	77.78	<77.99
JF-60S	75.2	0.707688	>72.58	72.69	<72.80
JF-57S	77.85	0.707488	>82.68	82.88	<83.07
JF-49S	90.65	0.707503	>81.77	81.98	<82.19
JF-14S	145.15	0.707852	>32.83	32.98	<33.15
NFS-5S	0.4	0.707722	>71.43	71.56	<71.68
NFS-3S	4.8	0.707603	>75.83	76.00	<76.17
NFS-1S	55.8	0.707727	>71.24	71.38	<71.52
GS-6S	0.2	0.707841	>33.03	33.21	<33.38
GS-4S	3.25	0.708411	>20.59	20.74	<20.88
GS-1S	5	0.708761	>15.42	15.62	<15.8

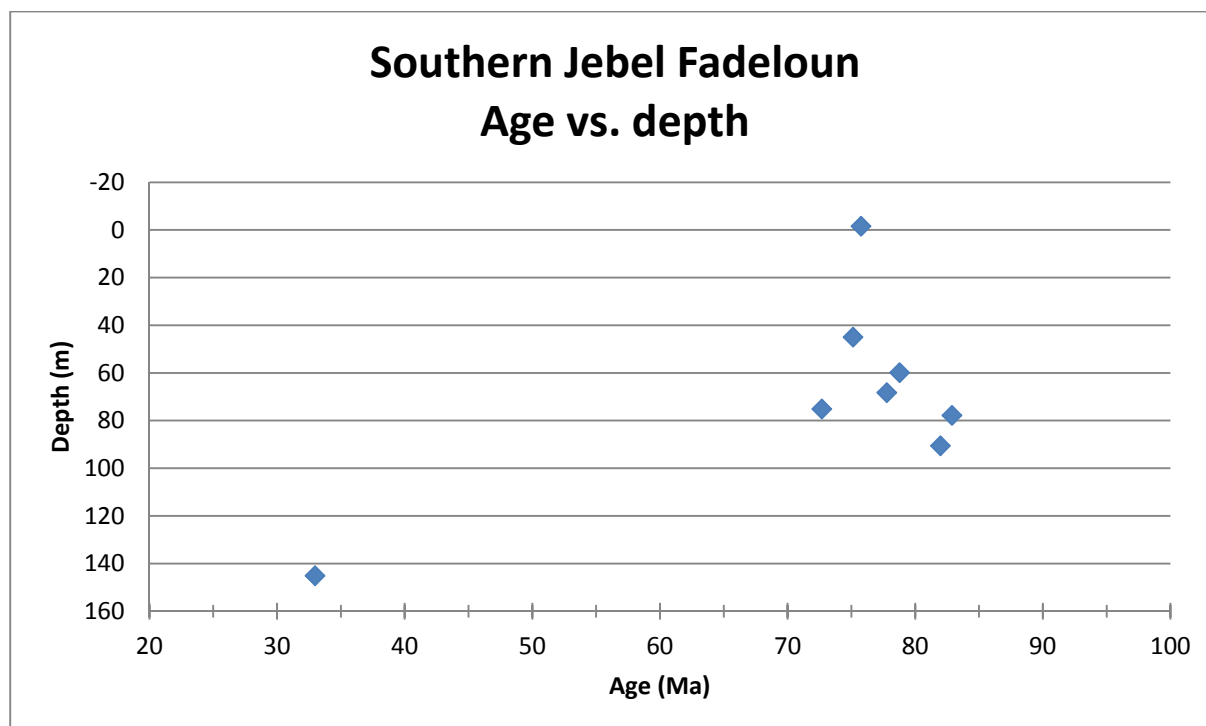


Figure 4.56: Age derived from strontium isotope analysis of southern J.Fadeloun versus depth. Note that the reported ages are scattered, with no clear trend, and that the deepest sample has the youngest predicted age. The reported ages are also younger than the expected Aptian age (see Chapter 5.1.3). Obviously, the age determinations are unreliable and cannot be applied (see additional comments in Chapter 5.1.3). Zero depth represents top Aptian.

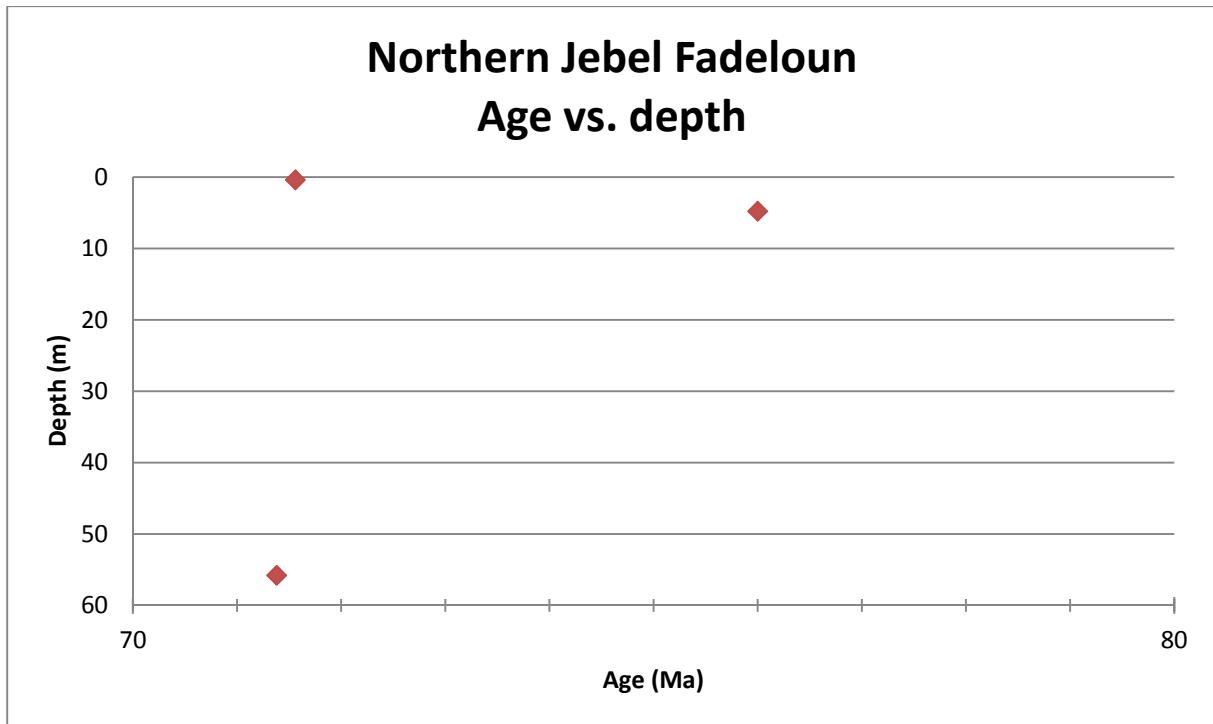


Figure 4.57: Age derived from strontium isotope analysis of northern J.Fadeloun versus depth. Note that the reported ages are scattered and that there is no clear trend. The reported ages are also younger than the expected Aptian age (see Chapter 5.1.3). Zero depth represents top Aptian.

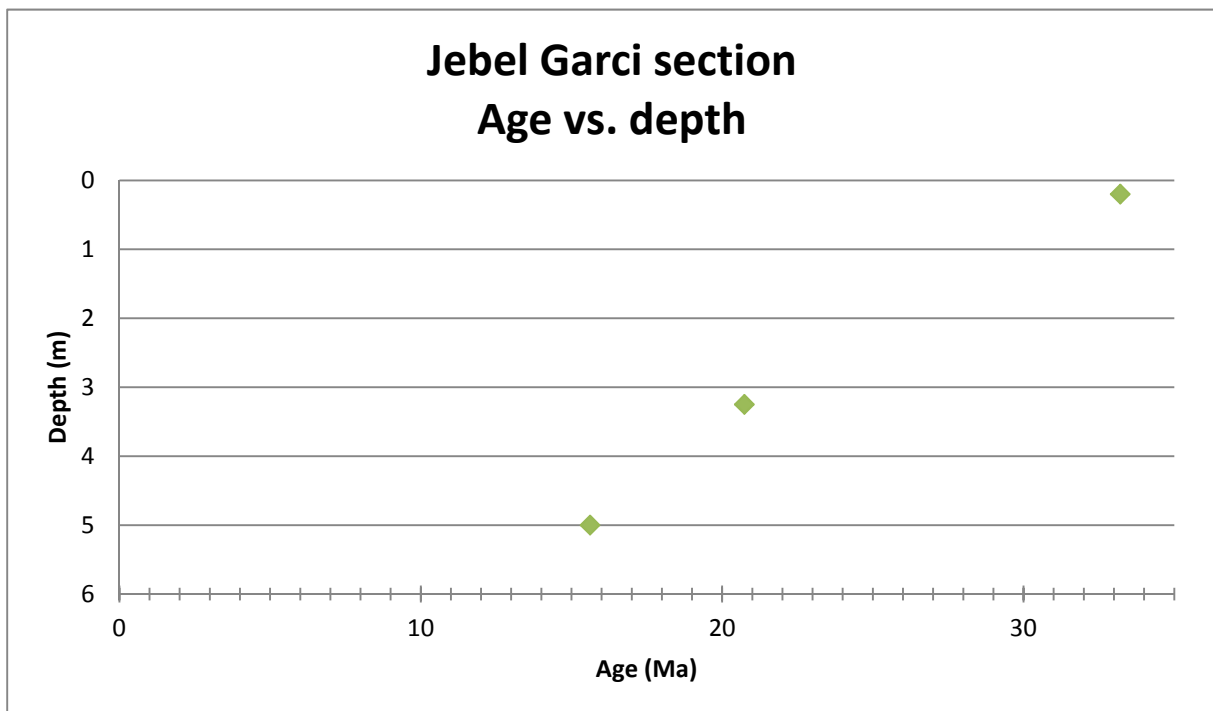


Figure 4.58: Age derived from strontium isotope analysis of the J.Garci section versus depth. Note that the trend indicates that the sedimentary rocks surprisingly get progressively younger with burial depth. Moreover, all estimated ages are much younger than the expected Aptian age (McArthur et al., 2001), and date to Oligocene and Miocene (Chapter 5.1.3). Zero depth represents top Aptian.

4.7 Fractures

Fractures with various apertures, and often in cross-cutting relationships, are observed throughout J.Fadeloun and J.Garci. There are no observed offset between the cross-cutting fractures. Observed fractures show all variations of cementation, from completely open to completely cemented. Fracture-filling cements are granular to equant, non-ferroan and ferroan calcite cements. Some of the open fractures may have been induced during sampling.

4.8 Porosity and permeability

The quality of a reservoir is mainly determined by the porosity and permeability of the rock. These properties are functions of both depositional and diagenetic processes, and determine (along with saturation) the estimated volume of hydrocarbons that can be produced from a reservoir. Porosity and saturation are important for determination of the possible hydrocarbon pore volume, while permeability relates to the ease at which the hydrocarbons can be recovered (Lucia, 1999).

4.8.1 Introduction to porosity

Porosity (ϕ) is defined as the fraction of volume in a rock that is not occupied by any grains, cement or matrix, and is given as percentage or fraction of the bulk rock volume. The pore volume is either occupied by water, oil, gas or a combination of these, and is crucial for the reservoir's fluid/gas storage capacity (Lucia, 1999). It is often convenient to distinguish between absolute (or total) porosity and effective porosity on the basis of connectivity of the pores. Absolute porosity (ϕ_A) of a rock body is determined by the ratio between the total volume of pore space (V_{ps}) and the bulk volume of the rock (V_b), expressed in Equation 4-2:

Equation 4-2: Absolute porosity. ϕ_A expressed as percentage.

$$\phi_A = \frac{V_{ps}}{V_b} * 100$$

The effective porosity (ϕ_{Ef}) of a rock is determined by the ratio between the total volume of interconnected pore space (V_{cps}) and the bulk volume of the rock (V_b), and is expressed in percent in Equation 4-3:

Equation 4-3: Effective porosity. Φ_{Ef} expressed as percentage

$$\phi_{Ef} = \frac{V_{cps}}{V_b} * 100$$

To determine fluid flow properties, effective porosity is often considered. There is no simple relationship between porosity, grain size and sorting in carbonates (Lucia, 1999), so the effective porosity is often dependent on a combination of several factors such as grain type, fabric, sorting, weathering, clay content and cementation. Effective porosity in carbonate reservoirs are commonly in the range of 1 to 35%, with an average of approximately 10% for dolomite reservoirs and approximately 12% for limestone reservoirs (Schmoker et al., 1985). The percentage of visible (in thin section) porosity can be used to obtain a qualitative estimate of the reservoir quality (Table 4-4) using the Archie (1952) classification (Table 4-4):

Table 4-4: Reservoir quality based on visible porosity (modified from Ahr (2008))

Porosity:	Qualitative Description:
<5%	Poor
10%	Fair
15%	Good
<20%	Excellent

Porosity is usually subdivided into primary and secondary porosity on the basis of the process of formation. Sedimentologists also commonly use the term minus-cement porosity, when discussing potential porosity of a reservoir (Flügel, 2004).

Primary porosity consists of pore space developed during depositional and early post depositional processes. The porosity and pore geometry developed during these processes strongly vary with packing of grain, sorting, roundness, and the abundance and distribution of clay (Choquette and Pray, 1970; Ahr, 2008).

Secondary porosity (also often referred to as post depositional porosity), develop after burial of the sediment and/or during subsequent uplift. The voids developed, are results of either dolomitization, dissolution, fracturing or a combination of these processes (Choquette and Pray, 1970; Ahr, 2008).

Minus-cement porosity is the porosity available after removal of cements, i.e. the pore volume of cements plus open pores. Minus-cement porosity thus represents a measure of pre-cementation porosity (Flügel, 2004).

4.8.2 Classification of pore types

Carbonate pore types are varied and complex as a consequence of different depositional settings and diagenetic alteration. In order to better understand the elements affecting permeability, several different porosity classification systems have been developed on the basis of deposition, diagenesis, geometric features, flow properties and pore size.

In 1952 Guastavus E. Archie developed a classification system with focus on estimating porosity. He realized that not all pore space is visible with an optical light microscope and he divided pore space into matrix and visible porosity (Lucia, 1995). Later, Choquette and Pray (1970) developed a pore-type classification system that is based on pore geometries and which is related to depositional and diagenetic processes. This classification system consists of 15 pore types. Lucia's (1983) pore-type classification system focuses more on the geometric features and flow properties of the pores.

Lønøy (2006) noticed that several other elements than those described by Choquette and Pray (1970) and (Lucia, 1983, 1995, 1999) had an effect on permeability, and he therefore developed a new classification system (Table 4-5) that integrates the Choquette & Pray and Lucia systems and incorporates some new elements. In his classification system, Lønøy subdivided interparticle, intercrystalline and mouldic porosity into subclasses based on their pore size. Lønøy (2006) also recognized the importance of pore type distribution, and distinguished between uniform and patchy pore space. The pore type classification of Lønøy is based on an empirical optimization of global permeability relationships, and it includes 21 pore type classes. The system shows a predictable relationship between porosity and permeability, and it combines both sedimentologic and diagenetic features with flow related

properties (Lønøy, 2006). The pore type classification system developed by Lønøy (2006), is applied in current study (Table 4-5).

Table 4-5: Lønøy's pore type classification system for carbonate rocks (modified from Lønøy (2006))

Pore Type	Pore Diameters	Pore Distribution	Pore Fabric	Code
Interparticle				1
Interparticle (BP)	Micropores (10-50 µm)	Uniform	Interparticle, uniform micropores	1.11
		Patchy	Interparticle, patchy micropores	1.111
	Mesopores (50-100 µm)	Uniform	Interparticle, uniform mesopores	1.12
		Patchy	Interparticle, patchy mesopores	1.112
	Macropores (>100 µm)	Uniform	Interparticle, uniform macropores	1.13
		Patchy	Interparticle, patchy macropores	1.113
Vuggy				2
Vuggy				2
Mouldic				3
Mouldic (MO)	Micropores (10-20 µm)		Mouldic micropores	3.11
	Macropores (20-30 µm)		Mouldic macropores	3.13
Intercrystalline				4
Inter-crystalline	Micropores (10-20 µm)	Uniform	Intercrystalline, uniform micropores	4.11
		Patchy	Intercrystalline, patchy micropores	4.111
	Mesopores (20-60 µm)	Uniform	Intercrystalline, uniform mesopores	4.12
		Patchy	Intercrystalline, patchy mesopores	4.112
	Macropores (>60 µm)	Uniform	Intercrystalline, uniform macropores	4.13
		Patchy	Intercrystalline, patchy macropores	4.113
Intraparticle				5
Intraparticle (WP)				5
Mudstone microporosity				6
Mudstone microporosity	Micropores (<10 µm)		Tertiary chalk	6.01
			Cretaceous chalk	6.02
		Uniform	Chalky micropores, uniform	6.03
		Patchy	Chalky micropores, patchy	6.04

4.8.2.1 Interparticle (BP) porosity

Interparticle (BP – Between Particles) porosity, often also referred to as intergranular porosity, is the porosity occurring between grains (Choquette and Pray, 1970). The porosity is commonly primary in origin, but may also be formed by secondary dissolution of matrix or cements. Interparticle porosity is divided into six subclasses based on pore size (micro-, meso- and macropores; 10–50µm, 50-100µm and >100µm pore diameters, respectively) and pore distribution (uniform or patchy), as shown in Table 4-5. Patchy interparticle porosity is commonly related to diagenetic overprint, either by selective dissolution of matrix or cements, and/or patchy cementation of both primary and secondary porosity.

Depositional settings commonly associated with interparticle porosity are medium to high energy shallow-marine settings, such as rimmed platform-margin shoals, platform-interior shoals, ramp shoal complexes, middle-ramp barrier shoals, beaches, wash-over fans, gravity-driven flow deposits and other settings. While macropores are most common in high energy grainstones; micropores commonly occur within recrystallized mud of mud-lean packstones (Lønøy, 2006).

4.8.2.2 Vuggy (VUG) porosity

Vuggy porosity are secondary solution pores that are not fabric selective, and can therefore cut grain and/or cement boundaries (Choquette and Pray, 1970; Lønøy, 2006). The pores are commonly of irregular shape and size, and are either isolated or interconnected. It can be very difficult to determine the interconnectivity of vuggy pores, in 3D. Many vuggy pores are solution enlarged mouldic pores with little or no evidence of the precursor grain (Lønøy, 2006). Vugs commonly form by dissolution under the influence of chemically aggressive pore fluids during sea-level low-stands. Dissolution commonly occurs by meteoric diagenesis in humid climates, but can also form in the deep subsurface by dissolution from basinal fluids. (Budd et al., 1995).

Vuggy porosity is separated from cavern and channel porosity based on the size and geometry, respectively. Whereas vuggy porosity is commonly in the range of approximately 1mm to 1m, cavern porosity is significantly larger, i.e. man-sized. In the oil industry cavern

porosity is typically defined by drill-bit drops. Channel porosity consist of elongated tabular and flat channels, whilst vuggy porosity is commonly more spherical (Lønøy, 2006).

4.8.2.3 Mouldic (MO) porosity

Lønøy (2006) defines mouldic pores as secondary pores formed by complete or partial dissolution and recrystallization of grains or crystals. This definition is somewhat different from the one proposed by Choquette and Pray (1970); by including partial dissolution and recrystallization of grains or crystals. Mouldic porosity is subdivided into micro (<10-20 μ m pore diameters) and macropores (>20-30 μ m pore diameters), based on the pore size (Lønøy, 2006).

There must be a distinctive difference in solubility between grains and framework in order for mouldic porosity to form. This difference commonly relates to mineralogical differences. Mouldic pores are often recognized by their size, shape and relict features, indicating the former presence of a grain or crystal.

4.8.2.4 Intercrystalline porosity

Intercrystalline porosity is porosity between primary and/or secondary crystals (Choquette and Pray, 1970). Intercrystalline porosity is divided into six subclasses by Lønøy (2006), based on pore size and pore distribution.

Reflux dolomitization of lagoonal micrite, commonly favor the development of uniform micro- and mesoporosity (10-20 μ m and 20-60 μ m pore diameters, respectively)(Lucia, 2007). Intercrystalline macroporosity with uniform distribution can occur in any depositional setting but commonly relates to slow dolomitization during deeper burial and are also common in high-energy settings. The distribution of pores is often controlled by fluid migration pathways (pers. comm. A.Lønøy, 2015).

Patchy intercrystalline porosity (micro-, meso- and macroporosity) often relates to patchy cementation. The cement is commonly composed of silica or evaporites. Compared to

uniform porosity distribution, patchy cement distribution tend to increase the permeability to porosity ratio (Lønøy, 2006).

4.8.2.5 Intraparticle porosity (WP)

Intraparticle porosity is pore space occurring within grains. The porosity is either primary in origin, or it can be formed through decay and removal of organic material in carbonate skeletons (Lønøy, 2006). This definition is slightly different than the one proposed by Choquette and Pray (1970), by excluding porosity related to dissolution. Lønøy (2006) considers porosity related to dissolution as mouldic porosity, and is the nomenclature applied in this work.

The pores are commonly fauna dependent, and often form within carbonate skeletons of gastropods, foraminifera, corals, bryozoans and calcispheres (Lønøy, 2006).

4.8.2.6 Mudstone microporosity

Mudstone microporosity is interparticle- or intercrystalline porosity comprised of pores with extremely small pore sizes (typically on the scale of only a few micrometers). Individual pores are not visible under a standard petrographic microscope although the porosity may be discerned by a weak bluish colour to the thin section using blue-dyed-epoxy (method briefly described in section 3.2.2) (Lønøy, 2006).

Mudstone microporosity is subdivided into chalk and chalky microporosity (Lønøy, 2006). Chalk porosity is commonly diagnostic for deposition in deeper marine settings, and porosity constitutes of voids between the carbonate skeletons of coccolithophorid algae.

4.8.3 Introduction to permeability

Permeability (k) is a rock property that relates to the potential migration rate of fluids through a reservoir, and hence to the rate at which hydrocarbons can be recovered. Permeability is measured in Darcy (D) and milliDarcy (mD), and the values range considerably within a

reservoir from below 0.01 mD to well above 1 D. 1 Darcy (D) is defined as the permeability through a porous medium with a flow of 1cm³/s and a fluid with a viscosity of 1cP (1 mPa*s) under atmospheric pressure, acting across an area of 1cm². A permeability of 0.1 mD is by Lucia (1999) considered as the absolute minimum permeability for oil production and is qualitatively described by North (1985) and Ahr (2008) in Table 4-6.

Table 4-6: Qualitative ranking of reservoir permeability (modified from North (1985))

Permeability (mD)	Qualitative description
< 1.0-15	Poor to fair
15-50	Moderate
50-250	Good
250-1000	Very Good
>1000	Excellent

Permeability is expressed by Darcy's law as shown in Equation 4-4, principle illustrated in Figure 4.59:

Equation 4-4: Darcy's law. Q is flow rate, k is permeability, μ is fluid viscosity, $\Delta P/L$ relates to the pressure drop across a horizontal sample and A to the cross-sectional area of the sample.

$$Q = A \left(\frac{k}{\mu} \right) \left(\frac{\Delta P}{L} \right)$$

Where Q is flow rate expressed with SI unit m³/s, k is permeability expressed in Darcy (1 Darcy $\approx 10^{-12}$ m²), μ is viscosity expressed in pascal seconds (Pa * s), P is pressure expressed in Pascal (Pa), L is length expressed in meters (m) and A is cross-sectional area of sample expressed in meters (m).

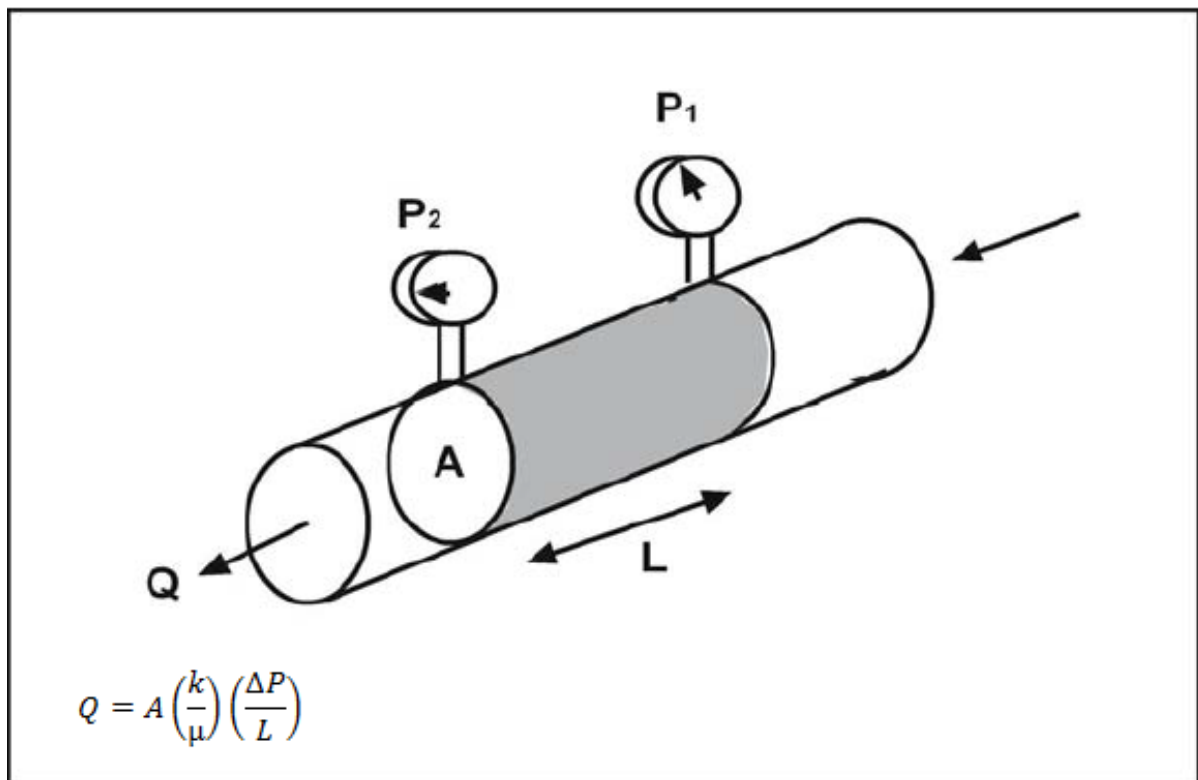


Figure 4.59: Darcy's law explained with a core plug injected with a fluid of known viscosity, in an air-tight sleeve with length L and areal A . The confining pressure should be as equivalent to *in situ* reservoir conditions as possible (modified figure from Lucia, 2007).

Permeability measurements are typically carried out using one single fluid, commonly air or water, and the results must be corrected for the varying saturations that occur in a reservoir. Permeability measured at atmospheric pressure tends to be higher than those measured at confined subsurface pressures. As a consequence the measured permeability must be corrected to restore true value at reservoir conditions (Gluyas and Swarbrick, 2009). Permeability is therefore expressed as either *absolute*, *effective* or *relative permeability* (Lucia, 1999; Ahr, 2008):

Absolute permeability: Permeability of a rock which is 100% saturated with one fluid phase (Lucia, 1999; Gluyas and Swarbrick, 2009).

Effective permeability: Permeability of a rock with two fluids measured at a specific saturation state. The measured effective permeability will always be lower than the absolute permeability and will change as the saturation changes.

Relative permeability: Permeability measured at a specific fluid saturation and expressed as a fraction of the absolute permeability (Lucia, 1999). Thus relative permeability is the ratio of

the effective permeability of a given fluid with a particular saturation, to absolute permeability of the given fluid at total saturation. In a reservoir it is useful to know the relative permeability versus the saturation in order to predict the production rate changes with changes in water saturation (Lucia, 1999). The water and oil saturations are not constant in a reservoir (e.g. Figure 4.60), and will vary both laterally and vertically in response to the position in the oil column, petrophysical differences (controlled by sedimentological and diagenetic processes) and as the hydrocarbons are produced (Gluyas and Swarbrick, 2009).

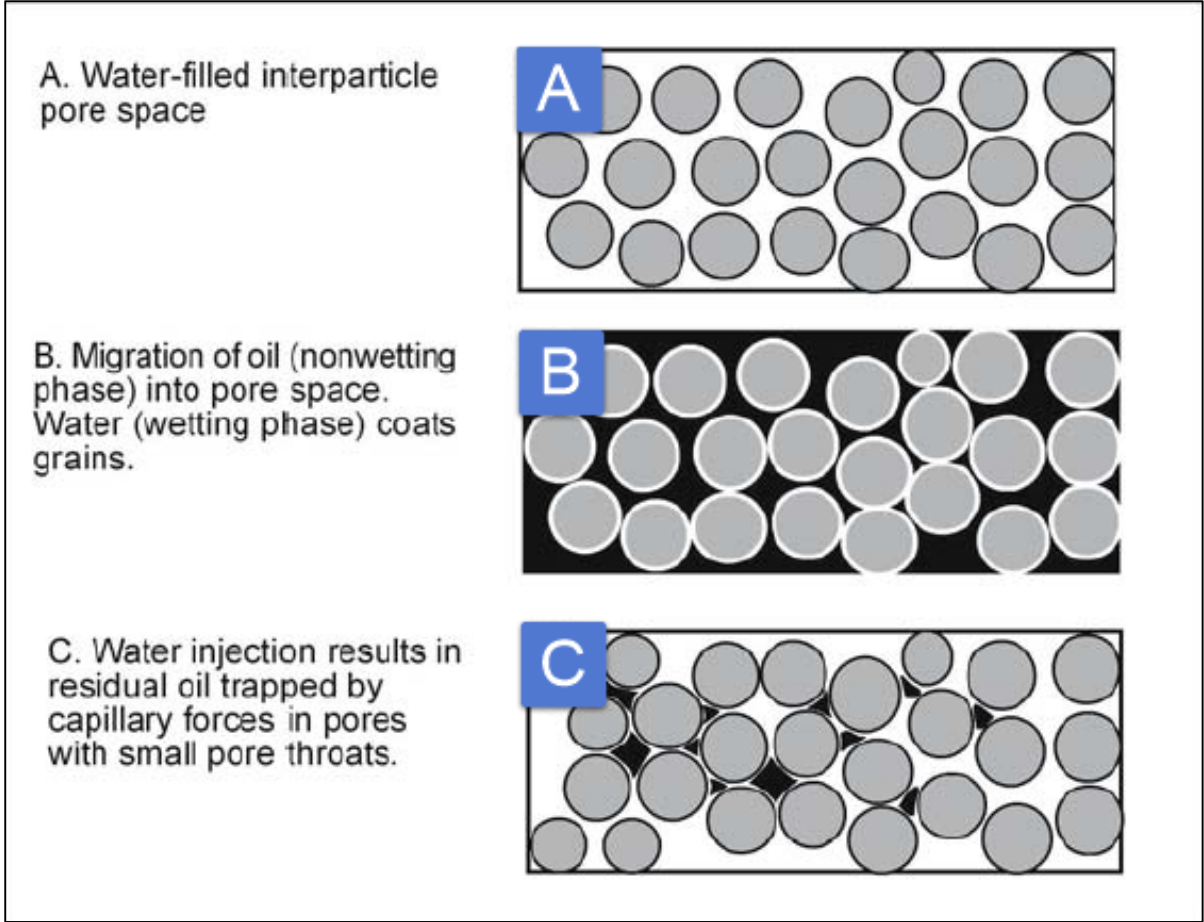


Figure 4.60: Diagram showing water and oil distribution under different conditions for a water-wet rock. A. 100% water saturation (before oil migration), B. Injection of oil (non-wetting fluid; accumulation of oil), C. Injection of water (wetting fluid; production of oil) (modified from Lucia, 2007). Black = oil, white = water, gray = grains.

4.8.4 Pore types, porosity and permeability

In this section the pore types in the studied samples are described, and porosity and permeability estimation and measurement are reported. Pore types are determined by detailed thin section analyses and classified according to Lønøy (2006) pore-type classification system for carbonate rocks (Table 4-5). Porosity is estimated by means of image analysis of 37 thin sections (method described in chapter 3.3.3) and permeability was measured by means of the TinyPerm instrument (method described in chapter 3.3.1). Permeability measurements were measured parallel to the bedding plane, both vertically through the successions, and (where possible) also laterally within the same bed (approximately 5m distance between each sample). Permeability was estimated based on porosity calculations from image analysis of thin sections and published porosity-permeability transforms for different pore-type classes published by Lønøy (2006). Two plugs were also sampled, and porosity, permeability and grain density data were derived by conventional laboratory methods.

4.8.4.1 Pore types

The pore-type distribution within each microfacies and section is presented in Figure 4.61. Mud-supported microfacies are dominated by mouldic macropores. Grain-supported microfacies (MF2, MF3, MF5, MF6 and MF7) are dominated by mouldic and interparticle pores. Microfacies MF3 and MF6, which are rich in chambered fossils (e.g. benthic foraminifera, bryozoan etc.), additionally have a high abundance of intraparticle pore space. The pore types present tend to reflect the grain types, abundance of matrix, mineral stability and diagenetic evolution of each microfacies.

Microfacies with high abundance of echinoderm fragments commonly show extensive syntaxial calcite cementation of primary interparticle pores. Microfacies with terrigenous quartz tend to have open fractures and interparticle pore space. The volumetrically most important pore types are primary interparticle- and secondary mouldic macro-pores (Figure 4.61). However, most pores are infilled with ferroan and non-ferroan calcite cements.

Micro-facies	Microfacies name	Location			Pore type	
		JF	NFS	GS	Dominant	Minor
MF1	Pelagic Mudstone/Wackestone	X			MO	WP
MF2	Bivalve-Echinoderm-Peloidal Pack-/Grainstone	X	X	X	BP, MO	WP
MF3	Miliolid-Orbitolina-Peloidal Pack-/Grainstone	X			BP, WP	MO
MF4	Silty-Peloidal Pack-/Grainstone	X			MO	BP, WP
MF5	Intraclastic-Peloidal-Echinoderm Grainstone	X			BP, MO	
MF6	Bioclastic-Peloidal Pack-/Grainstone	X			MO, WP	
MF7	Red algae-Peloidal-Echinoderm Grainstone	X			BP,MO	WP
MF8a	Spiculitic-Peloidal Wackestone/Packstone	X			MO	
MF8b	Spiculitic-Peloidal Packstone	X	X		MO	WP
MF9	Peloidal Wacke-/Packstone			X	MO	
MF10	Foraminifera-Echinoderm-Peloidal Packstone			X	MO, WP	BP

Figure 4.61: Distribution of pore types within the studied microfacies and localities. Abbreviation: JF = northern J.Fadeloun section, NFS = northern J.Fadeloun section, GS = J.Garci section, BP = Interparticle porosity, MO = Mouldic porosity and WP = Intraparticle porosity.

4.8.4.2 Porosity and permeability

Plug-measured permeabilities and porosities are presented in Table 4-7. Tiny-Perm permeabilities and image analysis porosities are given in Appendices B and C. The data are plotted in Figure 4.62, and the total porosity distributed by microfacies is given in Figure 4.63.

Table 4-7: Porosity, permeability and grain density from plug measurements.

Plug Measurements				
Sample	He-Porosity (%)	Permeability (K _i) (mD)		Grain density (g/cm ³)
		Vertical	Horizontal	
JF-56S	2.52	<0.1	<0.1	2.71
JF-16S	0.91	<0.1	<0.1	2.70

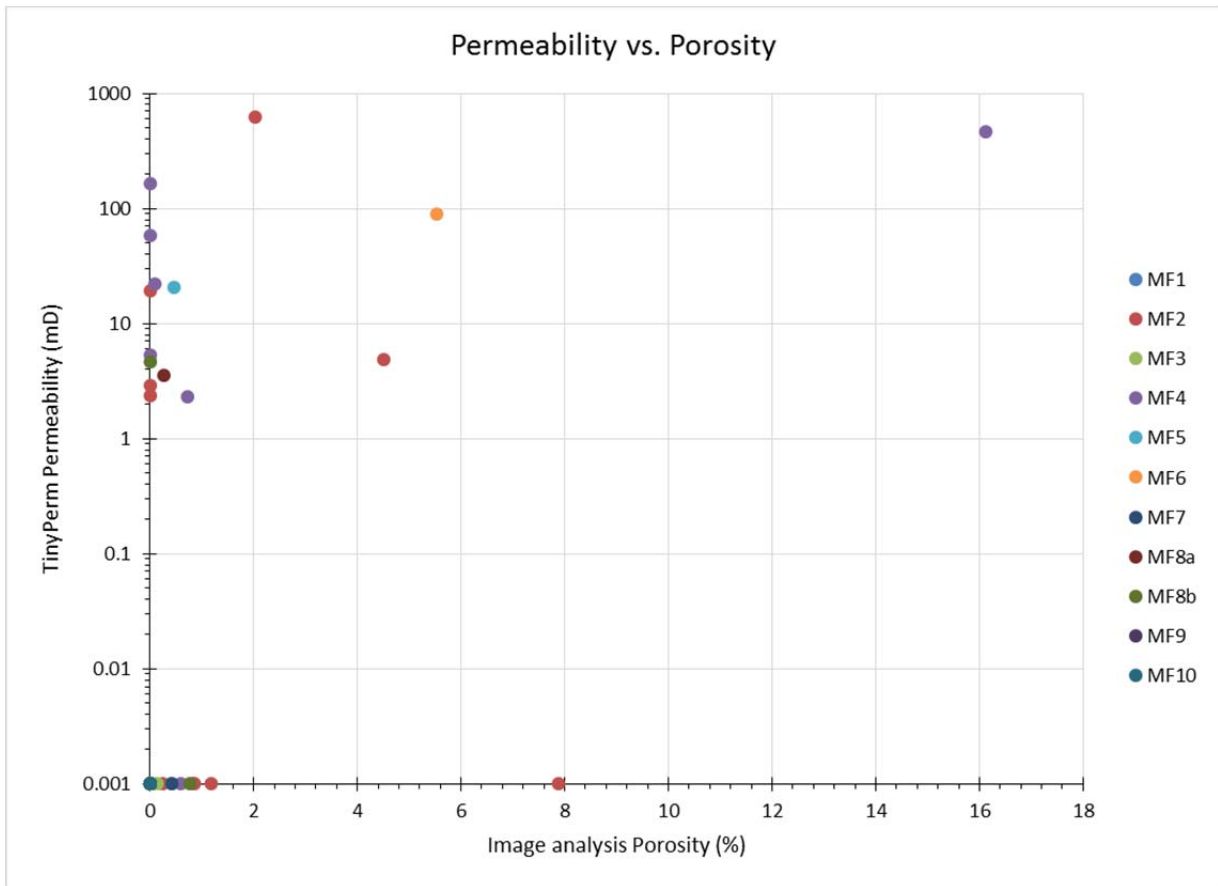


Figure 4.62: TinyPerm permeability vs. image analysis porosity for all microfacies within southern J.Fadeloun, northern J.Fadeloun and J.Garci. Very high permeabilities (>200 mD) probably indicate the presence of open fractures (Chapter 5.4). Note that permeabilities are presented as average values for lateral measurements within each bed (six samples within each bed, with ca. 5 meter lateral separation between each sample).

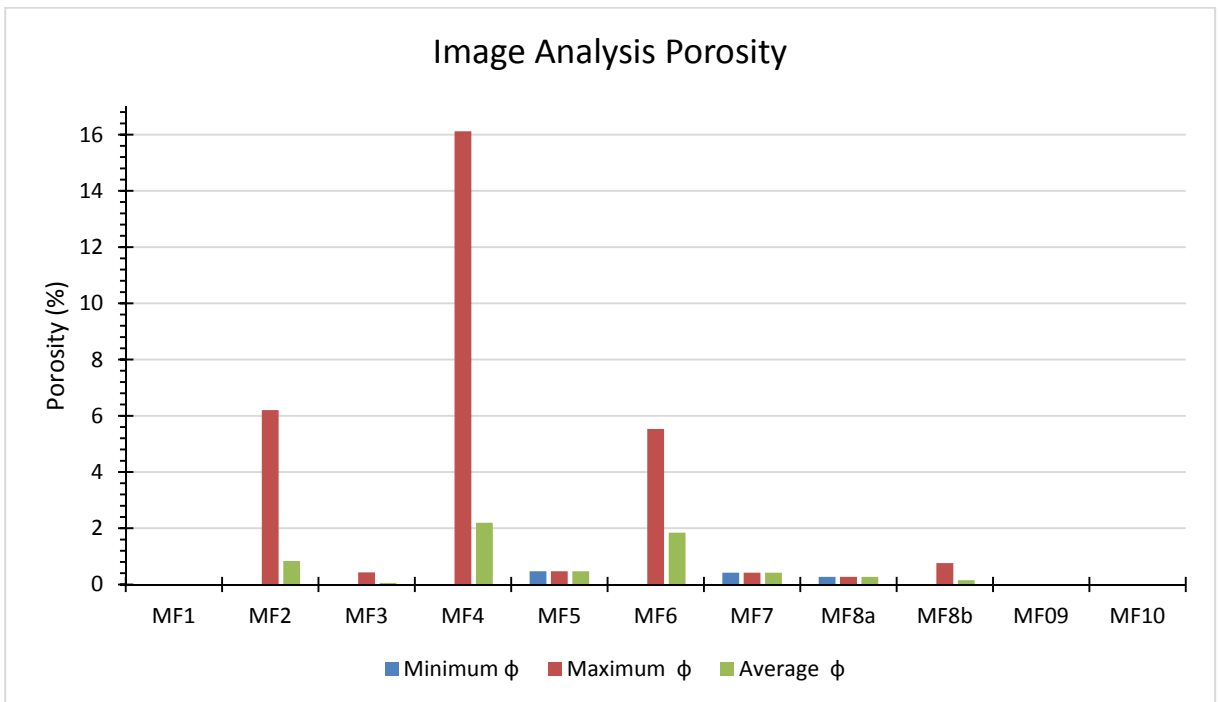


Figure 4.63: Distribution of porosity given as a percentage of total porosity by microfacies (e.g. 35% of the open pore volume occurs within MF4). Φ = Porosity.

Image analysis was performed on all thin sections in order to estimate the average porosity and the dominant pore type. Based on the dominant pore type and the estimated porosity, permeability predictions were carried out for each sample using the permeability vs. porosity cross-plots developed by Lønøy (2006) (Figure 4.64 and Figure 4.65). The estimated porosity and permeability, together with predicted permeability values are presented in Table 4-8.

Figure 4.66 to Figure 4.69 and Table 4-8 show that there is no or poor agreement between measured and predicted permeabilities, based on predictions from Lønøy's (2006) equations. The relatively high measured TinyPerm permeabilities, even at low porosities, do not make sense, and measured porosity-permeability relationships are only comparable to connected vug systems and/or fractured samples (Lønøy, 2006). It is thus reasonable to believe that the TinyPerm measurements are either affected by open fractures or by measurement errors caused by gas leakage. In fact, several open fractures have been observed in many of the thin sections. The measured plug permeabilities are reported to be $<0.1\text{mD}$ (apparently the lower limit of permeability detection reported by the laboratory), and may therefore correspond to predicted values.

The prediction cross-plots developed by Lønøy (2006) do not include circum-granular cracking, and samples JF-27S and JF-42S were therefore excluded from Figure 4.66 to Figure 4.69.

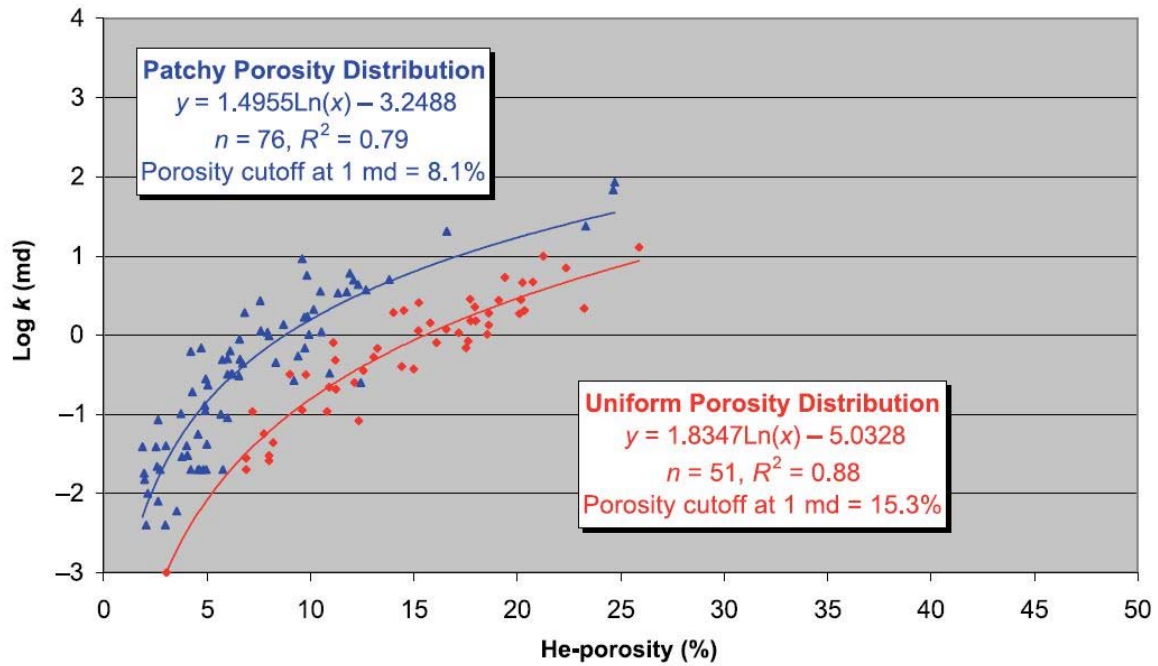


Figure 4.64: Permeability vs. interparticle microporosity cross-plot. After Lønøy (2006). This is one of the dominant pore types in the Serdj Fm.

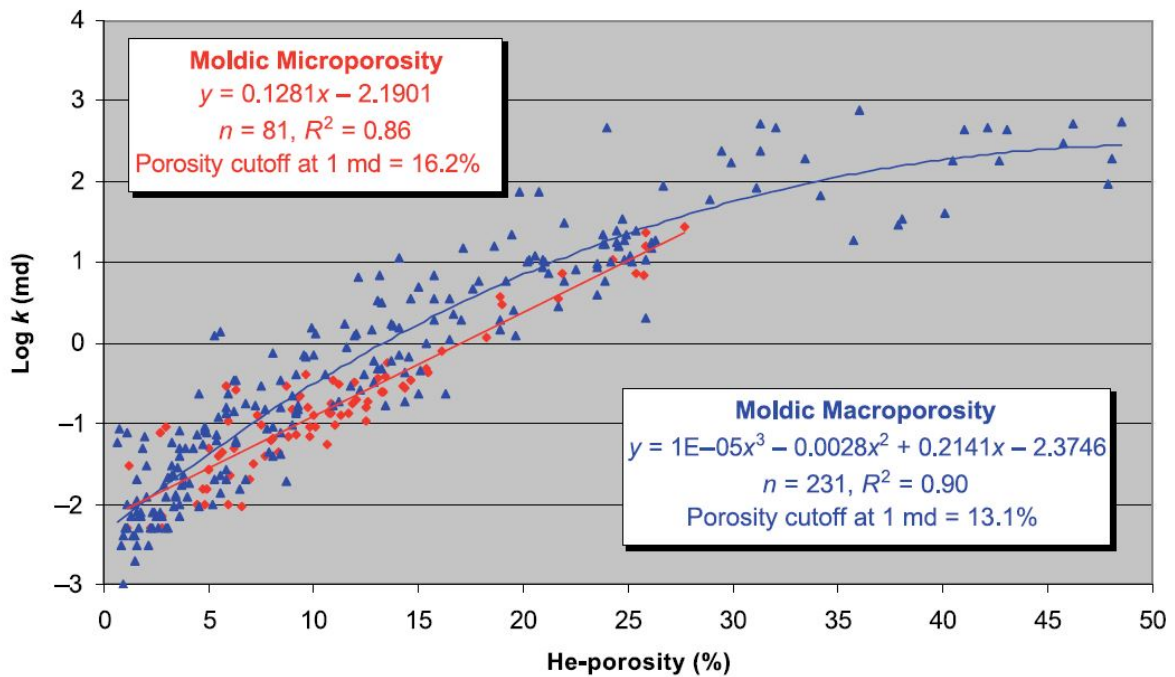


Figure 4.65: Permeability vs. mouldic porosity cross-plot. After Lønøy (2006). This is one of the dominant pore types in the Serdj Fm.

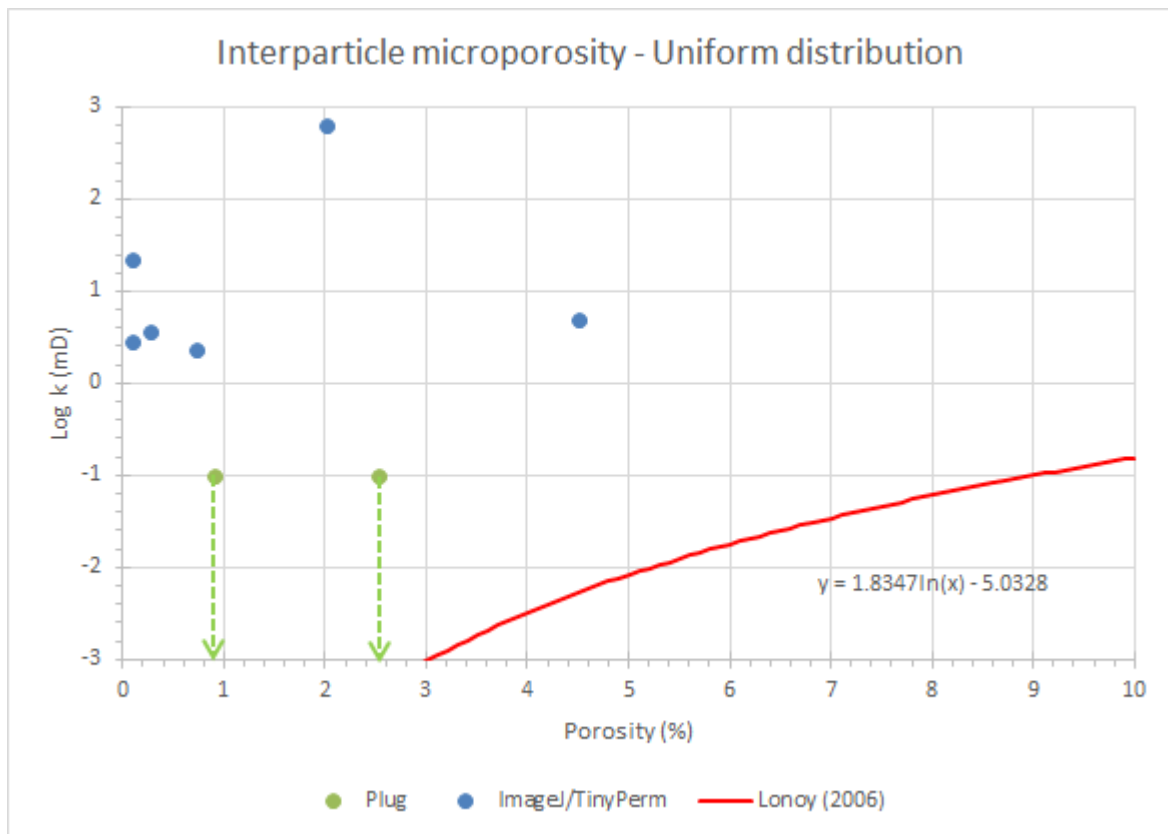


Figure 4.66: Permeability vs porosity for interparticle micropores with uniform distribution at the southern J.Fadeloun locality. Only six samples have both permeability and porosity values available. Note that the plug permeability was reported to be <0.1mD. The green dashed lines show the possible range of the measured plug permeabilities. There is no clear relationship between measured permeabilities and the permeabilities predicted from Lønøy (2006) equation.

The relatively high measured TinyPerm permeabilities, even at low porosities, do not make sense, and measured porosity-permeability relationships are only comparable to connected vug systems and/or fractured samples (Lønøy, 2006). It is thus reasonable to believe that the TinyPerm measurements are either affected by open fractures or by measurement errors caused by gas leakage. In fact, several open fractures have been observed in many of the thin sections.

Measured plug permeabilities are reported to be <0.1mD, and may therefore correspond to predicted values (green dashed lines).

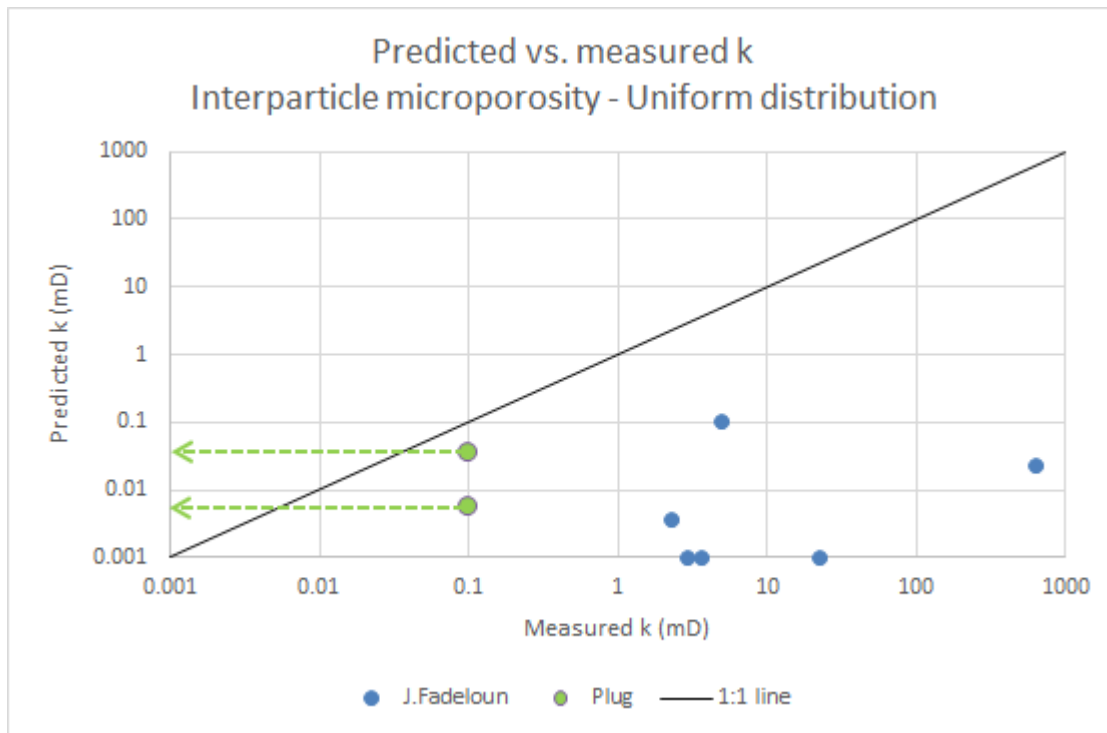


Figure 4.67: Predicted (based on Lønøy, 2006) vs. measured permeability for uniformly-distributed interparticle micropores. Please see Figure 4.66 for additional comments regarding plotted plug permeabilities and deviation between measured and predicted permeability values. Green dashed lines = possible plug permeability range (reported to <0.1mD by laboratory).

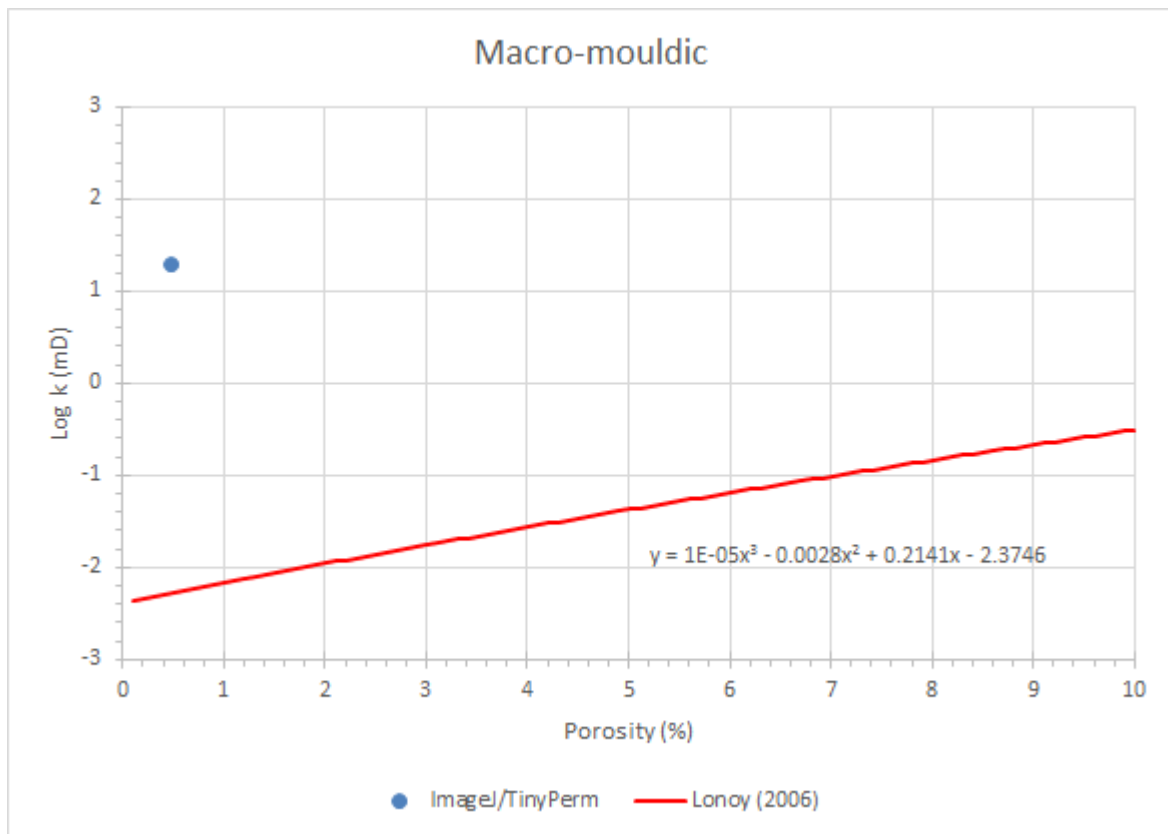


Figure 4.68: Permeability vs porosity for macro-mouldic porosity at the southern J.Fadeloun locality (only one sample).

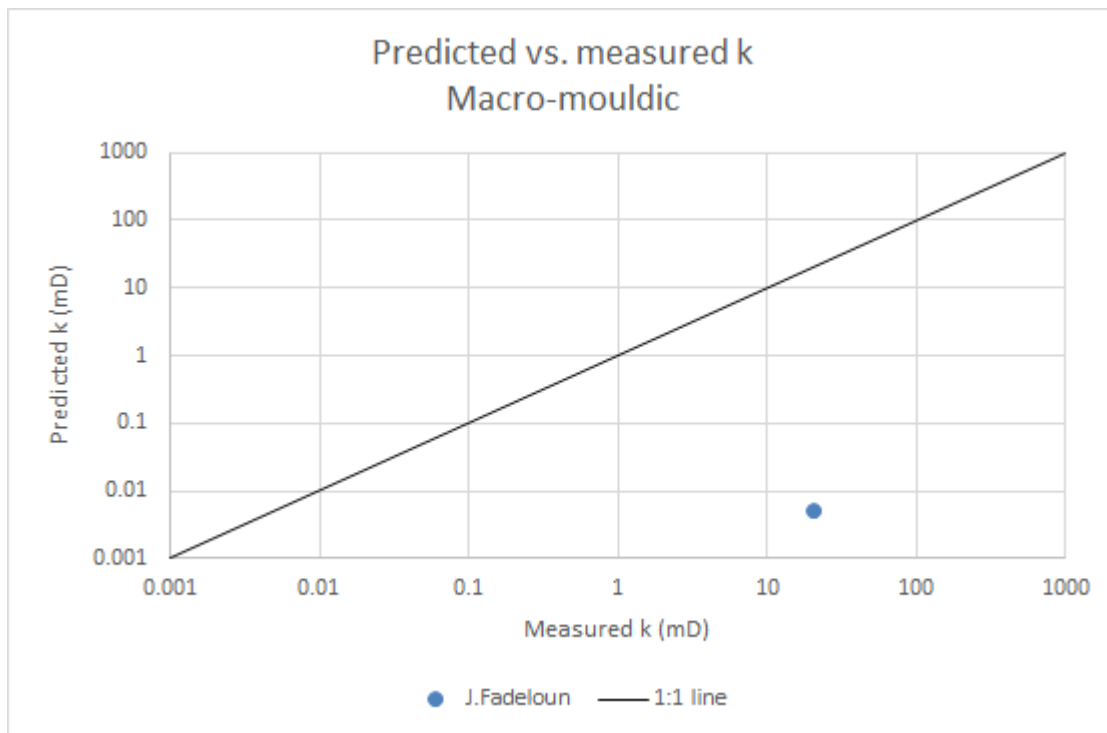


Figure 4.69: Predicted (based on Lønøy, 2006) vs. measured permeability for macro-mouldic porosity (only one sample).

Table 4-8: Sample overview with associated measured image analysis porosity and TinyPerm permeability, and predicted permeability values (Lønøy, 2006). Reported TinyPerm permeabilities of 0.00mD refer to measurements where no flow was recorded within the time-frame of the measurement. Measured permeabilities Red numbers represents measured permeabilities that can only be explained by open fractures, connected vugs or measurement errors (pers. comm. A. Lønøy, 2015). * MO = Mouldic; BP = Between-particle (interparticle); CGC = Circum-granular cracking.

Porosities, Permeabilities and Pore Types				
Sample	Image analysis porosity (%)	TinyPerm permeability (mD)	Predicted permeability (mD)	Dominant pore type*
JF-86S	0.42	0.00	0.0052	Macro MO
JF-78S	0.47	20.50	0.0053	Macro MO
JF-71S	1.18	0.00	0.0088	Micro BP
JF-70S	0.84	0.00	0.0047	Micro BP
JF-64S	0.14	0.00	0.0002	Micro BP
JF-56S	0.60	0.00	0.0026	Micro BP
JF-54S	0.73	2.29	0.0037	Micro BP
JF-51S	4.50	4.88	0.1030	Micro BP
JF-50S	2.02	623.95	0.0237	Micro BP
JF-47S	0.09	22.22	0.0001	Micro BP
JF-45S	0.85	0.00	0.0048	Micro BP
JF-42S	16.12	461.21	1.0701	Micro BP/CGC
JF-37S	6.20	0.00	0.1854	Micro BP/CGC
JF-36S	0.76	0.00	0.0039	Micro BP/CGC
JF-27S	5.53	88.63	0.1503	Micro BP/CGC
JF-26S	0.10	0.00	0.0001	Micro BP
JF-24S	0.10	2.87	0.0001	Micro BP
JF-22S	0.43	0.00	0.0014	Micro BP
JF-17S	0.10	0.00	0.0001	Micro BP
JF-11S	0.27	3.59	0.0006	Micro BP

5. Discussion and summary

This chapter discusses the results presented in Chapter 4 with respect to depositional environments, diagenetic history and reservoir properties. The depositional environments of the three studied sections are reviewed, and their diagenetic history is presented. The reservoir quality of the Serdj Fm. is evaluated, and the reservoir potential of the Fkirine permit is discussed. Suggestions for further studies are presented.

5.1 Depositional environment

The evaluation of depositional environments within the studied area is mainly based on detailed sedimentological logging, microfacies associations, geochemical analysis and mapping of sedimentary surfaces. The depositional environment for each section (J.Fadeloun and J.Garci) is presented separately, and the possibility of merging the southern- and northern J.Fadeloun log into one composite log is discussed.

5.1.1 Jebel Fadeloun

The J.Fadeloun section consists of a tectonically folded carbonate ramp outcropping in an anticline, and is characterized by limestones with alternations between massive limestone beds and more loosely consolidated mixed siliciclastic-carbonate beds (often highly eroded and covered by debris). The studied section consists of extensively faulted and fractured wackestones, packstones and grainstones and is part of the eastern limb of the anticline.

In the literature, several terms are used to describe climate-related grain assemblages. The descriptive terms applied in this work are heterozoan and photozoan, as described by Lees and Buller (1972). The faunal composition of the Aptian section at J.Fadeloun and J.Garci is consistent with a heterozoan faunal assemblage, being dominated by foraminifera, molluscs, bryozoans, red algae, echinoderms, ostracods and sponges. Stable isotope analyses of oxygen show paleotemperatures of ambient sea water ranging between 13 and 17°C (Chapter 4.6.1), indicating temperate waters (<20°C). All this is consistent with literature descriptions of temperate carbonate ramp settings (James, 1997). However, even though several features

suggest a heterozoan association, peloids and ooids are commonly indicative for the photozoan association and elevated oceanic salinities (Lees, 1975; James, 1997). Ooids are absent in the studied sections, but are in the literature observed and described for Aptian deposits at other localities (Lehmann et al., 2009). The combination of heterozoan and photozoan associations could thus indicate temperature fluctuations.

Carbonate ramps are commonly subdivided into inner- mid- and outer ramp settings on the basis of water depth, wave energy, depositional processes and facies characteristics (Burchette and Wright, 1992). The inner ramp is defined as the part of the ramp profile that is above the fair weather wave-base (FWWB) and is often associated with lagoonal-, tidal flat-, sabkha- and strand plain settings. This part of the ramp may have a wide range of sedimentary textures but are often dominated by grain-supported textures. The mid-ramp is often associated with thin-bedded storm deposits and/or mud mounds, and comprises the part of the ramp profile between FWFB and the storm wave-base (SWM). This part of ramp is commonly characterized by mud-supported textures. The outer ramp extend out to the basin plain and is associated with pelagic limestones and marls deposited below the SWM (Burchette and Wright, 1992; Flügel, 2004).

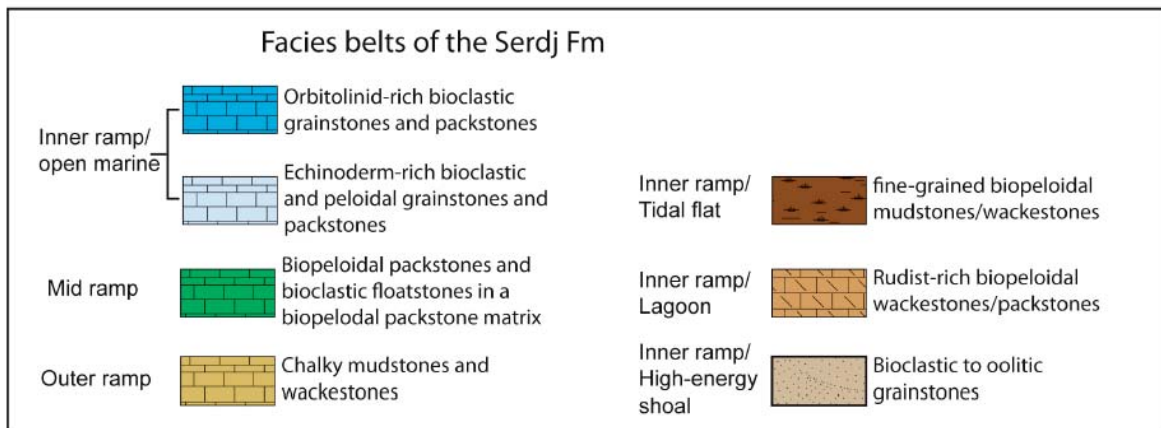
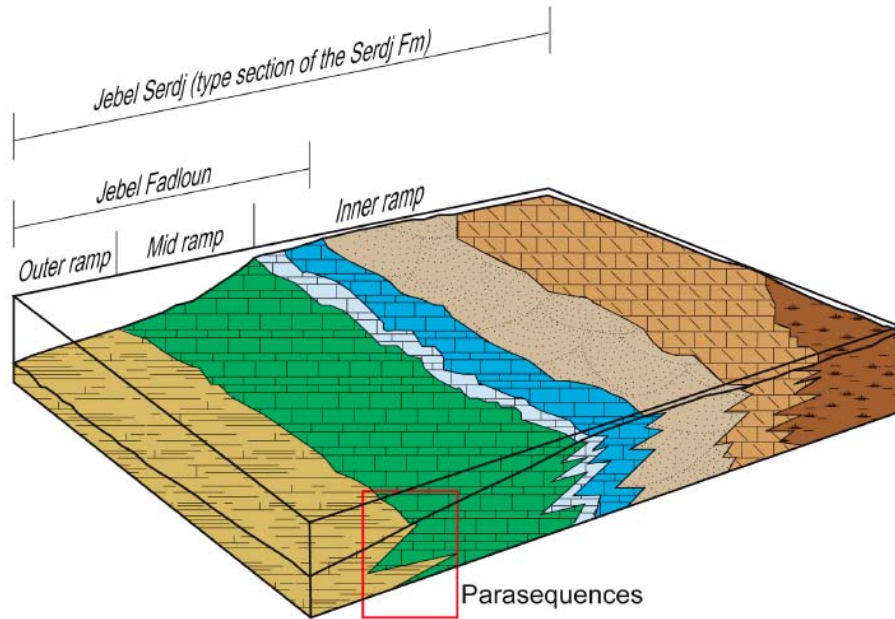


Figure 5.1: Depositional model for the Serdj Fm. Note that the J.Fadeloun succession only contains the more distal facies of the depositional system (from inner ramp/open marine to outer ramp), whereas Jebel Serdj represent the type locality and include all of the Serdj Fm. (from inner ramp/high energy shoal to outer ramp). Figure after Spalluto (2012).

5.1.1.1 Inner-ramp

The inner-ramp setting of J.Fadeloun is dominated by packstones and grainstones with high abundances of bivalve fragments, benthic foraminifera, echinoderm fragments and peloids (Figure 5.1). In units A, B, C and D the inner ramp is represented by packstones and grainstones of MF2, MF3, MF4, MF5 and MF6, and contains significant amounts of intraclasts (only MF5), miliolids, orbitolinids, bivalves, echinoderm fragments and peloids. Unit E is interpreted to be a repetition of top Aptian/base Albian, as it shifts from outer ramp

deposits characterized by Albian wackestones (MF1) into Aptian inner ramp deposits characterized by MF2 and MF7 (see discussion in chapters 4.2.1 and 5.1.1.5). Unit E thus does not represent a chronological correct shallowing upwards sequence, but represents a repetition of top Aptian/base Albian.

The rich and diversified heterozoan faunal assemblage of the inner ramp packstones and grainstones indicate deposition in relative open waters (Lees and Buller, 1972; James, 1997). The few observed coral fragments observed in MF3 of Unit A may be derived from patch reefs developed in back-barrier lagoons. Extensive and continuous reef complexes are commonly absent in carbonate ramps (Tucker and Wright, 2009). The low abundance of coral fragments, heterozoan faunal assemblage and $\delta^{18}\text{O}$ isotope derived temperatures, indicate that the inner ramp setting of the Serdj Fm. at J.Fadeloun comprise open, temperate-water carbonates (Lees and Buller, 1972; James, 1997; Tucker and Wright, 2009).

5.1.1.2 Mid-ramp

The mid-ramp setting of J.Fadeloun is dominated by wackestones and packstones (MF8a and MF8b) with high abundance of calcispheres, sponge spicules and peloids, and minor intraclasts and benthic foraminifera (miliolids and orbitolinids). The presence of miliolids and orbitolinids, commonly indicative of inner ramp deposits (Kalantari, 1986; Flügel, 2004), mixed with intraclasts and grains typical for outer ramp settings, could indicate deposits proximal to the slope break (mid-ramp) in a distally steepened ramp.

5.1.1.3 Outer-ramp

Albian deposits are represented by outer-ramp facies at J.Fadeloun, as discussed in Chapter 4.2.1. These deposits were not the focus of this study, and were only included to establish the Aptian/Albian boundary.

5.1.1.4 Depositional trends

Microfacies associations and grain size distributions (Figure 5.2 and Figure 4.24) define four shallowing upward cycles related to relative sea level fluctuations. These cycles correspond to the four lowermost units (A-D).

Carbonate ramps experience rapid shifts of facies belts during minor relative sea level fluctuations, due to their gentle slope (typically $<1^\circ$). A minor fall in sea level will shift inner ramp facies belts basinwards in a “forced regression”, possibly associated with a reduction in carbonate production due to reduced accommodation space on distally steepened ramps (Burchette and Wright, 1992). Drop in sea level may also be associated with subaerial exposure of the former inner ramp deposits, possibly exposing the sediment to meteoric water and associated diagenesis.

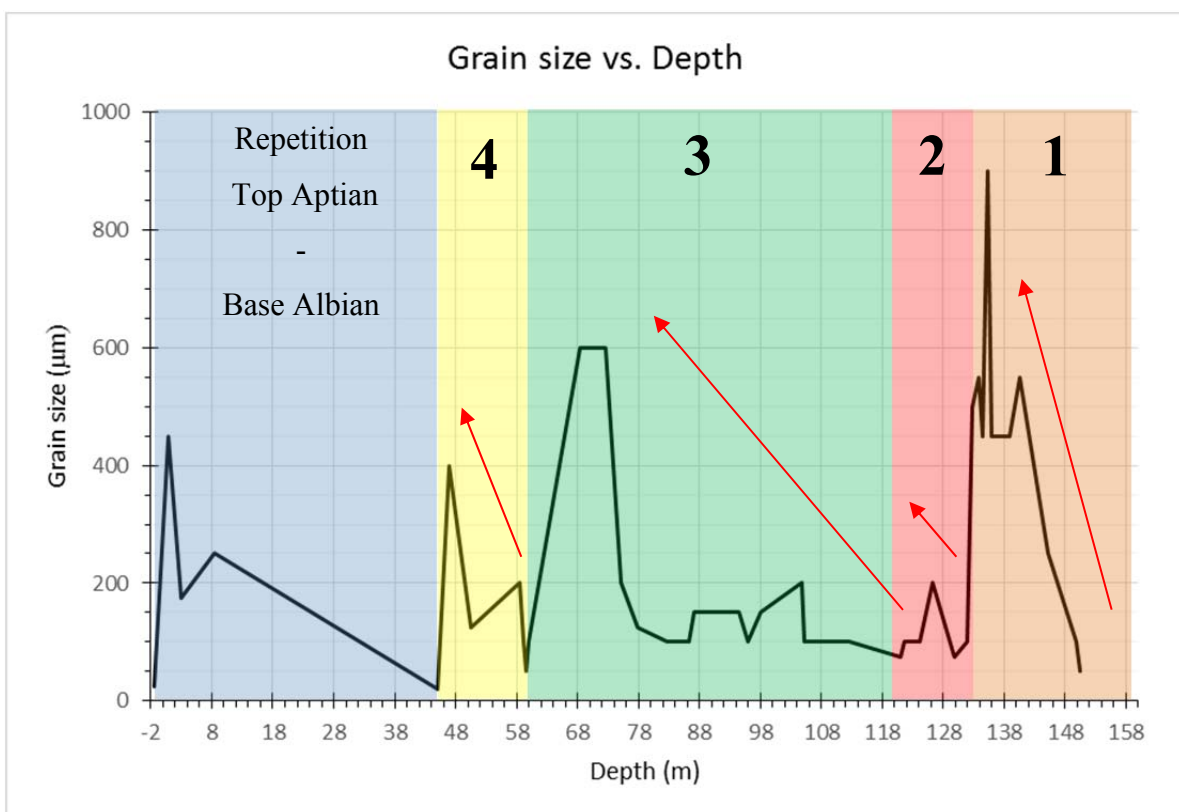


Figure 5.2: Grain size vs. Depth plot showing four shallowing upward sequences (numbered 1 to 4). Zero depth (0m) represents base Albian. The purple area shows the repetitive sequence of top Aptian and base Albian.

The oldest shallowing upwards cycle, represented by Unit A, shows a transition from mid- to inner ramp deposits, and is capped by a subaerial exposure surface and paleosol. The paleosol and karst may potentially be related to post-Aptian processes, as no dating is available. However, their presence within the uppermost part of the shallowing upward cycle suggests a development during the Aptian.

Karst caves observed at northern J.Fadeloun show horizontal alignment typical for caves developed in the upper part of the phreatic zone (Figure 4.32). The karst surface in southern J.Fadeloun seems to represent a lateral continuation of the karst caves at northern J.Fadeloun, and may represent reduced karstification towards the south.

Overlying Unit A there is a second shallowing upwards cycle represented by Unit B. This shows a transition from mid- to inner ramp deposits, as in Unit A, but with no observed subaerial exposure. This cycle is relatively thin compared to underlying and overlying cycles.

Unit C forms the third shallowing upward cycle and shows a transition from mid- to inner ramp deposits, interbedded with riverine or eolian-derived quartz. A few beds show development of fenestral structures, probably formed by expulsion of gas on a tidal flat or in the shallow subtidal. The presence of circum-granular cracking (Figure 4.25) and pendant cement (Figure 4.49) indicate periodic subaerial exposure of the ramp, with vadose diagenesis and development of a paleosol. The relatively thick inner ramp and thin mid ramp deposits may reflect strong progradation of the ramp due to low accommodation space (Burchette and Wright, 1992; Moore, 2001)

The uppermost shallowing upward cycle, represented by Unit D, shows a transition from mid/inner- to inner ramp deposits with a gradual coarsening upward trend. The top of the cycle shows early marine cementation, typically occurring in shallow agitated waters near the sediment-sea water interface. Shallow agitated waters are supported by the abundance of intraclasts. The cycle marks the end of the Aptian sequence, and is capped by Albian deposits.

5.1.1.5 Repetition of top Aptian/base Albian

The isotopic signature of samples JF-87S (Unit F) and JF-80S (Unit E) in the southern J.Fadeloun section shows $\delta^{18}\text{O}$ and $\delta^{13}\text{C}$ isotopic compositions which deviate from those of Aptian age. The isotopic composition in association with texture, faunal assemblage and

geological map (Figure 1.2), suggest that the samples could be Albian of age. The samples below JF-80S and between JF-80S and JF-87S, show $\delta^{18}\text{O}$ and $\delta^{13}\text{C}$ isotopic compositions (Table 4-1) and microfacies associations that are similar to other inferred Aptian-age samples. Aptian samples (below JF-80S and between JF80S and JF87S) show minor variation in composition, but are by and large similar. Taking all observations into consideration it is reasonable to assume that the Aptian sequence ends after Unit D and that units E represents a repetition of the top Aptian/base Albian.

5.1.1.6 Correlation

An attempt was made to combine the southern and northern J.Fadeloun sections. The base of the southern section has a microfacies association that is somewhat similar to the top of the northern section, and mid-ramp deposits represented by MF8a and MF8b are restricted to these parts of the sections.

$^{87}\text{Sr}/^{86}\text{Sr}$ analyses could give an indication of correlative beds. However, the Sr-isotopes are all higher than expected for Aptian and Albian oceanic values (McArthur et al., 2001), and a radiogenic source must be responsible for the discrepancy. The radiogenic strontium could have been brought in together with terrigenous quartz during sea-level lowstands, and may also have accumulated in the meteoric cements. Thus, the reported ages were not useful for correlation

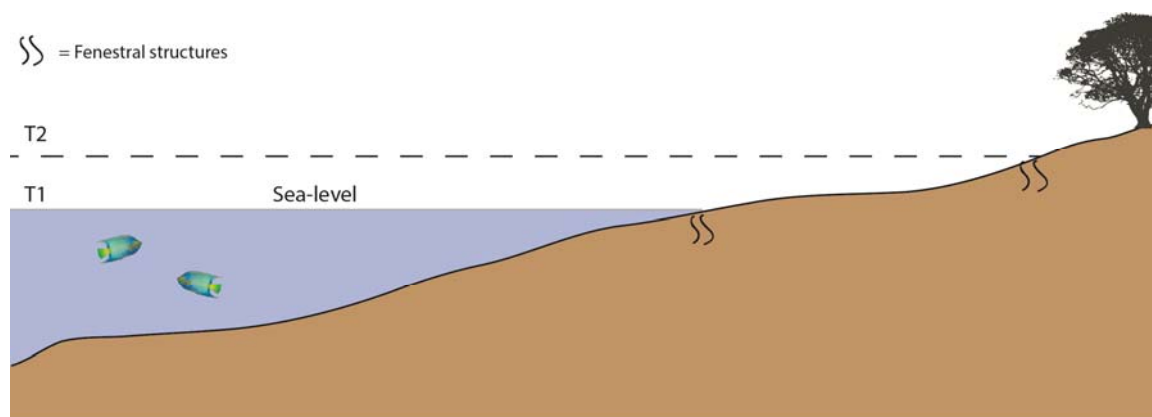


Figure 5.3: Sketch of a ramp profile showing fenestral structure distributions during a relative sea-level rise. The fenestral structures at initial sea-level (T1) shift landwards during the relative sea-level rise (T2). Note that scales are highly exaggerated.

Beds with fenestral structures observed at the base of the southern section and at the top of the northern section may represent marker beds for correlation. However, even though the distance between the southern and northern sections is only ca. 600m, correlation based on fenestral structures may be uncertain as the structures may have formed during different times of the ramp development. Changes in relative sea-level rise may impose lateral shifts of depositional environments, as illustrated in Figure 5.3.

Karst surfaces are developed in Lower Aptian limestones of both the southern and northern sections and their development could represent time-equivalent events. However, they might relate to post-Aptian karstification.

There is no single feature that clearly correlates the northern and southern sections. However, combined observations suggest that the northern section can be correlated to the lower part of the southern section.

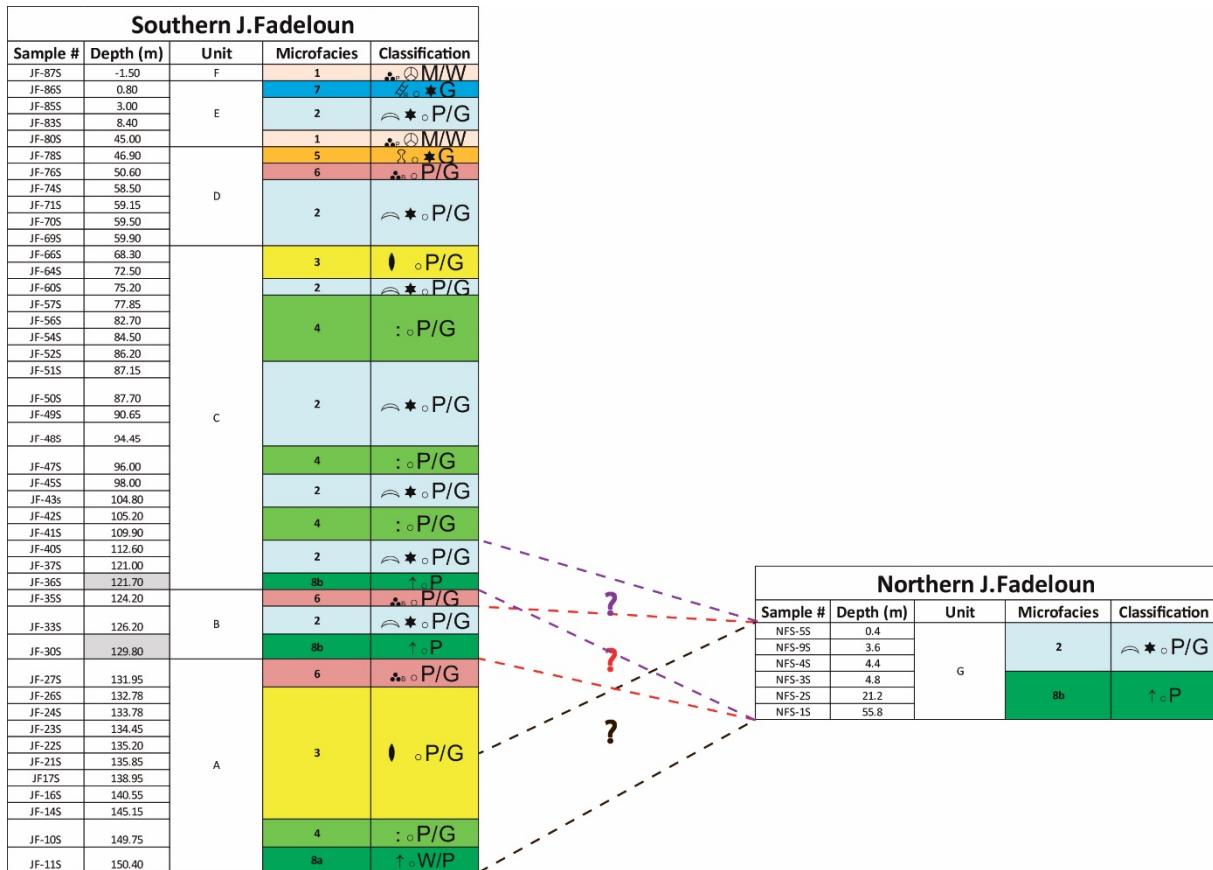


Figure 5.4: Lithostratigraphy of the southern and northern J.Fadeloun sections. MF8 is restricted to the lower part of the Serdj Fm., suggesting that the northern J.Fadeloun sections most likely correspond to the lowermost part of the southern J.Fadeloun section. Dashed lines show three potential correlations, and is based on microfacies distribution. The lowermost proposed correlation is also based on possible correlative karstification. Colour coding represents different microfacies. Symbols are presented in Appendix WellCAD logs

5.1.2 Jebel Garci

The studied J.Garci section (6m thick) consists of a condensed Aptian section, characterized by fine-grained limestones in a mid- to outer ramp setting. The deposits alternate between outer ramp/basinal and mid-outer ramp deposits. A mixture of grains typical for inner ramp settings (especially miliolids) and grains typical for outer ramp settings (planktonic foraminifera and calcispheres), suggest deposition below FWWB (Flügel, 2004). The Aptian sequence of the J.Garci section indicates a more distal depositional environment than in the J.Fadeloun section.

5.1.3 Paleotemperature, burial depth and age

Paleotemperatures

Paleotemperature for each sample was estimated by using Equation 4-1, and all paleotemperature ranges are presented in Figure 4.54. Because stable isotope compositions were based on bulk samples, the compositions and calculated temperatures are affected by grains, matrix and cements.

Marine calcite cement is commonly indicative of early diagenesis (as discussed in Chapter 4.5.2) and would probably have an oxygen isotopic composition close to, but not necessarily identical to, that of the grains.

Equant non-ferroan calcite cement is considered to have formed at shallow burial, and precipitated either from modified marine and/or meteoric waters. The effect of these cements on the bulk isotopic compositions and the calculated paleo-temperatures can vary.

Late diagenetic ferroan calcite cement is probably precipitated at elevated temperatures and would therefore have a more significant impact on the bulk oxygen isotopic composition and on calculated temperatures. Prediction of the paleo sea water temperature should therefore preferentially be based on samples where ferroan calcite cements are absent, and on micritic samples (low content of non-ferroan calcite cement). Unfortunately, most Aptian samples have grain-supported textures and therefore generally have some non-ferroan calcite cement that may bias the results. Assuming that the pore fluids are derived from modified marine water during compaction, the early diagenetic cements would tend to give slightly too high calculated sea water temperatures. If the non-ferroan calcite cement precipitated from meteoric water the calculated sea water temperatures may also be too high.

Excluding samples containing ferroan calcite cement, and assuming that the non-ferroan calcite cement has insignificant effect on the bulk isotopic composition, the calculated sea water temperature ranges from 13-17 °C (Figure 4.55). This suggests deposition in a temperate waters setting.

Samples with low content of ferroan calcite cement generally show lower calculated sea water temperatures than for samples with high ferroan calcite content. This reflects a lighter oxygen isotopic composition of the ferroan-rich calcite cement, suggesting higher temperature during precipitation. This is supported by textural relationships indicating that the ferroan calcite

cement is a relatively late cement. Samples JF-35S, JF-57S and NFS-5S have calculated paleotemperatures within the lowermost part of the Aptian temperature range (Figure 4.54). This may relate to vital effects as some organisms (Weber, 1968; Baumiller, 2001), especially echinoderms, biologically concentrate the isotopically lighter isotopes ^{16}O and ^{12}C during shell secretion. However, the echinoderm distribution and abundance in the studied Serdj Fm. do not show any clear relationship to the oxygen isotopic composition.

Burial depth

Vitrinite analysis collected by Thibault Cavailhes (DNO International ASA) indicated a burial depth of 2500-3500m for the Serdj Fm., within the Fkrine permit (Cavailhes, 2015).

Estimated precipitation temperature for the Fe-rich calcite is 160°C (see Chapter 4.5.2). Using the present geothermal gradient of 40°C/km (Bathurst, 1966) and a surface temperature of 15°C (based on Aptian sea water temperature of 13-17°C, which is roughly similar to the present annual surface temperature, 18°C), the Fe-rich calcite precipitated at burial depths of ca. 3600m. This depth is close to the depth range derived from vitrine analyses.

Age

Strontium-isotope ages for the southern J.Fadeloun section range from 32 to 82Ma (Rupelian-Maastrichtian). The estimated ages of northern J.Fadeloun show a smaller age span, ranging from 71 to 76Ma (Maastrichtian-Campanian). No depth-related age trends are observed within J.Fadeloun. The J.Garci section shows ages ranging from 15 to 33Ma (Langhian-Rupelian), and unexpectedly shows progressively older age towards the top of the succession. This may be explained by tectonic inversion of the sequence, but is considered unlikely as no other indications of inversion have been observed.

The strontium isotope-derived ages deviate from the Aptian (113-125Ma), and must relate to an influx of strontium ^{87}Sr (McArthur, 1994). The $^{87}\text{Sr}/^{86}\text{Sr}$ dating method is based on sediments incorporating strontium from well-mixed ambient sea-water. Continental weathering supply the ocean with higher $^{87}\text{Sr}/^{86}\text{Sr}$, thus resulting in predicted ages to be younger than expected (McArthur, 1994). Thin-section studies show that several beds within the Aptian sections have input of terrigenous quartz, and precipitates within the test tubes

were reported during laboratory analyses. It is reasonable to assume that the input of fluvial and/or eolian sediments resulted in the apparently to young ages. The studied ramp probably faced open oceanic conditions, and combined with the fact that ramps commonly experience high wave energies in their proximal parts make it unlikely that the waters of the inner to mid ramp could have had Sr-isotope compositions significantly different those of the open ocean (Burchette and Wright, 1992; McArthur, 1994; Flecker and Ellam, 2006). It is more likely that significant amounts of radiogenic strontium could have been introduced during lowstand karstification.

5.2 Diagenetic evolution

Diagenetic studies of the J.Garci and J.Fadeloun sections are based on detailed petrographic and geochemical analyses. The diagenetic events may broadly be grouped into eogenetic (early stage - shallow burial), mesogenetic (intermediate stage - deep burial) and telogenetic (late stage - uplift) processes (Figure 5.5) (Choquette and Pray, 1970).

Microbial micritization of skeletal grains and precipitation of marine and syntaxial calcite cements are probably some of the first eogenetic processes affecting the sediment (Chapter 4.5.1). Syntaxial calcite cementation probably continued during progressive burial of the sediment, possibly into the mesogenetic realm (Chapter 4.5.2.1). Non-ferroan equant calcite cement precipitated during shallow burial, as indicated from petrographic studies and stable isotope analyses (Chapter 4.5.2.1), or from meteoric water during subaerial exposure (eogenetic or telogenetic).

Pendant cement is probably related to cementation within the fresh-water vadose zone after a relative drop in sea level, or during late telogenetic uplift which re-exposed the sedimentary rocks (Chapter 4.5.2.1).

Mouldic porosity formation is related to dissolution of carbonate grains, preferentially aragonitic grains. This type of dissolution is often associated with meteoric diagenesis (eogenetic and telogenetic), but can also form during burial diagenesis. The formation of mouldic porosity commonly relates to differences in mineral solubility, maturation of organic material and shale dewatering.

Ferroan equant calcite cement precipitated during deep burial (chapters 4.5.2 and 5.1.3). The precipitation takes place by uptake of Fe^{2+} from connate waters, and continues as long as Fe^{2+} is available (Chapter 4.5.2.1). Later dissolution of the ferroan calcite relates to uplift and exposure to the meteoric environment (telogenetic), possibly during present day exposure. Under-saturated freshwater is highly aggressive and dissolution starts immediately after exposure (Flügel, 2004).

Dissolution seams form by physical and chemical compaction at shallow depths, and develop at greater depths into stylolites by pressure-solution and recrystallization (Park and Schot, 1968; Choquette and James, 1987). Increased pressure along the grain or crystal contact during burial results in increased solubility along the contact zone, and stylolitization will increase proportionally with increased pressure. Stylolite orientation will reflect the stress direction. Compaction-related dissolution will therefore often show horizontal stylolite development.

Figure 5.6 summarizes and illustrates the relative sequence of diagenetic events in the Serdj Fm. at J.Fadeloun and J.Garci.

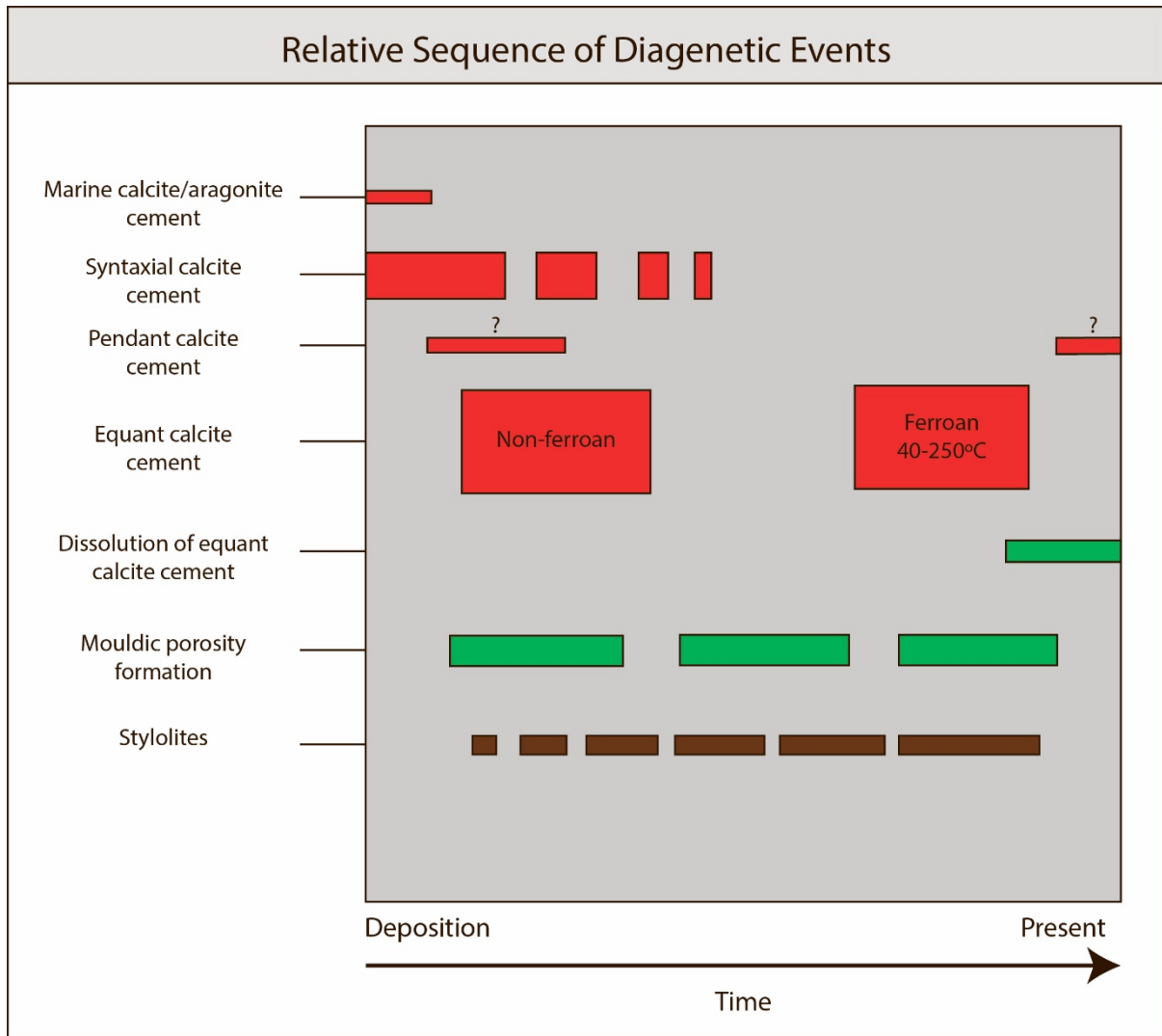


Figure 5.6: Relative sequence of diagenetic events. Red colour indicates porosity-destructive cementation. Green colour indicates porosity-enhancing dissolution. Bar thickness shows the relative importance of the different diagenetic events. Note that pendant calcite cement precipitated during subaerial exposure, either shortly after deposition of the sediment (eogenetic) or during later (present?) telogenetic diagenesis.

5.3 Diagenetic evolution in a sequence stratigraphic framework

Thick carbonate ramp successions can often be subdivided into sequences and para-sequences in order to define a sequence stratigraphic framework (Burchette and Wright, 1992). An attempt was made to establish the diagenetic evolution into a sequence stratigraphic framework. With no age dating available, the shallowing upward cycles and sedimentary surfaces are difficult to correlate between the two studied (uncondensed and condensed) sections. The sequence stratigraphic framework was therefore established mostly based on the uncondensed section (J.Fadeloun).

Due to the low slope angle of carbonate ramps, there will be only minor changes in ramp microfacies between sea-level high-stand (HST) and low-stand (LST) systems tracts (Burchette and Wright, 1992). A 3rd order sea-level fall exceeding the depth of the FWWB is necessary for inner ramp deposits of a relative LST to be completely separated from those of a previous HST. This further complicates sequence stratigraphic evaluation of carbonate ramps, and may explain why so few sequence boundaries have been observed within the studied Serdj Fm. Potential sequence boundaries observed at J.Fadeloun include paleosols and epigenic karst (Burchette and Wright, 1992).

The Serdj Fm. at J.Fadeloun consists exclusively of mid- to inner ramp microfacies (Chapter 5.1). The shallowing upward cycles (from mid- to inner ramp) indicate that deposition mostly took place during a HST. The presence of meteoric cements, karst cavities, the lack of evaporites, and the stable isotopic composition suggests deposition in a humid climate. Stable isotopic compositions in sea water dominated by evaporation are expected to be enriched in heavy isotopes, which is not the case for the Serdj Fm. The sequence boundaries represent periods of subaerial exposure during a LST, and are followed by flooding (transgressive system tract – TST). In J.Fadeloun there is virtually no difference in sedimentation (mid to inner ramp) above and below the sequence boundaries, indicating sea-level fluctuations less than the depth of the FWWB.

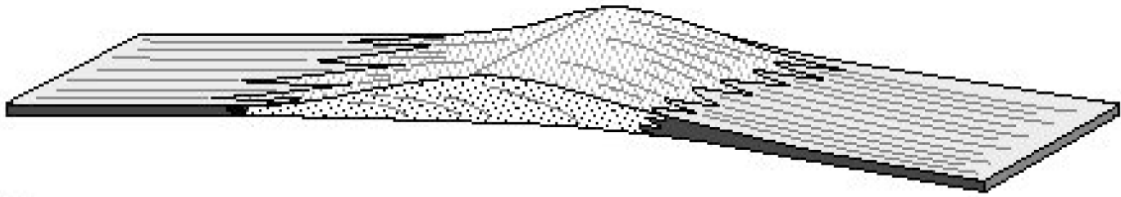
During the LST no or insignificant new accommodation space is generated. The generation of accommodation space first starts to accelerate during rising sea level (TST), and will progressively decelerate during the following HST. If there is sufficient sediment supply during the HST, there will be a strong progradation of the carbonate ramp due to low

accommodation space (Burchette and Wright, 1992; Moore, 2001), and sheet-like geometries are typically formed (Figure 5.7).

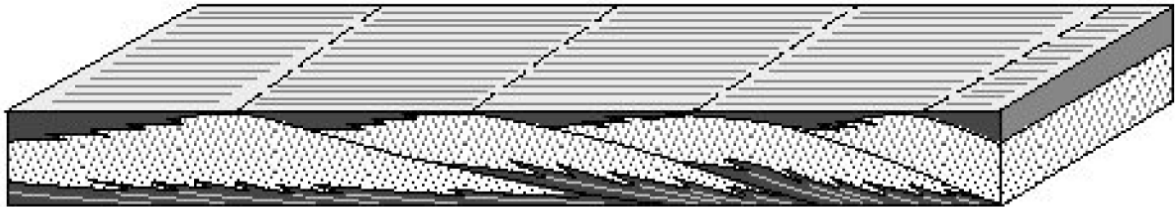
The hardground observed within the condensed section at J.Garci occurs at the Aptian-Albian transition. This may represent a maximum flooding surface during a transgressive system tract (TST), consistent with eustatic sea-level curves showing an Albian increase in eustatic sea level after a late Aptian sea-level low stand (Figure 2.9). Flooding surfaces on ramps are in general hard to detect, as they commonly are diachronous and fossil assemblage tend to migrate with their environment of formation (Burchette and Wright, 1992).

Diagenesis and associated porosity modifications during HST are controlled by the sedimentology, climatic setting and accommodation space, and are extremely variable (Moore, 2001). Due to the gentle slope of a ramp, fluctuations in relative sea level will develop several overlapping freshwater lenses. Significant parts of the ramp may thus be exposed to meteoric diagenesis (Moore, 2001). Meteoric diagenesis at J.Fadeloun seems to be concentrated to the sequence boundaries. The origin of the non-ferroan equant calcite cement is uncertain, but may be related to cementation in the fresh water phreatic zone. Minor diagenetic modification usually occurs within the vadose zone, and is only represented by pendant cement in J.Fadeloun. Porosity modification is commonly centered along the water table, and is typically associated with karstification, as seen in J.Fadeloun.

LINEAR STRING



SHEET



Carbonates International database

WEDGE

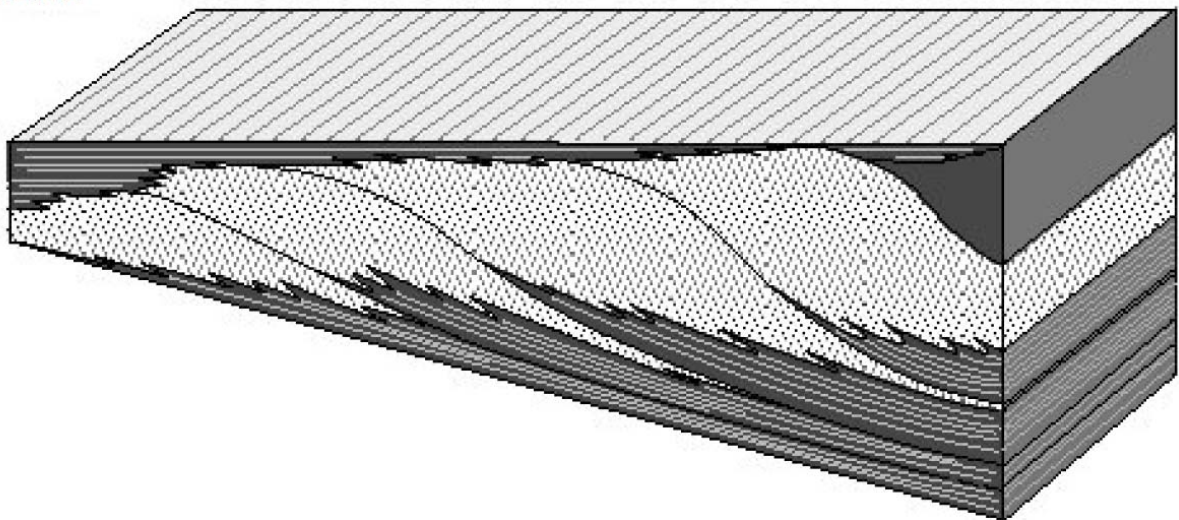


Figure 5.7: Linear strings: Individual carbonate sand shoals. Sheet-like geometries: Progradation of shoal complexes or linear strings of shoals in areas with reduced accommodation space. Wedge: Progradation of shoal complexes in areas with important variations in subsidence or accommodation space (Esteban et al., 1997).

5.4 Reservoir quality/potential

Carbonate ramp plays typically have subtle variations in reservoir quality and great opportunities for stratigraphical and structural trapping of hydrocarbons (Burchette and Wright, 1992). The wide facies distributions in carbonate ramps make them perfect sites for structural and halokenetic traps. Low-energy ramps commonly have a sparse distribution of potential reservoir facies, whereas high-energetic ramps typically have a wide range of potentially good reservoir facies (Read, 1985; Burchette and Wright, 1992). Grainstone reservoirs are commonly relatively thin and have a wide lateral extent. The proportion of reservoir to non-reservoir facies generally decreases basinwards as the proportion of deep marine facies increases (Burchette and Wright, 1992).

The Aptian section of J.Fadeloun is dominated by packstones and grainstones deposited in carbonate sand shoals on the mid- to inner ramp. The inner ramp of the J.Fadeloun probably reflects carbonate sand bodies formed along a high-energy shoreline, as the sedimentary sequences show a general coarsening upwards trend. The geometry of wave-dominated carbonate sand bodies on ramps varies from string-like to sheet-like depending on sediment influx and associated progradation. Wedge-like geometries normally do not develop due to limited accommodation space (Figure 5.7).

The porosity and permeability of the Serdj Fm. at J.Fadeloun and J.Garci are controlled by both depositional and diagenetic processes. Porosity estimates from image analysis and plug-measurements show that the J.Fadeloun section is dominated by porosities of 0-6% (Figure 4.63), and permeabilities of 0-88 mD (Table 4-8 and Figure 4.62). The J.Garci section shows virtually no porosity and permeability. Most microfacies within the Serdj Fm. show low porosities and permeabilities due to extensive micritization and cementation, and poor sorting (Chapter 4.5). In spite of the general poor reservoir quality of the studied sections, the Serdj Fm. may have some reservoir potential in a hydrocarbon-saturated scenario, as discussed below.

Figure 4.62 shows that the porosity in general is low, with most samples having a porosity <1%. Samples with poor reservoir quality commonly have high abundance of syntaxial calcite cement overgrowths and/or interparticle equant calcite cements (ferroan and/or non-ferroan). Most samples show a high permeability/porosity ratio that only fit the Lønøy (2006) porosity-permeability transform for vuggy pore systems. However, vugs are not observed in any of the

studied samples. The high permeability/porosity ratios in the Serdj Fm. can therefore only be explained in terms of open fractures or by TinyPerm measurement inaccuracies (gas leakage). Open and partly open fractures are frequently observed in outcrop and in thin sections. Only four samples show relatively high porosity and permeability, which are controlled by circum-granular cracking and/or mouldic porosity.

Microfacies containing high abundance of late-diagenetic equant ferroan calcite cement could potentially have good reservoir quality. Ferroan calcite cement constitutes as much as 15-20% of the total rock volume in some samples (Figure 4.44), giving a relatively high minus-cement porosity (Figure 5.8). If hydrocarbon migration predated the late-diagenetic cementation, the sediment may have significant porosities and permeabilities.

The late ferroan calcite is most abundant as cement infilling interparticle and/or mouldic pore space of inner ramp microfacies. Fractures in the outer ramp setting are commonly cemented by ferroan calcite (Figure 4.44), but the fractures may enhance permeability if cementation was stopped due to oil emplacement.

The studied outcrops at J.Fadeloun show large areas covered with scree. These areas could potentially have good reservoir quality, as porous carbonate rocks are more prone to weathering than non-porous carbonate rock. Shales and marls also easily weather, but these lithologies were not observed in the scree material. Scree-covered areas are commonly located within quartz-rich beds or within the uppermost part of Unit D. These areas may represent porous zones within the Serdj Fm. and could potentially have better reservoir quality than encountered within the more competent units.

Early marine and meteoric cementation could inhibit physical compaction during sediment burial (Tucker, 1993; Moore, 2001), and could thus preserve primary porosity. Even though the cementation reduces compaction, deep burial pressure dissolution will eventually reduce the porosity and permeability. Stylolites can act as barriers to vertical flow, but increased flow rates may sometimes be expected along stylolite surfaces.

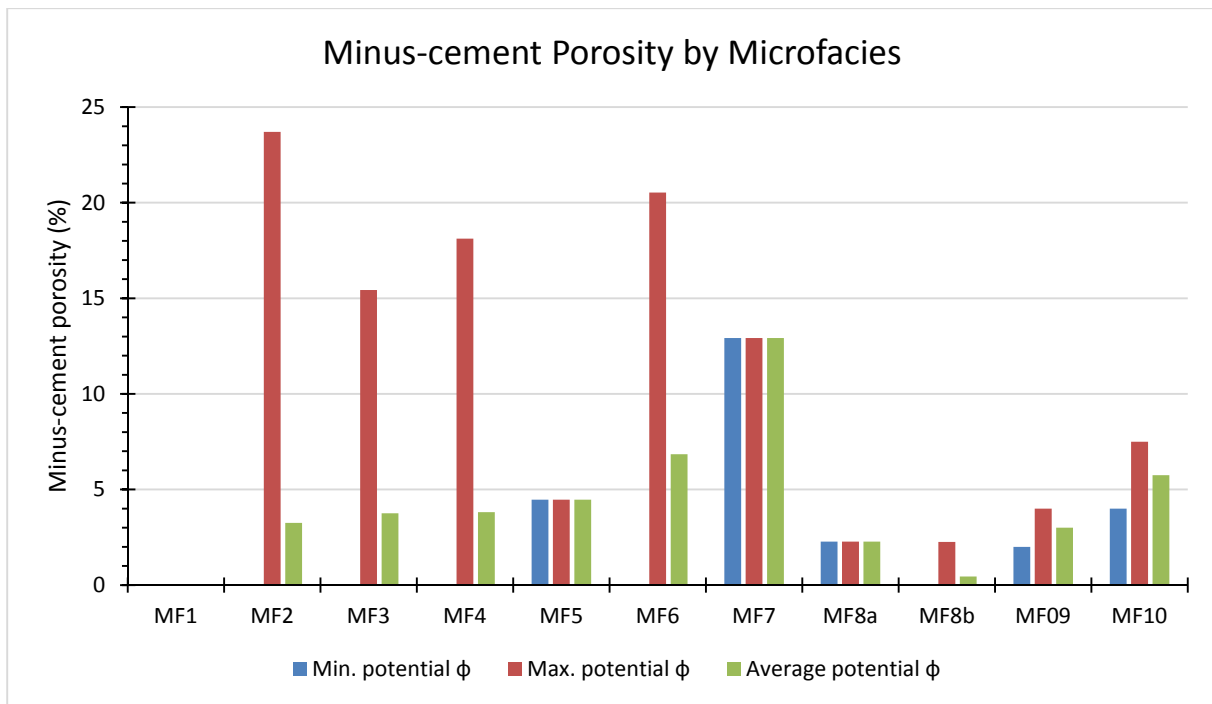


Figure 5.8: Minus-cement porosity with associated microfacies. The minus-cement porosity represents the porosity derived from image analysis and the volumetrically abundance of ferroan calcite cement. Note that the inner-ramp deposits (MF2, MF3, MF4, MF5, MF6 and MF7) have the highest porosity potential.

The present pore space cemented by ferroan calcite cement is estimated subjectively by visual comparison with Terry and Chilingar (1955) comparison chart for visual percentage estimation (Appendix D; Appendix G; WellCAD logs).

An interactive tool for predicting potential hydrocarbon pore volume (HCPV) of the Serdj Fm. has been developed. HCPV is the product of Bulk Rock Volume (BRV), net/gross ratio (N/G), oil saturation (S_o) and porosity (in this case minus-cement porosity). The tool requires several inputs, some of which have to be assumed. The intention of the tool is to predict HCPV given a set of input values (“what if” type of analyses). User-defined net average values for N/G, S_o and minus-cement porosity (porosity plus ferroan calcite cement), can be used as input in the interactive tool, given on the following page, to estimate potential HCPV relative to BRV. Note that N/G in J.Fadeloun is based on number of samples and not thickness.

NB! The interactive prediction tool will only work if use of Flash is accepted. Once the user press “allow one time” (or “always allow”), the file must be closed and reopened. Failure to do so, or if Flash is not installed, will give a blank page. Instructions on using the interactive tool are given within the tool.

The interactive prediction tool has been applied to estimate the potential HCPV for the Serdj Fm., using input data from the J.Fadeloun section, and assuming that the late ferroan calcite cement is absent (postdates oil migration) in a reservoir case situation. Porosity cut-offs depend on hydrocarbon composition and phase, pore geometry, and pore size (Lønøy, 2006). For simplicity a minus-cement porosity cut-off of 5% was applied to define net reservoir, and was based on the porosity definition of Ahr (2008). Input on oil saturation is uncertain, and a net average saturation of 70% was applied.

11 of the 50 samples show a minus-cement porosity exceeding 5%, giving a N/G ratio of 0.22. The average net minus-cement porosity was calculated to 10.8% based on the J.Fadeloun samples. The default input values in the interactive tool presented on the previous page are set to the aforementioned values, where N/G and net average minus-cement porosity is based on actual data from J.Fadeloun.

The interactive tool gives the HCPV as a function as BRV, and the STOOIP (Stock Tank Oil Originally In Place) or GIIP (Gas Initially In Place) can be calculated by dividing the HCPV with the formation volume factors (B_o and B_g for oil and gas, respectively). For a tentative BRV of 1250 million m^3 , the default input values give a HCPV of 20.8 million m^3 .

Low and high case HCPV scenarios were calculated using a N/G and minus-cement porosity of 0.1 and 5%, and 0.5 and 15%, respectively. Average net S_o and BRV were fixed at previously applied values (70% and 1250 million m^3 , respectively). This gave a HCPV of 4.4 million m^3 for the low case, and 65.6 million m^3 for the high case.

A case was run based on actual N/G and ImageJ porosities (not minus-cement porosity), using the same porosity cutoff, net average S_o and BRV as in previous cases. This gave a N/G of 0.06, a net average porosity of 12.6%, and a HCPV of 6.6 million m^3 .

The use of minus-cement porosity instead of porosity gives the hydrocarbon potential of the Serdj Fm. based on input data from the J.Fadeloun section.

UV-microscopy studies have shown fluorescent hydrocarbons trapped in ferroan calcite cemented fractures at J.Garci (Figure 4.22). This indicates that oil migration in fact may predate at least some of the ferroan calcite cement, and that the use of minus-cement porosity in the HCPV calculations may be reasonable.

5.5 Proposed further studies

- Additional stratigraphical logging covering a laterally more extensive area to better understand lateral variations in facies distribution, heterogeneity and thickness. A more extensive stratigraphical logging could also better reveal the diagenetic evolution in a sequence stratigraphic framework.
- More extensive and systematic measurements of plug-derived porosities and permeabilities. This will help to establish the reservoir potential for the Serdj Fm. within the Fkririne permit.
- Integrate reservoir characterization studies with structural analyses, especially related to fracture studies.
- A geostatistical reservoir model comprising larger and more systematic data sets could be developed in order to determine fluid flow.

6. Conclusions

The study of Serdj Fm. in Jebel Fadeloun and Jebel Garci has shown several interesting features. The main findings is based on field observations, petrographic studies, porosity estimations, permeability measurements and estimations, fluid inclusions, stable isotope $\delta^{18}\text{O}$, $\delta^{13}\text{C}$ analyses, and radiogenic $^{87}\text{Sr}/^{86}\text{Sr}$ analyses.

The main conclusions are:

- The Aptian carbonate ramp at Jebel Fadeloun and Jebel Garci constitutes a distally steepened carbonate ramp composed of four shallowing upward cycles. The carbonate ramp was defined on the basis of microfacies distribution and the heterozoan or temperate water grain assemblage.
- The Serdj Fm. of Jebel Garci constitutes a condensed section of Aptian deep marine deposits. The deposits represent deposition below SWB in an outer ramp/basinal setting, and were defined on the basis of microfacies distribution and association. Jebel Garci deposits are interpreted to be more distal ramp deposits compared to those at Jebel Fadeloun.
- Eleven microfacies were defined on the basis of detailed thin section studies, of which nine were exclusively observed within the Jebel Fadeloun section, whereas the last two were exclusively found within the Jebel Garci section. Ten of the microfacies observed occur within Aptian deposits, whereas one microfacies (MF1) occur within Albian deposits. The observed microfacies within Jebel Fadeloun and Jebel Garci closely fit the typical, published facies models for a carbonate ramp.
- Three sedimentary surfaces were observed within the studied sections:
 - Paleokarst surface (Jebel Fadeloun)
 - Hardground (top Aptian Jebel Garci)
 - Paleosol (Jebel Fadeloun)

- The paleokarst surface is observed as an irregular bedding surface in the Jebel Fadeloun section and probably relates to karstification within the vadose zone.
- A 10-20cm thick hardground was observed at the top of the Aptian section in Jebel Garci. The hardground consists of an extensively bored and massive bed composed of bioclastic wacke- to packstone. The bed, which is rich in iron and has a high abundance of echinoderms, belemnites and some bivalve fragments, probably represented a longer period of non-deposition.
- Paleosol horizons are observed within the Jebel Fadeloun section and indicate periods of subaerial exposure and soil development.
- Eogenetic alteration in Jebel Fadeloun and Jebel Garci occurred shortly after deposition in the marine diagenetic environment. Microbial micritization by endolithic organisms and early marine cementation produced:
 - Isopachous rims of fibrous to granular calcite cement on benthic foraminifera, bivalves and red algae fragments.
 - Syntaxial calcite cement overgrowths on echinoderm fragments. Cement precipitation probably started shortly after deposition of the sediment, possibly synchronously with the precipitation of the early marine isopachous calcite cement (see above), and may have continued during burial of the sediment.
- Mesogenetic and telogenetic alteration occurred after burial and later uplift, respectively, and are represented by precipitation of a wide range of different cements:
 - Non-ferroan equant calcite cement is filling interparticle pore space, and relates to precipitation in the meteoric (phreatic or vadose) or burial environments.
 - Ferroan equant calcite is related to deep burial cementation.
 - Pendant cement (gravitational or micro-stalactitic cement) developed within the meteoric-vadose zone.

- Speleothems are commonly related to cement precipitation induced by degassing of supersaturated fresh water pore fluids, and typically occur within karst caves (“surface karst”).
- Fractures are observed with different degrees of cementation, from open to completely cemented. Open and partly open fractures are expected to give good field permeabilities and high flow rates. Ferroan calcite cemented fractures may be open in an oil saturated reservoir, giving increased permeabilities and flow rates.
- The reservoir quality of the Serdj Fm. is relatively poor with porosities and permeabilities mostly in the range 0-6% and 0-88mD, respectively. Pore types are predominantly composed of interparticle (uniformly distributed micro and meso) and macro-mouldic pores. Most of the high permeabilities are probably related to measurement inaccuracies (instrument gas leakage) or fractures.
- Equant ferroan calcite cement related to deep burial diagenesis postdates at least some of the oil migration. Given an oil trap, the ferroan calcite may be absent and the reservoir quality may potentially be significantly better. The minus-cement porosity may thus be a better measure of the reservoir potential of the Serdj Fm.
- The Serdj Fm. has some reservoir potential given that oil migration predates late ferroan calcite cementation. In this case the average N/G increases from 0.06 to 0.22 and average net porosity decreases from 12.6% to 10.8%, all based on a 5% porosity cutoff. The resulting HCPV depends on BRV, and at a BRV of 1250 million m³, the HCPV increases from 6.6 to 20.8 million m³. Using a tentative B_o of 1.1, the potential STOOIP increases from ca. 6 to 19 million m³.

7. References

- Ahlbrandt, T. S., 2001, The Sirte Basin Province of Libya: Sirte-Zelten Total Petroleum System, US Department of the Interior, US Geological Survey.
- Ahr, W. M., 2008, Geology of carbonate reservoirs, Wiley publication. 277p.
- Archie, G. E., 1952, Classification of carbonate reservoir rocks and petrophysical considerations: AAPG Bulletin, v. 36, no. 2, p. 278-298.
- Bathurst, R., 1966, Boring algae, micrite envelopes and lithification of molluscan biosparites: Geological Journal, v. 5, no. 1, p. 15-32.
- , 1971, Carbonate sediments and their diagenesis: Developments in sedimentology (no. 12).
- Baumiller, T., 2001, Light stable isotope geochemistry of the crinoid skeleton and its use in biology and paleobiology: Echinoderms, p. 107-112.
- Ben Ferjani, A., Burolet, P. F., and Mejri, F., 1990, Petroleum geology of Tunisia: ETAP, Tunis.
- Berner, R. A., 1974, Kinetic models for the early diagenesis of nitrogen, sulfur, phosphorus, and silicon in anoxic marine sediments: The sea, v. 5, p. 427-450.
- Bishop, W. F., 1975, Geology of Tunisia and adjacent parts of Algeria and Libya: AAPG bulletin, v. 59, no. 3, p. 413-450.
- , 1988, Petroleum geology of east-central Tunisia: AAPG Bulletin, v. 72, no. 9, p. 1033-1058.
- Bjorlykke, K., 2010, Petroleum geoscience: From sedimentary environments to rock physics, Springer Science & Business Media.
- Boop, L. M., 2014, Characterization of the Depositional Environment of Phreatic Overgrowths on Speleothems in the Littoral Caves of Mallorca (Spain): a Physical, Geochemical, and Stable Isotopic Study.
- Boote, D. R., Clark-Lowes, D. D., and Traut, M. W., 1998, Palaeozoic petroleum systems of North Africa: Geological Society, London, Special Publications, v. 132, no. 1, p. 7-68.
- Bouaziz, S., Barrier, E., Soussi, M., Turki, M. M., and Zouari, H., 2002, Tectonic evolution of the northern African margin in Tunisia from paleostress data and sedimentary record: Tectonophysics, v. 357, no. 1, p. 227-253.
- Brandano, M., Frezza, V., Tomassetti, L., and Cuffaro, M., 2009, Heterozoan carbonates in oligotrophic tropical waters: the Attard member of the lower coralline limestone formation (Upper Oligocene, Malta): Palaeogeography, Palaeoclimatology, Palaeoecology, v. 274, no. 1, p. 54-63.
- Budd, D. A., and Perkins, R. D., 1980, Bathymetric zonation and paleoecological significance of microborings in Puerto Rican shelf and slope sediments: Journal of Sedimentary Research, v. 50, no. 3.
- Budd, D. A., Saller, A. H., and Harris, P. M., 1995, Unconformities and porosity in carbonate strata, American Association of Petroleum Geologists.
- Burchette, T., and Wright, V., 1992, Carbonate ramp depositional systems: Sedimentary Geology, v. 79, no. 1, p. 3-57.
- Burolet, P., 1991, Structures and tectonics of Tunisia: Tectonophysics, v. 195, no. 2, p. 359-369.
- Burolet, P., Mugniot, J., and Sweeney, P., 1978, The geology of the Pelagian Block: the margins and basins off southern Tunisia and Tripolitania, The ocean basins and margins, Springer, p. 331-359.
- Burruss, R. C., 1991, Practical aspects of fluorescence microscopy of petroleum fluid inclusions.
- Calner, M., 2002, A lowstand epikarstic intertidal flat from the middle Silurian of Gotland, Sweden: Sedimentary Geology, v. 148, no. 3, p. 389-403.
- Cavailles, T., 2015, Vitrinite analysis of Serdj Fm. .
- Chilingarian, G. V., Mazzullo, S. J., Rieke, H. H., Dominguez, G., and V., F. S., 1992, Carbonate reservoir characterization: a geologic-engineering analysis, Elsevier Amsterdam.

- Choquette, P. W., and James, N. P., 1987, Diagenesis# 12. Diagenesis in Limestones-3. The deep burial environment: *Geoscience Canada*, v. 14, no. 1.
- Choquette, P. W., and Pray, L. C., 1970, Geologic nomenclature and classification of porosity in sedimentary carbonates: *AAPG bulletin*, v. 54, no. 2, p. 207-250.
- Coward, M., and Dietrich, D., 1989, Alpine tectonics—an overview: Geological Society, London, Special Publications, v. 45, no. 1, p. 1-29.
- Dewey, J., Helman, M., Knott, S., Turco, E., and Hutton, D., 1989, Kinematics of the western Mediterranean: Geological Society, London, Special Publications, v. 45, no. 1, p. 265-283.
- Dickson, J. A. D., 1966, Carbonate Identification and Genesis as Revealed by Staining: *Journal of Sedimentary Petrology*, v. 36, no. 2, p. 491-&.
- Dunham, R. J., 1962, Classification of carbonate rocks according to depositional textures.
- Embry, A. F., and Klovan, J. E., 1971, A Late Devonian reef tract on northeastern Banks Island, NWT: *Bulletin of Canadian Petroleum Geology*, v. 19, no. 4, p. 730-781.
- Entreprise Tunisienne d'Activités Pétrolières, 1997, Tunisian Stratigraphic Chart: Tunis, Tunisia, Entreprise Tunisienne d'Activités Pétrolières, Entreprise Tunisienne d'Activités Pétrolières.
- Epstein, S., Buchsbaum, R., Lowenstam, H. A., and Urey, H. C., 1953, Revised carbonate-water isotopic temperature scale: *Geological Society of America Bulletin*, v. 64, no. 11, p. 1315-1326.
- Esso, 1988, Esso - Carbonate manual.
- Esteban, M., and Klappa, C. F., 1983, Subaerial exposure environment, Carbonate depositional environments, Volume 33, American Association of Petroleum Geologists Tulsa, Okla, p. 1-54.
- Esteban, M., Purdy, E. G., and Wilson, J. L., 1997, Carbonates fields database.
- Fadhel, M. B., Zouaghi, T., Amri, A., and Youssef, M. B., 2014, Radiolarian and planktic foraminifera biostratigraphy of the Early Albian organic rich beds of Fahdene Formation, Northern Tunisia: *Journal of Earth Science*, v. 25, no. 1, p. 45-63.
- Filomena, C., Hornung, J., and Stollhofen, H., 2014, Assessing accuracy of gas-driven permeability measurements: a comparative study of diverse Hassler-cell and probe permeameter devices: *Solid Earth*, v. 5, no. 1, p. 1-11.
- Finetti, I., 1982, Structure, stratigraphy and evolution of central Mediterranean: *Bollettino di Geofisica Teorica e Applicata*, v. 14, p. 247-312.
- Flecker, R., and Ellam, R., 2006, Identifying Late Miocene episodes of connection and isolation in the Mediterranean—Paratethyan realm using Sr isotopes: *Sedimentary Geology*, v. 188, p. 189-203.
- Flügel, E., 2004, *Microfacies of carbonate rocks: analysis, interpretation and application*, Springer.
- George, S. C., Ruble, T. E., Dutkiewicz, A., and Eadington, P. J., 2001, Assessing the maturity of oil trapped in fluid inclusions using molecular geochemistry data and visually-determined fluorescence colours: *Applied Geochemistry*, v. 16, no. 4, p. 451-473.
- Given, R. K., and Wilkinson, B. H., 1985, Kinetic control of morphology, composition, and mineralogy of abiotic sedimentary carbonates: *Journal of Sedimentary Research*, v. 55, no. 1.
- Gluyas, J., and Swarbrick, R., 2009, *Petroleum geoscience*, John Wiley & Sons.
- Goldstein, R. H., and Reynolds, T. J., 1994, Systematics of fluid inclusions in diagenetic minerals: *SEPM Short Course 31: Society for Sedimentary Geology*, p. 199.
- Grossman, E., 2012, *Oxygen isotope stratigraphy*.
- Grossman, E. L., 1987, Stable isotopes in modern benthic foraminifera; a study of vital effect: *The Journal of Foraminiferal Research*, v. 17, no. 1, p. 48-61.
- Guiraud, R., 1998, Mesozoic rifting and basin inversion along the northern African Tethyan margin: an overview: Geological Society, London, Special Publications, v. 132, no. 1, p. 217-229.
- Hammuda, O., Van Hinte, J., and Nederbragt, S., 1992, Geohistory analysis mapping in central and southern Tarabulus Basin, northwestern offshore of Libya: *The geology of Libya*, v. 5, p. 1657-1680.

- Harrison, R. S., and Steinen, R. P., 1978, Subaerial crusts, caliche profiles, and breccia horizons: comparison of some Holocene and Mississippian exposure surfaces, Barbados and Kentucky: Geological Society of America Bulletin, v. 89, no. 3, p. 385-396.
- Hays, P. D., and Grossman, E. L., 1991, Oxygen isotopes in meteoric calcite cements as indicators of continental paleoclimate: *Geology*, v. 19, no. 5, p. 441-444.
- Huysmans, M., Peeters, L., Moermans, G., and Dassargues, A., 2008, Relating small-scale sedimentary structures and permeability in a cross-bedded aquifer: *Journal of hydrology*, v. 361, no. 1, p. 41-51.
- James, N., 1997, The cool-water carbonate depositional realm: Special Publication-SEPM, v. 56, p. 1-22.
- James, N. P., and Choquette, P. W., 1983, Diagenesis 6. Limestones—the sea floor diagenetic environment: *Geoscience Canada*, v. 10, no. 4.
- , 1984, Diagenesis 9. Limestones-the meteoric diagenetic environment: *Geoscience Canada*, v. 11, no. 4.
- , 1988, *Paleokarst*, Springer.
- Jongsma, D., van Hinte, J. E., and Woodside, J. M., 1985, Geologic structure and neotectonics of the North African continental margin south of Sicily: *Marine and petroleum Geology*, v. 2, no. 2, p. 156-179.
- Kalantari, A., 1986, Microfacies of carbonate rocks of Iran, Geological Laboratories, National Iranian Oil Company.
- Kjelkenes, F., 2015, Cross-cutting relationships.
- Klett, T. R., 2000, Total Petroleum Systems of the Illizi Province, Algeria and Libya—Tanezzuft-Illizi.
- , 2001, Total Petroleum Systems of the Pelagian Province, Tunisia, Libya, Italy, and Malta--the Bou Dabbous-Tertiary and Jurassic-Cretaceous Composite, US Department of the Interior, US Geological Survey.
- Lees, A., 1975, Possible influence of salinity and temperature on modern shelf carbonate sedimentation: *Marine Geology*, v. 19, no. 3, p. 159-198.
- Lees, A., and Buller, A. T., 1972, Modern temperate-water and warm-water shelf carbonate sediments contrasted: *Marine Geology*, v. 13, no. 5, p. M67-M73.
- Lehmann, J., Heldt, M., Bachmann, M., and Negra, M. E. H., 2009, Aptian (Lower Cretaceous) biostratigraphy and cephalopods from north central Tunisia: *Cretaceous Research*, v. 30, no. 4, p. 895-910.
- Lindholm, R., and Finkelman, R. B., 1972, Calcite Staining: Semiquantitative Determination of Ferrous Iron: *NOTES: Journal of Sedimentary Research*, v. 42, no. 1.
- Lloyd, R., Porosity reduction by chemical compaction - stable-isotope model, *in Proceedings Aapg bulletin-american association of petroleum geologists* 1977, Volume 61, Amer assoc petroleum geologist 1444 s boulder ave, po box 979, tulsa, ok 74101, p. 809-809.
- Longman, M. W., 1980, Carbonate diagenetic textures from nearsurface diagenetic environments: *AAPG Bulletin*, v. 64, no. 4, p. 461-487.
- Lønøy, A., 2005, Carbonate grains, texture, cements and porosity manual: University of Tromsø.
- , 2006, Making sense of carbonate pore systems: *AAPG bulletin*, v. 90, no. 9, p. 1381-1405.
- Lucia, F. J., 1983, Petrophysical parameters estimated from visual descriptions of carbonate rocks: a field classification of carbonate pore space: *Journal of Petroleum Technology*, v. 35, no. 03, p. 629-637.
- , 1995, Rock-fabric/petrophysical classification of carbonate pore space for reservoir characterization: *AAPG bulletin*, v. 79, no. 9, p. 1275-1300.
- , 1999, *Carbonate reservoir characterization*, Springer.
- , 2007, *Carbonate reservoir characterization: an integrated approach*, Springer Science & Business Media.
- M'rabet, A., 1984, Neocomian deltaic complex in Central Tunisia: a particular example of ancient sedimentation and basin evolution: *Sedimentary geology*, v. 40, no. 1, p. 191-209.

- Martin, E., Shackleton, N., Zachos, J., and Flower, B. P., 1999, Orbitally-tuned Sr isotope chemostratigraphy for the late middle to late Miocene: *Paleoceanography*, v. 14, no. 1, p. 74-83.
- Mattoussi Kort, H., Gasquet, D., Ikenne, M., and Laridhi Ouazaa, N., 2009, Cretaceous crustal thinning in North Africa: Implications for magmatic and thermal events in the Eastern Tunisian margin and the Pelagic Sea: *Journal of African Earth Sciences*, v. 55, no. 5, p. 257-264.
- McArthur, J., 1994, Recent trends in strontium isotope stratigraphy: *Terra nova*, v. 6, no. 4, p. 331-358.
- McArthur, J., Howarth, R., and Bailey, T., 2001, Strontium isotope stratigraphy: LOWESS version 3: Best fit to the marine Sr-isotope curve for 0–509 Ma and accompanying look-up table for deriving numerical age: *The Journal of Geology*, v. 109, no. 2, p. 155-170.
- McCutchan, J. H., Lewis, W. M., Kendall, C., and McGrath, C. C., 2003, Variation in trophic shift for stable isotope ratios of carbon, nitrogen, and sulfur: *Oikos*, v. 102, no. 2, p. 378-390.
- Mejri, F., Burollet, P., and Ben Ferjani, A., 2006, Petroleum geology of Tunisia, a renewed synthesis: *Entrep Tunis Activ Petrol, Mem*, no. 22, p. 233.
- Moez, B. F., Mohamed, S., Taher, Z., Layeb, M., Ahlem, A., and Mohamed, B. Y., 2012, Radiolarian Age Constraints of Mid-Cretaceous Black Shales in Northern Tunisia.
- Moore, C. H., 2001, Carbonate reservoirs: Porosity, evolution & diagenesis in a sequence stratigraphic framework: Porosity evolution and diagenesis in a sequence stratigraphic framework, Elsevier.
- Morgan, M. A., Grocott, J., and Moody, R. T., 1998, The structural evolution of the Zaghuan-Ressas structural belt, northern Tunisia: *Geological Society, London, Special Publications*, v. 132, no. 1, p. 405-422.
- Munnecke, A., Westphal, H., Reijmer, J. J., and Samtleben, C., 1997, Microspar development during early marine burial diagenesis: a comparison of Pliocene carbonates from the Bahamas with Silurian limestones from Gotland (Sweden): *Sedimentology*, v. 44, no. 6, p. 977-990.
- North, F., 1985, *Petroleum geology*, Allen & Unwin Boston.
- Park, W. C., and Schot, E. H., 1968, Stylolites: their nature and origin: *Journal of Sedimentary Research*, v. 38, no. 1.
- Read, J. F., 1985, Carbonate platform facies models: *AAPG bulletin*, v. 69, no. 1, p. 1-21.
- Richter, D. K., and Füchtbauer, H., 1978, Ferroan calcite replacement indicates former magnesian calcite skeletons: *Sedimentology*, v. 25, no. 6, p. 843-860.
- Rykkje, J., 2015, Fluid inclusions.
- Saadi, J., 1990, Exemple de sédimentation syntectonique au Crétacé inférieur le long d'une zone de décrochement NS.: les structures d'Enfidha (Tunisie nord-orientale): *Géodynamique*, v. 5, no. 1, p. 17-33.
- Salaj, J., 1978, The geology of the Pelagian block: the eastern Tunisian platform, The ocean basins and margins, Springer, p. 361-416.
- Schmoker, J. W., Krystinik, K. B., and Halley, R. B., 1985, Selected characteristics of limestone and dolomite reservoirs in the United States: *AAPG Bulletin*, v. 69, no. 5, p. 733-741.
- Seilacher, A., 2007, *Trace fossil analysis*, Springer Science & Business Media.
- Seilacher, A., Buatois, L. A., and Gabriela Mángano, M., 2005, Trace fossils in the Ediacaran–Cambrian transition: Behavioral diversification, ecological turnover and environmental shift: *Palaeogeography, Palaeoclimatology, Palaeoecology*, v. 227, no. 4, p. 323-356.
- Sharp, Z., 2007, *Principles of stable isotope geochemistry*, Pearson education Upper Saddle River, NJ.
- Shinn, E. A., 1969, Submarine lithification of Holocene carbonate sediments in the Persian Gulf: *Sedimentology*, v. 12, no. 1-2, p. 109-144.
- Smith, A. M., and Nelson, C. S., 2003, Effects of early sea-floor processes on the taphonomy of temperate shelf skeletal carbonate deposits: *Earth-Science Reviews*, v. 63, no. 1, p. 1-31.
- Spalluto, L., 2012, Microfacies analysis of the Jurassic and Cretaceous carbonate units from the Fkirine permit (Jebel Zaress, Jebel Fkirine, Jebel Fadloun, and Bent Saidane), Jebel Stah (Hill 442) and Jebel Zaghuan area (Sisi Taya).

- Suchý, V., 2002, The "white beds"—a fossil caliche of the Barrandian area: its origin and paleoenvironmental significance: *Journal of the Czech Geological Society*, v. 47, no. 1-2, p. 45-54.
- Tawadros, E., 2011, *Geology of North Africa*, CRC Press.
- Tebbutt, G. E., Conley, C. D., and Boyd, D. W., 1965, Lithogenesis of a distinctive carbonate rock fabric: *Rocky Mountain Geology*, v. 4, no. 1, p. 1-13.
- Terry, R. D., and Chilingar, G. V., 1955, Summary of "Concerning some additional aids in studying sedimentary forams": *Journal of Sedimentary Research*, v. 25, no. 3.
- Tucker, M. E., 1993, Carbonate diagenesis and sequence stratigraphy, *Sedimentology Review 1*, Blackwell Scientific Publications Oxford, p. 57-72.
- Tucker, M. E., and Wright, V. P., 1990, Carbonate mineralogy and chemistry: *Carbonate Sedimentology*, p. 284-313.
- , 2009, *Carbonate sedimentology*, John Wiley & Sons.
- Walter, L. M., and Morse, J. W., 1984, Reactive surface area of skeletal carbonates during dissolution: effect of grain size: *Journal of Sedimentary Research*, v. 54, no. 4.
- Weber, J. N., 1968, Fractionation of the stable isotopes of carbon and oxygen in calcareous marine invertebrates—the Asteroidea, Ophiuroidea and Crinoidea: *Geochimica et Cosmochimica Acta*, v. 32, no. 1, p. 33-70.
- Wilson, J. L., 1975, *Carbonate facies in geologic history*, Springer-Verlag New York.
- Winland, H., 1968, The role of high Mg calcite in the preservation of micrite envelopes and textural features of aragonite sediments: *Journal of Sedimentary Research*, v. 38, no. 4.
- Wright, V. P., 1989, Terrestrial stromatolites and laminar calcretes: a review: *Sedimentary Geology*, v. 65, no. 1, p. 1-13.
- , 1992, A revised classification of limestones: *Sedimentary Geology*, v. 76, no. 3, p. 177-185.
- , 1994, Paleosols in shallow marine carbonate sequences: *Earth-Science Reviews*, v. 35, no. 4, p. 367-395.
- Wright, V. P., and Burchette, T. P., 1998, *Carbonate ramps: an introduction*: Geological Society, London, Special Publications, v. 149, no. 1, p. 1-5.
- Zeff, M. L., and Perkins, R. D., 1979, Microbial alteration of Bahamian deep-sea carbonates: *Sedimentology*, v. 26, no. 2, p. 175-201.

APPENDIX

Appendix A:

Stable isotope data for oxygen and carbon (‰ VPDB), and radiogenic strontium data.

Unit #	MF #	Sample #	Mean $\delta^{18}\text{O}/^{16}\text{O}$	Mean $\delta^{13}\text{C}/^{12}\text{C}$	Mean $\delta^{87}\text{Sr}/^{86}\text{Sr}$	Sampled Material	Locality*
		JF-14S	-2.76	3.15	0.707852	Bulk	JF
		JF-16S	-2.35	3.37	-	Bulk	JF
		JF-17S	-3.19	2.93	-	Bulk	JF
		JF-22S	-2.66	3.2	-	Bulk	JF
		JF-30S	-2.56	3.09	-	Bulk	JF
		JF-35S	-2.05	2.26	-	Bulk	JF
		JF-40S	-2.19	3.14	-	Bulk	JF
		JF-45S	-2.45	2.93	-	Bulk	JF
		JF-49S	-2.4	3.29	0.707503	Bulk	JF
		JF-57S	-2.06	3.35	0.707488	Bulk	JF
		JF-60S	-2.44	2.64	0.707688	Bulk	JF
		JF-66S	-3.16	3.08	0.707568	Bulk	JF
		JF-69S	-2.46	3.08	0.707551	Bulk	JF
		JF-74S	-3.16	2.33	-	Bulk	JF
		JF-80S	-1.78	2.09	0.707622	Bulk	JF
		JF-87S	-1.75	0.82	0.707608	Bulk	JF
		NFS-1S	-2.46	3.69	0.707727	Bulk	NFS
		NFS-3S	-2.69	3.96	0.707603	Bulk	NFS
		NFS-5S	-1.83	3.54	0.707722	Bulk	NFS
		GS-1S	-3.32	3.1	0.708761	Bulk	GS
		GS-4S	-2.76	2.91	0.708411	Bulk	GS
		GS-6S	-3.15	3.67	0.707841	Bulk	GS

*JF = Southern J. Fadeloun, NFS = Northern J.Fadeloun, GS = J.Garci Section

Appendix B:

Porosity and permeability data from image analysis, plug and Tiny Perm II measurements.

MF #	MF – Name	Sample #	Porosity (%)	Permeability (mD)	Grain density (g/cm ³)	Measurement type*
Southern J.Fadeloun (JF)						
		JF-87S (ALBIAN)	0	0	-	TP
		JF-86S	0.42	0	-	TP
		JF-85S	0	0	-	TP
		JF-83S	0	0	-	TP
		JF-80S (ALBIAN?)	0	0	-	TP
		JF-78S	0.47	20.50	-	TP
		JF-76S	0	0	-	TP
		JF-74S	0	0	-	TP
		JF-71S	1.18	0	-	TP
		JF-70S	0.84	0	-	TP
		JF-69S	0	0	-	TP
		JF-66S	0	0	-	TP
		JF-64S	0.14	0	-	TP
		JF-60S	0	0	-	TP
		JF-57S	0	58.22	-	TP
		JF-56S	0.60 (2.52)	0 (<0.1)	2.71	TP - PL
		JF-54S	0.73	2.29	-	TP
		JF-52S	0	163.09	-	TP
		JF-51S	4.50	4.88	-	TP
		JF-50S	2.02	623.95	-	TP
		JF-49S	0	0	-	TP
		JF-48S	0	0	-	TP
		JF-47S	0.09	22.22	-	TP
		JF-45S	0.85	0	-	TP
		JF-43s	0	2.35	-	TP
		JF-42S	16.12	461.21	-	TP
		JF-41S	0	5.34	-	TP
		JF-40S	0	19.31	-	TP
		JF-37S	6.20	0	-	TP
		JF-36S	0.76	0	-	TP
		JF-35S	0	0	-	TP
		JF-33S	0	2.87	-	TP
		JF-30S	0	4.63	-	TP
		JF-27S	5.53	88.63	-	TP
		JF-26S	<1	0	-	TP
		JF-24S	<1	2.87	-	TP
		JF-23S	0	0	-	TP
		JF-22S	0.43	0	-	TP

		JF-21S	0	0	-	TP
		JF17S	<1	0	-	TP
		JF-16S	0 (0.91)	0 (<0.1)	2.70	TP - PL
		JF-14S	0	0	-	TP
		JF-10S	0	0	-	TP
		JF-11S	0.27	3.59	-	TP
Northern J.Fadeloun (NFS)						
		NFS-5S	0	0	-	TP
		NFS-9S	0	0	-	TP
		NFS-4S	0.25	0	-	TP
		NFS-3S	0	0	-	TP
		NFS-2S	0	0	-	TP
		NFS-1S	0	0	-	TP
J.Garci (GS)						
		GS-6S	0	-	-	TP
		GS-5S	0	-	-	TP
		GS-4S	0	-	-	TP
		GS-3S	0	-	-	TP
		GS-2S	0	-	-	TP
		GS-1S	0	-	-	TP

*TP = Tiny Perm II air permeability, PL = Plug Hg measurement.

NB! All porosity values are estimated values derived from image analyses. The only exceptions are the bold values in brackets, which are results derived from plug measurements. A decrease in sample number represents progressively older strata. All permeability results are presented as average permeability as some beds also have lateral measurements within the same bed. It is important to note that samples that show 0% porosity could have some porosity, but the pore spaces are too small to estimate using image analysis. Permeability of 0mD indicates a tight rock, and TinyPerm measurement did not give any result.

Appendix C:

Permeabilities are measured laterally within the same bed, and horizontally throughout the stratigraphy. Results are shown in both measured TinyPerm II values and calculated permeability values in mD (as described in 3.3.1.). All measurements are made parallel to bedding plane. Red colour indicates thin section sample. Measured value of 16, indicates tight rock.

South on limb	Measured values				North on limb	Sample #	Avg. perm.	South on limb	Calculated permeability in mD				North on limb:
11.82	11.87	11.98	11.92	11.8	11.56	JF-78	20	19.23	16.72	12.28	14.53	20.34	39.89
16	16	16	16	16	16	JF-77	0	0	0	0	0	0	0
16	16	16	16	16	16	JF-76	0	0	0	0	0	0	0
16	16	16	16	16	16	JF-75	0	0	0	0	0	0	0
16	16	16	16	16	16	JF-74	0	0	0	0	0	0	0
							0						
16	16	16	16	16	16	JF-58	0	0	0	0	0	0	0
10.88	16	16	11.31	16	16	JF-57	58.22	268.88	0	0	80.46	0	0
16	16	16	16	16	16	JF-56	0	0	0	0	0	0	0
16	16	16	16	16	16	JF-55	0	0	0	0	0	0	0
16	16	11.94	16	16	16	JF-54	2.29	0	0	13.73	0	0	0
16	16	16	16	16	16	JF-53	0	0	0	0	0	0	0
11.22	10.98	10.61	11.51	11.72	11.7	JF-52	163.09	103.57	203.10	573.58	45.90	25.46	26.93
16	16	11.67	16	16	16	JF-51	4.88	0	0	29.30	0	0	0
10.58	11.34	10.6	10.26	10.61	10.79	JF-50	623.16	623.95	73.96	589.90	1531.47	573.58	346.13
16	16	16	16	16	16	JF-49	0	0	0	0	0	0	0
-	-	16	-	-	-	JF-48	0	-	-	0	-	-	-
-	-	11.13	-	-	-	JF-47	22.22	-	-	133.32	-	-	-
16	16	11.93	16	16	16	JF-43	2.35	0	0	14.13	0	0	0
-	10.91	11.59	10.88	11.36	10.14	JF-42	461.21	-	247.18	36.67	268.88	69.92	2144.58
16	16	16	16	11.76	12.08	JF-41	5.34	0	0	0	0	22.76	9.27
16	16	16	11.18	16	16	JF-40	19.31	0	0	0	115.87	0	0
-	10.84	10.75	10.41	10.77	-	JF-39	343.25	-	300.82	387.24	1005.35	366.11	-
16	16	16	16	16	16	JF-35	0	0	0	0	0	0	0
16	11.86	16	16	16	16	JF-33	2.87	0	17.19	0	0	0	0
16	12.16	16	16	11.8	-	JF-30	4.63	0	7.41	0	0	20.34	-
12.19	11.91	10.94	10.87	12.22	-	JF-27	88.63	6.81	14.94	227.22	276.53	6.26	-
16	16	16	16	16	16	JF-25	0	0	0	0	0	0	0
16	16	11.86	16	16	16	JF-19	2.87	0	0	17.19	0	0	0
-	-	-	16	16	-	JF-17	0	-	-	-	0	0	-
16	16	16	16	16	16	JF-16	0	0	0	0	0	0	0
16	16	16	16	16	16	JF-9B	0	0	0	0	0	0	0
16	16	16	16	16	16	JF-15	0	0	0	0	0	0	0
16	16	16	16	16	16	JF-14	0	0	0	0	0	0	0
16	16	16	16	16	16	JF-13	0	0	0	0	0	0	0
16	16	16	16	16	16	JF-12	0	0	0	0	0	0	0
16	16	16	16	16	16	JF-10	0	0	0	0	0	0	0
16	16	11.78	16	16	16	JF-11	3.59	0	0	21.52	0	0	0

Appendix D:

Stable isotope data sorted by relative abundance of ferroan- (Fe^{2+}) rich cement. The abundance is a subjective estimate of the Fe-rich cement content. The colour codes are the same as used in Figure 4.50.

$\delta^{13}\text{C}$ and $\delta^{18}\text{O}$ sorted by ferroan cement abundance					
Sample*	$\delta^{13}\text{C}$ Mean	$\delta^{18}\text{O}$ Mean	Fe-rich calcite cement abundance	Estimated Fe-rich calcite cement (%)	Fracture cement (FR)
JF-16S	3.37	-2.35	0	0	
JF-22S	3.2	-2.66	0	0	
JF-30S	3.09	-2.56	0	0	
JF-69S	3.08	-2.46	0	0	
JF-87S	0.82	-1.75	0	0	
NFS-1S	3.69	-2.46	0	0	
NFS-5S	3.54	-1.83	0	0	
JF-14S	3.15	-2.76	1	1	
JF-40S	3.14	-2.19	1	1	FR
JF-45S	2.93	-2.45	1	1-3	
JF-49S	3.29	-2.4	1	<1	FR
JF-57S	3.35	-2.06	1	1-3	
JF-60S	2.64	-2.44	1	<1	
JF-66S	3.08	-3.16	1	5	
JF-80S	2.09	-1.78	1	<1	FR
NFS-3S	3.96	-2.69	1	<1	
JF-17S	2.93	-3.19	2	3-5	
JF-74S	2.33	-3.16	2	3-5	
GS-1S	3.1	-3.32	2	3-5	
JF-35S	2.26	-2.05	3	15	
GS-4S	2.91	-2.76	3	5-10	
GS-6S	3.67	-3.15	3	3-5	FR

*JF = Southern J.Fadeloun, NFS = Northern J.Fadeloun, GS = J.Garci section

Abbreviation Ferroan Calcite Cement	
0	None
1	Traces/Minor
2	Some
3	Abundant

Appendix E:

Stable isotope data showing estimated associated temperature ranges.

$\delta^{13}\text{C}/^{12}\text{C}$ and $\delta^{18}\text{O}/^{16}\text{O}$ values with associated minimum and maximum temperatures					
Sample*	Depth	d 13C/12C Mean	d 18O/16O Mean	T (C°) min	T (C°) max
JF-14S	145.15	3.15	-2.76	16.84	19.08
JF-16S	140.55	3.37	-2.35	15.05	17.24
JF-17S	138.95	2.93	-3.19	18.77	21.06
JF-22S	135.20	3.2	-2.66	16.40	18.63
JF-30S	129.80	3.09	-2.56	15.96	18.18
JF-35S	124.20	2.26	-2.05	13.76	15.92
JF-40S	112.60	3.14	-2.19	14.36	16.53
JF-45S	98.00	2.93	-2.45	15.48	17.69
JF-49S	90.65	3.29	-2.4	15.27	17.46
JF-57S	77.85	3.35	-2.06	13.80	15.96
JF-60S	75.2	2.64	-2.44	15.44	17.64
JF-66S	68.3	3.08	-3.16	18.63	20.92
JF-69S	59.90	3.08	-2.46	15.53	17.73
JF-74S	58.50	2.33	-3.16	18.63	20.92
JF-80S	45	2.09	-1.78	12.62	14.75
JF-87S	-1.5	0.82	-1.75	12.50	14.62
NFS-1S	55.8	3.69	-2.46	15.53	17.73
NFS-3S	4.8	3.96	-2.69	16.53	18.77
NFS-5S	0.4	3.54	-1.83	12.83	14.96
GS-1S	5	3.1	-3.32	19.36	21.66
GS-4S	3.25	2.91	-2.76	16.84	19.08
GS-6S	0.2	3.67	-3.15	18.58	20.87

*JF = Southern J.Fadeloun, NFS = Northern J.Fadeloun, GS = J.Garci section

Appendix F:

Radiogenic $^{87/86}\text{Sr}$ values with associated ages.

$^{87/86}\text{Sr}$ associated ages					
Sample*	Depth	$^{87/86}\text{Sr}$ corrected	Age (Ma)		
			Min	Best fit	Max
JF-87S	-1.50	0.707608	>75.59	75.76	<75.93
JF-80S	45	0.707622	>74.94	75.13	<75.30
JF-69S	59.9	0.707551	>78.54	78.78	<79.03
JF-66S	68.3	0.707568	>77.60	77.78	<77.99
JF-60S	75.2	0.707688	>72.58	72.69	<72.80
JF-57S	77.85	0.707488	>82.68	82.88	<83.07
JF-49S	90.65	0.707503	>81.77	81.98	<82.19
JF-14S	145.15	0.707852	>32.83	32.98	<33.15
NFS-5S	0.4	0.707722	>71.43	71.56	<71.68
NFS-3S	4.8	0.707603	>75.83	76.00	<76.17
NFS-1S	55.8	0.707727	>71.24	71.38	<71.52
GS-6S	0.2	0.707841	>33.03	33.21	<33.38
GS-4S	3.25	0.708411	>20.59	20.74	<20.88
GS-1S	5	0.708761	>15.42	15.62	<15.8

*JF = Southern J.Fadeloun, NFS = Northern J.Fadeloun, GS = J.Garci section

Appendix G:

Sample	Unit	MF #	Fe-cem.*	Vis. Fe-cem. Est. (%)	Avg. Vis. Fe-cem. (%)	ImageJ porosity (%)	Potential porosity (%)
NFS-9S	G	MF2	2.5	10-15	12.5	0	12.5
NFS-5S			0	0	0	0	0
NFS-4S			0	0	0	0.25	0.25
NFS-3S		MF8b	1	<1	0	0	0
NFS-2S			1	<1	0	0	0
NFS-1S			0	0	0	0	0
JF-87S	F	MF1	0	0	0	0	0
JF-86S	E	MF7	3	10-15	12.5	0.42	12.92
JF-85S		MF2	3	15-20	17.5	0	17.5
JF-83S			1	1-3	2	0	2
JF-80S		MF1	1 (FR)	<1	0	0	0
JF-78S	D	MF5	2	3-5	4	0.47	4.47
JF-76S		MF6	1 (FR)	<1	0	0	0
JF-74S		MF2	2	3-5	0	0	0
JF-71S			1 (FR)	<1	0	1.18	1.18
JF-70S			0	0	0	0.84	0.84
JF-69S			0	0	0	0	0
JF-66S	C	MF3	1.5	5	5	0	5
JF-64S			2	5	5	0.14	5.14
JF-60S		MF2	1 (FR)	<1	0	0	0
JF-57S		MF4	1	1-3	2	0	2
JF-56S			1	1-3	2	0.6	2.6
JF-54S			1	1-3	2	0.73	2.73
JF-52S			1	1-3	2	0	2
JF-51S		MF2	1	3	3	4.5	7.5
JF-50S			1	1-3	2	2.02	4.02
JF-49S			1 (FR)	<1	0	0	0
JF-48S			2	3-5	4	0	4
JF-47S		MF4	1	1-3	2	0.09	2.09
JF-45S		MF2	1	1-3	2	0.85	2.85
JF-43s			1	1	1	0	1
JF-42S		MF4	0	0	0	16.12	16.12
JF-41S		MF4	1	1	1	0	1
JF-40S			MF2	1	1	1	0

JF-37S			1	<1	0	6.2	6.2	
JF-36S		MF8b	1	1-3	1.5	0.76	2.26	
JF-35S	B	MF6	3	15	15	0	15	
JF-33S		MF2	1	1	1	0	1	
JF-30S		MF8b	0	0	0	0	0	
JF-27S	A	MF6	0	0	0	5.53	5.53	
JF-26S		MF3	1	<1	0	0	0	
JF-24S			1	1-3	2	0	2	
JF-23S			3	15	15	0	15	
JF-22S			0	0	0	0.43	0.43	
JF-21S			2 (FR)	5	5	0	5	
JF17S			2	3-5	4	0	4	
JF-16S			0	0	0	0	0	
JF-14S			1	1	1	0	1	
JF-11S			MF8a	3 (FR)	1-3	2	0.27	2.27
JF-10S			MF4	1	1-3	2	0	2
GS-6S			H	MF9	3 (FR)	3-5	4	0
GS-5S		1 (FR)			1-3	2	0	2
GS-4S	MF10	3		5-10	7.5	0	7.5	
GS-3S	MF9	2		1-3	2	0	2	
GS-2S	MF10	2		3-5	4	0	4	
GS-1S	MF9	2		3-5	4	0	4	

*Fe-cement abbreviation: 0 = None; 1 = Traces/Minor; 2 = Some and 3 = Abundant

Appendix H:

Paleotemperatures of pore fluids during precipitation of ferroan calcite cement.

Temperature during percipitation of Fe-Cement						
Sample	$\delta^{13}\text{C}$	$\delta^{18}\text{O}$	Fe-cem. *	Est. Fe-cem. (%)	$\delta^{18}\text{O}$ at 100% Fe-cem.	Temp. percipitation of Fe-Cem. ($^{\circ}\text{C}$)
JF-16	3.37	-2.35	0	0		
JF-22	3.2	-2.66	0	0		
JF-30	3.09	-2.56	0	0		
JF-69	3.08	-2.46	0	0		
JF-87	0.82	-1.75	0	0		
NFS-1	3.69	-2.46	0	0		
NFS-5	3.54	-1.83	0	0		
JF-14	3.15	-2.76	1	1		
JF-40	3.14	-2.19	1	1		
JF-45	2.93	-2.45	1	2		
JF-49	3.29	-2.4	1	1		
JF-57	3.35	-2.06	1	2		
JF-60	2.64	-2.44	1	1		
JF-66	3.08	-3.16	1	5	-15.70	94
JF-80	2.09	-1.78	1	1		
NFS-3	3.96	-2.69	1	1		
JF-17	2.93	-3.19	2	4	-19.75	127
JF-74	2.33	-3.16	2	4	-19.00	120
GS-1	3.1	-3.32	2	4	-23.00	156
JF-35	2.26	-2.05	3	15	0.50	4
GS-4	2.91	-2.76	3	8	-5.97	32
GS-6	3.67	-3.15	3	4	-18.75	118

*Fe-cement abbreviation: 0 = None; 1 = Traces/Minor; 2 = Some and 3 = Abundant

Appendix I-2

Northern Jebel Fadeloun																																					
Sample #	Unit	Microfacies #	Simplified Microfacies	Depth	Texture	Sorting	Grain size (µm) dominant	Microfacies	Grains																	Open Poretypes			Cemented Poretypes			Ferroan calcite cement abundance	Ferroan calcite cement (%) - Visual estimation				
									Echinoderm	Red Algae	Green Algae	Peloids	Quartz	Bivalve	Mollusca	Orbitolina	Other Bentic	Planctonic	Bryozoan	Cephalopods	Gastropod	Ostracoda	Calcisphere	Coral frag.	Sponge spicules	Undifferentiated fossil	Intraclast	BP	MO	WP	BP			MO	WP		
NFS-55	G	2	P/G	0.4	P/G	Moderate	150	Echinoderm-Bivalve-peloidal G	3.5	2	0	4	0	4	2	1	2.5	2.5	0	0	0	0	1.5	0	0	1	2	0	0	0	3	2	2	0	0		
NFS-55				3.6	G	Poor to moderate	150	Echinoderm-Bivalve-Peloidal G	4	0	0	4	0	4	3	2	2	1.5	0	0	0	0	0	0	0	0	0	1	0	0	0	3	3.5	2.5	2.5	10-15	0
NFS-45				4.4	P	Moderate to well	40	Peloidal P	2.5	0	0	4.5	0	2	1	0	2	1	0	0	0	0	1	1.5	0	0	0	0	0	0	0	0	0	1.5	1	0	0
NFS-35		4.8	P	Well	40	Spiculitic-Peloidal P	1	0	0	4.5	0	1.5	0	0	1.5	1	0	0	0	0	1.5	2	0	4	0	0	0	0	0	0	0	1.5	1	1	1	<1	0
NFS-25		21.2	P	Well to very well	30	Spiculitic-Peloidal P	0	0	0	4.5	0	1	0	0	1	2.5	0	0	0	0	0	2	0	4	0	0	0	0	0	0	0	2.5	1	1	1	<1	0
NFS-15	55.8	P	Well	40	Spiculitic-Peloidal P	1	0	0	4	0	1	0	0	1	2.5	0	0	0	0	0	0	1.5	0	4	0	0	0	0	1	0	0	2.5	1	0	0	0	

Appendix I-3

Jebel Garci																																						
Sample #	Unit	Microfacies #	Simplified Microfacies	Depth	Texture	Sorting	Grain size (µm) dominant	Microfacies	Grains																	Open Poretypes			Cemented Poretypes			Ferroan calcite cement abundance	Ferroan calcite cement (%) - Visual estimation					
									Echinoderm	Red Algae	Green Algae	Peloids	Quartz	Bivalve	Foraminifera	Miliolid	Orbitolina	Other Bentic	Planctonic	Bryozoan	Cephalopods	Gastropod	Ostracods	Calcisphere	Coral Frag.	Large spicu	Undifferentiated fossil	Intraclast	BP	MO	WP			BP	MO	WP		
GS-65	H	9	○ W/P	0.20	W/P	Well	80	Foraminifera-Peloidal W/P	1.5	0	0	3.5	0	1	2	0	2.5	1.5	0	0	0	0	1	1	0	1	0	0	0	0	0	0	1.5	1.5	3 (FR)	3-5		
GS-55			○ W/P	3.10	P	Moderate	60	Foraminifera-Peloidal P	2	0	0	4.5	0	2.5	1	0	2.5	1.5	0	0	0	0	2	2	0	0	0	0	0	0	0	0	1.5	2	1 (FR)	1-3		
GS-45			10	▲* P	3.25	P	Moderate	100	Bivalve-Echinoderm-Peloidal P	2.5	0	0	4	0	2	0	0	2	1.5	0	0	0	0	2	1	0	1	1	0	0	1	0	1	2	1.5	3	5-10	
GS-35			9	○ W/P	3.55	P	Well	60	Peloidal P	2	0	0	4.5	0	2	0	0	1	2	0	0	0	0	2	1	0	0	0	0	0	0	1	1	0	2	2	2	1-3
GS-25			10	▲* P	4.30	P	Moderate to poor	120	Foraminifera-Echinoderm-Peloidal P	4	0	0	4	0	2	0	0	2	2	0.5	0	0	0	1.5	1	0	0	0	0	0	0	0	0	2	2	2	3-5	
GS-15		9	○ W/P	5.00	W/P	Well	60	Peloidal W/P	2	0	0	4.5	0	2	1	0	1	2.5	0	0	0	0	1	1	0	1	0	0	0	0	0	0	1.5	2.5	2	3-5		

COMPANY: DNO International ASA		WELL: Outcrop Jebel Garci	
FIELD: Fkirine Permit		COUNTRY: Tunisia	
FILE NAME:		COMPANY: DNO International ASA	
PERMANENT DATUM		WELL ID: Outcrop Jebel Garci	
LOG MEAS FROM		FIELD: Fkirine Permit	
DATE: 2014		COUNTRY: Tunisia	
GROUP/PERFORATION		BASIN:	
AGE: Barremian-Albian-Albian		COORDINATES:	
TPD DEPTH DRILLER		K.R.	
TPD DEPTH LOGGER		D.F.	
RECORDED BY: Bjarne Lassy		G.L.	
CORIS DESCRIBED		CORIS DESCRIBED	
NO.	INTERVAL (m)	RECOVERY (%)	NO.
NO.	INTERVAL (m)	RECOVERY (%)	NO.



LEGEND

Cores, Samples, Test Results			Sedimentological Log			Reservoir Quality/Oil
Test	Core	Samples	Lithology	Fauna/Grains	Sedimentary Structures	Pores/Stain

claystone	Intraclasts	continuous flat lamination	horizontal burrow
limestone	Lithoclasts	Bivalves	oblique burrow
	Echinoderms	Stylolites - horizontal	

